On the dielectrophoretic particle retention in porous media

Vom Fachbereich Produktionstechnik

der

UNIVERSITÄT BREMEN

zur Erlangung des Grades

Doktor-Ingenieur

genehmigte

Dissertation

von

Georg Pesch, M.Sc.

Gutachter: Prof. Dr.-Ing. Jorg Thöming
(Universität Bremen)
Dr. Pouyan Boukany
(Technische Universität Delft, Niederlande)

Tag der mündlichen Prüfung: 31.01.2018

Zusammenfassung

Die Abtrennung von Partikeln aus Flüssigkeiten, im Speziellen die mehrdimensionale Abtrennung von Partikeln kleiner 1 µm, ist eine schwierige und teils ungelöste Aufgabe mit Anwendungen in der chemischen, pharmazeutischen und biomedizinischen Industrie. Abseits der vielen bereits existierenden Technologien mit ihren spezifischen Vor- und Nachteilen ist Dielektrophorese (DEP) eine sehr geeignete Methode zur Lösung einer Reihe von Trennproblemen. DEP ist eine Technik zur Partikelmanipulation und basiert auf der Interaktion eines inhomogenen elektrischen Feldes mit einem induzierten Dipol. Es ist markierungsfrei, sehr sensitiv und, falls richtig eingesetzt, hoch selektiv bezüglich eines spezifischen Zielpartikeltyps.

Abgesehen von einigen wenigen Berichten wurde DEP zum großen Teil in der analytischen und bioanalytischen Chemie erforscht und eingesetzt um Trennprobleme im $\mu L\,min^{-1}$-Maßstab auf Lab-On-A-Chip-Geräten zu lösen. Die DEP-Kraft hängt vom Partikel*volumen* und vom *Gradienten* des *Quadrats* des elektrischen Feldes, $\nabla |\boldsymbol{E}|^2$, ab. Eine Maßstabsvergrößerung hin zu präparativen oder industriellen Durchsätzen ist schwierig, da $\nabla |\boldsymbol{E}|^2$ und damit die Fangkraft rapide mit Distanz von der Elektrodenanordnung abfällt. Das Fangen von 100 nm Partikeln benötigt bereits enorme Maximalwerte von $\nabla |\boldsymbol{E}|^2$ von circa $1 \times 10^{17}\,V^2\,m^{-3}$. Ein vielversprechender Ansatz zur Erzeugung von Gradienten, die stark genug sind um Partikel aus einem erheblichen Volumenstrom abzutrennen, ist die Störung eines ursprünglich homogenen Feldes an den Fest-Flüssig-Phasengrenzen einer hochporösen Trennmatrix, was als dielektrophoretische Filtration bezeichnet wird. Eine Machbarkeitsstudie, die in dieser Arbeit präsentiert wird, zeigt die Möglichkeit der Abtrennung von Nanokapseln die nach dem Layer-by-Layer-Verfahren hergestellt werden (340 nm) bei einem Volumenstrom von $60\,mL\,h^{-1}$ durch das Anlegen von $200\,V_{RMS}$ über einen 2 mm dicken Polyethylenfilter mit Porengrößen zwischen 20 und 60 µm bei einer Abtrennrate von 65 %. Die Ergebnisse wurden erzielt ohne Detailwissen, weder über den Mechanismus der Feldstörung an der Phasengrenze noch über die detaillierte Dynamik der dielektrophoretischen Partikeltrennung in dem porösen Medium. Solches Detailwissen ist allerdings notwendig um sachkundig Filter und Parameter für zukünftige hocheffiziente DEP-Filtrationsprozesse bei hohem Durchsatz auszuwählen.

Diese Arbeit beleuchtet den dielektrophoretischen Partikelrückhalt in quasi zweidimensionalen Säulenfeldern, die als Modell des porösen Mediums dienen. Die ist eine Vereinfachung des ursprünglich komplexen und zufälligen Mediums ohne sich zu weit von der eigentlichen Problemstellung zu lösen. Zum besseren Verständnis des Mechanismus der Feldstörung wird das Polarisationsfeld einer *einzelnen* Säule aus dem Säulenfeld mit Hinblick auf die Form der Phasengrenze erforscht. Hierzu werden die Multipolmomente der induzierten Ladungsverteilung der Säule als Funktion der Querschnittsflächengeometrie und dem Säulenmaterial untersucht. Um den Partikelrückhalt besser zu verstehen werden aus dem resultierenden Polarisationsfeld Trajek-

torien von Partikeln abgeleitet, die unter dem Einfluss von DEP- und Widerstandskraft stehen. Das Potential einer einzelnen Säule zum Partikelrückhalt wird durch den kritischen Anfangsabstand quantifiziert, den ein Partikel von der Säule haben kann um gerade noch aus dem Fluidstrom gefangen zu werden. Der kritische Abstand normalisiert durch den Säulendurchmesser kann als Fangeffizienz verstanden werden. Der Wert wurde als Funktion von Betriebs- und Designparametern (Säulengröße, Säulenform, angelegte Feldstärke, Partikelgröße und Volumenstrom) untersucht um die Parameterabhängigkeiten zu quantifizieren. Es zeigt sich, dass die Form der Säule im Vergleich zu den anderen Parametern nur einen kleinen Einfluss hat.

Zusätzlich wurde die Partikeldynamik an einer einzelnen Säule mit der Partikelabtrennung im *gesamten* Säulenfeld, welche durch Finite Elemente Simulationen und Experimente mit Mikrokanälen aus Polydimethylsiloxan bestimmt wurde, verglichen. Theoretisch hängt die Partikelabtrennrate η nur von einer einzigen Variable $\overline{x}$ ab, in der alle Betriebsparameter, also Feldstärke, Partikelgröße, Durchflussrate und Säulengröße, eingebunden sind. Der Einfluss der einzelnen Parameter auf $\eta(\overline{x})$ ist identisch zu dem Verhältnis des Einflusses der Parameter auf die Einzelsäulenfangeffizienz. Dies hält nur wenn die Säule ausreichend größer als der Säulenabstand ist. Damit lässt sich der Trennprozess durch eine beliebige Variation einer der Parameter einstellen. Der Säulenabstand definiert dabei wie sensitiv η auf eine Änderung von $\overline{x}$ reagiert. Experimente zeigen, dass solch simple Simulationen, basierend auf den Trajektorien von masselosen Partikelmittelpunkten, in den meisten Fällen ausreichen, um die Trenneffizienz unter Zuhilfenahme eines einzigen Anpaßparameters vorauszusagen. Die Simulationen überschätzen allerdings die Abtrennrate im Falle von hohen Durchsätzen, niedrigen angelegten Spannungen und bei kleinem Säulenabstand, was auf die Vernachlässigung des Partikelvolumens in den Simulationen zurückgeführt wird. Die Simulationensergebnisse lassen sich durch eine empirische Korrelation, basierend auf einer simplen Kräftebilanz zwischen DEP und Widerstandskraft an der Säulenoberfläche, korrigieren. Es wird davon ausgegangen, dass die vorgestellten Zusammenhänge auch auf die Abtrennung in realen porösen Medien übertragbar sind.

Die in dieser Arbeit vorgestellten Ergebnisse tragen maßgeblich zum fundamentalen Verständnis des dielektrophoretischen Partikelrückhalts in porösen Medien bei. Zusätzlich erlaubt der Einsatz von transparenten Modellstrukturen die In-situ-Beobachtung der Abtrennung für zukünftige Anwendungen, zum Beispiel den selektiven Partikelrückhalt eines Zielpartikels in einem Gemisch bei industriellen Durchsätzen.

Abstract

Particle separation from liquids and especially multidimensional separation of particles smaller than 1 µm is a challenging and unresolved task with applications in the chemical, pharmaceutical, and biomedical industry. Besides a variety of existing technologies with their respective drawbacks is dielectrophoresis (DEP), a very suitable particle manipulation technique that is able to solve a range of separation problems. DEP is based on the interaction of an inhomogeneous electric field with an induced dipole. It is label-free, very sensitive and, if applied correctly, highly selective towards a specific target particle.

Apart from a few reports, DEP has mostly been researched and applied in analytical or bioanalytical chemistry to solve separation problems on lab-on-a-chip devices at µL min^{-1} throughputs. The DEP force depends on the target particle's *volume* and on the *gradient* of the *square* of the electric field, $\nabla |\boldsymbol{E}|^2$. A scale-up towards preparative or industrial-scale throughputs is difficult since $\nabla |\boldsymbol{E}|^2$ and thus the trapping force rapidly drops with increasing distance from the electrode array. Trapping 100 nm particles already requires vast maximum values of $\nabla |\boldsymbol{E}|^2$ of approximately $1 \times 10^{17}\,\mathrm{V^2\,m^{-3}}$. A promising approach to generate values of $\nabla |\boldsymbol{E}|^2$ high enough to trap particles from a substantial volume flow is the distortion of an originally homogeneous field at the solid-liquid interface of a highly porous separation matrix, a process termed dielectrophoretic filtration. Proof-of-principle results presented in this thesis demonstrate the possibility to separate layer-by-layer-assembled PAH particles (340 nm) at a flow rate of 60 $\mathrm{mL\,h^{-1}}$ by applying 200 $\mathrm{V_{RMS}}$ over a 2 mm-thick polyethylene filter with pores in the range of 20–60 µm at an efficiency of almost 65 %. This was achieved without knowledge of the field distortion mechanism at the solid-liquid interface and detailed dynamics of the dielectrophoretic particle trapping in the porous medium. Such detailed knowledge, however, is important in order to make an informed decision on the employed parameters and filters for a highly efficient high-throughput dielectrophoretic filtration process.

This work scrutinizes the dielectrophoretic particle retention in a quasi two-dimensional array of posts as a model porous medium. This allows for easier description of the originally random complex medium without becoming too detached from the original problem. To gain deeper understanding of the field distortion mechanisms the polarization field of a *single* post is analyzed by investigating the multipolar moments of the post's induced charge distribution a function of the post's cross-sectional geometry and material. To understand the trapping mechanism the resulting polarization potentials were used to derive trajectories of particles subjected to DEP and fluid drag in the vicinity of the post. The trapping potential of single post was quantified by the critical distance a particle can initially have from it to just get trapped. The critical distance normalized by the post's size can be understood as the trapping efficiency and, to quantify the parameter dependencies, it was analyzed with respect to operational and

design parameters (post shape, post size, applied field strength, particle size, and volume flow). It was shown that the post's shape has a small influence compared to all other parameters. The dynamics around single posts were also compared to the particle trapping in the *entire* array of posts which was investigated by finite element simulations and experiments employing polydimethylsiloxane microchannels.

Theoretically, the separation efficiency η depends only on a single variable $\overline{x}$ that incorporates all operational parameters, that is applied voltage, throughput, particle size, and post size, and the influence of all parameters on $\eta(\overline{x})$ is equal to the relations of the parameter's influence on the trapping efficiency of a single post. This holds when the post size is sufficiently larger than the post-to-post spacing. By this the separation can be controlled by an interchangeable variation of the parameters. The post spacing defines how sensitive η reacts to a change of $\overline{x}$. Experiments show that in most cases these simple simulations based on tracking volume-less particle centers can predict the separation efficiency with the requirement of only a single fitting parameter. Simulations over-predict the experimentally obtained separation efficiencies at high throughput, low applied voltage, and narrow post spacing, which was attributed to the neglect of the target particle's finite size in the simulation. Adjusting for this effect is possible by employing an empirical correction factor on the simulated separation efficiencies based on a simple balance of drag and DEP forces on the post's surface. It is assumed that the relations derived here are equally applicable in separation processes employing real porous media.

The results presented in this thesis contribute to the fundamental understanding of DEP particle retention in porous media. Additionally, employing a transparent model porous medium allows for in-situ observation of trapping dynamics in future applications, for example the selective retention of a target particle from a mixture at industrial-scale throughputs, which is a highly relevant separation step in a variety of fields.

Acknowledgement

This work has been developed from October 2013 to October 2017 at the Center for Environmental Research and Sustainable Technology in the framework of the research training group (GRK 1860) "Micro-, meso- and macroporous nonmetallic Materials: Fundamentals and Application" (MIMENIMA) that is funded by the German Research Association (DFG). I would lie if I say that it was always fun. It was an interesting four years, filled with a lot of hard work that resulted in some rewarding experiences and heaps of personal and scientific growth. Simultaneously, at some points the entire undertaking felt just like a giant waste of time. This feeling was so strong that, especially in the third year, I had the profound wish to just leave it all behind and do something entirely else. Interestingly, so many people with doctorate degree tell you that there comes a time when you hit rock bottom and that this will pass since it is just one of the typical stages while working on a PhD. Nevertheless, when you are actually at the bottom it sometimes still feels like there would be no way out of that hole. Luckily I did not quit but instead finished this off which is also thanks to the support I have received from so many people on so many different levels.

I thank Jorg Thöming, not only for supervising my work and reviewing this thesis, but also for his (apparently) unquestionable confidence in my abilities, his unlimited support, his encouraging words, and his calm and thoughtful advice on personal and scientific matters. I am very glad that you have been my supervisor.

I thank Pouyan Boukany for his instant acceptance to be the second reviewer of my thesis, for his time to read and review it, for giving me the chance to present my work to his group, and for giving me the chance to work with the microfluidic channels that were so crucial for finalizing this thesis!

I thank my second supervisor Michael Baune, who is so upright, caring, supportive and with whom I share a great deal of mutual trust. He always has a potpourri of advice on solving my problems, not only in the lab, but sometimes also in my personal life. I enjoy the fact that I see you not only as a supervisor, but also as a friend.

I thank Fei Du, who is my mentor and friend since almost ten years. He helped me on so many levels during the development of this thesis that I have no idea how this work would look without his thoughtful advice. Every time I failed to see how to proceed, you instead never failed on knowing what to do next!

A special thanks to Lars Kiewidt who finished his PhD just weeks before I hand in mine. I thank him for his many scientific and personal advice, all the interesting conversation, and the company on long weekends in the office and on conferences. And of course for not letting me go through all of this alone. I wish him all the best for his next steps at Wageningen University.

I thank Samir Salameh, who appeared out of nowhere and presented such an easy solution to one of my biggest problems. I would also like to thank him for straightforwardly recommending me to his peers. Without you I would probably still sit at my desk thinking about how to produce microchannels on my own.

I thank all of my colleagues from MIMENIMA for all the fun we had when we met and for the fruitful and intense discussions on our workshops and during the progress reports. Apart from the MIMENIMA colleagues, I would like to thank all of the current and former members of my working group, Chemical Engineering – Recovery and Recycling, for making the countless hours I spent in the office productive, enjoyable (sometimes even fun!), and memorable. I also thank Robbert van Dinther and Shaurya Sachdev from the PPE group at the Technical University of Delft for their help in producing the microchannels used in this thesis.

I would like to thank the students who worked for me as assistants or who did their theses works with me for their hard work and their honest curiosity: Tristan Oltmanns, Anton Enns, Malte Lorenz, Harm Ridder, Lukas Büther, Simon Kunze, Anna Becker, and Jasper Giesler. Some of them were not only students who worked with me but became good friends in the process, from those I would like to especially thank Malte Lorenz for being such a pleasant office mate (albeit he somehow misses the green thumb). His agreement to proceed with my project in the second generation of MIMENIMA gave me more boost than he probably imagines.

I gratefully thank my parents who enabled me to get this excellent education. Without your unlimited support I would not be where I am right now! I also thank my brother Konrad Pesch for designing the cover art.

I thank Jonas Wloka for proofreading this thesis so carefully. Apart from finding all of the misplaced apostrophes, his adjustments put the finishing touches on this thesis.

List of publications

G. R. Pesch, F. Du, U. Schwientek, C. Gehrmeyer, A. Maurer, J. Thöming, and M. Baune (2014). Recovery of submicron particles using high-throughput dielectrophoretically switchable filtration. *Separation and Purification Technology* 132, 728–735

FD and MB developed the concept. GRP, FD, US, and CG developed the experimental setup. US, CG, and AM performed the experiments. JT and MB supervised the project. GRP analyzed the results and wrote the manuscript with input from FD, JT, and MB.

G. R. Pesch, L. Kiewidt, F. Du, M. Baune, and J. Thöming (2016). Electrodeless dielectrophoresis: Impact of geometry and material on obstacle polarization. *Electrophoresis* 37.2, 291–301

GRP developed the concept and model and performed all calculations. GRP and LK compiled the mathematic background. JT and MB supervised the project. GRP analyzed the results and wrote the manuscript with input from all other authors.

G. R. Pesch, F. Du, M. Baune, and J. Thöming (2017). Influence of geometry and material of insulating posts on particle trapping using positive dielectrophoresis. *Journal of Chromatography A* 1483, 127–137

GRP developed the concept, model, and methodology and performed all calculations. MB and JT supervised the project. GRP analyzed the results and wrote the manuscript with input from all other authors.

Contents

1 Prologue **1**

1.1 Introduction 2
1.2 Excursus: Exploiting the example of layer-by-layer produced nanocapsules . . . 2
1.3 Electric fields, (ac) electrokinetic particle movement, and filtration 3
1.4 Dielectrophoretic filtration, preliminary results 5
1.5 Putting the results into perspective 8
1.6 What to expect from this thesis 8

2 Dielectrophoresis: Theory and Application **11**

2.1 Coulomb's law, the electric field, and the electrostatic potential 11
2.2 Dipoles 13
2.3 Dielectric media and polarization 13
2.4 Non-ideal dielectrics and ac fields 15
2.5 Dielectric loss 16
2.6 Dipole moment of a polarized spherical particle 17
2.7 Effective moment of non-spherical or inhomogeneous particle 20
2.8 Dielectric dispersions of homogeneous materials and due to material interfaces 20
2.9 Electrokinetic forces in (ac) electric fields 22
2.9.1 Electrophoresis and electro-osmosis 22
2.9.2 Induced-charge electrophoresis and electro-osmosis 23
2.9.3 Dielectrophoresis, electrorotation, electro-orientation and traveling-wave dielectrophoresis 24
2.10 Practical considerations for calculation 27
2.10.1 Complex electric field and harmonically oscillating excitation 27
2.10.2 When the polarization is complex, why do we assume that the electric field is real? 28
2.10.3 Electric field calculation using the finite element method 28
2.10.4 Dielectrophoresis in a fluid 29
2.10.5 Other forces in (micro-)electrode structures 29
2.10.6 Refinement of the DEP force equation 30
2.10.7 Particle-particle interaction 31
2.10.8 The influence of the double layer on polarization of non-conducting particles 33
2.10.9 The influence of the double layer on polarization of conducting particles 37

2.11 Basic concept of DEP particle separation or retention 38
2.12 Application of dielectrophoresis: Biomedical applications 39
2.12.1 The slam-dunk of DEP: Separation of live and dead cells 39
2.12.2 Cell separation by type 41
2.12.3 DEP of DNA and proteins 42
2.13 Application of dielectrophoresis: Technical applications 43
2.13.1 Trapping and separation of particles by type or size 43
2.13.2 Self-assembly and alignment of nanoparticles 46
2.14 Device design 46
2.14.1 Non-equilibrium electrode-based designs 47
2.14.2 Equilibrium electrode-based designs 48
2.14.3 Electrodeless and insulator-based dielectrophoresis 50
2.14.4 Dielectrophoretic filtration 56
2.14.5 Performance evaluation of DEP devices 57

3 Aim and possible applications of DEP filtration 63

4 Simplification of the filter and polarization of a single post in the electric field 65
4.1 Overview and method 66
4.1.1 Finite element simulation 68
4.1.2 Important considerations: Complex permittivity and dimensionless parameters 69
4.2 Results 69
4.2.1 Potential and electric field due to the first three multipoles 70
4.2.2 Circle and diamond of equal width and height 70
4.2.3 Influence of the aspect ratio 71
4.2.4 Influence of the post's orientation 72
4.2.5 Influence of higher-order multipole moments on DEP force 75
4.3 Conclusion 76

5 Dielectrophoretic particle trapping at single posts 79
5.1 Overview 79
5.2 Method 81
5.3 Results 83
5.3.1 Influence of key design and operational parameters 83
5.3.2 Ideal aspect ratio 84
5.3.3 Sensitivity 86
5.3.4 Summarizing discussion 87
5.4 Side note: Material influence 87
5.5 Conclusion 88

6 Dielectrophoretic particle trapping in a model porous medium 91

6.1 Materials and method 91
6.1.1 Microchannel and experimental setup 92
6.1.2 Experimental procedure 93
6.1.3 Simulation 94
6.1.4 About measurement uncertainties 96
6.2 Results 96
6.2.1 Experimental observations 96
6.2.2 Comparison of experiment and simulation: Clausius-Mossotti factor . 96
6.2.3 Comparison of experiment and simulation: Influence of the applied voltage 97
6.2.4 Comparison of experiment and simulation: Influence of post spacing . 98
6.2.5 Comparison of experiment and simulation: The finite size effect 99
6.2.6 Comparison of experiment and simulation: Influence of the aspect ratio 101
6.2.7 Influence of geometry and operational parameters on separation efficiency 102
6.2.8 Correction of the simulated separation efficiency 104
6.3 Discussion and conclusion 106

7 Conclusion and outlook **109**

A Multipole potential in cylindrical coordinates (Chapter 4) **113**

B Simulation details of multipole extraction method (Chapter 4) **115**

C Comparison of analytical and simulated trajectories (Chapter 5) **117**

D Comparison with literature results (Chapter 5) **119**

E Additional experimental and simulative details (Chapter 6) **121**
E.1 Microchannel design, experiments and simulation 121
E.2 Experimental details 122
E.3 Simulation details 124

Bibliography **127**

List of symbols **141**

Prologue

1

> *In the beginning the Universe was created. This has made a lot of people very angry and been widely regarded as a bad move.*
>
> — **Douglas Adams**
> (The Hitchhiker's Guide To The Galaxy)

This thesis addresses the particle retention in porous media by an electrokinetic effect called dielectrophoresis (DEP). The effect was first termed by Herbert Pohl (Pohl, 1951) and described in detail in his well-known book (Pohl, 1978). Albeit initially applied by Pohl for the separation of carbon black from PVC in large scale separators, later it was mostly used for biomedical applications. The 1990s appear to the golden age of dielectrophoresis after the community discovered the possibility to fabricate microelectrodes using clean room technology[1]. Subsequently, a lot of research focused on the application of dielectrophoresis in microfluidic channels, which does make sense: The dielectrophoretic motion is driven by the gradient of the square of the applied field. This term has units $V^2\,m^{-3}$. The m^{-3}-dependence makes quite clear that a strong force requires small distance between the employed electrodes. Albeit some concepts and applications of large scale separators have been reported the majority of DEP applications found in the literature are aimed at the analysis of small samples while maintaining a high selectivity and efficiency; a task which is ideally suited for microfluidic *lab-on-a-chip* applications.

Nevertheless, DEP is a very versatile technology, because it is—if applied correctly—highly selective and does neither require particle labeling nor particle charge. It has been the aim of our research group for the past 12 years to apply DEP as a separating force in industrial-scale separation processes to solve separation problems that do not have a solution so far or which are not economically reasonable using existing technology. An example for such a separation problem and a solution employing DEP is given in this section. One of the main differences between the biomedical industry and technical applications of DEP might be the required throughput and the purity of the result. Whereas the biomedical or chemical industry (and especially analytical applications) usually employ (comparably) low sample volumes (with a low target particle concentration) and require a high purity (above 99 %) of the results, in industrial scale processes the throughput is much larger while at the same time the required separation efficiency can be expressed on a scale from 0 to 99 %.

This chapter gives results on a dielectrophoretic separation process. In a way this serves as an appetizer on the DEP possibilities: The results describe a dielectrophoretic separation process and the experiments were already conducted when the author started his work on this thesis. They served as a proof-of-principle to show the possibility for particle retention with DEP in porous media. As it will be outlined towards the end of this chapter, there is much

[1] Ronald Pethig—one of the key researchers of dielectrophoresis in the past 40 years—states in the introduction of his recent book (Pethig, 2017) that they applied the first microelectrode in 1986.

room for improving the process and it is one aim of this thesis to give guidelines on how to that. These first results should thus serve as a foundation for a very detailed analysis of dielectrophoresis in porous media, including theoretical models, predictions, and experimental verifications aimed at the overall improvement of the concept: Achieve higher throughput and separation efficiency while reducing the required applied voltage). The results shown in this chapter are published as G. R. Pesch, F. Du, U. Schwientek, C. Gehrmeyer, A. Maurer, J. Thöming, and M. Baune (2014). Recovery of submicron particles using high-throughput dielectrophoretically switchable filtration. *Separation and Purification Technology* 132, 728–735. Although the experiments have not been planned and conducted by the author of this thesis, it was his task to sort, analyze, and publish them. After this (rather introductory) chapter follows a recap of technical and mathematical background necessary to fully understand the possibilities of DEP. This goes hand-in-hand with a literature survey of important concepts, applications, and employed devices. After this theory and literature part follow three content chapters from which two are published by the author (and co-workers). The thesis will be enclosed by a summarizing discussion and a promising outlook.

1.1 Introduction

Albeit DEP is highly suited for numerous separation tasks (as will be outlined in the literature survey), this chapter focuses on the separation of layer-by-layer produced nanocapsules from suspending polyelectrolyte solution. Generally, the separation of sub-micron particle's from a suspending solution can become a challenging and cumbersome task. This especially holds if large quantities of sensitive particles need to be recovered. Conventional separation techniques, such as membrane filtration and centrifugation, show some inevitable drawbacks: In most cases, centrifugation is a batch-wise process and has only limited throughput. Particularly sensitive particles require small centrifugation velocities to reduce induced shear stress. Membrane filtration techniques, micro filtration (MF), ultra filtration (UF), and nano filtration (NF) have several advantages, including easy operation, low cost, and ease in scale-up. They are, however, always linked to time dependent flux reduction caused by increasing flow resistance due to concentration polarization and membrane fouling (Zhang et al., 2015). To put it the other way round: the formation of a filter cake increases the required pressure drop to maintain a constant flux through the membrane and this might cause destruction of sensitive particles due to too high mechanical stress. For example, layer-by-layer produced nanocapsules can only be separated using membranes if the particles are suspended at all time (by stirring) to avoid aggregation, which will result in a very low flux (Voigt et al., 1999).

1.2 Excursus: Exploiting the example of layer-by-layer produced nanocapsules

Albeit the concept, ideas, and preliminary results presented in this chapter and throughout the thesis are generally applicable, the example of layer-by-layer (LbL) nanocapsules shall be further exhausted as it is a good illustration of the concept's exploitability (and simply because

the preliminary results presented later in this chapter show the separation of LbL nanocapsules from the suspending polyelectrolyte solution). LbL capsules are very promising in the biomedical industry where, for instance, drugs can be protected in a multilayer shell that protects them from external influences during their journey through the human body until they reach the desired spot at which they are triggered to open and release the drug by a certain stimuli (Delcea et al., 2011; Polomska et al., 2016).

Their production itself requires very elaborate separation techniques as it usually requires the separation of very small colloidal matter from a polyelectrolyte suspension of identical charge (Decher, 1997). Generally, a charged substrate is immersed into a polyelectrolyte solution of opposing charge. Due to electrostatic attraction, the polymers will adsorb on the charged substrate and form a shell. The substrate is subsequently taken out of the solution and immersed into a polyelectrolyte solution of, again, opposing charge. This will cause adsorption of the second polymer onto the (charged) first polymer and thus the formation of an additional layer. The process can be repeated until the desired number of shells is reached. A thorough washing step is required between two adsorption steps to avoid solution contamination.

This requires separation of the charged colloidal multishell particles from the similarly charged polyelectrolyte solution, which can be a very cumbersome task. This holds especially if the particles are very small. Up to today, sequential adsorption, membrane filtration, and centrifugation methods are state-of-the-art (Voigt et al., 1999) but all show individual drawbacks, such as high cost (filtration, centrifugation), low throughput (filtration, centrifugation), or tedious control of added substances in the case of sequential adsorption.

1.3 Electric fields, (ac) electrokinetic particle movement, and filtration

The thesis deals with the alternating current (ac) electrokinetic phenomenon of dielectrophoresis in porous structures and with it's application towards dielectrophoretic filtration. Albeit being a very specific subject, for the sake of completeness, an overview of the application of electric fields for assistance in or enhancement of filtration processes is in order.

Traditionally, the electrophoretic effect has been used in electrofiltration for fouling reduction. Electrophoresis (EP) is the movement of charged particles in a dc electric field due to Coulomb interaction. The EP movement velocity is proportional to the zeta potential of the particle (but independent of it's particle size) and the position dependent electric field value. Particles will thus move, depending on the sign of their charge (or zeta potential), either towards the cathode (negatively charged particles) or the anode (positively charged particles). Since most particles carry negative charge in aqueous suspension (Huotari et al., 1999) it is possible to keep particles from forming a fouling layer by placing the cathode on the feed side. This keeps particles from settling on the surface of the membrane. It has been succesfully applied as a method for flux enhancement in cross-flow (Huotari et al., 1999) and dead-end filtration (Loginov et al., 2013). Another prominent electrokinetic effect is electro-osmosis which describes the electric field induced movement of a fluid around a stationary interface (depending on the reference frame one could also move the interface and the body attached to it in a stationary

fluid) due to the Coulomb forces acting on charge carriers in the double layer. Electro-osmosis can be used to further enhance flux through the membrane (Chuang et al., 2008) or to reverse the flux for backwashing of particles attached to the membrane (Bowen and Sabuni, 1994).

In contrast to these methods, dielectrophoresis (DEP), is based on the interaction of an *induced* dipole (or multipole) with an *inhomogeneous* electric field. Since it is based on induced charge separation it does not require net charge on the particle but particle polarizability. The acting force is then *dependent on the spatial change (gradient) of the square of the electric field magnitude* and the induced multipole moments, for particles (as opposed to, e. g., macro molecules) this usually means that *the force depends on the particle's volumetric polarization, i. .e., volume times relative polarizability*. Depending on their polarizability, the particles will either move towards (better polarizability than suspending medium) or against (less polarizability) the electric field gradient.

Dielectrophoresis has been researched (Molla et al., 2005; Molla and Bhattacharjee, 2007) and successfully applied (Du et al., 2013, 2009; Hawari et al., 2015) for the fouling reduction in membrane filtration by placing electrodes in a way that drives particles away from the membrane. For example, Du et al. (2013) investigated the application of interdigitated electrodes for fouling reduction in cross-flow filtration and found a 9-fold longer service time for a permeate flux of at least 69 %. The interdigitated electrodes were placed under the membrane so that there was an electric field maximum on the surface of the membrane that exponentially decayed with perpendicular distance from it. Then, particles less polarizable than the suspending medium were driven away from the membrane and prevented from forming a filter cake.

This thesis investigates the concept of using DEP to immobilize particles in potential wells (particle traps) where they stay until the field causing the traps is turned off. In the case of particles that are better polarizable than the surrounding medium (that move in direction of the field gradient) a particle trap is a local maximum of the electric field. In order to generate traps that are strong enough to immobilize small particles from a significant volume flow, very strong electric field gradients are required. This could either be achieved by a tailored electrode configuration (Wang, 2016) or by electric field scattering at material boundaries (Srivastava et al., 2011b). The latter is known as electrodeless or insulator-based dielectrophoresis (iDEP) and is usually applied in analytical chemistry or biomedical research for the detection of a target particle in a mixture of particles (for example the detection of circulating tumor cells in blood (Salmanzadeh et al., 2011)). Usually, an array of insulating posts (or any other geometry) is employed in a microfluidic channel (that has dimensions between tens of micrometer to some millimeter). An electric field is applied across the post array that scatters at the post surface. This creates particle traps (i. e., extrema of the electric field) at the surface of the post or in between them. Then, one sort of particle (to stay with the above example: the tumor cells) is immobilized at the traps whereas all other particles simply flow through. The discrimination is usually achieved due to differences in the net polarization. Either because the target particle polarizes with a different magnitude and thus interacts much stronger with the traps than all other particles or because the target particle moves in a different direction under the influence of the inhomogeneous field than all other types of particles present. For example, the target

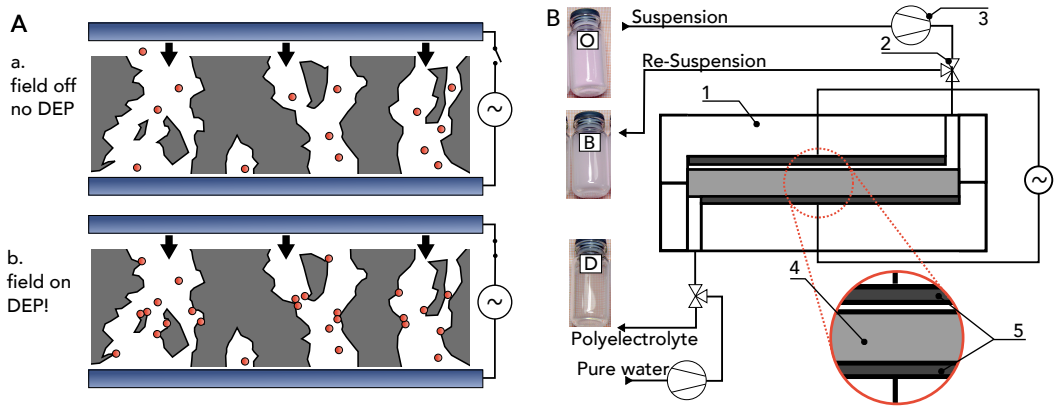

Fig. 1.1: A: Sketch of the proposed separation mechanism. a. When there is no voltage applied on the blue electrodes (hence no electric field), the red particles simply flow through the filter because the pores of the filter are much larger than the particle diameter (particles are not to scale); b. When a voltage is applied to the electrodes the dielectrophoretic effect will cause a particle movement towards traps in the filter medium at which a particle accumulation will occur. The particles will stay there until the field is turned off. B: Schematic of the separation process employed. The original suspension (O) is pumped (3) through the filter (4), which is embedded between two electrodes (5) in the PMMA filtration chamber (1). After passing the filter and due to the influence of the electric field, the liquid should only contain polyelectrolyte solution with less particles than before. When switching the valves (2) it is possible to reverse flow and to re-suspend the trapped particles (B). (Pesch et al., 2014).

particles are trapped in electric field maxima whereas all other particles are trapped at electric field minima.

The motivation of this research is the wish to scale up such an iDEP-separation process from the micrometer scale dealing with sample sizes between nanoliter and microliter and throughputs in the microliter per minute range towards setups in the centimeter scale that are able to separate particles from volume flows in the milliliter per minute range. Preliminary results (from which excerpts will be shown in this chapter) were very promising and lay the basis for all the investigations presented in the following chapters.

1.4 Dielectrophoretic filtration, preliminary results

In a preliminary study (Pesch et al., 2014) $d_\mathrm{p} = 340\,\mathrm{nm}$ LbL-particles were successfully separated from their suspending polyelectrolyte solution using dielectrophoretic filtration (Fig. 1.1). In this process, a porous medium is sandwiched between two electrodes that generate an electric field, that becomes highly inhomogeneous inside the porous medium due to the scattering at the interfaces between the liquid (suspension) and the solid (filter) medium. This results in a high number of particle traps (electric field maxima) at the surface of the pores. The highly polarizable LbL-particles can therefore be moved towards the traps where they stay until the field is turned off. Without any electric field, the pores of the filter are large enough in order to let the particles through without any noticeable filtration effect (Fig. 1.1 A). In fact, the pores were at least 60 times larger than the particle diameter and this not only reduces the membrane fouling to a negligible amount but also causes a much lower pressure loss across the filter as

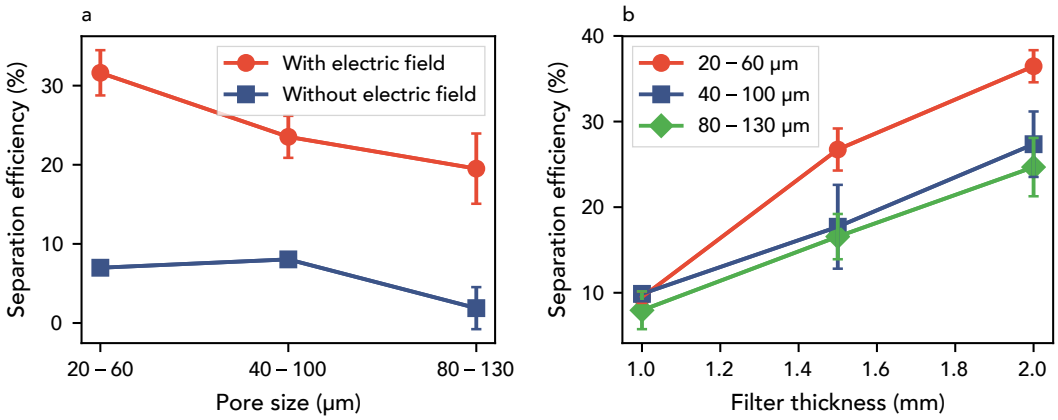

Fig. 1.2: Separation of $d_p = 340$ nm LbL particles from suspending polyelectrolyte solution using dielectrophoretical filtration. The electric field was generated by applying 200 V_{RMS} over a gap of 20 mm with a sine waveform of frequency 210 kHz. Three different pore sizes have been tested at a flow rate of 0.5 mL min^{-1} using a filter with 1 mm thickness (a). Also investigated was the influence of the filter thickness for the same filter pore sizes at a flow rate of 1 mL min^{-1} (b). (Pesch et al., 2014)

compared to conventional filtration processes. The particles can therefore be separated without mechanical stress and easily resuspended into a different solution. When voltage is applied (Fig. 1.1 A), the particles are directed towards the almost infinite number of field traps inside the filter. Depending on the pore size and the volume flow through the pores, the particles have more or less time to travel towards the traps (that defines the separation efficiency). A schematic of the setup is shown in Fig. 1.1 B. As a porous medium polyethylene (PE) filters (DIA-Nielsen GmbH & Co. KG) with different pore sizes (~20–130 µm) and thicknesses (1–2 mm) were used. A titanium grid (mesh size 9.4 mm^2) was used as top electrode and a stainless steel plate (V2A) as bottom electrode. The distance between the electrodes was 20 mm and the effective filter area 1500 mm^2. The LbL nanocapsules were suspended with a concentration of 0.1 %w/w in 0.1 M NaCl solution with 10 mM NaAc buffer and 1 g L^{-1} PSS.

After the separation step it was possible to switch the valves (with the field turned off) and to flush the setup in the reverse direction with a suitable backwashing liquid (pure water in our case) to resuspend the trapped particles. See also the inset in the figure: the polyelectrolyte solution was transparent whereas the particles itself were rhodamine labeled and thus pink in color.

It is possible to observe a clear difference in separation efficiency with and without an applied electric field (cf. Fig. 1.2 a). The separation efficiency is defined as the percentage of particles from the input stream that were immobilized in the filter and it was measured with UV/Vis. Without any field, the separation efficiency is below 10 % for all investigated pore sizes; with an applied field (200 V over 20 mm) it increases two to threefold to values of 20–30 % with a maximum of 32 % at a flow rate of 0.5 mL min^{-1} using a filter with a thickness of 1 mm and 20–60 µm pore size. The separation efficiency also shows a significant dependence on the filter pore size: it increases from 20 % at 80–130 µm pore size to 32 % at 20–60 µm pore size.

The separation efficiency also depends on the thickness of the filter. At a flow rate of 1 mL min^{-1} all three pore sizes show a separation efficiency of 8–10 % (cf. Fig. 1.2 b, note the

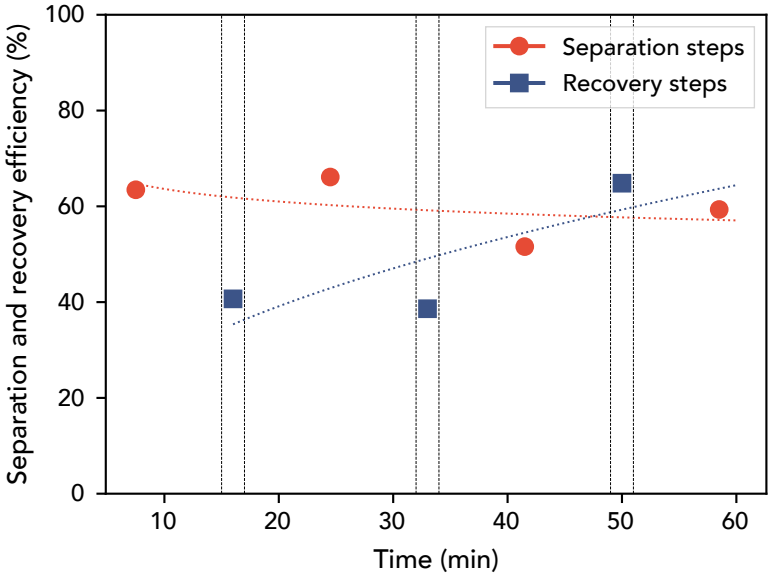

Fig. 1.3: Separation and recovery of particles in semi-continuous operation mode with four 15-minute separation steps at 1 mL min^{-1} and three 2-minute recovery steps at 6 mL min^{-1}. The vertical lines indicate the switch from separation to recovery or vice versa. The dotted lines are to guide the eye and are fitted assuming a function of type $y = a \cdot x^b$. (Pesch et al., 2014)

different flow rate between a and b and thus the different separation efficiencies). With an increase from 1 to 2 mm the separation efficiency increases to values of almost 40 % for a 20–60 µm filter. This increase in separation efficiency is steeper for filters with small pores since the 80–130 µm filter only increases to ~25 %.

When this study was conducted, the results mainly served as a proof-of-principle. The influence of the separation efficiency on the investigated parameters was not surprising (but supported the proposed mechanism): Smaller pore sizes will a) reduce the distance a particle has to travel until it reaches the pore wall and b) will cause a higher electric field gradient since the field lines need to squeeze through smaller holes in the filter (using a picturesque description). An increase in filter thickness (at constant electrode distance) will increase the residence time of the particle in the filter and thus increase the chances that it becomes trapped during the passage.

Recovery of particles was investigated in a semi-continuous operation mode with four 15-minute separation steps (at 1 mL min^{-1} throughput) and three intermediate 2-minute recovery steps (at 6 mL min^{-1}). Using a filter with 20–60 µm pore size and 1.5 mm thickness the separation efficiency decreased during the experiment from 63 % at the first separation step to 52 % after the fourth separation step (cf. Fig. 1.3). Conversely, the recovery efficiency increased from 40 % to almost 65 % from the first to the third recovery step. It is defined as the absolute number of particles recovered during the two minutes recovery step divided by the absolute number of particles trapped in the preceding 15 minutes of separation as calculated from the separation efficiency. Obviously, since the recovery efficiency does not start with 100 %, the trapped particles accumulate over time in the filter. This causes two effects: First, a filter that is partially filled with particles shows a lower separation efficiency which indicates that the filter saturates. Secondly, the recovery efficiency increases over time, although it is more difficult to calculate

since theoretically it would be possible at the second recovery step to have a recovery efficiency above 100 %. This indicates that the two minutes of recovery at high throughput (6 mL min^{-1}) are not enough for full cleaning of the filter.

Under the light that this is (to the best of the author's knowledge) the first time that monolithic porous media are used for high-throughput dielectrophoretic particle separation, the results are quite impressive.

1.5 Putting the results into perspective

As stated above, DEP is mainly used in microfluidics to serve as a force in lab-on-a-chip applications for particle sorting, detection, and separation. These applications are quite similar to what is presented here but with a different focus. As an arbitrary example, a lot of effort has for example been put into the development of on-site bacterial detection systems on single, self-sustaining cm-sized chips. These applications will be discussed in Sections 2.12 and 2.13. Nevertheless, a smaller fraction of publications reports the application of DEP as a force for particle separation at larger scales. There are some old reports of particle filters and even a patent on a separator that was used in industry for the separation of cat fines from oil, the Gulftronic separator (Fritsche et al., 1994). Benguigui and Lin (1982) and Lin and Benguigui (1982, 1985) and later Wakeman and Butt (2003) developed DEP filters that were able to separate large 10–50 µm metal oxide particles from non-polar (Benguigui and Lin, 1982; Wakeman and Butt, 2003) (kerosene or oil) or polar (Lin and Benguigui, 1982, 1985) solvents (mixtures). The flow rate was very high, up to 180 L h^{-1} with a maximum flux of 31 $m^3\,m^{-2}\,h^{-1}$. However, to achieve high separation efficiencies (up to 100 %), applied voltages of almost 10 kV were required. Later developed smaller devices where aimed at the separation of yeast cells (Iliescu et al., 2007c; Suehiro et al., 2003) from water and were able to operate at a flux of $q = 0.06\,m^3\,m^{-2}\,h^{-1}$ and much lower voltages of 400 V_{pp}. Neither the early studies nor the later performed filter studies on yeast cells have been followed; the reason for this is unknown to the author. In the present report, a flux of 0.04 $m^3\,m^{-2}\,h^{-1}$ is achieved. The DEP force is volume dependent, thus, the force on 300 nm particles is 1×10^3 times smaller in this case compared to yeast cells and 1×10^6 times compared to the particles employed by Lin and Benguigui (1982). This explains the differences in achieved throughput (and, of course, the much smaller employed voltage). Further, the polyelectrolyte solution used in this study has a very high conductivity, which makes application of electric fields quite challenging. This is the first study employing a solid foam as the separation matrix (this is much easier to handle compared to micron-sized glass beads and has a much higher porosity) and the results are promising enough to justify further scrutinization of the separation mechanism.

1.6 What to expect from this thesis

This was a proof-of-principle study; hence, to achieve an easy realization, commercially available filter where used as separation media without any further knowledge of the trapping or recovery mechanisms or detailed knowledge of the filter structure itself. The aim of this work is to (i) elucidate the particle immobilization behavior in porous media due to dielectrophoresis,

especially with respect to the underlying geometry of the matrix, (ii) optimize the matrix structure towards a more efficient separation (that is, apply less voltage, achieve higher throughput and separation efficiency), and finally, (iii) investigate the influence of operational parameters on the separation.

This thesis is composed of three content chapters. The overall approach to understand and optimize the trapping behavior in porous media is very similar to the approach taken when trying to understand an unknown technical device: The overall device (the filter …) will be taken apart to the smallest unit. This unit will be investigated in detail, to understand how it works. When the mechanism is understood, it can be optimized and put back together.

To be more specific: The separator consists of a liquid flowing through a porous medium, that is sandwiched between two electrodes that generate an electric field. The separator will be simplified by replacing the real, complex porous medium by an array of posts as a model filter that are instead placed between the two electrodes (cf. Fig. 1.4). As a first step, a single post will be investigated. Because particles are trapped due to the electric field gradient, it is helpful to study *how* the electric field gradient (due to the post polarization) will be influenced by the *shape of the material boundary*, i. e., by the geometry of the post. This is done in Chapter 4. In Chapter 5 the machine is already partly reassembled; here the interplay between electric

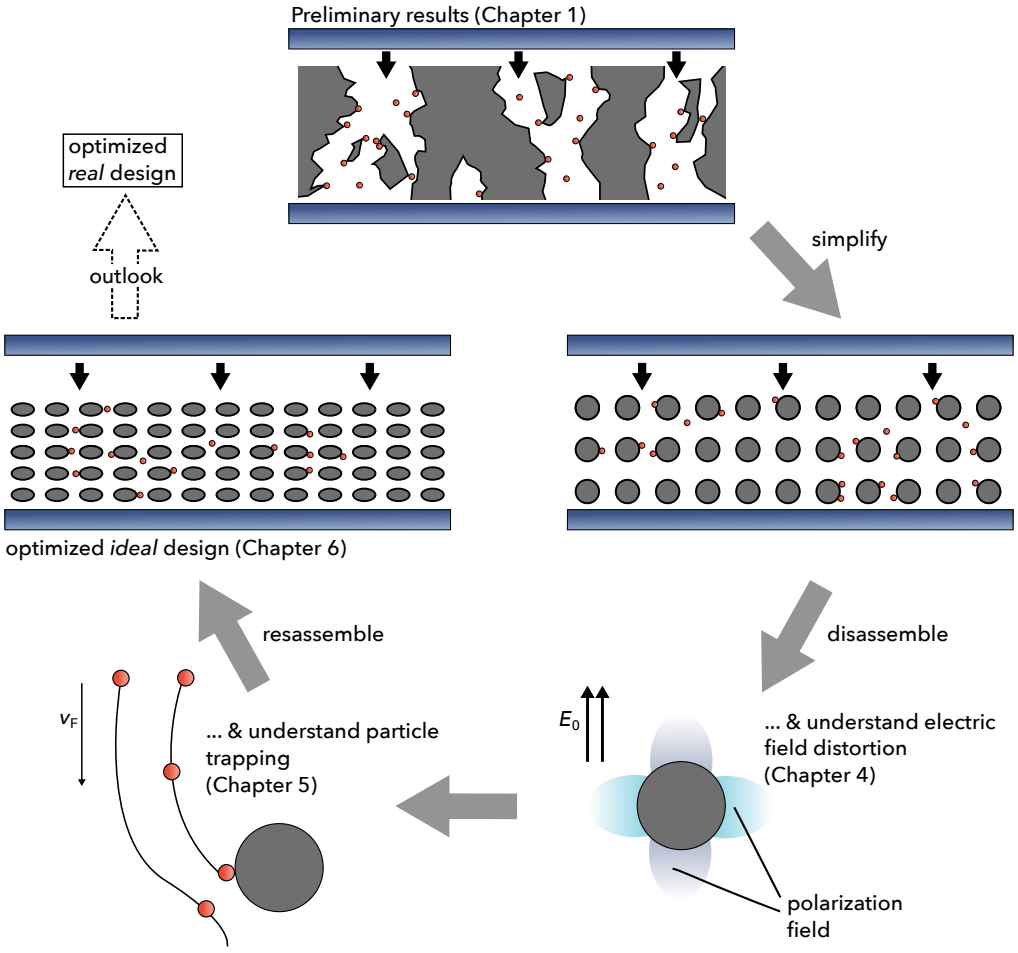

Fig. 1.4: Graphical outline and workflow of this thesis.

field, pore size, particle size, and volume flow is investigated. To do so the same model porous filter (a single post of a post array) is employed for calculating particle trajectories. It is thus possible to learn about all the parameters influencing the trapping and how it is possible to tune the trapping efficiency by changing the values of the parameters. As the penultimate step on the route to reassembling the device, in Chapter 6 the particle trapping in an entire array of posts is simulated. This can be considered as the preliminary stage to the actual (chaotic and random) porous medium. Whereas in the preceding chapters only single posts have been investigated, here, an integrated system will be analyzed. To back the results, the simulated data will be verified by experimental results performed in transparent polymer microfluidic channels using fluorescent particles. This allows real-life in-situ observations of the particle motion and immobilization in the model porous medium.

The device will not be entirely reassembled at the end of this thesis and—as an outlook for future studies—the application of the lessons learned from these investigations shall result in an actual dielectrophoretic filtration process using not model porous structures but real, random porous media. Then, an investigation on the possibility to selectively trap particles and on how to improve the recovery efficiency is in order.

Dielectrophoresis: Theory and Application

2

> *It's still magic even if you know how it's done.*
>
> — **Sir Terry Pratchett**
> (A Hat Full of Sky)

In this chapter we will first review electrostatic field theory, including the Coulomb force, electric dipoles, and polarization of dielectric matter. Further, the chapter describes various ac electrokinetic effects. The latter part of the chapter focuses specifically on dielectrophoresis including a literature survey of various applications and recent research. The theoretical descriptions are supposed to be exhaustive while at the same time on point. The literature review tries to list and discuss common applications as well as device designs with their respective achievements, strengths and drawbacks. Since this thesis is mainly of technical nature, i. e., it is aimed at developing a process, not at solving a specific problem, the review is supposed to give a broad overview of existing technologies and in which fields they might be of use to put the presented results into perspective. Most of the following pages cover the basic theory; the busy reader might skip all of this until Eq. (2.30). It might further be helpful to study Section 2.10. Section 2.14 is crucial to put the developed technology into context.

2.1 Coulomb's law, the electric field, and the electrostatic potential

Around 1785 Charles Augustin de Coulomb (that's why it's called Coulomb's law) using a torsion balance was able to visualize the force between two electrostatic point charges (unit C) depending on the distance between them. In general Coulomb's law (Fig. 2.1 a) describes the force exerted by one stationary point charge Q_1 (named source charge out of convenience) on a second stationary point charge Q_2 (test charge) (Jackson, 2013, Sec. 1.1):

$$\boldsymbol{F} = \frac{Q_1 Q_2}{4\pi\varepsilon_0 r^2}\hat{\boldsymbol{r}}_{12}. \tag{2.1}$$

Here, $\hat{\boldsymbol{r}}_{12}$ is the unit vector pointing from Q_1 to Q_2 and r is the distance between the charges. The constant ε_0 is the permittivity of free space and is experimentally determined to a value of $8.854 \times 10^{-12}\,\mathrm{F\,m^{-1}}$.

By definition, the electric field $\boldsymbol{E}(\boldsymbol{x})$ is the force $\boldsymbol{F}$ that acts on a hypothetic test charge Q_2 at a given point $\boldsymbol{x}$ normalized by that charge, $\boldsymbol{E} = \boldsymbol{F}/Q_2$. By plugging $\hat{\boldsymbol{r}}_{12}$ and $\boldsymbol{E} = \boldsymbol{F}/Q_2$ into Eq. (2.1) we find the electric field generated by the source charge Q_1 (Jackson, 2013, Sec. 1.2):

$$\boldsymbol{E}(\boldsymbol{x}) = \frac{1}{4\pi\varepsilon_0 Q_1}\frac{\boldsymbol{x}-\boldsymbol{x}_1}{|\boldsymbol{x}-\boldsymbol{x}_1|^3}, \tag{2.2}$$

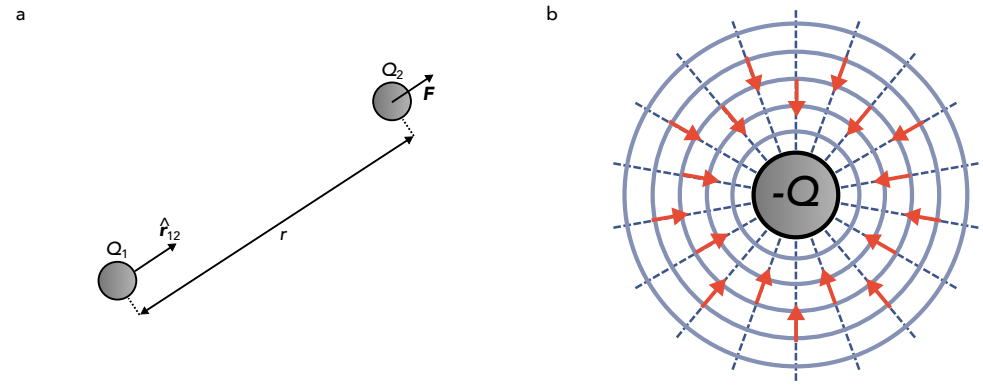

Fig. 2.1: a) Representation of Coulomb's law with the two point charges Q_1 and Q_2, the unit vector $\hat{r}_{12}$ pointing from Q_1 to Q_2, the resulting force $\boldsymbol{F}$ on Q_2 and the distance r between Q_1 and Q_2 and b) electric field due to a single point charge with the electric field lines (blue dashed), the electric field vector (red arrows) and the isopotential lines $\Phi = \text{const.}$ (blue solid).

with the test charge's (or now observer's) position $\boldsymbol{x}$ and the source charge position $\boldsymbol{x}_1$ (see also Fig. 2.1 b). A more convenient description of the electric field is given by Gauss's law, which states that the total flux of $\boldsymbol{E}$ through an enclosed surface equals the total amount of charge inside that surface (the volume integral of the the volumetric electric charge density ρ with unit $\mathrm{C\,m^{-3}}$). In the differential form Gauss's law reads (Jackson, 2013, Sec. 1.4)

$$\nabla \cdot \boldsymbol{E} = \frac{\rho}{\varepsilon_0}, \tag{2.3}$$

with the del operator ∇ and it's usual definition depending on the coordinate system.

The superposition principle states that the total effective electric field at an arbitrary point can be calculated from the vector sum of the electric fields at that point that are generated by an arbitrary number number of point charges. Instead of the sum of point charges $\sum Q_i$ we calculate the integral over the volumetric charge density $\int_V \rho$ and get (Jackson, 2013, Sec. 1.2):

$$\boldsymbol{E}(\boldsymbol{x}) = \frac{1}{4\pi\varepsilon_0} \int_V \rho\left(\boldsymbol{x}'\right) \frac{\boldsymbol{x} - \boldsymbol{x}'}{|\boldsymbol{x} - \boldsymbol{x}'|^3} \mathrm{d}^3\boldsymbol{x}'. \tag{2.4}$$

The electric field is conservative (i. e., $\nabla \times \boldsymbol{E} = 0$, which can be easily proven—the interested reader is referred to any textbook on electric field theory or electrostatics) and can thus per definition be described as the gradient of a scalar potential, the *electrostatic potential* (or voltage) Φ: $\boldsymbol{E} = -\nabla\Phi$. Using the gradient theorem it is possible to show that the work required per unit charge to move a charge from one point a to another b is the potential difference between those two points (i. e., the required work is independent of the actual path taken, Jackson (2013, Sec. 1.5)):

$$-\int_a^b \boldsymbol{E}\mathrm{d}\boldsymbol{l} = \Phi(\boldsymbol{b}) - \Phi(\boldsymbol{a}). \tag{2.5}$$

Combining the definition of the electrostatic potential and the differential form of Gauss's law yields Poisson's equation (which is quite useful, since it can be used to calculate any electric field when the appropriate boundary conditions are known, Jackson (2013, Sec. 1.7)):

$$\Delta \Phi = \frac{\rho}{\varepsilon_0}, \tag{2.6}$$

with the Laplacian $\Delta = \nabla \cdot \nabla$.

Equation (2.4), that is, the concept that the overall electric field at a point is just the sum of an infinite (or finite) amount of electric fields generated due to Coulomb's inverse-square law applied on an infinite (or finite) amount of point charges, together with the definition of the electrostatic potential ($\boldsymbol{E} = -\nabla \Phi$) is quite enough to describe the electric field for any charge configuration in the so-called *free space*. Albeit being the basis for all that follows, this alone is quite useless as we are seldomly forced to solve electrostatic problems in a perfect vacuum. Before coming to dielectric media, we want to shortly introduce the dipole.

2.2 Dipoles

Frequently, positive or negative charges are not occurring alone but in pairs. A dipole is the combination of two equivalent (but opposite in sign) charges $\pm Q$ that are separated by a distance $d = |\boldsymbol{d}|$ (cf. Fig. 2.2 a). It is a fundamental configuration for many electrokinetic effects and also for DEP. It forms, for instance due to the action of an electric field on polarizable matter (next section). The dipole moment is a vector pointing from the negative to the positive charge. It is given by (Morgan and Green, 2002, Sec. 2.2.1)

$$\boldsymbol{p} = Q\,\boldsymbol{d} \tag{2.7}$$

with the vector $\boldsymbol{d}$ pointing from the negative to the positive charge. From geometric considerations (Jones, 1995, Appendix B) it is possible to find the electrostatic potential due to a point dipole (i. e., the dipole distance $|\boldsymbol{d}|$ is very small compared to the observation distance r) in spherical coordinates with azimuthal symmetry (r, θ):

$$\Phi_{\text{dipole}} = \frac{|\boldsymbol{p}| \cos\theta}{4\pi\varepsilon_0 r^2}. \tag{2.8}$$

Consequently, the electric field due to a point dipole is

$$\boldsymbol{E} = \frac{|\boldsymbol{p}|}{4\pi\varepsilon_0 r^3}(2\cos\theta\,\hat{\boldsymbol{r}} + \sin\theta\,\hat{\boldsymbol{\theta}}). \tag{2.9}$$

2.3 Dielectric media and polarization

A dielectric medium is a medium that polarizes when subjected to an electric field. That means that bound charges in the material will move over short distances when the field is applied (depending on their sign in opposite directions) to form induced dipoles. Per definition an *ideal*

dielectric is an insulator, therefore the conductivity $\sigma = 0$. The polarization $\boldsymbol{P}$ (the volumetric dipole moment density, dipole moment per volume) is (Morgan and Green, 2002, Sec. 2.3)

$$\boldsymbol{P}(\boldsymbol{x}) = \alpha \boldsymbol{E}(\boldsymbol{x}) \tag{2.10}$$

with an yet unknown proportionality factor α.

The small movement of the bound charges gives rise to a net charge (that will disappear together with the excitatory field and, due to charge neutrality, is zero when integrated over the entire volume; it is a matter of distribution). These bound charges could be calculated as (Morgan and Green, 2002, Sec. 2.3.1)

$$\rho_\mathrm{b} = -\nabla \cdot \boldsymbol{P}. \tag{2.11}$$

Three basic polarization mechanisms exist (cf. Fig. 2.2 b) which give rise to the net polarization under the influence of an electric field (Morgan and Green, 2002, Sec. 2.3.3): (i) When the electron clouds around an atom move slightly with respect to the center of the nucleus it is called *electronic polarization*. (ii) Ions of different sign can move into opposite directions under the influence of an electric field. The resulting charge displacement gives rise to *atomic polarization*. (iii) Some dielectric materials are polar (for instance water): Due to the nature of their molecules, they possess a permanent dipole independent of the electric field. These dipoles are randomly oriented (and thus cancel each other out). The application of an electric field causes an alignment of these permanent dipoles and thus gives rise to *orientational polarization*.

At interfaces or inhomogeneities of the dielectric material (i. e., at regions where the material changes) the microscopic polarization mechanisms give rise to macroscopic dipoles. One example is that the two sides of the dipole cancel each other out inside the material but right

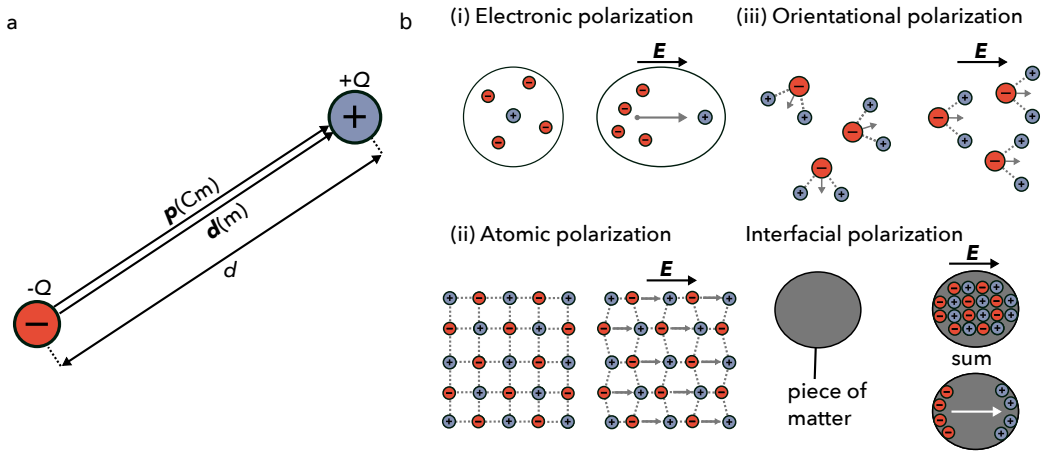

Fig. 2.2: a) Dipole with the vector $\boldsymbol{d}$ that points from the negative charge $-Q$ to the positive charge $+Q$ and the dipole moment $\boldsymbol{p} = Q\,\boldsymbol{d}$. b) The three basic polarization mechanisms (i) electronic, (ii) atomic, and (iii) orientational polarization (in the undisturbed situation on the left and the polarized situation under application of the electric field $\boldsymbol{E}$ on the right). The gray vector shows the induced dipole $\boldsymbol{p}$. Also shown is the mechanism of interfacial polarization, in which the dipoles in the medium cancel each other out but become eminent on the surface of the material (Pethig (2017, Sec. 7.2); Morgan and Green (2002, Sec. 2.3.3.)).

at the boundary this does not happen, so the two sides of a piece of dielectric matter appear to be charged opposingly. This is called *interfacial polarization* (Green, 2011b).

Assuming that the total volumetric charge density in the investigated space is composed of free and bound charges, $\rho = \rho_\mathrm{b} + \rho_\mathrm{f}$, then together with Gauss's law (Eq. (2.3)) Eq. (2.11) reads (Jackson, 2013, Sec. 4.3):

$$\nabla\cdot(\varepsilon_0 \boldsymbol{E} + \boldsymbol{P}) = \rho_\mathrm{f}, \tag{2.12}$$

with the electric flux density $\boldsymbol{D} = \varepsilon_0 \boldsymbol{E} + \boldsymbol{P}$. Analogous to Eq. (2.11) we can write $\nabla\cdot\boldsymbol{D} = \rho_\mathrm{f}$. In linear and isotropic dielectrics $\boldsymbol{P}$ and $\boldsymbol{E}$ are proportional: $\boldsymbol{P} = \varepsilon_0 \chi_\mathrm{ae} \boldsymbol{E}$, with the electric susceptibility χ_ae. Then (Jackson, 2013, Sec. 4.3)

$$\boldsymbol{D} = \varepsilon_0 (1 + \chi_\mathrm{ae}) \boldsymbol{E} = \varepsilon_0 \varepsilon_\mathrm{r} \boldsymbol{E}, \tag{2.13}$$

which is the constitutive relation for ideal dielectrics with the material's relative permittivity $\varepsilon_\mathrm{r} = (1 + \chi_\mathrm{ae})$. Also (Jackson, 2013)

$$\Delta\Phi = \frac{\rho_\mathrm{f}}{\varepsilon_0 \varepsilon_\mathrm{r}}, \tag{2.14}$$

which is Poisson's equation for dielectric media (notice the ρ_f and $\varepsilon_0\varepsilon_\mathrm{r}$ in contrast to ρ and ε_0 in Eq. (2.6)).

The polarization density field $\boldsymbol{P}$ is the negative of the field induced by the bound charges (which exist due to the polarization mechanisms outlined above in response to $\boldsymbol{E}$). Conversely, the electric flux density $\boldsymbol{D}$ is the field due to the free charges. Media that don't polarize very good (for example most polymers) have ε_r close to 1 (and thus χ_ae almost 0). Then, there are almost no bound charges and the polarization density is close to 0. Media with good polarizability have $\varepsilon_\mathrm{r} \gg 1$, e. g., water has ε_r of approx. 80.

2.4 Non-ideal dielectrics and ac fields

A non-ideal dielectric has a finite conductivity and its polarization behavior depends not only on ε_r but also on the conductivity σ and the frequency of the applied field f (Zangwill, 2013, Sec. 17.6). Also for a non-ideal dielectric, ε_r is a function of the frequency as will be discussed in the next section.

To derive an expression for the polarization of lossy (non-ideal) dielectrics in ac fields, we require Ohm's law, $\boldsymbol{J} = \sigma \boldsymbol{E}$, that relates the electric current density to the electric field through the conductivity. We also need the charge conservation equation $\nabla\cdot\boldsymbol{J} = -\partial\rho/\partial t$ that states that charge cannot be created or destroyed and that the only way for charge to change at a given point is by a current flowing into or out of that point (Zangwill, 2013, Sec. 2.1.3). In an harmonic field of angular frequency $\omega = 2\pi f$ the time derivative simplifies to $\partial/\partial t = j\omega$ with $j^2 = -1$, the imaginary number. Only the free charge part of ρ is responsible for the conductivity and we can thus write (Morgan and Green, 2002, Sec. 2.3.6)

$$\partial\rho_\mathrm{f}/\partial t = j\omega\rho_\mathrm{f} = -\nabla\cdot\boldsymbol{J} = -\nabla\cdot(\sigma \boldsymbol{E}). \tag{2.15}$$

We further know that

$$\begin{aligned} \nabla\cdot\boldsymbol{D} &= \rho_{\mathrm{f}}, && \text{so from (2.15)} \\ \nabla\cdot(\varepsilon_0\varepsilon_{\mathrm{r}}\boldsymbol{E}) &= -\nabla\cdot\left(\frac{\sigma}{j\omega}\boldsymbol{E}\right), && \text{and} \\ \nabla\cdot\left(\varepsilon_0\varepsilon_{\mathrm{r}} + \frac{\sigma}{j\omega}\boldsymbol{E}\right) &= 0. \end{aligned} \tag{2.16}$$

The phrase $\varepsilon_0\varepsilon_{\mathrm{r}} - j\sigma/\omega = \tilde{\varepsilon}$ is the complex permittivity. There are also other ways to derive this quantity. Then, Poisson's equation modifies to (Pesch et al., 2016)

$$\nabla\cdot\left(\tilde{\varepsilon}\nabla\tilde{\phi}\right) = 0. \tag{2.17}$$

Note that the free charge density ρ_{f} vanishes in Eq. (2.17) because all free charges in the dielectric medium would participate in polarization. Also note that the electrostatic potential $\tilde{\phi}$ is now potentially a complex value, which will be further discussed in section 2.10.

2.5 Dielectric loss

In the last section we derived an expression for the complex permittivity in which the real part consisted of the real permittivity and the complex part consisted of the real conductivity of the medium. In reality (this is of course another model and reality itself is even more complex) the permittivity itself is a function of the frequency of the applied field and the complex permittivity is more generally expressed as (Morgan and Green, 2002, Sec. 2.4)

$$\tilde{\varepsilon}(\omega) = \varepsilon'(\omega) + j\left(\varepsilon''(\omega) + \frac{\sigma}{\omega}\right). \tag{2.18}$$

The imaginary part of this quantity is the energy loss that occurs when an electric field is applied (for example as heat), whereas the real part is the fraction of the input energy (field) that is converted to dielectric polarization. Note that the loss consists of a part that is due to the permittivity ε'' and a part due to conductivity ω. The latter dependency is straightforward: When the conductivity is high a large portion of the applied field is used to conduct current through the material. This plays no part in volumetric polarization but instead causes a lot of loss as resistive heating. With increasing frequency this effect decreases since the charges do not have ample time to follow the alterations of the field (Morgan and Green, 2002, Sec. 2.4).

The reason for the frequency dependence of the permittivity is dielectric relaxation. As outlined above, polarization occurs due to a finite and small displacement (or rearrangement) of charges. This charge movement and rearrangement requires a specific amount of time to be complete. If the field alternates faster than the required time period the charge movement is stopped and reversed before maximum polarization is achieved. At the relaxation frequency one half-period exactly matches the time for the dipoles to "relax". Then, maximum energy is dissipated in the system. Below that frequency, maximum polarization is achieved and above that frequency, there is no response to the field (and no polarization) and the permittivity drops. Each of the polarization mechanisms outlined above has a specific time associated with them,

with orientational polarization having the lowest relaxation frequency, followed by atomic polarization. Electronic polarization has the largest relaxation frequency. As an example, water has a very high relative permittivity of 80 at frequencies below 1×10^8 Hz due to the permanent dipoles. The relaxation frequency of water is $\sim 2 \times 10^{10}$ Hz and above this frequency the relative permittivity drops to 2, a value that is associated with the electronic polarization. At even higher frequencies the permittivity will drop again due to the relaxation associated with the electronic polarization (Morgan and Green, 2002, Sec. 2.4).

The loss tangent of the angle δ is the ratio of the lossy reaction of the dielectric to $\boldsymbol{E}$ compared to the lossless reaction (Morgan and Green, 2002, Sec. 2.3.7):

$$\tan\delta = \frac{\varepsilon'' + \sigma/\omega}{\varepsilon'}. \tag{2.19}$$

The difference between an ideal lossless dielectric (which does not exist in reality) and a lossy dielectric is now obvious: In a lossless dielectric, the tan and hence δ in Eq. (2.19) are 0 and all energy that is put into the system is converted to polarization of the dielectric. In a lossy dielectric, δ must be larger than 0 because energy is dissipated due to dielectric relaxation and macroscopic movement of charge carriers (conduction).

Eqs. (2.18) and (2.19) are introduced for completeness. Since dielectric relaxations occur in the GHz and above range they are negligible for most DEP applications. For the remainder of the thesis it is therefore assumed that the permittivity is constant and that all loss in the dielectric is just due to the conductivity, $\varepsilon \neq f(\omega)$ and as before

$$\tilde{\varepsilon} = \varepsilon_0 \varepsilon_\mathrm{r} - \frac{j\sigma}{\omega}. \tag{2.20}$$

2.6 Dipole moment of a polarized spherical particle

As already discussed, under the presence of an electric field there will be interfacial polarization at boundaries of dielectric material. That means that polarization charges will build up on both sides of the material boundary. This is key for DEP particle movement. In an ideal case the DEP exercise is to move a homogeneous spherical particle of radius R. Such a particle will experience a dipole polarization with a charge separation distance d that equals the particle diameter. The direction and magnitude of the dipole moment $\boldsymbol{p}$ of the induced dipole depends on the particle size, the excitatory field strength and the polarizability of the particle in the medium. To equate the acting force on that particle it is necessary to calculate $\boldsymbol{p}$.

Assume a spherical homogeneous particle of complex permittivity $\tilde{\varepsilon}_\mathrm{i}$ and radius R in a homogeneous dielectric medium of permittivity $\tilde{\varepsilon}_\mathrm{o}$ (cf. Fig. 2.3 a). The induced dipole can be calculated by solving Poisson's equation in axisymmetric (r, θ) coordinates. Since the inside and the outside of the sphere are homogeneous, it is possible to drop $\tilde{\varepsilon}$ from Eq. (2.17) and

to account for the material boundary by applying appropriate boundary conditions. A general solution of $\Delta\tilde{\Phi}=0$ for $\tilde{\Phi}$ in azimuthal symmetry reads (Zangwill, 2013, Sec. 7.6)

$$\tilde{\Phi}=\sum_i\left[A_i r^i + B_i r^{-(i+1)}\right] C_i P_i(\cos\theta), \tag{2.21}$$

where A_i,B_i,and C_i are constants and $P_i(x)$ are the first order Legendre functions. The potential inside the sphere must be finite at $r = 0$ and the potential at the outside must match $-E_0 z = -E_0 r\cos\theta$ at $r = \infty$, so Eq. (2.21) can be simplified for the inside ($\tilde{\Phi}_\mathrm{i}$) and outside potential ($\tilde{\Phi}_\mathrm{o}$) (Jackson, 2013, Sec. 4.4):

$$\tilde{\Phi}_\mathrm{i} = \sum_i a_i r^i P_i(\cos\theta), \tag{2.22a}$$

$$\tilde{\Phi}_\mathrm{o} = -E_0 r\cos\theta + \sum_i b_i r^{-(i+1)} P_i(\cos\theta). \tag{2.22b}$$

Here, a_i and b_i are again constants. The appropriate boundary conditions at $r = R$ (Jones, 1995, Sec. 2.2 B)

$$\tilde{\Phi}_\mathrm{i}\,(r=R,\theta)=\tilde{\Phi}_\mathrm{o}\,(r=R,\theta), \tag{2.23a}$$

$$\tilde{\varepsilon}_\mathrm{i}\left.\frac{\partial\tilde{\Phi}_\mathrm{i}}{\partial r}\right|_{r=R} = \tilde{\varepsilon}_\mathrm{o}\left.\frac{\partial\tilde{\Phi}_\mathrm{o}}{\partial r}\right|_{r=R}. \tag{2.23b}$$

The first equation states that the potential must be continuous over the boundary and the second that the normal component of the electric flux density $\boldsymbol{D}$ must be continuous. Under application of the boundary conditions the outside potential takes the form (i. e., all constants $b_i = 0$ for $i > 1$) (Green, 2011b)

$$\tilde{\Phi}_\mathrm{o} = E_0 R^3\left(\frac{\tilde{\varepsilon}_\mathrm{i}-\tilde{\varepsilon}_\mathrm{o}}{\tilde{\varepsilon}_\mathrm{i}+2\,\tilde{\varepsilon}_\mathrm{o}}\right)\frac{\cos\theta}{r^2} - E_0 r\cos\theta. \tag{2.24}$$

The second term is the potential due to the applied field and the first term the potential due to the dipole. Comparison with Eq. (2.8) shows that the dipole moment of the sphere is (Green, 2011b)

$$\tilde{\boldsymbol{p}} = 4\pi\varepsilon_\mathrm{o}\left(\frac{\tilde{\varepsilon}_\mathrm{i}-\tilde{\varepsilon}_\mathrm{o}}{\tilde{\varepsilon}_\mathrm{i}+2\,\tilde{\varepsilon}_\mathrm{o}}\right)R^3\,\tilde{\boldsymbol{E}} = 4\pi\varepsilon_\mathrm{o}\,\tilde{f}_\mathrm{CM}\,R^3\,\tilde{\boldsymbol{E}}\,. \tag{2.25}$$

In the derivation of Eq. (2.24) it was assumed that the excitatory field was real whereas in the general form of the dipole moment of a sphere it is assumed that $\tilde{\boldsymbol{E}}$ might be complex for generality. Note also that the first ε_o in Eq.(2.25) is the real permittivity ($\varepsilon_\mathrm{o} = \varepsilon_{\mathrm{r,o}}\varepsilon_0$) and not the complex permittivity.

The Clausius-Mossotti function $\tilde{f}_\mathrm{CM}(\omega)$ is defined as

$$\tilde{f}_\mathrm{CM}(\omega) = \frac{\tilde{\varepsilon}_\mathrm{i}\,(\omega)-\tilde{\varepsilon}_\mathrm{o}\,(\omega)}{\tilde{\varepsilon}_\mathrm{i}\,(\omega)+2\,\tilde{\varepsilon}_\mathrm{o}\,(\omega)} \tag{2.26}$$

with the complex permittivities as given by Eq. (2.20). The $\tilde{f}_\mathrm{CM}$ gives the relative polarizability of the particle in the medium. It is complex and dependent on the angular frequency. Its

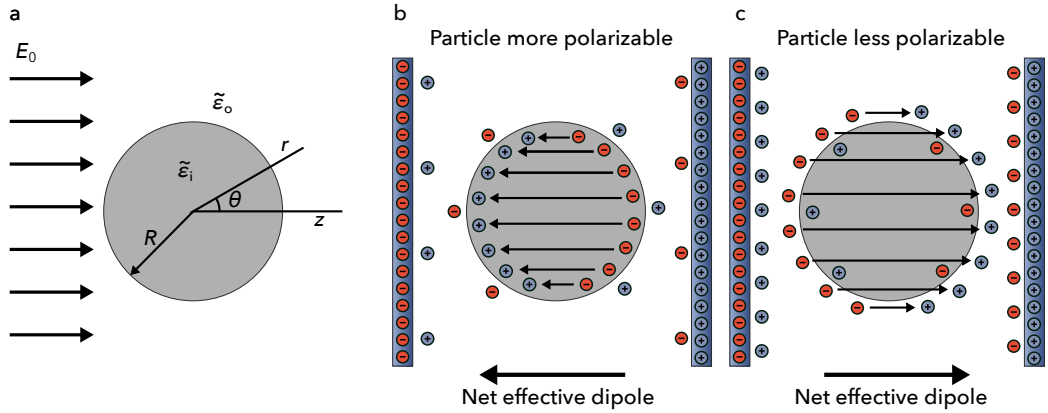

Fig. 2.3: Particle polarisation. a) A spherical homogeneous particle with complex permittivity $\tilde{\varepsilon}_i$ and radius R is located in a homogeneous medium with complex permittivity $\tilde{\varepsilon}_o$. The electric field is applied along the z axis and the problem has azimuthal symmetry. b) The particle in the electric field is better polarizable than the surrounding medium, more surface charge accumulates on the inside of the particle and the dipole moment $\boldsymbol{p}$ points in opposite direction than the electric field $\boldsymbol{E}$. c) The particle is less polarizable than the surrounding medium and more charge accumulates on the outside of the particle. The dipole moment $\boldsymbol{p}$ points in the same direction as $\boldsymbol{E}$ (Jackson (2013, Fig. 4.6); Green (2011b); Hughes (2002b, Fig. 2.10)).

complex part gives the dielectric loss due to the interfacial polarization and its real part gives the effective relative polarizability of the particle in the medium. It is bound between –0.5 and 1. If it is < 0 then the particle is less polarizable than the surrounding medium and vice versa. When the particle is better polarizable than the surrounding medium, the dipole moment points in the opposite direction than the electric field (cf. Fig. 2.3 b). Conversely, when the particle is less polarizable then $\boldsymbol{p}$ points in the same direction as $\boldsymbol{E}$ (cf. Fig. 2.3 c). The explanation of this behavior is straightforward: Polarization charges will accumulate at every interface in the system and on both sides of the interface (the polarizability is a measure for the amount of accumulated charges). When the situation of Fig. 2.3 b and c is considered, the charges will accumulate at the interface between the electrodes and the liquid medium and at the interface between the liquid medium and the particle. If the particle is better polarizable, the amount of accumulated surface charges on the inside is much larger than on the outside; consequently, the dipole moment $\boldsymbol{p}$ points from right to left and thus against the applied electric field. The surface charges on the outside of the particle will partly shield the inside potential, this is negligible if the polarizability difference is rather large ($\tilde{f}_{\mathrm{CM}}(\omega) = 1$). If both polarizations are equal, the outside charges entirely shield the inside charges and the particle does not appear to be polarized. If $\tilde{f}_{\mathrm{CM}}(\omega) < 0$, then more charges accumulate between electrodes and medium and on the outside of the particle compared to its inside. Effectively, the liquid left and right of the particle is polarized in a way that the moment points against the direction of the electric field (from the particle surface to the left electrode and from the right electrode to the particle surface). Since it is just a matter of perspective, it is also possible to see a net dipole moment that points *in direction* of $\boldsymbol{E}$ and that forms across the outside charges. Since the separation between

inside and outside charges is negligible it is unimportant whether the charges accumulate on the inside or outside (Hughes, 2002b, Sec. 2.6).

2.7 Effective moment of non-spherical or inhomogeneous particle

Equation (2.25) was derived for a spherical and homogeneous particle. If the particle is not spherical (Green and Jones, 2007) or if the particle is not small compared to the change of the electric field (Nili and Green, 2014) (i. e., the electric field changes considerably in magnitude over the diameter of the particle), the resulting charge distribution due to the polarization will not be a dipole: There are also higher order multipoles superimposed (Green and Jones, 2007). In Eq.(2.22b) not all b_i will vanish for $i > 0$ due to the different boundary shape in Eq.(2.23a) or due to inhomogeneity of $E_0(\boldsymbol{x})$ itself. It is possible to estimate the net polarization by assuming a sphere of constant volume with the electric field value taken at the center of the particle but then an error is made that increases together with deviation of the particle from a perfect sphere or with increasing curvature of the field.

To obtain a value of the polarization field due to the presence of the particle and to compute the resulting force it is necessary to obtain the effective moment of the particle (Green and Jones, 2007; Nili and Green, 2014), which is only in very few instances possible using analytical methods (i. e., ellipsoids; cf. Winter and Welland (2009)). Instead, numerical integration from FEM calculations of Φ around the particle (Green and Jones, 2007) or integration of the polarization field over the entire particle volume (Zhao et al., 2017) can be used.

When the particle (spherical or non-spherical) is inhomogeneous, the resultant effective moment can be of order 2 (dipole, spherical particle or prolate ellipsoid with multiple homogeneous shells, like an onion) or of higher orders (non-spherical particles or complex inhomogeneity). Analytical expressions for the dipole moment exist for multi-layered spheres (Turcu and Lucaciu, 1989) and prolate ellipsoids (Gimsa, 2001). The generally applicable volume integration method by Zhao et al. (2017) or the effective moment extraction method of Green and Jones (2007) have to be used to extract the effective moments of more complex particles.

2.8 Dielectric dispersions of homogeneous materials and due to material interfaces

A word on nomenclature: *Dispersion* means that a physical property depends on the frequency of a wave. *Dielectric relaxation* is the lag of the dielectric constant of the material due to the inability of the polarization effects to keep the pace of the changing ac field.

As discussed in Section 2.3, a dielectric material can have several dispersions (that is, changes in the overall polarizability) at different frequencies. Some of them appear within the material and are due to *Debye relaxations* and some only at material interfaces which are caused by the *Maxwell-Wagner relaxation* (Hughes, 2002b, Sec. 2.5.3).

We take another look at Eq.(2.18), $\tilde{\varepsilon}(\omega) = \varepsilon'(\omega) + j(\varepsilon''(\omega) + \sigma/\omega)$, and keep in mind that the imaginary part of this quantity defines the dielectric loss whereas the real part states

how much energy is converted to dielectric polarization. It is obvious that the Debye relaxations (that is, again, relaxation processes that are happening *within* the material without any material interfaces) must be accompanied by changes of $\varepsilon'(\omega)$. The amount of dispersions due to Debye relaxations (maximum three) depend on how many polarization mechanisms (orientational, atomic, and electronic) participate in the net polarization of that material. A typical plot of ε' and ε'' as a function of ω is given in Fig. 2.4 a including the typical frequency ranges. Every time a dispersion occurs, ε'' peaks due to the energy dissipation.

Consider now the case of a parallel plate capacitor (as shown in Fig. 2.4 b) containing two slabs of lossy dielectrics with different dielectric properties. The net effective permittivity of such a system is then (Morgan and Green, 2002, Sec. 3.1)

$$\widetilde{\varepsilon} = \varepsilon_0 \left(\varepsilon_{\mathrm{hf}} + \frac{\varepsilon_{\mathrm{lf}} - \varepsilon_{\mathrm{hf}}}{1 + \omega^2 \tau^2} \right) - j \left(\frac{(\varepsilon_{\mathrm{lf}} - \varepsilon_{\mathrm{hf}})\omega\tau}{1 + \omega^2 \tau^2} + \frac{\sigma}{\varepsilon_0 \omega} \right), \tag{2.27a}$$

$$\varepsilon_{\mathrm{hf}} = \frac{(d_1 + d_2)\varepsilon_1 \varepsilon_2}{d_1 \varepsilon_1 + d_2 \varepsilon_2}, \tag{2.27b}$$

$$\varepsilon_{\mathrm{lf}} = \frac{(d_1 + d_2)(d_1 \varepsilon_1 \sigma_2^2 + d_2 \varepsilon_2 \sigma_1^2)}{(d_1 \sigma_2 + d_2 \sigma_1)^2}, \tag{2.27c}$$

$$\tau = \varepsilon_0 d_1 \varepsilon_2 + d_2 \varepsilon_1 d_1 \sigma_2 + d_2 \sigma_1, \tag{2.27d}$$

$$\sigma = \frac{(d_1 + d_2)\sigma_1 \sigma_2}{d_1 \sigma_2 + d_2 \sigma_1}. \tag{2.27e}$$

Here, $\varepsilon_{\mathrm{lf}}$ and $\varepsilon_{\mathrm{hf}}$ are the effective low and high-frequency permittivities of the composite medium and τ is the relaxation time at which the dispersion occurs. When inspecting the equations it is obvious that another dispersion was added solely because of the interface and due to the differences in ε and σ between them. This Maxwell-Wagner interfacial dispersion occurs at frequencies much lower than all other dispersions and depends on the differences in the dielectric properties and on the charge separation distances (d_1 and d_2). In general, $\varepsilon_{\mathrm{hf}}$ should not be constant but itself a function of the frequency to account for the dispersions due to the Debye relaxation processes occurring in ε_1 and ε_2 at higher frequencies. A plot of $\mathrm{Re}[\widetilde{\varepsilon}]$ and $\mathrm{Im}[\widetilde{\varepsilon}]$ including all dispersions in shown in Fig. 2.4 b.

Looking now at the Clausius-Mossotti factor (and on the polarization of a spherical particle, Fig. 2.4 c) we see that it shows the same Maxwell-Wagner interfacial dispersion than the composite material in Fig. 2.4 b. As stated before, for simplicity and since the Debye relaxations occur at such high frequencies, we ignore all material-dependent dispersions and only consider the Maxwell-Wagner dispersion for the definition of $\widetilde{f}_{\mathrm{CM}}$ (hence, assume that all real ε take their respective low-frequency value before any Debye relaxations occur). Due to the definition of $\widetilde{\varepsilon}$, $\widetilde{f}_{\mathrm{CM}}$ depends mainly on the conductivities of the medium and the particle at low frequencies and on their permittivities at high frequencies. The last panel of Fig. 2.4 shows the $\widetilde{f}_{\mathrm{CM}}$ for a multi-shell particle. Now, since there are two interfaces present, two relaxations occur. At low frequency, there is a transition from the particle appearing to be less polarizable than the surrounding medium to being more polarizable. At high frequency, the behavior changes again and the particle is again less polarizable than the surrounding medium. This the classical case for biological particles in buffer solution (Pethig, 2010).

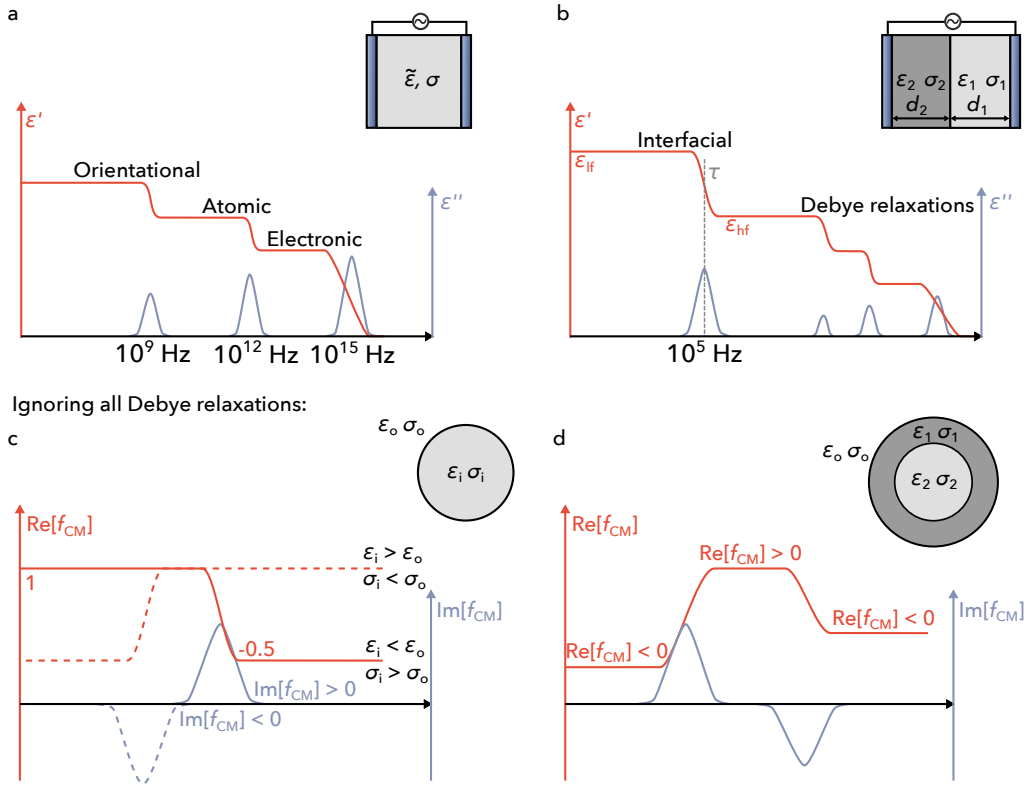

Fig. 2.4: Net permittivity of a single homogeneous material including all three possible dispersions with typical relaxation frequencies (a). Introducing a second material causes a Maxwell-Wagner interfacial dispersion that occurs at lower frequency and that is caused by the differences in ε and σ (b). From the dipole moment of a polarized sphere one can derive the Clausius-Mossotti factor: Panel (c) shows the real and imaginary part of the factor for a homogeneous particle that has a lower permittivity but higher conductivity than the surrounding medium (solid) and vice versa (dashed). The Clausius-Mossotti factor for a multishell particle with one shell shows two dispersions because two interfaces are present (d) (Morgan and Green, 2002, Figs. 3.2, 3.5, and 3.7).

2.9 Electrokinetic forces in (ac) electric fields

This thesis focuses on particle movement caused by dielectrophoresis, that is, a field gradient acting on an induced dipole (or multipole). There are other important electrokinetic effects that could occur and for completeness most of them will be covered very briefly before explaining dielectrophoresis and its application in detail.

2.9.1 Electrophoresis and electro-osmosis

The most common electrokinetic effect is electrophoresis; it describes movement of a charged particle in a (in most cases) dc field. In a dielectric (non-conducting) liquid it is due to the Coulomb force ($F = QE$) that act s on the particle charge. In a conducting liquid, i. e., a liquid containing dissolved ions, the charged particle will be screened so that there is a zero net interfacial charge of the particle plus its double layer. This double layer is obviously *not* electrically neutral (the double layer will not be explained in-depth in this thesis) but has the opposing charge from the particle (so that it screens it). Therefore, a field that is applied tangential to the surface will cause a motion of these charges in opposite direction than the Coulomb

force would drive the particle. If the surface is fixed, the ions move and drag fluid with them causing a net fluid velocity on the surface (Bazant, 2011). Since the particle is, however, freely suspended, the fluid itself will actually not move but the ion movement propels the particle in the opposing direction (now again the same direction as the Coulomb force would drive it). The imaginative reader might think the ions paddle. The same effect together with a fixed surface will cause fluid motion and is termed electro-osmosis (Bazant, 2011). It is important to note that no net movement occurs from this effect in ac fields (because the particle will just oscillate back and forth) or when the surface (particle) is not charged (because, well …).

2.9.2 Induced-charge electrophoresis and electro-osmosis

If the particle is uncharged but polarizable, fluid motion or in some cases even particle motion that is not attributed to dielectrophoresis is still observable in dc and even in ac fields of low frequency. This is especially true for metal particles in liquids of high ionic strength. The movement is attributed to induced-charge electrophoresis (ICEP, if the particle moves) or induced-charge electro-osmosis (ICEO, if the fluid moves). A metal particle in a conducting liquid will polarize under the application of an electric field. Subsequently, the field drives a current that transports charges (ions) towards the two poles of the polarized particle in order to charge the double layer around it. This continues until all polarization charges are screened by the double layer. The tangential component of the field will act on the two opposingly charged double layers on both sides of the particle which will cause a quadrupolar ICEO fluid flow from the poles of the particle to the equator. The particle itself will not move due to the symmetry of the flow pattern. The same flow will also occur on dielectric surfaces but to a much smaller extend (with metal particles the velocity scales with particle size whereas with dielectric particles it scales with double layer thickness) (Bazant, 2011). If the symmetry is broken there will be either a net pumping (fixed object) or a net particle movement (suspended particle) as described in depth by Squires and Bazant (2006). Breaking the symmetry means either applying an inhomogeneous field, or looking at a particle of irregular shapes or with non-uniform surface properties, like Janus particles (Gangwal et al., 2008).

These induced-charge effects are frequency dependent and vanish when the ac frequency is greater than the inverse of the required time to charge the double layer. Since they will act on a polarizable particle in an inhomogeneous field they will potentially be present when DEP also occurs. This is negligible for dielectric particles in conductive or dielectric liquid (since the effect will be very small) but needs to be considered for a metallic particle in a conductive medium (Ramos et al., 2016). Then, at low frequencies, in theory the ICEP will point in the opposite direction than the DEP effect. ICEO can also be used to pump liquids over interdigitated electrodes of unequal shape (Green et al., 2000a, 2002a; Rouabah et al., 2011) which is termed ACEO micropump.

2.9.3 Dielectrophoresis, electrorotation, electro-orientation and traveling-wave dielectrophoresis

Dielectrophoresis occurs because the induced charge separation (dipole or multipole) interacts with an *inhomogeneous* field. It is present in both, ac and dc fields, but ac fields are preferred to avoid dc electrokinetic effects such as electrophoresis and electro-osmosis.

From geometric considerations (cf. Fig.2.5 a), the time-averaged dielectrophoretic force on a *dipole* can be derived as (Green, 2011a)

$$\langle \boldsymbol{F}_{\mathrm{DEP}} \rangle = \frac{1}{2} \mathrm{Re}\left[(\tilde{\boldsymbol{p}} \cdot \nabla)\, \tilde{\boldsymbol{E}}^{*} \right] \tag{2.28}$$

with the complex conjugate of the complex electric field vector $\tilde{\boldsymbol{E}}^{*}$. Without further simplifications in full form this reads (Green, 2011a)

$$\langle \boldsymbol{F}_{\mathrm{DEP}} \rangle = \frac{3}{4} V_{\mathrm{P}} \varepsilon_{\mathrm{m}} \mathrm{Re}\left[\tilde{f}_{\mathrm{CM}} \right] \nabla \left| \tilde{\boldsymbol{E}} \right|^{2} - \frac{3}{2} V_{\mathrm{P}} \varepsilon_{\mathrm{m}} \mathrm{Im}\left[\tilde{f}_{\mathrm{CM}} \right] \left(\nabla \times \left(\mathrm{Re}\left[\tilde{\boldsymbol{E}} \right] \times \mathrm{Im}\left[\tilde{\boldsymbol{E}} \right] \right) \right). \tag{2.29}$$

with the particle's volume V_{P}.

Conventionally, the ac field is applied with a single sine wave against ground or with two sine waves shifted by 180° (Hughes, 2002b, Sec. 2.7.1); then, in most cases it is safe to assume that there is no phase shift across the system and Eq. (2.29) simplifies to

$$\langle \boldsymbol{F}_{\mathrm{DEP}} \rangle = \frac{3}{4} V_{\mathrm{P}} \varepsilon_{\mathrm{m}} \mathrm{Re}\left[\tilde{f}_{\mathrm{CM}} \right] \nabla |\boldsymbol{E}|^{2}. \tag{2.30}$$

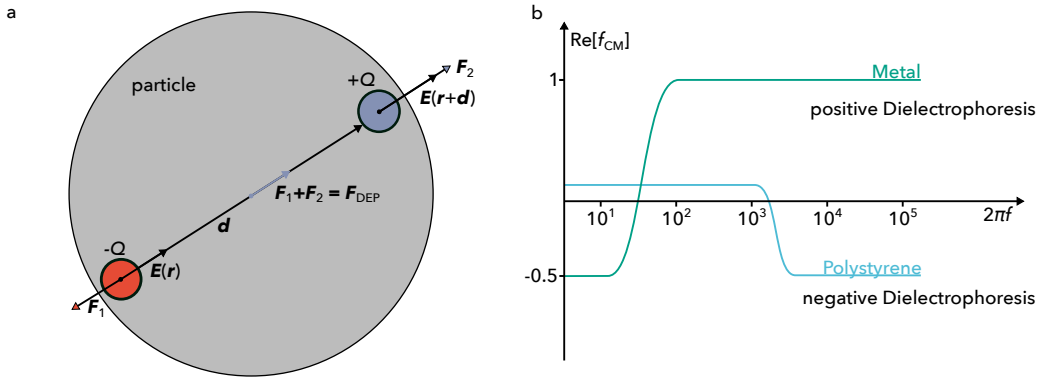

Fig. 2.5: a) Derivation of the dielectrophoretic force of a particle with position vector $\boldsymbol{r}$ and diameter $d = |\boldsymbol{d}|$. Since the electric field is inhomogeneous, it will be different on both sides of the induced dipole. Then, since the charges are equal, the acting force will be slightly higher on one end of the dipole which results in a net force. b) Qualitative sketch of the Clausius-Mossotti factor for a 5 µm gold particle and a polystyrene particle of the same size as a function of the angular frequency $\omega = 2\pi f$. If the frequency is high enough, gold will experience positive dielectrophoresis and polystyrene will experience negative dielectrophoresis. This allows for property dependent particle sorting because both types of particle will move towards different directions in the electric field gradient (Ermolina and Morgan, 2005; Ren et al., 2011).

where $\boldsymbol{E}$ is the vector of the field amplitude. This equation employs the real part of the Clausius-Mossotti function that was defined in Eq. (2.26). As stated above (cf. Sec. 2.6) it gives the relative polarizability of a spherical particle in a given medium and is bound between 1 (perfectly polarizable) and −0.5 (non-polarizable compared to the surrounding medium). This equation is the point-dipole equation: it assumes that the electric field vector does not change significantly over the volume of the particle and that the polarization of the particle can be approximated using a dipole, which is only valid for spherical particles. The calculation methods for more complex particles will be given in Sec. 2.10.

The DEP force (Eq. (2.30)) depends on the volume of the particle and the gradient of the electric field magnitude square. The force direction and magnitude is defined by the real part of the Clausius-Mossotti function. The effective polarizability defines the direction of the movement which is (ignoring all electrophoresis effects) independent of the polarization of the field (plus and minus) but only dependent on the field curvature. If $\mathrm{Re}\left[\tilde{f}_{\mathrm{CM}}\right] < 0$, the particle is less polarizable and it will move against the gradient of the field (cf. Fig. 2.6 a, termed *negative dielectrophoresis*). Vice versa, if $\mathrm{Re}\left[\tilde{f}_{\mathrm{CM}}\right] > 0$, the particle is better polarizable and will move in direction of the field gradient (cf. Fig. 2.6 b, termed *positive dielectrophoresis*).

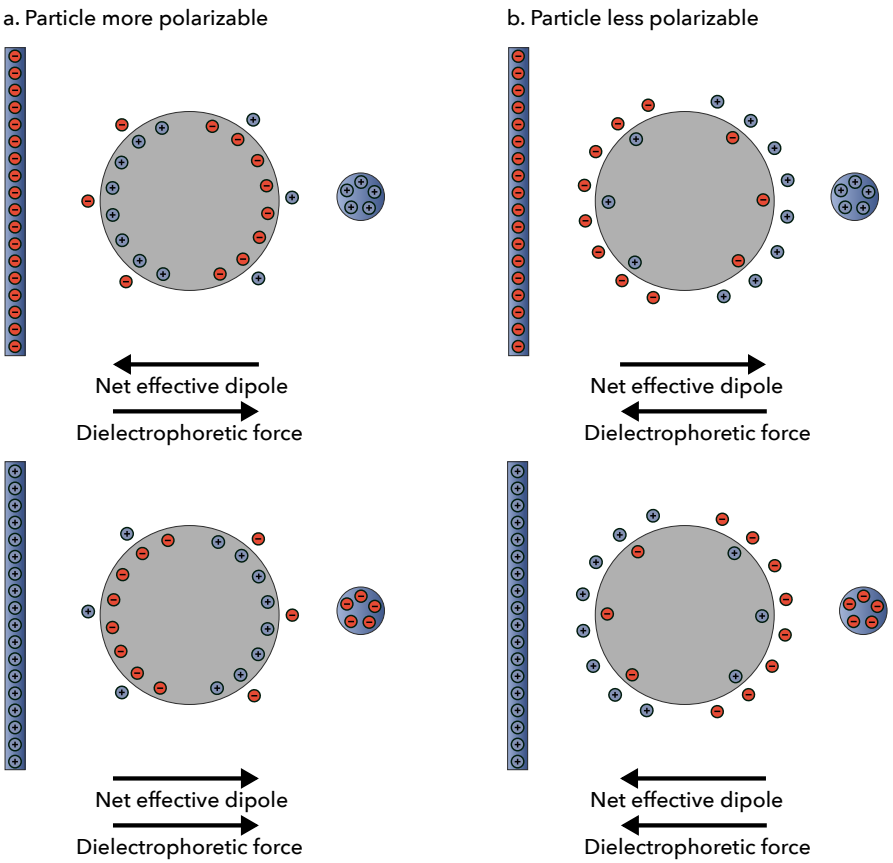

Fig. 2.6: Polarization, induced net dipole and dielectrophoretic force direction for a particle that is (a) better polarizable than the surrounding medium and (b) less polarizable. Top and bottom are two different arrangements of the background electric field (Green, 2011a).

Due to the dependence on volume and gradient of the magnitude of the field square it is obvious that the movement of small particles (for example in the nanometer size range) requires either very strong fields or very advanced ways to create field inhomogeneities. The most common approaches for generating field inhomogeneities are: (i) the application of a two-dimensional electrode array with very small electrodes; for example interdigitated electrode arrays. These electrodes will generate a field that is strongest at the electrodes and that decays with logarithmic distance from the array (Green et al., 2002b; Morgan et al., 2001) and that shows stronger force with decreasing electrode distance (Aoki et al., 2016; Markx et al., 1997a; Wang et al., 2015). (ii) The application of three-dimensional electrodes in which the generated forces greatly depend on the employed geometry; generally, the forces are expected to be slightly higher in three-dimensional electrode arrangements compared to planar electrodes (Choongho Yu et al., 2005; Iliescu et al., 2007a, 2006; Suehiro and Pethig, 1998). (iii) The electric field scattering or distortion at material boundaries, that is, introduction of conducting or isolating structures in a homogeneous electric field as particle traps (Braff et al., 2012; Cummings and Singh, 2003; Jones et al., 2017).

The dependence of the force direction and magnitude on the particle polarizability is one of the main features of dielectrophoresis because it allows for particle sorting by type (for example by selectively trapping only one kind of particle). As an example Fig.2.5 b shows (qualitatively) $\tilde{f}_{\mathrm{CM}}$ for a 5 µm gold particle and a polystyrene particle of same size. At sufficiently high frequencies, the gold particle will show positive dielectrophoresis whereas the polystyrene particle will present negative dielectrophoresis. This can be used to selectively trap the gold particles from a mixture of non-conducting particles (Du et al., 2008). Another very common example is the discrimination between live and dead (biological) cells (Pohl and Hawk, 1966).

There is the possibility that the dipole has an angle towards the electric field. Then, the electric field will exert a torque on the dipole in order to align it. This happens mainly at two occasions, electrorotation (ROT) and electro-orientation (EOr).

Using ROT it is possible to rotate a spherical particle by applying a rotating field. If the field changes it's direction quite fast the induced dipole does not have sufficient time to form. Consequently, the field will already have rotated when the dipole is established, causing a net rotation of the particle (so that the particle follows the field). Normally, ROT is used for particle analysis by applying a circularly polarized field which is established by the superposition of two perpendicularly applied fields with 90° phase shift. The particle then experiences a constant torque that is, assuming a harmonic ac field, given by (Green, 2011a)

$$\langle \mathbf{\Gamma}_{\mathrm{ROT}} \rangle = -3\varepsilon_{\mathrm{m}} V_{\mathrm{P}} \mathrm{Im}\left[\tilde{f}_{\mathrm{CM}}\right] \left(\mathrm{Re}\left[\tilde{\boldsymbol{E}}\right] \times \mathrm{Im}\left[\tilde{\boldsymbol{E}}\right]\right). \tag{2.31}$$

Since the field is rotating, now $\mathrm{Im}\left[\tilde{\boldsymbol{E}}\right]$ will not be zero. Electrorotation only occurs if the imaginary part of the Clausius-Mossotti factor is non-zero, that is, when the real part changes its sign (when the particle is crossing from negative to positive DEP or vice versa). The fact that $\mathrm{Im}\left[\tilde{f}_{\mathrm{CM}}\right]$ is maximum when $\mathrm{Re}\left[\tilde{f}_{\mathrm{CM}}\right] = 0$ allows to gather information on the DEP spectrum of a particle by analyzing its rotational spectrum (Wang et al., 1992).

Electroorientation occurs when a non-spherical particle, that is not initially aligned perpendicular to the field, is polarized. Since the charge separation is always biggest over the longest axis of the particle, it will try to realign itself with the electric field vector (Green, 2011a). This can be used, for instance, for the specific alignment and collection of carbon nanotubes (Liu et al., 2004) in interdigitated electrode arrays.

Traveling-wave DEP occurs in a system in which the applied voltage "travels" across an interdigitated electrode array. In this case the signal on one electrode finger is identically to the signal of the previous finger with a superimposed 90° phase shift. Then, the fifth electrode carries the same signal as the first, and so on. Then, the force on a spherical particle would be (Green, 2011a)

$$\langle \boldsymbol{F}_{\mathrm{DEP}} \rangle = \frac{3}{4} V_{\mathrm{P}} \varepsilon_{\mathrm{m}} \mathrm{Re}\left[\tilde{f}_{\mathrm{CM}}\right] \nabla |\boldsymbol{E}|^2 - \frac{3}{2} V_{\mathrm{P}} \varepsilon_{\mathrm{m}} \mathrm{Im}\left[\tilde{f}_{\mathrm{CM}}\right] \left(\nabla \times \left(\mathrm{Re}\left[\tilde{\boldsymbol{E}}\right] \times \mathrm{Im}\left[\tilde{\boldsymbol{E}}\right]\right)\right). \tag{2.32}$$

The first part is the conventional DEP force and the second part is a force that propels the particle against the traveling direction of the field. Traveling-wave DEP can only occur, if the particle experiences negative DEP and is lifted above the electrode array. Also, its $\mathrm{Im}\left[\tilde{f}_{\mathrm{CM}}\right]$ must not be zero, which limits the applicability of the concept.

2.10 Practical considerations for calculation

2.10.1 Complex electric field and harmonically oscillating excitation

Throughout this thesis, complex values are assumed for the electric potential and the electric field. This assumes an ac electric field which is harmonically oscillating with a single angular frequency ω. The time dependent values can then be represented using phasors. The electrostatic potential at time t and position $\boldsymbol{x}$ is then Morgan et al. (2001)

$$\Phi(\boldsymbol{x}, t) = \mathrm{Re}\left[\tilde{\Phi}(\boldsymbol{x})\, e^{j\omega t}\right] \text{and} \tag{2.33a}$$

$$\tilde{\Phi} = \Phi_{\mathrm{R}} + j\Phi_{\mathrm{I}}. \tag{2.33b}$$

The electric field will then be given by Morgan et al. (2001)

$$\boldsymbol{E}(\boldsymbol{x}, t) = \mathrm{Re}\left[\tilde{\boldsymbol{E}}(\boldsymbol{x})\, e^{j\omega t}\right] \text{and} \tag{2.34a}$$

$$\tilde{\boldsymbol{E}} = -\nabla\tilde{\Phi} = -(\nabla\Phi_{\mathrm{R}} + j\Phi_{\mathrm{I}}). \tag{2.34b}$$

We can also write $\tilde{\boldsymbol{E}}(\boldsymbol{x}) = \boldsymbol{E}_{\mathrm{R}}(\boldsymbol{x}) + j\boldsymbol{E}_{\mathrm{I}}(\boldsymbol{x}) = |\boldsymbol{E}(\boldsymbol{x})|\, e^{j\varphi(\boldsymbol{x})}$. Here $|\boldsymbol{E}(\boldsymbol{x})|$ is the magnitude of the complex number $\sqrt{\mathrm{Re}\left[\tilde{\boldsymbol{E}}(\boldsymbol{x})\right]^2 + \mathrm{Im}\left[\tilde{\boldsymbol{E}}(\boldsymbol{x})\right]^2}$ and not the vector norm. The left expression is the cartesian form and the right expression is the Euler notation of the complex number. In this, $\varphi(\boldsymbol{x}) = \mathrm{atan2}\left(\mathrm{Im}\left[\tilde{\boldsymbol{E}}(\boldsymbol{x})\right], \mathrm{Re}\left[\tilde{\boldsymbol{E}}(\boldsymbol{x})\right]\right)$ is the phase shift of the electric field towards the excitation which we (for simplicity) assign a phase shift of 0. A phase shift occurs always when energy is lost due to the polarization of non-ideal dielectrics. A phase shift occurs also in traveling-wave DEP and electro-orientation due to the excitation which is with more than

one sine wave that have a phase shift towards each other (for example 4 sinusoids with 90° shift each). The phase shift is not constant but a function of $\boldsymbol{x}$. For example, due to the lag of the polarization of a non-ideal dielectric, the polarization field might not follow the excitatory field immediately but with a small delay. This causes a shift in the electric field vector in the vicinity of the dielectric that vanishes at a large enough distance. Note that when $\widetilde{\boldsymbol{E}} = \boldsymbol{E}$ is real there is no phase shift; this is also called a constant phase. This is a common assumption in classical DEP application.

2.10.2 When the polarization is complex, why do we assume that the electric field is real?

As already mentioned, the common assumption for DEP force calculations is that the electric field causing the motion is real (so there is no phase shift at any point). Since the induced-dipole $\tilde{\boldsymbol{p}}$ might have a non-zero imaginary part the potential field due to the dipole would also be complex. Then, the assumption of a field without phase shift would not be correct. This is essentially true every time dielectrophoresis is used at a frequency at which the particles have a non-zero $\mathrm{Im}\left[\tilde{f}_{\mathrm{CM}}\right]$. For simplification, however, the effect of the particles on the field is ignored in most instances. That is, the field is calculated ignoring all present particles. Then, the effect of the field on the particles is calculated but not the other way round. This causes problems when many particles are present because it neglects the interactions between the particles (one particle will interact with the polarization field of the neighboring particles) and those close to dielectric boundaries (Çetin et al., 2017). Since we exclude the effect from the particle on the field any possible phase shift due to dielectric loss in the particle polarization will also be ignored.

2.10.3 Electric field calculation using the finite element method

The solution strategy to find an arbitrary electric field distribution is usually to solve Poisson's equation for the electrostatic potential in the calculation domain. The boundaries of the calculation space either carry a predefined potential ($\Phi = \Phi_0$), this is usually the applied voltage drop, or are insulating ($\partial\Phi/\partial\hat{\boldsymbol{n}} = 0$). Only very few electrode configurations with relevance to dielectrophoresis possess analytical expressions (for example the interdigitated electrode array that is explained by Morgan et al. (2001) or the electric field distribution around cylindrical posts which was developed in our working group, Pesch et al. (2016)). The calculation of the field distribution in more complex geometries usually requires the application of numerical methods, for example the finite element method (Logg et al., 2012a) or the finite volume method. In the finite element method the solution space is subdivided into a number of nodes that are the corners of enclosed elements. These elements have to loosely follow a given shape (the common shape is a triangular, but also quadrilateral or hexahedral elements are possible). Our target equation (in this case Poisson's equation) is approximated in these elements using ansatz functions with yet unknown coefficients. The elements are coupled with each other and the entire problem is mapped onto a system matrix which is solved as a series of simultaneous equations. In the simplest approach the electric field is mapped linearly across the elements.

In reality, the potential close to multipolar charge distributions might have a much higher dependence on the spatial coordinate (Pesch et al., 2016). In order to approximate this behavior with linear elements a large number of very densely distributed elements is required. This is usually achieved by automatic meshing procedures. In this thesis both FEniCS (Logg et al., 2012a) and COMSOL Multiphysics®[1] have been used to solve for the electrostatic potential. COMSOL comes with its own meshing algorithm whereas GMSH (Geuzaine and Remacle, 2009) was used to produce the mesh for the solution with FEniCS.

2.10.4 Dielectrophoresis in a fluid

A fluid will exert a viscous drag force on the particle when there is a relative velocity between fluid and particle that is given by

$$\boldsymbol{F}_{\mathrm{D}} = -f\boldsymbol{v}_{\mathrm{rel}} \tag{2.35}$$

with the friction factor f and $\boldsymbol{v}_{\mathrm{rel}}$ the relative velocity between the particle and the fluid. When an external force acts on the particle or when the fluid's velocity around the particle changes it will accelerate until the external forces and the drag force are equal or until the relative velocity between the particle and the fluid is 0 (that is in the absence of other forces the particle follows the fluid movement). After this acceleration period the particle moves with terminal velocity. For a particle in a *stationary fluid* under the influence of only DEP, this is

$$\boldsymbol{v}_{\mathrm{DEP}} = \frac{\boldsymbol{F}_{\mathrm{DEP}}}{f}. \tag{2.36}$$

Assuming a spherical particle of radius R and Stokes' drag ($f = 6\pi\mu_{\mathrm{F}}R$, μ_{F} is the dynamic viscosity of the liquid), the dielectrophoretic terminal velocity is

$$\boldsymbol{v}_{\mathrm{DEP}} = \frac{a^2\varepsilon_{\mathrm{m}}\mathrm{Re}\left[\tilde{f}_{\mathrm{CM}}\right]\nabla\left(|\boldsymbol{E}|^2\right)}{6\mu_{\mathrm{F}}} = \mu_{\mathrm{DEP}}\nabla|\boldsymbol{E}|^2. \tag{2.37}$$

with the dielectrophoretic mobility $\mu_{\mathrm{DEP}} = \left(R^2\varepsilon_{\mathrm{m}}\mathrm{Re}\left[\tilde{f}_{\mathrm{CM}}\right]\right)/(6\mu_{\mathrm{F}})$ defined with respect to the amplitude of the electric field $\boldsymbol{E}$.

Usually, the fluid will also be calculated using the finite element method, except for very simple geometries.

2.10.5 Other forces in (micro-)electrode structures

There are other forces occurring in electrode structures that might disturb the desired DEP effect. Apart from the electrokinetic forces described above they are mostly due to resistive heating of the fluid. When an electric field is applied across a conductive medium, some of the energy that is put into the system will be lost as heat. The amount is proportional to the conductivity of the liquid and the the applied voltage squared. If the fluid heats up to much it starts to boil which disrupts the entire separation process (additionally, the presence of gas bubbles disturbs the electric field distribution). Before boiling, the liquid will develop circulation flow patterns, either due to temperature-induced density differences or due to temperature-induced

[1] Commercial software package, http://www.comsol.com

differences in ε and σ which is termed electrothermal flow. A very comprehensive overview of the forces that are acting apart from DEP in electrode structures including equations on how to calculate them can be found in the reviews of Castellanos et al. (2003), Green et al. (2000b), and Ramos et al. (1998). Additionally, a very recent paper describes the influence of non-linear electrokinetic effects (ICEO and electrothermal) in insulator-based DEP applications (Wang et al., 2017).

2.10.6 Refinement of the DEP force equation

Equation (2.30) is only valid for a spherical particle (or to some extent for ellipsoids having the right orientation towards the field) under the assumption of a point-dipole: that is, the particle is much smaller than the spatial change of the field. Actually, the derivation of $\tilde{f}_{\mathrm{CM}}$ in Eq. (2.30) requires the field to be homogeneous, which is of course in contrast to the requirement of an inhomogeneous field for the calculation of a force on a dipole.

The polarization occurs at every point in the particle (because every atom and molecule in the dielectric contribute to the overall polarization); therefore, the macroscopic polarization depends on the local electric field at every point inside the particle. If the field causing the polarization is inhomogeneous, then the polarization of the particle is also inhomogeneous (Pethig, 2017, Sec. 10.3.1). However, the potential generated by the arbitrary polarized particle can always be expressed by a system of multipoles (cf. Fig. 2.7) that are located at the centre of the particle. This is also true if the particle is not spherical, but only for distances from the center larger than the longest axis of the particle (Green and Jones, 2007).

For particles that have rotational symmetry we can assume that the multipoles are linear, that is the charges are distributed along the axis of symmetry. The force acting on the particle is then given as a function of the multipole moments $\tilde{\boldsymbol{p}}_n$ (Jones and Washizu, 1996):

$$\langle \boldsymbol{F}_{\mathrm{DEP}} \rangle = \frac{1}{2} \mathrm{Re} \left[\sum_n \frac{\tilde{\boldsymbol{p}}_n \, [\cdot]^n \, (\nabla)^n \, \tilde{\boldsymbol{E}}^*}{n!} \right] \tag{2.38}$$

with the n dot product $[\cdot]^n$ performed on the dyadic tensors and $(\nabla)^n$ is n times the vector ∇ operation. The sum is present since the overall DEP force depends on the contributions on the forces on all multipole moments. In case of a spherical particle of radius R, the $\tilde{\boldsymbol{p}}_n$ can be calculated for arbitrary fields (Jones and Washizu, 1996):

$$\tilde{\boldsymbol{p}}_n = \frac{4\pi\varepsilon_{\mathrm{m}} R^{2n+1} n}{(2n-1)!!} \, \tilde{f}_{\mathrm{CM}}^{(n)} \, (\nabla)^{n-1} \, \tilde{\boldsymbol{E}} \tag{2.39}$$

with the multipole form of the Clausius-Mossotti factor $\tilde{f}_{\mathrm{CM}}^{(n)} = \left(\tilde{\varepsilon}_{\mathrm{p}} - \tilde{\varepsilon}_{\mathrm{m}}\right) / \left(n\,\tilde{\varepsilon}_{\mathrm{p}} + (n+1)\,\tilde{\varepsilon}_{\mathrm{m}}\right)$.

Later Green and Jones (2007) developed a method to calculate the effective moments for arbitrary particles having rotational symmetry with the symmetry axis aligned perpendicular to the field. The method relied on numerical calculations to solve for the potential. Then, from the potential around the particle it is possible to derive the effective multipole moments that would cause such a potential field by numerical integration.

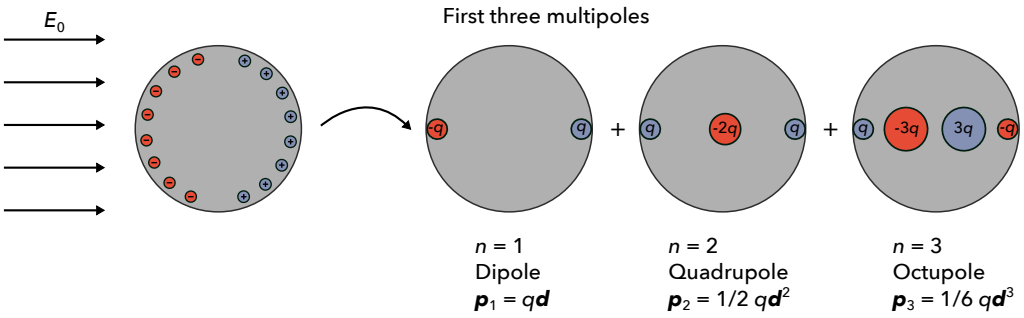

Fig. 2.7: An arbitrary polarization field of a particle can be substituted by a superposition of an infinite amount of linear multipoles. The first three linear multipoles are at most times enough for an accurate force expression. They are shown here together with the simple equations to calculate their moment (Green and Jones, 2007).

Another common approach to calculate the force on arbitrary particles is based on the Maxwell stress tensor (MST) where a stress tensor is integrated over the surface of the particle. This is considered as the most rigorous approach to the derivation of field induced forces (Wang et al., 1997). Recently Zhao et al. (2017) presented a volume integration method to calculate the force on the particle: they calculate the force as the integral over the forces acting on infinitesimal small particle unit. This naturally gives the correct force even if the particle is highly inhomogeneous or is of irregular shape. They claim that the MST approach, in contrast to their method, cannot deal with inhomogeneous particles due to an inappropriate use of Gauss's theorem.

Rosales and Lim (2005) and Nili and Green (2014) compared the MST method against the effective moment force calculation (Eq. (2.38)). In all cases considered, inclusion of the octupole moment ($n = 3$) is sufficient for an accurate description of the force (compared to the MST approach). When the curvature of the field is low, the dipole approach gives accurate results (even for highly non-spherical particles). This, however, is no justification to rely on the point-dipole approach as the field curvature (that is, the value of the higher order derivatives of $\tilde{E}$) is not always intuitive. Differences of up to 30 % between the point-dipole and the MST approach are possible (Nili and Green, 2014).

2.10.7 Particle-particle interaction

A polarized particle creates an inhomogeneous electric field (polarization field). A second particle in the vicinity of the first one interacts with this polarization field, which is termed particle-particle interaction. This also holds for more than two particles. If all particles exhibit the same general DEP behavior (that is, either nDEP or pDEP), they will all align in direction of the electric field. Two particles with different behavior (one pDEP and one nDEP) will align perpendicular to the field. The reason is as follows (see also Fig. 2.8): The polarization field around a particle exhibiting pDEP shows two field maxima at the two points parallel to the electric field. Other particles showing pDEP will be attracted by these points, causing a particle chain parallel to the field. A particle that experiences nDEP will be attracted by the two minima which are located at the two points perpendicular to the field. The situation is inverse if the first particle experiences nDEP; then, the field maxima are located at the two

points perpendicular to the applied field and the polarization field is minimal at the two points parallel to the field. More nDEP particles will be attracted by these minima, again causing a chain in direction of the applied field (and a pDEP particle will align perpendicular to the nDEP particle) (Morgan and Green, 2002, Sec. 4.6.2).

Accurate description of the particle-particle interaction could be obtained using the MST or volume integration method. This, however, requires mesh treatment at every time step, because the influence of the particle on the resulting field needs to be calculated. This could be done using an arbitrary Lagrangian-Euler scheme (Ai and Qian, 2010; Ai et al., 2014; Xie et al., 2015) or using an immersed interface method (Hossan et al., 2013). A simpler approach is the iterative dipole method which, according to the authors, delivers results just as precise as the MST method but at greatly reduced computational cost (Liu et al., 2015). These methods enable studies to elucidate the interactive motion between two or more particles of equal or with different polarizabilities (Kang, 2014). Understanding the attraction and repulsion of particle ensembles is crucial for field-induced assembly of colloidal structures (Bharti et al., 2014; Bharti and Velev, 2015), for example the assembly of gold nanoparticles (Gierhart et al., 2007) and microwires (Hermanson et al., 2001) or carbon nanotubes (Vijayaraghavan et al., 2007).

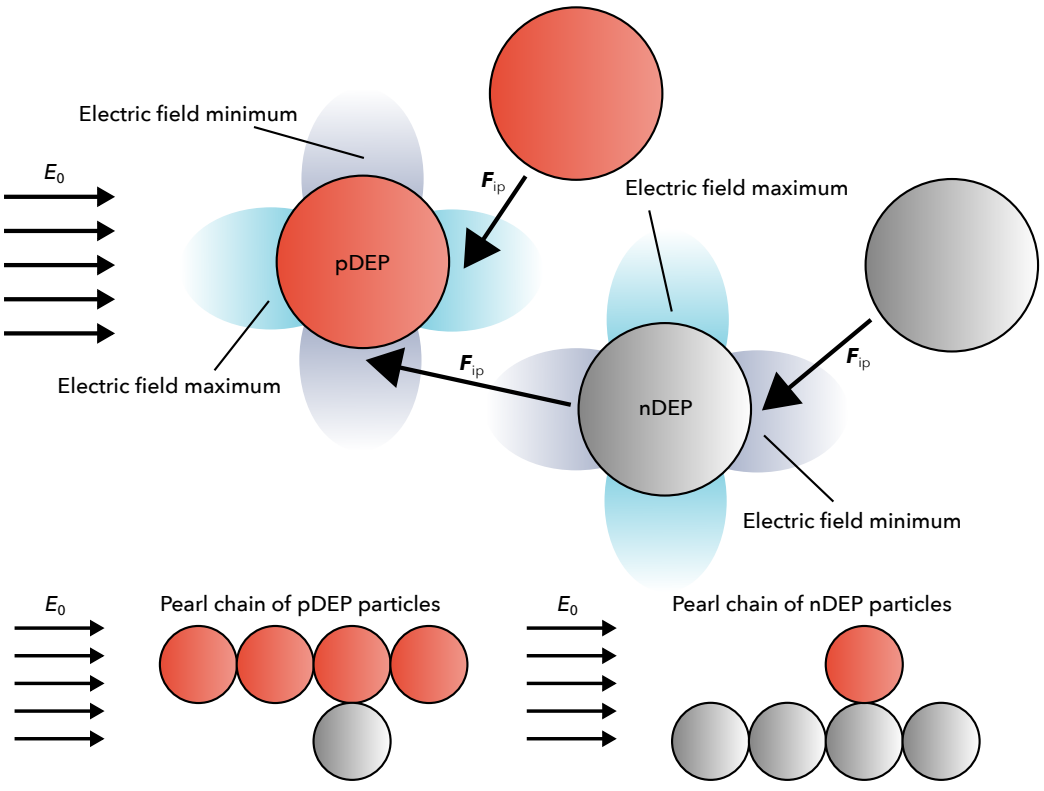

Fig. 2.8: Sketch of particle-particle interaction due to the interaction of a polarized particle with the potential field of an induced dipole. Similar particles (with respect to their polarizability) will always align parallel to the applied field whereas differing particles will align perpendicular to the applied field. Red particles are better polarizable than the surrounding medium and are attracted by field maxima whereas gray particles are less polarizable and experience nDEP (thus are attracted by field minima) (Morgan and Green, 2002, Sec. 4.6.2).

A simpler approach to estimate the acting force between two particles is to consider their geometrical relation and then rigorously apply the point-dipole approach. This was done, for example, by Aubry and Singh (2006). Considering only similar particles of size R with a Clausius-Mossotti factor of $\tilde{f}_{\mathrm{CM}}$, the force on the i-th particle (at position $\boldsymbol{x}_i$) due to the polarization field of the j-th particle (position $\boldsymbol{x}_j$) is then given by

$$\boldsymbol{F}_{\mathrm{ip}} = \frac{12\pi\varepsilon_{\mathrm{m}}\mathrm{Re}\left[\tilde{f}_{\mathrm{CM}}\right]^2 R^6}{\left|\boldsymbol{r}_{ij}\right|^6}\left(\boldsymbol{r}_{ij}\left(\boldsymbol{E}(\boldsymbol{x}_i)\boldsymbol{E}(\boldsymbol{x}_j)\right)+\left(\boldsymbol{r}_{ij}\boldsymbol{E}(\boldsymbol{x}_i)\right)\boldsymbol{E}(\boldsymbol{x}_j)+\right. \tag{2.40}$$
$$\left.+\left(\boldsymbol{r}_{ij}\boldsymbol{E}(\boldsymbol{x}_j)\right)\boldsymbol{E}(\boldsymbol{x}_i)-5\boldsymbol{r}_{ij}\left(\boldsymbol{r}_{ij}\boldsymbol{E}(\boldsymbol{x}_i)\right)\left(\boldsymbol{r}_{ij}\boldsymbol{E}(\boldsymbol{x}_j)\right)\right).$$

The vector $\boldsymbol{r}_{ij} = \boldsymbol{x}_j - \boldsymbol{x}_i$ points from the i-th to the j-th particle. Interestingly, $\boldsymbol{F}_{\mathrm{ip}}$ scales with $\mathrm{Re}\left[\tilde{f}_{\mathrm{CM}}\right]^2$ instead of the linear dependence in the DEP force equation (that is because the polarization field of the i-th particle depends on $\mathrm{Re}\left[\tilde{f}_{\mathrm{CM}}\right]$ as well as the force on the j-th particle due to that polarization field). This can be used to control the occurence of particle-particle interaction by varying the frequency (Kadaksham et al., 2005).

It is possible to estimate the ratio between particle-particle force and DEP force (Kadaksham et al., 2005, Addendum)

$$\frac{\boldsymbol{F}_{\mathrm{ip}}}{\boldsymbol{F}_{\mathrm{DEP}}} \sim \frac{6\mathrm{Re}\left[\tilde{f}_{\mathrm{CM}}\right]R^3 L}{(4/3\pi/c)^{4/3}a} \tag{2.41}$$

with the number concentration of particles c and the characteristic dimension of the electrode array L. If the factor is greater or equal to one, particles will form chains, whereas if the factor is smaller than one, the particles will move freely.

2.10.8 The influence of the double layer on polarization of non-conducting particles

Everything that was discussed so far concerning forces on particles in suspensions did (almost) never include the influence of the double layer. However, the response of micro, submicro, and nanoparticles to alternating inhomogeneous electric fields is mostly determined by the double layer surrounding these particles. Everything presented in the following is explained using latex beads, as they seem to be the classical example. The effect, however, is also present for silica particles (Honegger et al., 2011; Wei et al., 2009) and viruses (for example HSV-1 as discussed by Hughes (2002b, Sec. 5.5)).

Assuming a spherical polystyrene (PS) particle that sits in an aqueous suspension of conductivity $\sigma_{\mathrm{m}} = 1 \times 10^{-3}\,\mathrm{S\,m^{-1}}$ one would expect a DEP response that is negative at all frequencies: The relative permittivity of polystyrene is approximately 2.6 and the conductivity is virtually non-existent. Experimental data however shows a positive DEP response of such particles at low frequencies (Green and Morgan, 1997; Green and Morgan, 1999) and a single crossing from positive DEP to negative DEP that depends on particle size and conductivity of the liquid medium. Usually, these particles are characterized by their cross-over frequency because it is much easier to measure than the velocity of the particle in a given field. It has been shown that

the smaller the particle becomes, the larger this anomaly of pDEP at low frequencies becomes (that is, the cross-over frequency becomes larger).

The unusual pDEP response of the non-conducting latex particle in aqueous suspension is attributed to the movement of charges in the double layer. As a consequence, the effects explained in the following are always present when the particle (be it latex or something else) has a non-zero zeta potential. In a very simple picture (Hughes, 2002b, Sec. 4.3.1) the double layer around the particle is forming a conductive shell and is thus increasing the net conductivity of the particle (up to a point where it is actually defining the particle's net conductivity). In principle, it does not matter whether the conduction of charges is inside of the particle (a conducting particle) or around it (through the double layer of a non-conducting particle). This can easily be modeled by adding a term that accounts for the surface conductance to the bulk conductivity of the latex particle $\sigma_P = \sigma_{PS} + 2K_s/R$ where K_s is the surface conductance that is usually approximated with 1 nS for polystyrene particles. This is a very valid assumption when the particle diameer is greater than 100 nm (Ermolina and Morgan, 2005).

When the particle is smaller, it is necessary to separate the conduction through the double layer in two parts (cf. Fig.2.9 a and b): (i) The conduction of charge through the bound Stern layer occurs in a thin layer of finite thickness. This is governed by surface conductance and is independent of particle size (cf. Fig.2.9 a). (ii) The conduction of charge in the diffuse layer is different: Here the charges are distributed in an ionic cloud. The size of the cloud depends on the medium conductivity: The higher the conductivity, the smaller (denser) the cloud. The electric field will create an electro-osmotic force on that charge cloud so that it deforms. It will be compressed in front of the particle and elongated on the opposite side (Hughes, 2002b, Sec. 4.3.2) (cf. Fig.2.9 b). The full expression for the particle's conductivity then reads

$$\sigma_p = \sigma_{PS} + \frac{2K_s^s}{R} + \frac{2K_s^d}{R}. \tag{2.42}$$

Here, K_s^s is the conductance due to the Stern layer. Since the Stern layer is always of fixed size and is independent of the ionic strength of the liquid, this value is determined by the surface charge of the particle and is only slightly dependent on particle size. It is independent of the conductivity of the liquid.

The conductance due to charge movement in the diffuse layer, K_s^d, is very much dependent on the size of the particle. It increases with decreasing particle size. Since the ion concentration in the diffuse part of the double layer increases with medium conductivity, also K_s^d increases with conductivity. Fig. 2.9 c shows K_s^d and K_s^s for different medium conductivities and particle sizes. Equations for their calculation are given in the very comprehensive paper by Ermolina and Morgan (2005). As a consequence, a particle will respond to the ac electric field as shown in Fig. 2.9 d. The cross-over frequency will first rise with medium conductivity (due to the increase of K_s^d with σ_m). Then, the cross-over frequency drops.

This theory was later termed Maxwell-Wagner-O'Konski (MWO) theory, because it extends the classical Maxwell-Wagner theory (where the interfacial polarization only depends on the bulk values) by surface conductance, which was first proposed by O'Konski (1960). The theory fails to account for a second, low frequency dispersion which is evident at two points:

(i) Particles in low conductive media appear to show higher polarizability than suggested by the MWO theory at a specific frequency (Huang and Ou-Yang, 2017; Hughes et al., 1999). (ii) At the same frequency small particles are crossing from negative to positive DEP although they should only be showing negative DEP according to Eq.(2.42) and the Clausius-Mossotti model (Hughes, 2002a).

The refinement of the MWO theory was later explained in detail by Zhao (2011). In the limiting case of a thin double layer, the low-frequency behavior can be modeled using the Dukhin-Shilov (DS) model (Zhao, 2011). This model assumes that the double layer is in equilibrium with the environment (hence the model is only applicable at low frequencies). Then, under the application of an electric field, the double layer around the particle polarizes so that the counter-ions accumulate on one side and depleted on the opposite side. This difference in charge concentration causes a diffusion of salt ions against the concentration gradient (against the applied field direction). This diffusion acts against the induced dipole (cf. Fig. 2.10a). Since it is a second-order process that exists due to the polarization field of the original induced dipole, the net dipole still points in the direction of the original field (Zhou and Schmid, 2015). This

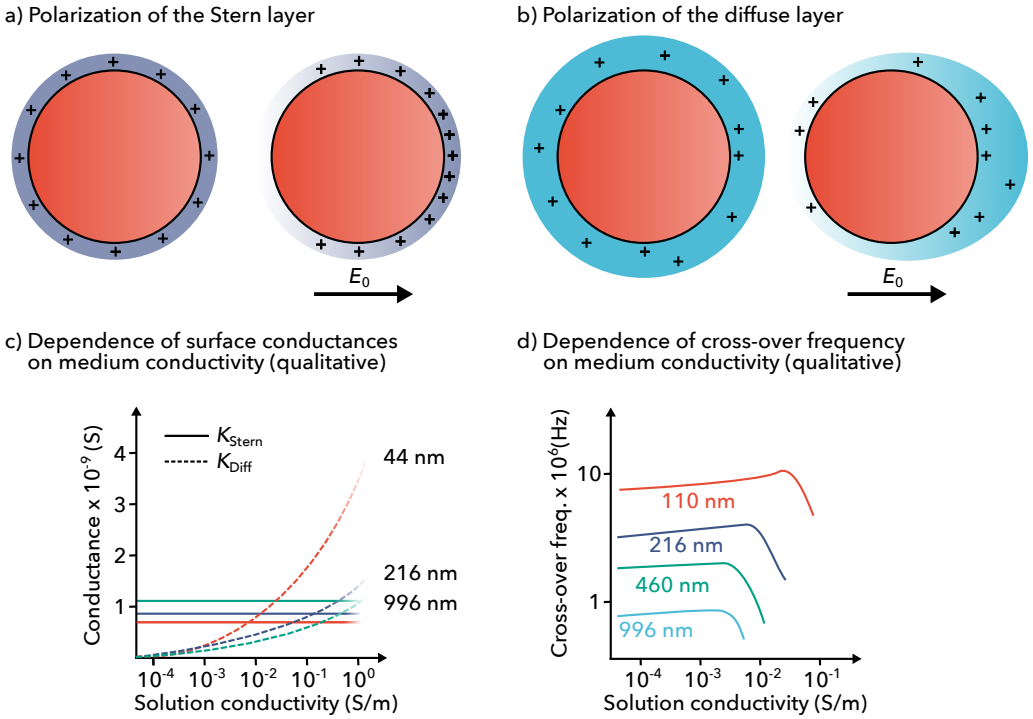

Fig. 2.9: Polarization of double layer (a and b) (Hughes, 2002b). The Stern layer is a very thin layer in which the charges are bound to the surface. Hence, the charges can only realign in this plane in order to react to the electric field. The conductivity is then due to conduction (a). The ions are more loosely bound in the diffuse layer. It will experience an electro-osmotic force when a field is applied and will consequently deform in order to react to the field (b). As a result, two different surface conductance values can be derived, the Stern layer conductance K_{Stern} that is almost independent of particle size and conductivity and the diffuse layer conductance K_{Diff} that is strongly dependent on salt concentration in the medium (and thus conductivity) and that becomes increasingly important for small particles (c) (Ermolina and Morgan, 2005). Due to the dependence of K_{Diff} on σ_m, especially small particles experience an increase in cross-over frequency with σ_m before the cross-over frequency drops (d) (Ermolina and Morgan, 2005).

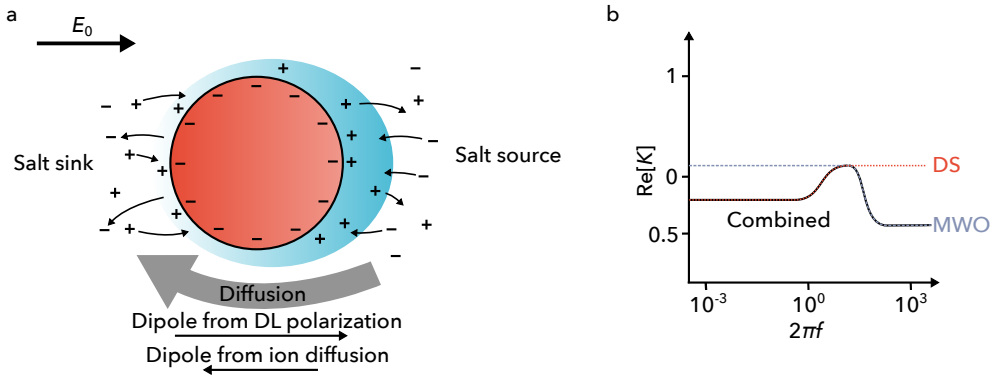

Fig. 2.10: a) Ion diffusion across the polarized double layer as proposed by the DS model. The diffusion reduces the actual double layer polarization (Zhao, 2011). b) Qualitative plot of the polarization as predicted by the DS model and the MWO theory. The DS model gives the accurate polarization in the low frequency limit and the MWO theory in the high frequency limit (Zhao, 2011).

results in a slightly decreased polarization at low frequency. The low-frequency dispersion is then a peak in the polarization (Zhao, 2011; Zhou and Schmid, 2015). A combination of MWO at high frequencies and DS at low frequencies then gives the overall polarization of the particle (cf. Fig. 2.10b).

In the limit of thick double layers it is necessary to solve the Poisson-Nernst-Planck equation (PNP) to obtain the polarization coefficient, which was done by Zhao and Bau (2009) (other methods are discussed by Zhou and Schmid (2013) and Zhou and Schmid (2015)). They could successfully model the behavior of nanoparticles (that is, showing positive DEP at low frequencies and negative DEP at high frequencies, even when the MWO model suggests negative DEP at all frequencies). They could also predict the high-frequency cross-over of Ermolina and Morgan (2005) for 55 nm and 105 nm.

When the hydrodynamic slip is considered, the polarizability of the particles in the low frequency limit (for all double layer thicknesses) increases (Zhao, 2010) with increasing slip length. Hydrodynamic slip occurs on hydrophobic surfaces (such as polystyrene but not silica).

The reports of Zhao (2010, 2011), Zhao and Bau (2009), and Zhou and Schmid (2013, 2015) are highly interesting because in the thick double layer limit they are able to predict the correct DEP behavior of latex nanoparticles at low frequencies. Apart from this the work is very theoretical and up to now has not been used to scrutinize experimental results. Further, the peak in polarization (that is, the appearance of two frequency dispersions) has not been reported in the literature in a reproducible manner. Nevertheless, in the author's experiments he observed 1 µm latex beads to present a stronger pDEP effect with increasing frequency (which does not make sense when explained using the MWO theory in which $\mathrm{Re}\left[\tilde{f}_{\mathrm{CM}}(\omega)\right]$ is monotonically decreasing with ω). Also, Saucedo-Espinosa et al. (2016) reported that 1 µm PS particles appear to show a stronger nDEP effect at very low frequencies (20–100 Hz) than at frequencies around 1000 Hz where they show almost no effect. This is against the MWO model that again suggests that $\mathrm{Re}\left[\tilde{f}_{\mathrm{CM}}(\omega)\right]$ is monotonically decreasing with ω. Such a behavior could be due to the polarization peak under the assumption that 20–100 Hz is below the polarization peak.

Despite any low-frequency effects, the common approach is to fit experimentally determined cross-over frequencies using Eq. (2.42). The resulting values for the surface conductance are by no means identical for two types of particles of the same material and the same size. This was shown by Romero-Creel et al. (2017) but is also evident when comparing the extracted surface conductances from Ermolina and Morgan (2005), Honegger et al. (2011), and Wei et al. (2009). The polarizability depends highly on the surface charge density which is apparently very much depending on the particle functionalization (Arnold et al., 1987; Hughes and Morgan, 1999) and supplier (Romero-Creel et al., 2017).

2.10.9 The influence of the double layer on polarization of conducting particles

From the definition of the Clausius-Mossotti function (Eq. (2.25)) one would assume a positive DEP response of a conductive (e. g., metal) particle in almost any medium at all frequencies (except for very, very high frequencies) due to the virtually infinite conductivity (compared to any liquid medium) (Du et al., 2008). Nevertheless, the DEP response of a metal particle (as qualitatively shown in Fig. 2.5) is negative at low frequencies, presents a clear cross-over and is positive only at high frequencies. The reason for this behavior is again the double layer. A very excellent review by Ramos et al. (2016) covers most of the effects that occur when metal particles are exposed to ac electric fields. Briefly, when a conducting particle suspended in a conducting liquid (that is, a non-ideal dielectric liquid) is exposed to an ac field, it will polarize due to the induced charge separation. This is as expected from the simple theory outlined above. Since the medium is also conductive (has an ionic strength) a double layer will form around the two polarized poles of the particle. This double layer will effectively shield the induced polarization since it is in itself an induced dipole pointing in the opposite direction than the dipole that is induced on the conducting particle. The dipole from the double layer wins and the particle will appear to be less polarizable than the suspending medium. The particle will then show negative DEP. This is the low-frequency answer of the particle to the electric field. When the frequency increases, it becomes more difficult for the double layer to fully build-up (to become fully charged) and the effective polarizability of the particle increases. At a certain frequency both dipoles match and the particle does not show a net dipole. This is accompanied by a peak in the ROT spectrum. This is the resonance frequency (RC frequency) of the double layer, that is, the inverse of the time required to charge the double layer. Above that frequency, the particle shows positive DEP and behaves like shown in Fig. 2.6 a.

This behavior can be modeled (Miloh, 2011) and was, for example, observed for gold-coated polystyrene particles (García-Sánchez et al., 2012; Ren et al., 2011) and titanium microspheres (Arcenegui et al., 2013). The RC frequency f_{RC} can be calculated as (Ramos et al., 2016)

$$f_{RC} = \frac{\varepsilon_m R}{\lambda_D \sigma_m}. \tag{2.43}$$

Here, R is the particle radius, $\lambda_D = \sqrt{\varepsilon_m k_B T/(2N_A e^2 I)}$ is the Debye length, k_B the Boltzmann constant, T the absolute temperature, e the elementary charge, N_A the Avogadro constant and the ionic strength is I.

This is only valid for particles that are not charged (that is usually the case for colloidal metal suspensions with a particle size below 1 µm to avoid agglomeration). Then, due to the surface charge the particle has a highly charged double layer that will also participate in the polarization (Ramos et al., 2016).

2.11 Basic concept of DEP particle separation or retention

Dielectrophoresis could either be used to separate particles from a suspension (cf. Fig. 2.11 a), to separate a specific target particle from a mixture containing several types of particles (Fig. 2.11 b), or to sort a (mostly binary) mixture of particles by their type (Fig. 2.11 c).

Particle separation always requires particle traps. From Eq. (2.30) it is obvious that such traps are either maxima of $\boldsymbol{E}$ (in case particles are moving in direction of $\nabla|\boldsymbol{E}|^2$, $\mathrm{Re}\left[\tilde{f}_{CM}\right] > 0$) or minima of $\boldsymbol{E}$ ($\mathrm{Re}\left[\tilde{f}_{CM}\right] < 0$). Typically, such traps are generated by a *non-symmetrical* electrode array (an electrode array that generates a field that is higher on one side than on the other) and the traps are then located directly at the electrode edge. A selective particle separation is always possible when the dielectrophoretic mobility μ_{DEP} (Eq. (2.37)) differs between two types of particles. In the easiest case, μ_{DEP} is positive for the target particle and negative for all other particles; then, only one particle type is attracted by field maxima whereas all non-target particles are not. They are then washed out the by the suspending medium. Selective trapping is also possible (while being slightly more difficult) when all particles share the same μ_{DEP} sign but differ in magnitude. Then, target particles must interact much stronger with the traps (μ_{DEP} must be much larger) than all other particles. A careful balance between the drag force exerted by the fluid and the field forces due to the traps then achieves a selective retention

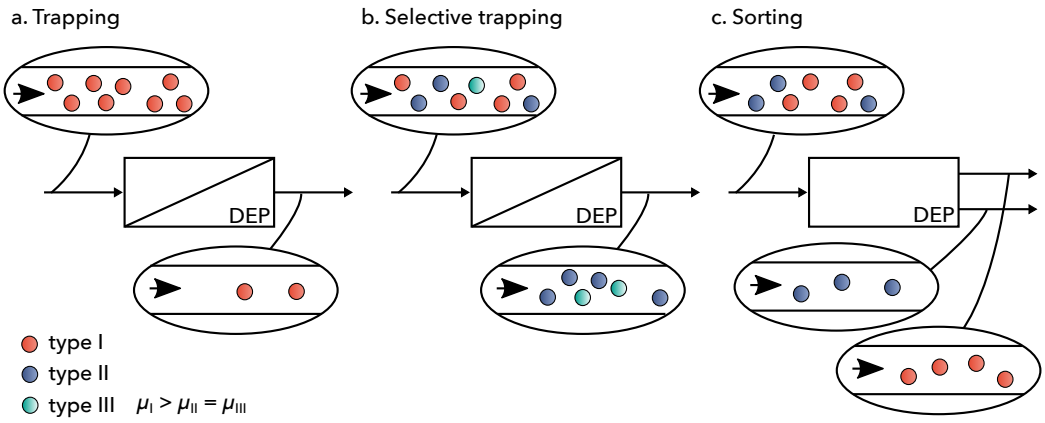

Fig. 2.11: Three basic application principles of DEP; a) Particles can be trapped due to DEP. In some cases this force can be particle type selective (b), when the differences in μ_{DEP} between the target particle (red) and all other particles are large enough. c) Particles can also be sorted according to their mobility.

of those particles with the highest μ_{DEP} while all other particles do not exhibit strong enough forces to be immobilized.

Particle sorting is possible due to a deflection of particles; that is, the DEP force is not strong enough for trapping but strong enough to move particles from one laminar flow line onto another. Particles that interact very strongly with a deflection site are then more deflected and moved across several fluid stream lines whereas particles that only interact weakly with the deflection site are only moved across a few fluid stream lines. Deflection sides can be equal to particle traps with a different force balance (that is, less $\boldsymbol{F}_{\mathrm{DEP}}$ and more $\boldsymbol{F}_{\mathrm{Drag}}$). By careful device design, this fluid stream lines could be directed towards different outlets and particles could be collected there.

2.12 Application of dielectrophoresis: Biomedical applications

Before the possible electrode configurations and typical device geometries are presented and discussed some examples for the application of dielectrophoresis shall be highlighted. This section is split in two parts, with the first part discussing biomedical applications and the second part discussing applications concerning technical particles. Chapter 10 of Pethig's book (Pethig, 2017) presents a very up-to-date and thorough review (on 70 pages with 259 references) of dielectrophoretic studies of bioparticles. Some of the important applications and studies will be presented in the following. This list is by no means complete and a simple repetition of all the references from Pethig's book is not in the author's interest; instead, the following section is supposed to briefly present some of the important (in the author's opinion) applications. Another comprehensive overview can also be found in the review of Abd Rahman et al. (2017).

All of the separation techniques usually work because the target type moves in a different direction under the influence of DEP than all other cells. This is mostly frequency dependent and sometimes the operation frequency has to be chosen very carefully. Separation occurs then usually because the target cells are either directed into a different outlet or because they are trapped while all other particles do not become trapped. Sometimes separation occurs because one particle type reacts stronger to the field than the other particles, that is, the particle polarization differs which allows separation if the device design is very finely tuned.

2.12.1 The slam-dunk of DEP[2]: Separation of live and dead cells

Using a very crude approximation, a cell can be modeled as a multi-shell particle with a non-conductive cell membrane and a conductive interior (Pethig, 2010). When a cell dies, the membrane becomes permeable and its conductivity increases. This changes the DEP behavior of a cell at low frequency: the non-conductive cell membrane will shield the interior and make a live cell behave like an insulator in an electric field at low frequencies. If the membrane becomes permeable the shielding effect decreases and the polarization at low frequencies increases. At suitable media conductivities, live cells will experience negative DEP at low frequencies and

[2] Cited from Pethig (2017, Sec. 11.2)

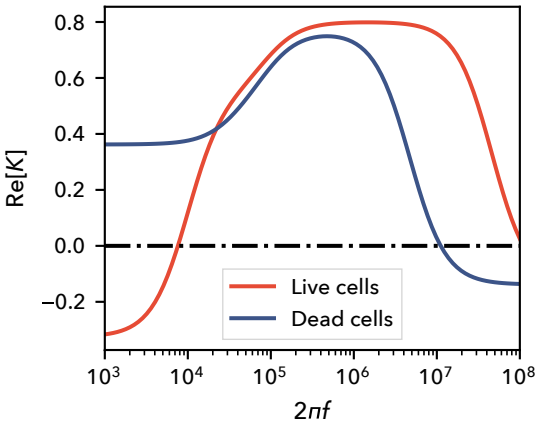

Fig. 2.12: Real part of the Clausius-Mossotti factor for a live (red) and dead (blue) yeast cell as calculated from the MATLAB program from Pethig (2017, Box 11.2) at a suspending medium conductivity of 1 mS m^{-1}.

dead cells positive DEP (see also Fig. 2.12). This allows for a separation between live and dead cells.

In reality, the situation is far more complex and also very much dependent on the investigated cell type. The most common investigated cell is the yeast cell. Pohl and Hawk (1966) already demonstrated the possibility of DEP to separate live from dead yeast cells. Since then yeast has often been used as a model cell for DEP studies (Pethig, 2017, Sec. 11.2.3), either in the early days for exploiting the possibilities of DEP (Crane and Pohl, 1968; Huang et al., 1992) or as a benchmark for newly developed DEP devices (Iliescu et al., 2007c; Moncada-Hernandez et al., 2011; Patel et al., 2012; Suehiro et al., 2003) (that might actually serve different and more complex purposes). An excellent example of yeast cells as model organisms is the one-chip DEP cell separator and counter described by Mernier et al. (2011). It highlights one of the main strengths of DEP to sort cells: it does not require labeling of the cells (if the right frequencies for application are known) and no magnetic or optical components. This makes it an excellent method for the development of point-of-care diagnostic devices. Such a cell sorter and counter could for example be used (as suggested by the authors) for the sorting and counting of blood cells for identification of cell deficiencies or bacterial contamination. In their study Mernier et al. (2011) used yeast cells as model organism due to their easy handling and availability.

Since the first reports on DEP it has been used extensively for the characterization of cells and to analyze how the dielectric properties of cells change when they are, for example, genetically modified or treated with a drug. As an example, Vahey et al. (2013) used a technique called iso-dielectrophoretic focusing to identify the DEP characteristics (and then extract the dielectric properties of the cell components from the respective DEP response) of genetically modified yeast cells. The work used the genetically barcoded yeast deletion library, which is a set of 21 000 mutant strains. Through the DNA (which acts as a barcode) it was possible to identify the strain type of the yeast cell. By measuring the DEP response at different frequencies it was possible to probe the cell interior and the cell envelope. As a result it was, for instance,

possible to find correlations between yeast cells that have different dielectric properties than the average of the pool and those, that have defects in fitness (e. g., growth under various stresses).

Dielectrophoresis has also been used to analyze how the structure of bacteria changes when exposed to biocides like antibiotics (cf. Pethig (2017, Sec. 11.2.4)); further, DEP has been used to investigate the response of mammalian cells like the human leukemia cell HL-60 (Wang et al., 2002) or Jurkat cells (Pethig and Talary, 2007) to toxicants. Dielectrophoresis was successfully used to test the resistance of bacteria against antibiotics. Jones et al. (2015) demonstrated, that antibiotic resistant strains of *Staphylococcus epidermidis* show electrophysical differences from regular strains that are sufficient for separation by DEP. Hoettges et al. (2007) demonstrated the possibility to use DEP to analyze the cell death of *Escherichia coli* after antibiotic treatment. This can be used as a clinical test for antibiotic resistant bacteria in patients.

Nikolic-Jaric et al. (2013) developed a DEP flow cytometer that is able to continuously monitor a cell's DEP response (negative, positive or no DEP) at a given frequency at a flow rate of 5–10 $\mathrm{nL\,s^{-1}}$. The cytometer was verified by Braasch et al. (2013) against four other methods for the detection of apoptotic events of Chinese hamster ovary (CHO) cells (where the aptoptosis of the cell causes a change of the DEP response from positive to negative at a given frequency) and found that DEP cytometry offers a potential as a low-cost, label-free electronic monitor of physiological changes in cells. Such a cell death detection system is, for example, desirable in the large-scale production of glycoproteins from mammalian cells which can be used as biopharmaceuticals for unmet medical needs (Braasch et al., 2013). Pethig (2013) also published a review that focused on the assessment of DEP for drug discovery and delivery.

2.12.2 Cell separation by type

This section offers virtually endless application possibilities. Srivastava et al. (2011a) demonstrated the sorting of blood cells by type (ABO-Rh) using a continuous flow DEP system. They discerned A+ blood with a 99 % confidence and B- with a 99.4 % confidence. Gascoyne et al. (2002) demonstrated that malaria infected blood cells show a different cross-over frequency (from negative to positive) than regular blood cells. They used this in order to isolate the parasitic cells (since healthy and infected cells move in different directions) from a much larger number of blood cells. This has a great value as front-end technology for on-chip microfluidic diagnostic devices (for pre-concentration of the particles to be analyzed).

A very similar problem is the detection of circulating tumor cells (CTC) in blood. The prognosis and treatment of various cancers is aided by the knowledge of the concentration of those cells in the blood stream. An elevated CTC concentration indicates a rapid disease progression and mortality for the patient. The main problem is that the CTC concentration (even at a level which would be considered to be high) is very low—just as hard as finding a needle in the haystack. A typical task would be to detect approximately 10 CTC in 15 mL of blood that contains about 8×10^{10} erythrocytes and other blood cells. A relative recent review by Gascoyne and Shim (2014) covers most of the research done so far on the CTC separation from other blood cells. Almost all solid tumor cells have a cross-over frequency that is lower compared to regular blood cells. The most common approach for the separation is the DEP field flow fractionation, where the tumor cells are attracted by an electrode array positioned at

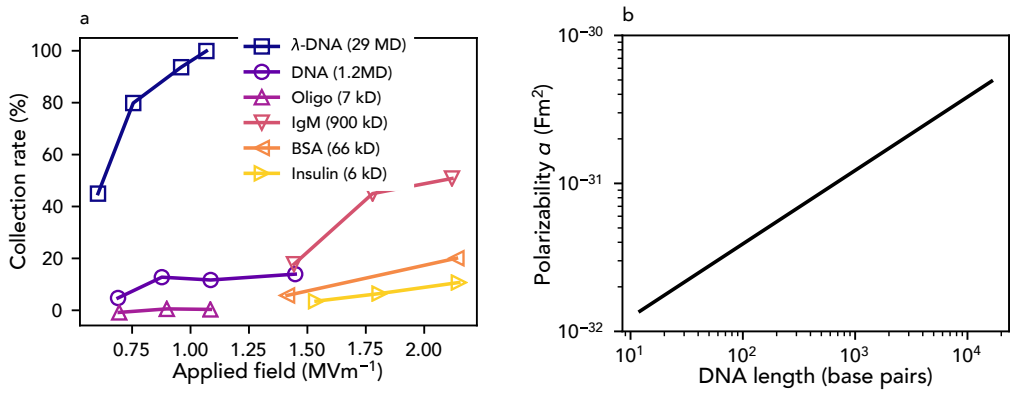

Fig. 2.13: a) Trapping rate of DNA and proteins at DEP traps according to their size (as expressed by their molecular weight in Dalton). With increasing size, DNA and proteins become more easily trapped (higher collection rate at lower voltage). Proteins of equal length experience less trapping than DNA in an identical field. b) Polarizability (dipole moment *per* electric field) of DNA according to their length (as expressed by the number of base pairs, 1 kDa ≈ 27 bp). Data extracted from Pethig (2017, Figs. 11.30 and 11.31).

the bottom of the channel, whereas all other blood cells are repelled and flow to waste. The CTC are then skimmed from the bottom of the array. Using a continuous-flow DEP field flow fractionation device, Gascoyne and co-workers (see references in Gascoyne and Shim (2014)) were able to recover 70–85 % of CTC at a flow rate of 10×10^6 cells per minute.

Additionally, dielectrophoresis has been employed for the sorting and enrichment of stem cells (Pethig, 2017, Sec. 11.3.3.) and (theoretically) for the sorting of spermatozoa based on their gender (Koh and Marcos, 2014).

2.12.3 DEP of DNA and proteins

As a last example, DEP has extensively been used for the trapping and sorting of DNA by length and type as well as for the immobilization and fractionation of protein molecules. Due to their complex structure, the polarization of macromolecules (such as DNA or proteins) cannot be described by the Clausius-Mossotti model. The net dipole moment rather depends on the structure, length, and confirmation of the molecule. As an example, Kawabata and Washizu (2001) used a dielectrophoretic chromatography concept in which the particle solution was flowing over an electrode array and particles where trapped by positive DEP on the array. Due to Brownian Motion, the particles will escape the trap after some time before they will become trapped again at a position downstream (of the first trapping location). As a consequence, particles of different polarizability will exit the channel at different times. This allows for the separation of DNA molecules by size and for the separation between DNA and proteins (cf. Fig. 2.13 a). The reason is that the dipole moment of the macromolecule increases with increasing length (cf. Fig. 2.13 c). Additionally, DNA molecules are not as compactly folded as proteins, so they exhibit a stronger polarization at the same size.

Using insulator-based dielectrophoresis, it was later possible to show that DNA of a specific size or structure could be selectively trapped in an array of insulating posts, while DNA of other size or type was not affected (Chou et al., 2002; Gan et al., 2013; Regtmeier et al., 2007,

2010). Jones et al. (2017) later introduced a continuous flow device based on the deflection of molecules due to insluator-based DEP that is able to rapidly sort DNA molecules by their size.

Mata-Gómez et al. (2016a,b) demonstrated the possibility to separate mono-PEGylated RNase A from di-PEGylated RNase A and from the unreacted protein, due to the difference in molecule size (caused by the grafting). This is of great importance, since mono-PEGylated RNase A has the highest biological activity when used as a cancer drug, whereas unreacted protein and di-PEGylated RNase A don't show such high activity. The grafting process, however, always results in a heterogeneous mixture of all three types of RNase, so that the mono-PEGylated form needs to be purified.

In a quite groundbreaking work Hölzel et al. (2005) demonstrated the trapping of freely diffusing proteins between two sharp nano electrodes (having 500 nm spacing) as a DEP version of a Paul trap. They used R-phycoerythrin from red algae due to its intense autofluorescence.

2.13 Application of dielectrophoresis: Technical applications

Despite the countless *biomedical* separation applications (by type or size) that have been reported in the literature, there are very few reports for the fractionation of non-biological particles. Almost all reports concerning technical particles describe the alignment or precise positioning of particles due to DEP for the production of new electronic devices or sensors. In most of the few reports dealing with the *separation* or *fractionation* of non-biological particles by size experiments are performed with polystyrene beads as a test vehicle and the reports are rather describing a technology than an application.

This section will give a comprehensive overview of the technical applications, firstly the reported applications of the separation of technical particles by type or by size. Secondly, it will give an overview of papers describing the manipulation or orientation of particles for the development of sensors or other electronic devices.

2.13.1 Trapping and separation of particles by type or size

The first conscious description of dielectrophoresis, by Herbert Pohl himself, was the separation or carbon-black filler particles from polyvinyle chloride dust in an open-gradient type setup. He used a non-polar solvent (1:1 mixture of carbon tetrachloride and benzene) and demonstrated that PVC would be attracted by the high-field regions in a dc field. This is, because the solvent and the PVC could be considered as almost ideal dielectrics and thus the motion direction is dictated by the permittivity differences. The permittivity of PVC was slightly higher than that of the solvent used, thus causing positive DEP. At the same time, the carbon-black filler particles where virtually unaffected by the field. This allowed for an enrichment of the PVC at the high-field regions (Pohl and Schwar, 1959; Pohl, 1951; Pohl, 1958).

Later, in a series of papers Benguigui and Lin (1982) and Lin and Benguigui (1982, 1985) actively investigated the possibility to separate metal oxide and PVC particles from a non-polar solvent (kerosene) and from a solvent that consisted of a mixture of kerosene and isopropyl alcohol (with quite low overall conductivity). They used a DEP filtration setup using glass-

beads as matrix medium. They could show, again due to the permittivity differences, that 10–50 µm PVC and metal oxide particles will be trapped in the matrix due to pDEP effects when the conductivity of the liquid medium is low. This research was aimed at improving a DEP separator, that was (apparently) actively used by the Gulf Company for the separation of FCC cat fines from decanted oil (termed Gulftronic separator). The work was later continued by Wakeman and Butt (2003) for the separation of metal oxide particles (so-called AC test dust) and PVC dust from hydraulic oil (Tellus 37).

More recently, some attempts have been made to separate metal particles from gangue (Du et al., 2008; Lungu, 2006). Metal particles have a virtually infinite conductivity and show positive DEP at sufficiently high frequencies, so that no double layer shielding occurs (cf. Sec. 2.10.9 on the polarization behavior of conductive particles). The DEP response of metal oxide or plastic particles is defined by their double layer conductivity, so that they show negative DEP when the particles are sufficiently large or the frequency is high enough (cf. Sec. 2.10.8). Du et al. (2008) experimentally demonstrated the possibility to continuously separate metal and metal oxide particles in an open-gradient type device into different outlets whereas Lungu (2006) theoretically demonstrates the possibility of DEP to concentrate metal particles at the surface of a domain containing metal and metal oxide particles. Apart from this, Jia et al. (2015) continuously fractionated pristine 10 µm polystyrene particles from gold-coated polystyrene particles of approximately the same size at a flow rate of approximately 1×10^{-2} mL h^{-1}. The work of Du et al. (2009) was a proof-of-principle with a lot of room for device improvement but was never followed. The work of Lungu (2006) never offered a proposal on a possible device design for a continuous fractionation.

Dielectrophoresis has also been used to separate specific minerals by type due to their permittivity differences, as demonstrated by Ballantyne and Holtham (2010, 2014) . The authors, however, only theoretically studied the separation possibility, that is movement in two opposing directions depending on the permittivity difference between the mineral and the surrounding medium. Their movement direction predictions where proven by simple single particle experiments but never applied for a separation process. (Chen et al., 2010) investigated the voltage necessary to move rare-earth oxide particles by dielectrophoresis. They found that the required voltage greatly depends on the electron valence of the oxide, thus offering the possibility to fractionate these oxides by DEP.

All of these works were quite promising but apparently never made it past the concept stage. More effort was invested into the development of concepts for separating conductive from semi-conductive carbon nanotubes. Common synthesis methods for carbon nanotubes (CNT) produce only heterogeneous mixtures of semi-conducting CNTs and conductive CNTs. Both types have their own specific application, thus a separation step is required after synthesis.

One method to obtain both fractions at high-purity is DEP separation. Krupke et al. (2003) demonstrated the possibility to separate metallic from semi-conducting single-walled CNT at the droplet scale. This work was later continued by Kang et al. (2013) and Shin et al. (2008) towards the continuous separation in a microfluidic channel at which the metallic CNTs could be collected at one exit whereas the semi-conducting CNTs would be flowing towards another exit. As pointed out by Kang et al. (2009), metallic CNTs always exhibit positive DEP whereas

the DEP answer of semi-conducting CNTs depends on their surface conductance and on the ionic strength and composition of the liquid. Their surface conductance could effectively be reduced by adding surfactants to the medium, so that the semi-conducting CNTs only show a very weak positive DEP or even negative DEP answer to the field. Due to the strong DEP answer it was always possible to obtain conducting CNTs at high purity at one outlet. Since the DEP answer of the semi-conducting CNTs was not as strong they where always found in a mixture together with conducting CNTs at the other outlet, thus limiting the applicability of that fraction. Another problem with CNTs is the presence of impurities from the production process. Liu et al. (2006) enriched CNTs from a mixture containing impurities by a fluid flow across an interdigitated electrode array.

Zhao and Li (2017a) developed a nano-orifice microfluidic channel that they successfully used to continuously separate micro and nano particles by size and by type (metal coated micro particles and pristine polystyrene particles) at a flow rate of 5×10^{-3} mL h^{-1}. They also simulated the separation of Janus particles by their coverage percentage in the nano-orifice device (Zhao and Li, 2017b). Janus particles are particles with two sides having different chemical or physical properties (for example polystyrene particles that are partly covered with gold). They have a variety of applications (Zhang et al., 2017) and the possibility to use DEP to separate them after synthesis and to characterize them by their properties offers a great potential but is not yet fully understood (which can also be inferred from the very crude assumptions made by Zhao and Li (2017b) for their theoretical study).

As already pointed out, a lot of researchers use polystyrene (PS) particles in order to show the applicability of their research for particle fractionation. Just to name a few examples, PS particle separation by size was performed by Kang et al. (2006a) who were able to effectively separate mixtures of 5.7 µm and 10.3 µm; and of 10.35 µm and 15.7 µm into two different outlets. Wang et al. (1998) introduced DEP field flow fractionation (which was later used for the enrichment of CTC) that was able to separate particles of different sizes by their residence time in a flow channel that contained interdigitated electrodes. Clearly, three different types of PS particles, 15 µm, 10 µm and 6 µm, eluted at different times even at a high flow rate of almost 1 mL min^{-1}. Saucedo-Espinosa et al. (2016) showed the possibility to use insulator-based dielectrophoresis to separate 1 µm and 500 nm particles using asymmetric posts and a dc-biased ac voltage signal.

As described in the introduction, Pesch et al. (2014) developed a dielectrophoretic filter that was based on the field gradients due to polarization of (in contrast to the previously described filters that used glass beads and organic solvents) a polymer foam in an aqueous suspension. It was used for the separation and recovery of LbL produced nano capsules. Due to their small size (340 nm) they had a high surface charge and always showed pDEP, even in their suspending polyelectrolyte solution of high conductivity. In a series of papers (Sano et al., 2013, 2012, 2014, 2016) Sano, Tamon, and coworkers developed and applied a mesh-stacked DEP separator system that operated batch wise but was, according to the authors, suitable for large-scale separation processes. It was applied for the selective trapping of tungsten carbide particles from a mixture containing diatomite particles in ethanol due to the comparatively higher conductivity of tungsten carbide compared to diatomite (Sano et al., 2013, 2012), for

the purification of titania nanotubes according to their bandgap in aqueous solution (Sano et al., 2014) and for the selective trapping of TiO_2 particles from a mixture containing also SiO_2 in ethanol (Sano et al., 2016). This was possible since titania has a larger permittivity than ethanol and silica has a lower permittivity.

2.13.2 Self-assembly and alignment of nanoparticles

This section is out of the general scope of this thesis. Due to its relevance in the construction of new electronic devices, e. g., nanoelectronic circuits, a *very* brief overview will be given. Carbon nanotubes have very specific physical and chemical properties and they are highly suited for a variety of innovative electric applications. For this applications, most of the time they need to be aligned between two electrodes, either as sheets or as single fibers. DEP and electro orientation were extensively researched for the alignment of single-walled (Gu et al., 2017; Kim et al., 2008b; Seo et al., 2005) and multi-walled carbon nanotubes (Shim et al., 2009). These methods can be used for the production of field effect transistors (Kim et al., 2008b; Li et al., 2004) and gas sensors (Lucci et al., 2005; Suehiro et al., 2007). This can be achieved since better conducting eccentric particles will always align in parallel to the electric field (due to electro orientation).

CNTs have also been attached to AFM tips (Tang et al., 2005; Wei et al., 2008) or spun into fibers of high tensile modulus (Zhang et al., 2009) by DEP. Conducting (Evoy et al., 2004; Freer et al., 2010; Oh et al., 2007; Raychaudhuri et al., 2009) and semiconducting (Kumar et al., 2005; Lee et al., 2008; Raychaudhuri et al., 2009) nano rods or wires have been aligned between electrodes, which has potential applications for the construction of sensors or integrated circuits (see also Wang and Gates (2009)).

Nanowires can be formed from colloidal conductive nanoparticle suspensions (Hermanson et al., 2001; Liu et al., 2016): Similarly to other DEP trapping applications, particles will form pearl chains at the electrodes (cf. Sec. 2.10.7). The tip of these chains presents a very high field region and attracts more particles until a wire is spun across two electrodes. It is even possible to grow metallic nanowires from solution containing dissolved metal salts by DEP (Nerowski et al., 2012; Ranjan et al., 2006). Such field assembled nanowires appear to be promising, for instance, in the miniaturization of electrical circuits; more details and examples for metal wire growth and assembly can be found in the review of Ramos et al. (2016, Sec. 5).

2.14 Device design

Generally, devices for dielectrophoretic particle sorting, isolation, or enrichment might be categorized into two main categories (Gascoyne and Shim, 2014): Non-equilibrium isolation approaches in which particles are trapped in DEP traps. These are either field maxima for in the case of pDEP particles or field minima in the case of nDEP particles. The particles can subsequently be released by changing the electric field or suspending medium conditions. These techniques could be used either for trapping particles (particle filtration) or for the *selective* retention of particles (for example for the enrichment of low abundant particles, for the purification of samples, or for particle concentration). The technique requires that a specific target particle type interacts with the trap whereas the other particles do not interact with it (or only

weakly). These techniques are called non-equilibrium approaches because for the target particles the $\boldsymbol{F}_{\mathrm{DEP}}$ exceeds the drag forces of the fluid flow across the trap while simultaneously, non-target cells are (virtually) unaffected and eluted by the fluid flow.

The second category are equilibrium approaches. Here, target and non-target cells are at different positions in the separation chamber because they experience different forces (mainly different $\boldsymbol{F}_{\mathrm{DEP}}$ but that could also be coupled with different gravitational forces or different fluid drag). This allows them to be positioned on different fluid stream lines so that they will exit the separation chamber from different outlets or at different times. This allows for particle sorting into different fluid streams or to increase the relative percentage of the target cell in one outlet. They are called equilibrium approaches because the forces acting on the particle are in constant equilibrium.

Another way to categorize devices for DEP particle manipulation is based on how they generate the electric field gradients. In electrode-based DEP (termed eDEP) the electric field gradient is generated by asymmetric electrodes. In this case, the field gradient is directly linked to the electrode distance and the electrodes are in constant contact with the liquid medium. A different approach is electrodeless DEP (interestingly also termed eDEP) in which the electrodes are placed far away from the separation region. In this case, the electric field gradient is produced by some sort of material boundary that causes a distortion of the applied field. The most common approach employs insulating field hurdles (for example an array of insulating posts), which is then commonly termed insulator-based DEP (luckily, iDEP).

2.14.1 Non-equilibrium electrode-based designs

In the early days of DEP, macroscopic setups employing thin sheet electrodes and metal wires were used. This considerably changed with the introduction of clean-room technology fabricated micro-electrodes. Since $\boldsymbol{F}_{\mathrm{DEP}}$ depends on $\nabla |\boldsymbol{E}|^2$, which has units $\mathrm{V}^2\,\mathrm{m}^{-3}$, the produced field gradient square should increase with decreasing electrode distance by the power of three. This makes the application of dielectrophoresis in microfluidic channels employing miniaturized electrodes very attractive, since much smaller voltages have to be applied to create equal field gradients.

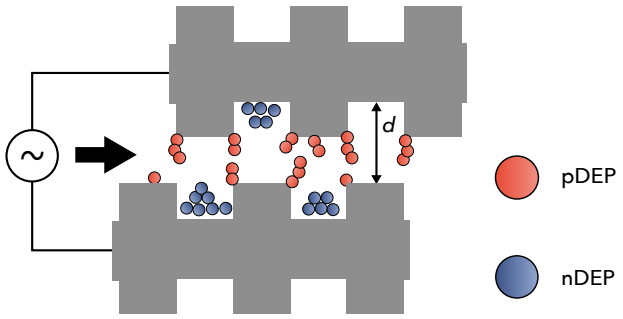

Fig. 2.14: Castellated electrodes as typically employed in electrode-based particle separation experiments. The setup allows the capture of nDEP and pDEP particles, where nDEP particles experience less trapping than pDEP particles (Pethig, 2017, Fig. 10.35).

The interdigitated, castellated geometry (cf. Fig. 2.14) allows the observation of positive and negative dielectrophoresis and provides quite high field gradients at low applied voltages. The electrodes usually have dimensions d that are between 10–120 µm—approximately 5 to 10 times the diameter of the target particles. They are commonly fabricated on microscope slides using photolithography with a height of approximately 100 nm. As shown in Fig. 2.14, pDEP particles will form pearl chains that are attached to the electrode edges, whereas nDEP particles will accumulate in triangular structures in the electrode gap. The nDEP will be slightly lifted from the glass slide and thus experience less holding force than the pDEP particles. This allows them to be removed by a constant fluid stream across the electrodes. Markx et al. (1994), for example, used this for the selective trapping of viable yeast cell. Markx and Pethig (1995) presented a semi-continuous sorting device employing castellated electrodes that could sort pDEP and nDEP particles into two specific outlets based on trapping and selective release. Markx et al. (1996) trapped a mixture of particles from a fluid stream using castellated electrodes and then employed a time-dependent conductivity gradient which allowed the selective release of particle fractions whose polarizability changed due to the medium conductivity change. Other interdigitated electrode structures have also been used as DEP traps (Becker et al., 1995; Olariu et al., 2017). Application of interdigitated electrodes pose restrictions on the channel geometry. If it is to high, particles are in average too far away from the *planar* electrodes (that are located at the channel bottom). To counter these effects, Gadish and Voldman (2006) introduced herringbone structures in the separation chamber in order to bring particles close to the electrode array by chaotic mixing. This would enhance their chance to become trapped.

2.14.2 Equilibrium electrode-based designs

The early design of Herbert Pohl employed a cylindrical outer electrode and a concentrically placed metal wire to produce an inhomogeneous field that is strongest in the symmetry axis of the cylinder (Pohl and Schwar, 1959; Pohl, 1958). A particle mixture in suspension is flowing through the cylinder (of approximate diameter 10–20 mm) from top to bottom and pDEP particles will be attracted towards the central electrode whereas nDEP particles will be repelled towards the cylinder wall. By carefully extracting only the fluid stream close to the central electrode it was possible to enrich the pDEP particles from the mixture (cf. Fig. 2.15 a). A similar approach was later employed by Du et al. (2008) for the enrichment of gold particles; the design was not concentric but consisted of a long wire and a plate, so that pDEP (gold) particles would be attracted by the wire while flowing in between the two electrodes.

In contrast to those macrofluidic designs a microfluidic approach for continuous sorting of particles by either type or size are planar angled electrodes (Cheng et al., 2007; Kim et al., 2008c; Kralj et al., 2006; Park et al., 2011). Different approaches exist for the realization, but in the simplest mode (Kralj et al., 2006) particles are flowing on top of a surface on which the angled electrodes are employed. Each time an nDEP particle passes an electrode it exhibits a small field gradient that deflects it away from the electrode (thus in the overall angle direction). Naturally, larger particles experience a stronger force and are more deflected than smaller particles. As a result, after traveling across the entire electrode array, larger particles are located at a slightly different perpendicular location than smaller ones (cf. Fig. 2.15 b).

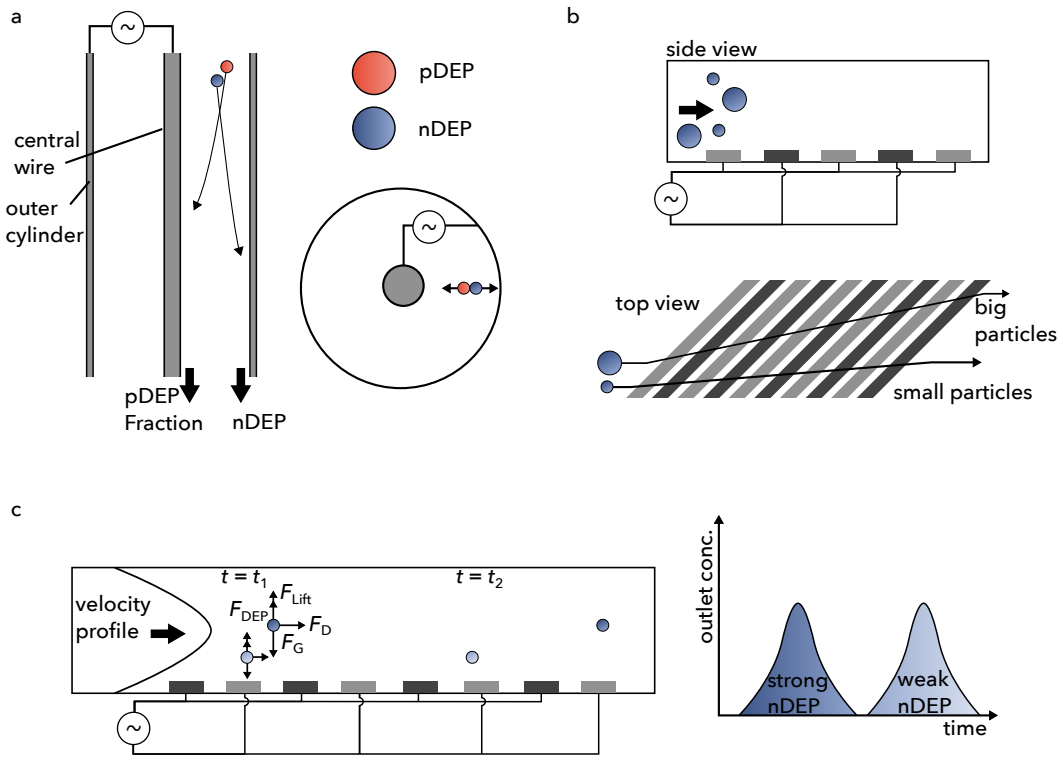

Fig. 2.15: Overview of equilibrium approaches for particle manipulation by DEP. a) Early concentric cylinder-and-wire arrangement as used by Pohl (1958). b) Angled electrodes are, for instance, able to separate particles by size via a slight deflection at each electrode pair (Kralj et al., 2006). c) Dielectrophoretic field flow fractionation lifts particles with different polarizability towards different heights in the channel so that they experience a different drag force. This allows for time-dependent separation (Huang et al., 1997).

A very common method to separate particles with different polarizabilities is dielectrophoretic field flow fractionation (DEP-FFF). This approach only works for nDEP or weakly polarized pDEP particles. An array of interdigitated electrodes is placed at the bottom of a separation channel which generates an electric field that is strongest at the electrode edges and which decays logarithmically with perpendicular distance from the array. Negative DEP particles will experience a balance between DEP force, gravity and lift forces (cf. Fig. 2.15 c). Depending on their polarizability (live vs. dead cells, tumor vs. blood cells, small vs. large particles) particles will be lifted towards a different height in the fluid stream. Due to the hyperbolic flow profile, particles on different heights experience different drag forces, resulting in polarizability-dependent residence times. In batch operation, this allows for a time dependent particle fractionation at fairly high throughputs in the mL min^{-1} range (Huang et al., 1997; Markx et al., 1997b; Vykoukal et al., 2008; Wang et al., 1998; Yang et al., 1999). Gascoyne et al. (2009) showed the possibility to separate rare tumor cells from cell mixtures (at a mixture rate of 1:1000 they showed 100 % separation) but due to the batch-wise operation and the requirement of a low loading capacity (to avoid particle interaction) the overall throughput was too low for an application of the device to detect circulating tumor cells in a blood sample (which is of approximate size of 15 mL). As a consequence, a continuous DEP-FFF device was developed by Shim et al. (2013) in which CTC particles experience pDEP and are thus directed towards

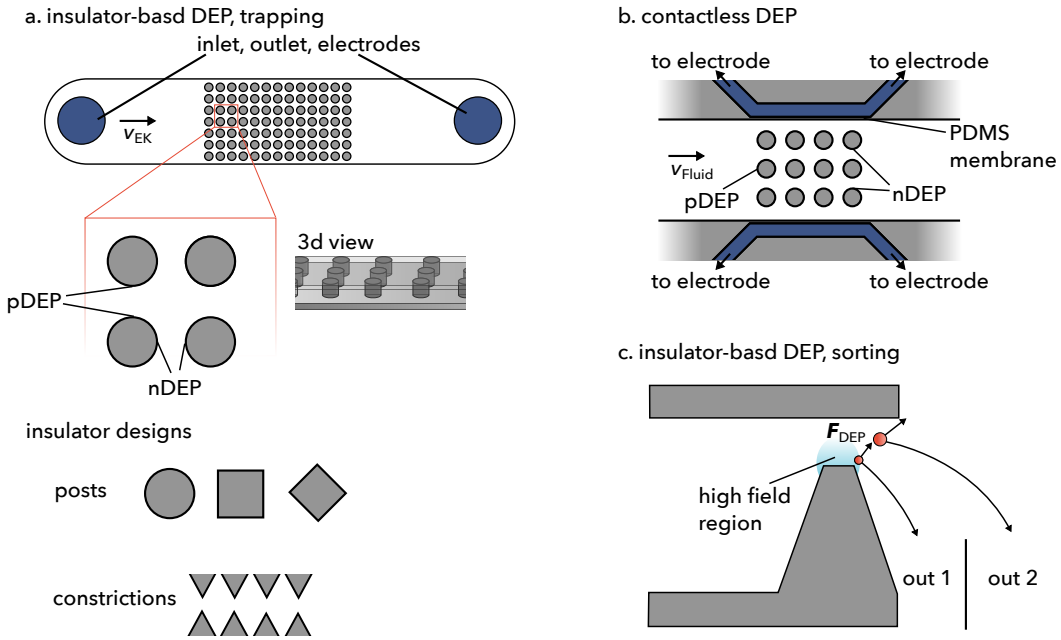

Fig. 2.16: Different designs for electrodeless dielectrophoresis. a) Designs for particle trapping in insulator-based DEP. A common approach is an array of insulating posts of different geometries. Liquid reservoirs are placed far away from the array. After filling the channel with liquid the electrodes are placed inside the reservoirs. Also common is a constricting channel containing sawtooth tips. b) In contactless dielectrophoresis the field is applied across two side channels of high conductivity. The separation channel and the side channels are separated by a thin PDMS membrane. c) In insulator-based DEP devices for particle sorting, particles are deflected due to the field of one or more obstacles. Then, depending on their DEP mobility they are deflected towards different flow paths and ultimately sorted into different outlets.

the electrode array at the bottom of the channel whereas all other blood particles experience negative DEP and are lifted away from the electrode array; the device operates at a much lower flow rate in order to maintain the separation quality. The commercially available ApoStream[3] device uses this technology and is under active investigation (Balasubramanian et al., 2017).

2.14.3 Electrodeless and insulator-based dielectrophoresis

In electrodeless or insulator-based dielectrophoresis the electrodes are placed far away from the separation region and the required field gradient $\nabla|\boldsymbol{E}|$ is generated due to the distortion of the field at a material boundary. In this thesis electrodeless dielectrophoresis generally means that an electric field is disturbed at a material boundary whereas insulator-based dielectrophoresis more specifically means that the electric field scatters at *insulating* material boundaries. The boundary could be an array of field hurdles, a constriction, or a single obstacle (cf. Fig. 2.16).

Quite similar to the polarization of particles, the polarization of stationary solid matter creates a polarization field that is highly suited for the dielectrophoretic manipulation of particles (cf. Fig. 2.8). Two basic schemes exist: particles are either sorted while flowing past the obstacles due to their differential interaction with the field gradient (caused by a difference in their dielectrophoretic mobility μ_{DEP}, as shown in Fig. 2.16 c) or particles are (selectively) trapped by

[3] www.apocell.co

the insulating geometries, either due to pDEP or nDEP. Particles could then also be selectively released according to their μ_{DEP} due to a change in the electric field conditions (cf. Fig. 2.16 a).

Nowadays, almost all applications of insulator-based DEP (iDEP) are in microfluidic channels. In the early reports, the channels where made of glass and the insulating features have been produced using photo lithography together with wet (Cummings and Singh, 2003) or dry etching (Chou et al., 2002) processes. Nowadays, channels are mostly produced by rapid prototyping of poly(dimethylsiloxane) from a negative master (Duffy et al., 1998).

Particle trapping by insulator-based dielectrophoresis

In the first iDEP descriptions, Chou and Zenhausern (2003) and Chou et al. (2002) used positive dielectrophoresis to trap single-stranded or double-stranded DNA. They used an array of constrictions with a 1 µm tip-to-tip distance and driving voltage of 1 kV. The constrictions were made from quartz wafers using reactive ion etching. Concentration and patterning of single-stranded and double-stranded DNA was observed at high-field regions of the constrictions. Studies on the selective trapping of DNA according to their length (cf. Sec. 2.12.3) and spatial confirmation were later also performed by Regtmeier et al. (2007, 2010), using a PDMS microchannel containing constrictions with 2.3 µm tip-to-tip spacing and an applied voltage of 400 V over a 5 mm electrode gap. Gan et al. (2013) trapped DNA origami in a PDMS post array with post diameters of approx. 10 µm and 2.1 µm spacing.

The term insulator-based DEP is attributed to Cummings and Singh (2003). They proposed a device design that is still state-of-the-art for insulator-based dielectrophoretic particle manipulation: a microfludidic chip of 7 µm height contained an array of insulating posts with diamond, square, and circular cross section. The post spacing was approx. 30 µm and the post's characteristic dimension 33 µm. The channel was filled with a suspension containing the analytes, which are allowed to settle. Then, under the application of a dc field across the post array, 200 nm PS particles where transported through the channel due to electro-osmosis and electrophoresis. Electro-osmosis and electrophoresis have a linear dependence on the applied field strength, whereas DEP has a quadratic dependence. It is thus possible to adjust which effect dominates by varying the applied field strength: When the field was weak (250 $\mathrm{V\,cm^{-1}}$), DEP was weak compared to the linear electrokinetic effects. Particles where thus simply transported through the channel. At moderate field strengths (800 $\mathrm{V\,cm^{-1}}$), DEP was stronger than diffusion and electrokinetic effects but not strong enough for trapping. This was considered streaming DEP, because particles where concentrated in narrow streamlines around the posts. At high field strengths, the particles exhibited a strong pDEP behavior and were trapped at high-field regions around the post.

In a subsequent study from the same group, Lapizco-Encinas et al. (2004b) trapped different bacteria using a similar device geometry. Different from the PS particles, the bacteria exhibited negative dielectrophoresis in dc fields due to the non-conductive cell wall. This resulted in so-called trapping bands in front of the posts (cf. Fig. 2.17). This is because the linear electrokinetic effects (EK) drive the particles through the post while, at the same time, DEP pushes the particles away from the high-field regions. At a point where DEP and EK match,

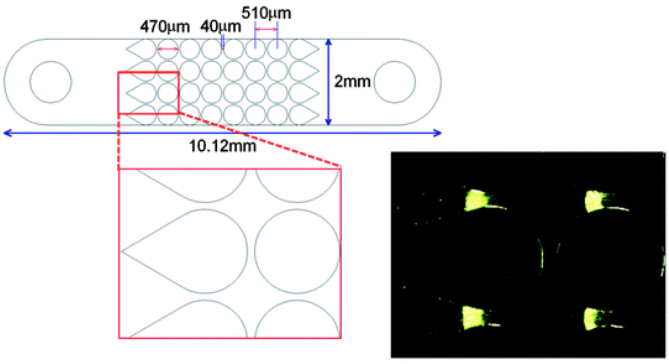

Fig. 2.17: Trapping bands of green fluorescent 1 µm latex particles in an insulator-based dielectrophoresis device due to the balancing of electrokinetic and dielectrophoretic forces. Diagram and photography reprinted with permission (Baylon-Cardiel et al., 2009).

the particles are standing still and accumulate. This could be used for the selective trapping of live bacteria from a mixture of live and dead ones. Live and dead bacteria have almost the same electrokinetic mobility (thus travel across the channel at the same velocity), but the μ_{DEP} of live bacteria is much higher compared to dead ones. Hence, live bacteria would become trapped at much lower voltage while dead bacteria only exhibit streaming DEP (Lapizco-Encinas et al., 2004a). From this point onwards, most dc iDEP studies focused on the enrichment of particles exhibiting negative DEP using exactly this operation mode.

Baylon-Cardiel et al. (2009) later developed a simple set of equations to derive the location and width of the trapping bands in iDEP devices. The velocity due to DEP is given by $\boldsymbol{u}_{\mathrm{DEP}} = \mu_{\mathrm{DEP}} \nabla |\boldsymbol{E}|^2$ (cf. Eq. (2.37)). In a similar manner, the electrokinetic particle movement will be given by

$$\boldsymbol{u}_{\mathrm{EK}} = \mu_{\mathrm{EK}} \boldsymbol{E}. \tag{2.44}$$

The elektrokinetic mobility $\mu_{\mathrm{EK}} = \mu_{\mathrm{EP}} + \mu_{\mathrm{EO}}$ is composed of the electrophoretic and electroosmotic mobility, μ_{EP} and μ_{EO}, resp. They can be calculated from the well-known Helmholtz-Smoluchowski equation. Trapping will be achieved if the DEP movement overcomes the EK movement, i. e.,

$$C \frac{\mu_{\mathrm{DEP}} \nabla |\boldsymbol{E}|^2}{\mu_{\mathrm{EK}} \boldsymbol{E}^2} \boldsymbol{E} > 1. \tag{2.45}$$

Here, C is a correction factor that "accounts for effects of unconsidered phenomena and measurement errors" (Moncada-Hernandez et al., 2011). The correction factor could be as high as $C = 500$ in order to match the simulated with experimentally observed trapping regions.

Such a design (insulating posts in a microchannel and particle immobilization due to Eq. (2.45)) has been extensively studied (Gallo-Villanueva et al., 2013; LaLonde et al., 2014, 2015a,b; Saucedo-Espinosa and Lapizco-Encinas, 2015; Saucedo-Espinosa et al., 2016; Saucedo-Espinosa and Lapizco-Encinas, 2017). The research group of Hayes developed a gradient insulator-based DEP device, that consists of a sawtooth channel in which the tip-to-tip distance of the tooth gradually decreases (Jones and Hayes, 2015; Jones et al., 2011; Pysher and Hayes, 2007). In such a device it is possible to spatially separate particles having a difference in their μ_{DEP}. Particles with comparably high DEP mobility would be immobilized in trapping

bands in early regions (at larger gates) whereas particles with smaller μ_{DEP} require larger field gradients for immobilization. They are thus trapped at smaller gate openings in the latter part of the channel.

Except for the studies on DNA, all studies focused on the separation of micron and sub-micron particles and cells. The trapping of macro-molecules requires much stronger forces in order to keep the molecules at their position against thermal diffusion. Swami and co-workers (Chaurey et al., 2013; Liao et al., 2012; Rohani et al., 2017) use constrictions that are only some tens or hundreds of nm apart. This allows the effective concentration of biomolecules in front of the constriction.

Apart from the classic scheme using negative DEP, other researchers used a combination of EK and positive DEP. Then, particles are attracted by high-field regions as originally described by Cummings and Singh (2003). This was used, for example, by Ding et al. (2016) for the trapping of Sindbid virus in an gradient iDEP device or by Mata-Gómez et al. (2016a,b) for the selective trapping of pegylated RNase.

Capabilities and limitations of iDEP devices for particle trapping

The advantages of insulator-based DEP (iDEP) over classical electrode-based dielectrophoresis are according to Pethig (2017), Regtmeier et al. (2011), and Srivastava et al. (2011b) (i) that the devices are far less complicated to manufacture since no metal deposition of the electrodes is required, (ii) that monolithic fabrication enables easy mass production from, e. g., PDMS, (iii) that no electrode fouling occurs which might reduce the established field gradient, and (iv) that no electrochemical side effects occur such as electrolysis in the separation region since the electrodes are far away. Additionally, (v) the electric field is equally distributed over the entire height of the channel, whereas in electrode-based DEP the electric field decays with distance from the electrode plan. Also (vi) low-frequency or dc fields could be used which would not be possible in case of electrode-based DEP due to the electrochemical side effects. Finally, (vii) the application of dc fields allows fluid and particle movement through the channel due to electrokinetic effects (electro-osmosis of the suspension and electrophoresis of the suspended particles).

Especially the work of LaLonde et al. (2015b) is a good example for the discrimination power of an iDEP device. Their device is able to selectively trap 2 µm-sized particles against a background of 100 000 1 µm-sized particles. The discrimination even was even higher, reaching 1:1 000 000 when the smaller particles were only 500 nm. According to Pethig (2017, Sec. 10.4.2.1) this is a very common capability of iDEP devices that is not found in classical eDEP devices.

Downsides of insulator-based DEP devices are the necessity to apply very high strengths, while simultaneously they show a lower throughput than classical electrode-based DEP devices. Due to the high field strengths, Joule heating occurs (Gallo-Villanueva et al., 2013) which could become strong enough to induce cell death (LaLonde et al., 2015a). Sometimes particle discrimination requires ac fields with a very carefully chosen frequency. Further, the throughput through the channel is inevitably linked to the applied voltage (cf. Eq. (2.44)). At the same

time, the applied voltage is the only tool to control the fraction of trapped particles. Thus, the throughput through the channel is not an independent variable. The review of Regtmeier et al. (2011, Sec. 5) also presents a thorough discussion of insulator-based dielectrophoresis compared to other analytical techniques inclusive conventional DEP approaches.

Improvement of iDEP devices for particle trapping

In an effort to overcome the last two points, researchers used ac electric fields with a dc offset (Lewpiriyawong et al., 2012; Rohani et al., 2017; Saucedo-Espinosa et al., 2016). Then, the dc offset produced net movement of the particles and suspension through the channel while the ac component produced the DEP effect. Then EK and DEP is decoupled and it is possible to tune the $\mathrm{Re}\left[\tilde{f}_{\mathrm{CM}}(\omega)\right]$ of the particles.

Lapizco-Encinas and co-workers made some attempts on reducing the required voltage for particle trapping (thus maximizing the $\nabla|\boldsymbol{E}|^2$) by tuning the device geometry. LaLonde et al. (2014) compared the minimum required voltage for iDEP trapping in channels using posts with diamond-shaped and circular cross sections with different cross-sectional width-to-height ratios. They found that the diamond-shaped posts outperform circular posts in every case and that diamonds that are aligned with their longer axis perpendicular to the applied field require considerably less applied voltage for trapping than those diamonds who are aligned with their longer axis parallel to the field. Saucedo-Espinosa and Lapizco-Encinas (2015) presented a method to find a flow channel with an optimized arrangement of insulating posts. For each cross-sectional base geometry (diamond, circle and square) they optimized the geometry of the setting using COMSOL simulations. They found that there exists a specific spacing in both directions (spacing in field direction and perpendicular spacing) at which the channel performs best. They achieved this by evaluating Eq. (2.45) for all post designs and possible arrangements. Further, they experimentally compared the three optimized setups and found that the optimized square posts require the least voltage for iDEP trapping, followed by the optimized circles, and concluded by the optimized diamonds (thus different than the study by LaLonde et al. (2014) in which the diamonds performed best). For a specific (e. g., circular) post they could reduce the required voltage for trapping from 800 V to 170 V employing ideal geometrical characteristica. Mohammadi et al. (2016) investigated numerically and experimentally how particle trapping changes with post diameter. As it will be described in this thesis, Pesch et al. (2017, 2016) further investigated the influence of the post design on the overall field distortion and trapping capabilities of iDEP devices.

Crowther and Hayes (2017) presented multi-length scale posts which have a "rough" surface. Thus, the field is not only squeezed by the presence of the posts but further modified on a smaller scale due to little bumps on the surface of the post. This produces a more homogeneously distributed $\nabla|\boldsymbol{E}|^2$-field and thus solves the problem that analytes experience different forces depending on their pathline through the channel which decreases the discrimination ability.

Saucedo-Espinosa and Lapizco-Encinas (2017) added inert filler particles to a particle mixture and found that, at a specific filler particle concentration, the enrichment of the target particles is greatly enhanced. For example, when 500 nm PS beads are added to a solution

containing yeast cells at a volumetric concentration of 1×10^{-5}, then the trapping of the yeast cells, as measured by the fluorescence intensity, is 115 times as strong as without filler particles. They attributed this to the particle interaction that was outlined in Sec. 2.10.7.

Contactless dielectrophoresis

A quite similar approach to insulator-based DEP is contactless DEP (Čemažar et al., 2016; Hanson and Vargis, 2017; Salmanzadeh et al., 2012; Shafiee et al., 2009, 2010). Here, the field is usually applied perpendicular to the fluid flow, which must then be achieved using pumps (cf. Fig. 2.16 b). The electric field is applied via side channels that are separated from the main channel via a small membrane (if the device is made from PDMS then the membrane is also PDMS). The separation between the two channels might be as thin as 20 µm. This has the advantage that the electrodes are not in contact with the fluid; thus avoiding electrolysis and fouling, while (as it appears from Hanson and Vargis (2017, Table 1)) reducing the required voltage since the field is applied over the shorter axis of the channel.

Quite groundbreaking for this technique is the work of Čemažar et al. (2016) who designed a device in which the pillars were of the same size as the cells to be trapped. Viability and trapping efficiencies of a mouse ovarian surface epithelial cell line was tested for a design consisting of 68 664 pillars with 20 µm diameter. At a throughput of 1.2 mL h^{-1} they were able to achieve separation efficiencies of 28 % at an applied voltage of 300 V. This is an almost 6-fold increase compared to trapping efficiencies when 100 µm pillars are used.

Insulator-based dielectrophoresis for particle sorting

As outlined in Fig. 2.16 c, iDEP can also be used to sort particles onto different flow paths so that they are directed towards different outlets according to their μ_{DEP}. Usually, as in iDEP applications for trapping, the particle motion is achieved using electrokinetic movement (electroosmis and electrophoresis). Particles pass one or more hurdles which slightly deflect them away or towards the hurdle (according to their μ_{DEP}). This usually requires dc fields so that a constant particle transport is achieved but also ac fields with dc offset Lewpiriyawong et al. (2008) or pressure-driven flow Jones et al. (2017) and Lewpiriyawong and Yang (2014) are reported.

This technique has been used to sort polystyrene particles (Abdallah et al., 2015; Kang et al., 2006a,b; Lewpiriyawong and Yang, 2014; Lewpiriyawong et al., 2008; Srivastava et al., 2011c), biological particles (Kang et al., 2008; Srivastava et al., 2011a), and DNA (Jones et al., 2017). For example, Kang et al. (2006a) sorted 5–15 µm PS particles using a single insulating block into two different outlets. A correction factor of 0.3 to 0.4 was employed to be able to match simulated and experimental trajectories.Lewpiriyawong and Yang (2014) used pressure-driven flow and ac fields to separate 5 µm and 10 µm particles at an efficiency of 99 %, a flow rate of approx. 3.6 µL h^{-1}, and a voltage of approx. 600 V. Other devices achieve much higher throughputs as presented by Abdallah et al. (2015). They sorted 2.5 µm and 500 nm particles with a 90 % efficiency at a flow rate of approx. 100 µL h^{-1} by applying voltages in the kV-range. The same working group used A similar device to sort DNA fragments according to their length at a (for DNA comparably) high throughput of 15 µL h^{-1} (Jones et al., 2017). This was achieved

by using ac fields and pressure driven flow. The reason for the much lower throughput is the much weaker DEP response of DNA compared to micron-sized PS particles.

2.14.4 Dielectrophoretic filtration

A special form of insulator-based dielectrophoresis that has not yet been discussed is dielectrophoretic filtration. Naturally, the throughput through a microfluidic iDEP device is quite limited due to its small dimensions. An attempt to scale-up a microfluidic iDEP device will ultimately fail because of a loss of discrimination that distinguishes iDEP devices from other DEP devices (and because in most cases the throughput is achieved by electro-osmosis which is in complex interplay with the dielectrophoretic retention and cannot be treated as a separate variable). A different approach that is not aimed at sample analysis (which requires very precise handling of particles that are low abundant in a small sample volume) but rather on large scale separation processes is dielectrophoretic filtration. In this, macroscopic setups are used in combination with pumps to be able to process liquids in the $L\,min^{-1}$ range. Instead of insulating pillars in a microfluidic channel the classic approach is to use a packed-bed of glass spheres (usually 500 µm in diameter) as a filtration matrix. Particles are then separated due to positive dielectrophoresis at a virtually unlimited number of particle traps (that exist due to the field distortion around the glass beads).

In the early days this was very successfully applied by Benguigui and Lin (1982) and Lin and Benguigui (1982) and later by Wakeman and Butt (2003) for the filtration of metal oxide, PVC, and catalyst fines from oil. Glass beads were filled into a concentric separator consisting of an outer electrode (shell) and an inner rod-shaped electrode. The diameter of the outer electrode could be as large as 12 cm at a device length of 15 cm. Separation efficiencies of almost 100 % at throughputs of up to $3\,L\,min^{-1}$ with applied field strengths of max. 10 kV for a particle size of approx. 50 µm could be achieved. These studies show unparalleled throughput for DEP devices while simultaneously requiring enormous voltages.

In the same year as the study of Wakeman and Butt (2003) Suehiro et al. (2003) proposed a dielectrophoretic filter chip that was much smaller. A quite similar looking setup was proposed 5 years later by Iliescu et al. (2007c). In both setups again glass beads were used as a matrix but the throughput was decreased to the $mL\,min^{-1}$-range while simultaneously reducing the applied field strength from several kV to approx. 100 V. Suehiro et al. (2003) used a 100 mm square chip with height of 0.8 mm using 200 µm glass beads. They studied the separation and recovery of yeast cells. Without applied voltage, yeast cells flowed freely through the gaps between the glass beads. When applying 140 V at the electrodes (positioned across the 0.8 mm gap) at a flow rate of $1\,mL\,min^{-1}$ the yeast cells were trapped by positive DEP at lateral surfaces of two adjacent beads. When removing the applied voltage, the yeast cells were released into the fluid flow. In a circulating operation mode they were able to decrease the cell count from 1×10^6 to 1×10^2 cells per mL in a period of 5 hours. Iliescu et al. (2007c) used a smaller chip, a 10 mm square with 1 mm spacing and 100 µm glass beads. They also performed experiments with viable yeast cells and demonstrated the possibility to capture 80 % at an inlet concentration of 3.6×10^6 cells per mL. Operation parameters were $0.1\,mL\,min^{-1}$ flow rate and 200 V applied voltage. Due to the reduced area this is a 10 times higher flux (flow rate per area) as employed

by Suehiro et al. (2003). In another study (Iliescu et al., 2007b) using the same device they demonstrated the possibility to selectively trap live yeast cells due to positive DEP while not trapping the dead cells. This was done at a flow rate of 0.2 mL min^{-1} and at an applied field strength of 140 V. Live cells were separated at a capture efficiency of 60 % while dead cells exhibited only 30 % capture efficiency (due to the unspecific adsorption on glass beads even without applied voltage).

As already shown in the introduction, Pesch et al. (2014) developed a separator that did not employ glass beads as a matrix but highly porous polymer foams. This causes a lower pressure loss (due to the higher porosity) and easier handling (because a macroscopic foam is easier to handle than microscopic glass beads). Using a square device with 38 mm edge length they could separate 340 nm highly polarizable nano-capsules (more than 10 times smaller than yeast cells, thus 1×10^3 times lower force) at a flow rate of 1 mL min^{-1} and an applied field strength of 200 V (across the filter of thickness 2 mm) with a separation efficiency of almost 40 %. The flux was approximately 7 times higher than the flux employed by Suehiro et al. (2003).

2.14.5 Performance evaluation of DEP devices

Table 2.1 gives a (by no means complete!) list of throughputs, separation/sorting/trapping efficiency and field parameters compiled from the references cited in this thesis. They are compiled so that they list typical throughputs of specific device types as well as unparalleled old or recent results. When interpreting these results it is necessary to compare them against other already existing non-DEP technologies for the envisaged application. It is also important to consider the required accuracy for the application and to look at the limitations of the presented technology. Further one has to keep the target particle concentration and—especially—size in mind. The results from iDEP devices seem to have a much lower throughput compared to electrode-based designs. Especially the results of Gadish and Voldman (2006) and Markx et al. (1994) have very high throughputs. One has to keep in mind that they are using interdigitated electrodes that are in the size range of the particles that are supposed to be trapped. Hence, they will be "filled" rather quickly, limiting the overall particle processing capability due to "electrode fouling". Also, the channels have to be very small overall in order to keep the target particles close to the array.

The batch-wise FFF approaches have the capability to sort particles at a very high throughput with a very high sorting efficiency. Due to their batch-wise approach, however, they have a limited overall capacity (for example, Gascoyne et al. (2009) lists a sample size of 1 mL to achieve good separation with a concentration of 2×10^6 cells per mL). Also, their application is restricted to low cell concentrations to avoid particle interaction.

The throughputs of the iDEP sorting devices appear to be quite moderate, however, they show a very good discriminatory ability and are much cheaper to manufacture than electrode-based sorting devices. The device of Shim et al. (2013) is commercially available but the current retail price is unknown to the author. However, the fabrication of the employed electrode array requires fabrication in a clean room, whereas modern iDEP devices can easily be replicated once the master has been produced. When looking at the very low throughput of the device described by Jones et al. (2017) it is important to keep in mind that the device reliably sorts

Tab. 2.1: List of DEP applications including their respective throughputs, applied field strengths, and sorting efficiencies. This list is by no means complete and is only supposed to show some typical values.

Author (year)	Study type	Particle type	Performance	E parameters	Comment
Electrode-based trapping					
Markx et al. (1994)	Continuous trapping, selective release	Live and dead yeast (~ 5 µm)	$Q = 30\,\mathrm{mL\,h^{-1}}$	$5\,V_{pp}$, 10 MHz	Castellated electrodes, feasibility study, performance according to Pethig (2010)
Markx and Pethig (1995)	Trapping and sorting	Live and dead yeast	100 % separation	$10\,V_{pp}$, 10 MHz	Castellated electrodes, flow rate unknown, semi-batch operation
Gadish and Voldman (2006)	Concentration	Beads or *B. Subtilis* spores	$Q = 30\,\mathrm{mL\,h^{-1}}$ for beads (40× enrichment), $Q = 6\,\mathrm{mL\,h^{-1}}$ for spores (9× enrichment)	$20\,V_{pp}$, 500 kHz for beads, $40\,V_{pp}$, 100 kHz for spores	Interdigitated array with herringbone mixer
Electrode-based sorting					
Pohl and Schwar (1959) and Pohl (1958)	Continuous sorting, concentric arrangement	PVC dust from non-polar solvent	$Q = 750\,\mathrm{mL\,h^{-1}}$, enrichment factor 2.5	$4000\,V_{pp}$, 60 Hz, 20 mm diameter	Macrofluidic, first conscious continuous DEP sorting
Du et al. (2008)	Continuous sorting, pin-plate arrangement	Gold (200 µm × 30 µm) from gangue	$Q = 8.5\,\mathrm{L\,h^{-1}}$, $q = 400\,\mathrm{m^3\,m^{-2}\,h^{-1}}$, 88 % separation	$565\,V_{pp}$, 200 kHz (6 mm electrode distance)	Macrofluidic, electrodes parallel to flow
Kim et al. (2008a)	Continuous sorting with angled electrodes	Tagged cells (~ 5 µm)	$Q = 0.15\,\mathrm{mL\,h^{-1}}$, enrichment factor 12 000	$200\,V_{pp}$, 200 kHz	
Cheng et al. (2009)	Traveling-wave DEP	Liposomes, red blood cells, PS particles, size-based	$Q = 0.6\,\mathrm{mL\,h^{-1}}$, high-purity size-based sorting for $d > 10\,\mu\mathrm{m}$	$\leq 24\,V_{pp}$, f sample dependent	
Wang et al. (1998)	batch DEP FFF	PS beads, 6–15 µm, size-based	$Q = 48\,\mathrm{mL\,h^{-1}}$	$1.5\,V_{pp}$, 10 kHz	No evaluation of sample purity

Tab. 2.1: *…(continued)*

Author (year)	Study type	Particle type	Performance	E parameters	Comment
Gascoyne et al. (2009)	batch DEP FFF	CTC (low conc.) from blood (~ 5 µm)	1 mL sample in 20 miuntes, 92 % CTC recovery at 1:1000 cell ratio	10 V_{pp}	Decreasing recovery rate with increasing cell loading
Shim et al. (2013)	continuous DEP FFF	CTC (low conc.) from blood	$Q = 1.2\,mL\,h^{-1}$, 70–80 % recovery at 1:10 000 cell ratio	4 V_{pp}	CTC recovery independent of cell ratio
Insulator-based DEP trapping					
Baylon-Cardiel et al. (2009)	(negative) iDEP trapping	1 µm PS particles	Throughput voltage dependent, $Q \sim 0.5\,mL\,h^{-1}$ at 500 V dc		Calculated by Pethig (2017, P. 288), typical throughput for iDEP devices with post array
LaLonde et al. (2015b)	selective iDEP (nDEP) trapping	Enrichment of 2 µm PS particles against 1 µm or 500 nm background particles	99 % trapping at target to background ratio of 1:100 000 (2 µm vs. 1 µm),1:1 000 000 (vs. 500 nm)	400 V dc	Example of discriminatory ability
Čemažar et al. (2016)	contactless pDEP trapping	Mouse ovarian cancer cell	$Q = 1.2\,mL\,h^{-1}$, 28 % sep. eff.	850 V_{pp}, 30 kHz	68 663 pillars at the size of the cells (20 µm)
Insulator-based DEP sorting					
Lewpiriyawong and Yang (2014)	nDEP and pDEP sorting	2 µm PS from a mixture of 2 µm, 5 µm, and 10 µm	$Q = 7.2\,\mu L\,h^{-1}$, 99 % efficiency	1300 V_{pp}, 5 kHz	Pressure-driven flow, three-component mixture
Abdallah et al. (2015)	nDEP sorting	2.5 µm from 500 nm PS	$Q = 100\,\mu L\,h^{-1}$ (approx.), 94 % efficiency	~ 1000 V dc	Electro-osmotic flow
Jones et al. (2017)	DNA sorting by length	1–48.5 kbp dSDNA	$Q = 12\,\mu L\,h^{-1}$, 90 % efficiency	0–2500 V_{pp}, 80–2 × 10^4 Hz	Pressure-driven flow and ac voltages, considered to be high-throughput

Tab. 2.1: *…(continued)*

Author (year)	Study type	Particle type	Performance	E parameters	Comment
DEP filtration					
Benguigui and Lin (1982) and Lin and Benguigui (1982)	Concentric, 500 µm glass beads	Metal oxide powder (50 µm) from kerosene	$Q = 60\,\mathrm{L\,h^{-1}}$, $q = 31\,\mathrm{m^3\,m^{-2}\,h^{-1}}$, 100 % separation efficiency	≤ 6 kV dc	Macrofluidic device, non-conductive liquid
Wakeman and Butt (2003)	Concentric, 500 µm glass beads	AC test dust (10 µm), PVC dust (30 µm) from oil	$Q = 180\,\mathrm{L\,h^{-1}}$, $q = 16\,\mathrm{m^3\,m^{-2}\,h^{-1}}$, 20–60 % separation efficiency	6–12 kV dc	Macrofluidic device, non-conductive liquid
Iliescu et al. (2007c)	100 µm glass beads, 1 mm electrode dist.	Yeast cells from water (?), suspension medium is assumed	$Q = 6\,\mathrm{mL\,h^{-1}}$, $q = 0.06\,\mathrm{m^3\,m^{-2}\,h^{-1}}$, 80 % sep. eff.	400 V_{pp}, 21.1 kHz	cf. Suehiro et al. (2003)
Pesch et al. (2014)	Polyethylene filter, 20–160 µm pore size	Polyelectrolyte nanocapsules from solution (~ 300 nm)	$Q = 60\,\mathrm{mL\,h^{-1}}$, $q = 0.04\,\mathrm{m^3\,m^{-2}\,h^{-1}}$, 38 % sep. eff.	565 V_{pp}, 200 kHz	

DNA by length over a wide range of kbp, which is a technology that previously did not exist. Further, the force acting on DNA is much smaller than the force acting on a micro particle. The former point also holds for the results of the filtration setups from Iliescu et al. (2007c), Suehiro et al. (2003), and Pesch et al. (2014). The possibility to trap yeast cells at these flow rates is not special and could be achieved using any conventional filtration process. Iliescu et al. (2007b) outlined the possibility to selectively trap live cells while not trapping dead cells, which instead is quite an achievement. Further, Pesch et al. (2014) trapped LbL nanocapsules of small size (340 nm). This separation step is difficult using conventional methods and thus imposes a substantial problem on the fabrication of such capsules. This makes their production tedious and a continuous separation would be quite the achievement (see also Sec. 1).

The very high throughput of Du et al. (2008) as well as of Wakeman and Butt (2003) have to be seen in the light that the separation efficiency was not too high, the applied voltage rather large (especially in the case of Wakeman and Butt (2003)), and that the particles here very large.

Generally speaking, DEP applications for analytical purposes might require very high purity and involve only small samples: then, throughput is not the issue rather than very high separation efficiencies at a low target particle count. Further, some applications require a continuous approach whereas for other applications a batch-wise approach is fine. Especially when the purity goes beyond 99 % the throughput naturally becomes very small because a single falsely sorted particle might already destroy the result. On the other hand, Du et al. (2008) separated gold particles from a mixture of gold and minerals. Even at a very low input concentration of gold, a recovery of 50 % might already have great economic value due to the high gold price. On the other end of the spectrum would be the recovery of cancer cells which might be present at a ratio of 1 to 1×10^9 other particles and knowing the exact number is crucial.

Aim and possible applications of DEP filtration

3

> *Science is about knowing; engineering is about doing.*
>
> **— Henry Petroski**

The last chapter covered all of the important theory and presented most of the DEP applications and technologies. Before the actual results are presented it shall briefly be discussed how the technology presented in this thesis fits into the technical context and what possible applications could be.

From the literature review in the previous chapter it is quite easy to see that a lot of DEP applications, especially biomedical and chemical, have a long history of gradual improvement making their state of the art quite advanced. A perfect example of this is the field flow fractionation, which has been reported first in 1997 (Huang et al., 1997) and which has been developed through several stages until it reached a commercially available product that is still under active development (Balasubramanian et al., 2017). Each of these existing technologies is researched by a very knowledgeable community that has, naturally, accumulated a lot of experience on their specific device type. As discussed before, most of the presented devices and applications serve analytical purposes, either for the detection of a specific sort of cell (e. g., disease detection) or as an upstream technique for pre-concentration. Most of the applications are aimed at the development of lab-on-a-chip devices which are self-sustaining, easy to produce, and that analyze samples in and below the mL range.

On the other end of the spectrum are macrofluidic DEP applications which range from the early reports of Pohl and Lin and Benguigui (which are from a time at which microfluidics was uncommon) to the filtration reports of Suehiro, Iliescu and from our own group. In the early days, DEP has been researched as a separation force in industrial scale processes but with the increasing reports of microfluidic DEP applications this mostly stopped. The aim of our working group and of this thesis is to re-establish DEP as a technique for the separation of particles in large scale processes. This work follows up on the old filtration reports and tries to improve them in several aspects. The final result is a versatile separation technique that has applications everywhere where conventional separation methods fail. An example for such an application is given in the introduction, the separation of the sub-micron LbL nanocapsules, which are too sensitive for high-throughput membrane filtration. Conventionally, they are separated batch-wise by centrifugation making their production very cumbersome.

Quite general, separation of nano and sub-micron particles according to their properties is a highly relevant topic that does not have a definitive answer. Even particle sorting according to their density or size due to gravity is problematic when the particles are very small or when the density differences are small compared to the medium's density. As already outlined for DEP, sorting according to density, size, or other properties, is possible with very high precision

in microfluidic devices employing low throughput. This is possible using DEP or a variety of other techniques. Nevertheless, at flow rates above the lab-scale, such separation tasks are still challenging [1].

Such a task could for example be the selective retention of noble metals from scrap. In waste recovery, such a separation is typically achieved using an air separation technique that is based on inertia differences due to the different materials involved. This requires an upstream milling process that reduces and homogenizes the particle sizes involved. During that milling, a substantial amount of the material is lost as dust which is an inevitable side product. This dust contains particles in the µm size range and is composed of highly valuable materials. A recovery of such a dust is not economically feasible using existing technology but could be easily achieved using a selective DEP filter. Another application is given by Du et al. (2008): Usually, gold appears as a free metal that is associated with oxides of other metals. In gold mining, the separation of gold from the ore is achieved by cyanidation. This is expensive and poses substantial environmental and process hazards. A DEP separator can be used as a selective non-chemical method to separate the gold particles from the metal oxide.

[1] As argued in a project proposal authored by Jorg Thöming within the framework of a DFG Schwerpunktprogramm, SPP 2045

4 Simplification of the filter and polarization of a single post in the electric field

> *On graduating from school, a studious young man who would withstand the tedium and monotony of his duties has no choice but to lose himself in some branch of science or literature completely irrelevant to his assignment.*
>
> **— Charles-Augustin Coulomb**

As discussed in Sec. 1.6 and shown in Fig. 1.4 the first step in understanding, describing, and optimizing the dielectrophoretic particle retention in porous layers (that are random and potentially very complex) is to disassemble it into a much simpler, very regular geometry. This allows for an easy description of the situation without becoming too detached from the original problem. This concept is shown in Fig. 4.1 a and b. The actual three-dimensional porous medium is replaced by a (conceptually) two-dimensional array of posts. A suggestion of how such a device could look like in practice is shown in Fig. 4.1 c. That means that a three-dimensional version of the conceptually two-dimensional array is just an extrusion of the cross-section in the drawing plane. If the field is applied as shown in Fig. 4.1 the actual size of the third dimension is not important because the field is homogeneous over that dimension. The size of the third dimension will just relate the fluid velocity through the post array with the volume flow through it (this ignores that the fluid will show a hydrodynamic flow profile which is, again, a simplification). The resulting device looks very similar to a kind of channel that would be used in insulator-based dielectrophoresis. The difference here is that the trapping is by positive DEP whereas in most iDEP cases, the immobilization is due to nDEP. Also, the fluid flows due to a pump (thus pressure-driven) as opposed to the electrokinetic movement that is usually employed in iDEP devices. Such a post array, embedded in a microfluidic channel, then essentially is a small-scale model of the actual macroscopic filter. However, due to its very regular design, it is much easier to describe and analyze how exactly the particle retention works.

The hypothesis is that it is possible to describe the influence of key parameters on the particle filtration (that is pore size, volume flow, field strength, porosity, …) by analyzing the particle trapping by one singular model instance of the filter, which would be one singular post. This is very similar to the concept of the single collector efficiency in regular filtration. If the assumption holds that the filtration is only due to dielectrophoresis (whereas there is no mechanical filtration which appears to be a valid assumption for circular posts that are several orders of magnitude larger than the target particles) it is key to acquire the electric field distribution around such a post. Due to the (excitatory) electric field the post will polarize—very much like a particle (cf. Fig. 4.1 d, it is not coincidental that the field distribution is drawn similar to

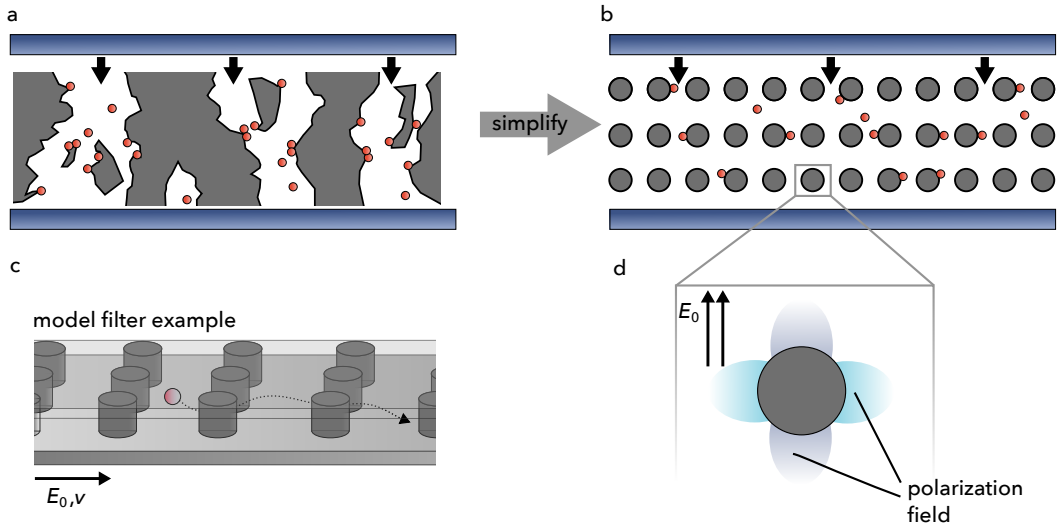

Fig. 4.1: Strategy for the simplification of the complex and random porous medium to a regular model structure (a and b). The post array (b) is quasi two-dimensional since a practical representation of it would just be an extrusion in the drawing plane. Panel (c) shows how the resulting model filter could look like. Due to the excitatory field that is applied by the dark blue colored electrodes the posts will polarize. One key aspect of the particle trapping behavior is how the field distribution around a single post will look like (d) and how this distribution is influenced by the geometry of the post.

Fig. 2.8)[1]. This polarization field will attract particles (depending on their DEP response they could also be repelled, but attraction is assumed since the filter is based on pDEP). Depending on the resulting field distribution, the particle's trajectory around such a post will be different.

Key aspect of this work is to understand how the geometry of the porous medium changes the electric field distribution, so it only makes sense to investigate the influence of the post geometry on the resulting field distribution. This was done in a theoretical study and will be presented in the following chapter. What follows is based on G. R. Pesch, L. Kiewidt, F. Du, M. Baune, and J. Thöming (2016). Electrodeless dielectrophoresis: Impact of geometry and material on obstacle polarization. *Electrophoresis* 37.2, 291–301.

4.1 Overview and method

For the investigation, two base geometries have been chosen: a post with elliptical cross section (called ellipse from now on) and a post with diamond-shaped (rhomboidal, called diamond) cross section. Their geometrical influence on the field was investigated by varying their aspect ratio (AR), which is their cross-sectional width-to-height-ratio (cf. Fig. 4.2 a). The reason for this descision is as follows: It is a well-known fact that Laplace's equation has a singularity at corners of 90° or less, see for example Wigley (1988). This causes a steep increase of the electric field in the vicinity of the corner towards infinity. That means that very large forces will be generated when the structure has sharp edges. The "sharpness" can be increased by skewing the post (i. e., reducing its aspect ratio). The steeper the field increase (with increasing sharpness

[1] The difference is that the polarization potential here is described by a solution of Laplace's equation in *cylindrical* coordinates as opposed to the spherical coordinates that are employed for spherical particles.

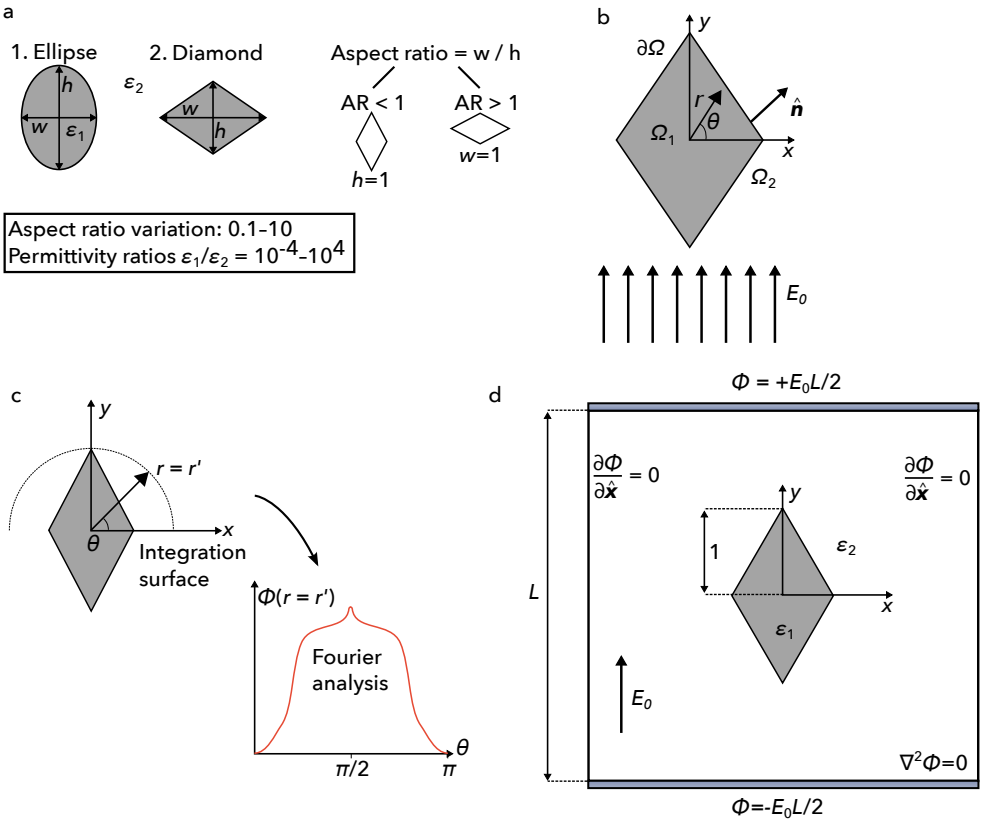

Fig. 4.2: a) Investigated post geometries and parameters b) Representation of the model system. The cross section of the post of domain Ω_1 is enclosed by the boundary $\partial\Omega$ and surrounded by the domain Ω_2. The unit normal vector $\hat{\boldsymbol{n}}$ points outwards. c) The multipole extraction method. d) Sketch of the simulation domain.

of the corner) the more localized (but higher) is the force factor $\nabla \left| E^2 \right|$. The two geometries and the aspect ratio variation were thus chosen in order to investigate the relationship between sharpness of the geometrical boundary, resulting field, and DEP force.

The singularity can not be modeled; there are no analytical expressions for the field around a 90° corner (well, probably there are, but they are at least not simple). In simulation methods it can only be approximated by a sufficiently fine mesh that recreates the correct field distribution up to a point very close to the edge (at which the field deviates). A semi-analytical method to describe the potential around polarized posts is a multipole expansion (note that this will also not be able to recreate the field distribution with 100 % accuracy).

The method described in this chapter works as follows: The multipole expansion in cylindrical coordinates will be presented (the full derivation can be found in Appendix A). Since the multipole moments are a priori unknown for a geometry it is necessary to extract them from a given solution. Finite Element Simulations of Laplace's equation are performed for all post geometries and subsequently the coefficients are extracted using numerical methods. Then, the distribution of the multipole coefficients (the shares of the overall polarization among the order n of the respective multipole) is analyzed for all geometries. From this we can learn (in a very well described manner) *how* the geometry of the post influences the resulting polarization potential and the resulting electric field. Assume a post in an electric field, as shown in

Fig. 4.1 d or more specifically in Fig. 4.2 b. The problem is best described in cylindrical coordinates (z,r,θ), but for the remainder of the study the z axis can be omitted (since the field is applied perpendicular to the post's z axis there is no field variation in that axis). The origin is at the center of the post. The inside domain of the post Ω_1 has permittivity ε_1 and is enclosed by the boundary $\partial\Omega$. The outside domain Ω_2 has permittivity ε_2. The potential can be separated into two potentials that are only valid in their respective domains Φ_1 and Φ_2. The potentials can be found by solving Laplace's equation in cylindrical coordinates under application of the appropriate coupling conditions at $\partial\Omega$. The electric field of value E_0 is applied from bottom to top (in direction of the y coordinate). For brevity, only the solution for Φ_2 is given, the full derivation can be found in Appendix A:

$$\Phi_2(r,\theta) = E_0 r \sin\theta + \sum_{n=1}^{\infty} \frac{p_n \sin(n\theta)}{r^n}. \tag{4.1}$$

Here, the p_n are constants. The first term of Eq. (4.1) is the potential due to the applied field and the second term is the potential due to the polarization. It is important to note that Eq. (4.1) is only valid for r larger than the largest dimension of the post's cross section. The polarization potential is expressed as a sum of an infinite amount of multipoles that are characterized by their respective moments p_n, with $n = 1,2,3$ (dipole moment, quadrupole moment, octupole moment, …).

Describing the polarization field for a specific post and thus the forces acting on a particle in it's vicinity is therefore possible using Eq. (4.1). It is just a matter of obtaining all p_n for that post (geometry, material, and size). For a post with circular cross section of AR = 1 and radius 1 at an applied field of $E_0 = 1$ applied from bottom to top, all parameters p_n are zero except for p_1:

$$p_1 = \frac{1-\varepsilon_2/\varepsilon_1}{1+\varepsilon_2/\varepsilon_1}. \tag{4.2}$$

All other geometries do not possess an analytical expression for the p_n (at least not known to the author). As an act of reverse engineering it is possible to extract the coefficients from a known potential field (for example from FEM simulations), Φ_{FEM}. If $r = r'$ is fixed in Eq. (4.1), then the sum is a Fourier series with respect to θ (cf. Fig. 4.2 c). The Fourier coefficients are

$$p_n = \frac{2}{\pi} \int_0^{\pi} \Phi_{\mathrm{FEM}}(\Phi, r') \sin(n\theta)\, \mathrm{d}\theta. \tag{4.3}$$

The posts employed in this study always have the same size of 1. When the aspect ratio deviates from unity, the longer dimension will always be fixed at 1. Thus, a post with AR < 1 will always have $h = 1$ and a post with AR > 1 will always have $w = 1$ (Fig. 4.2).

4.1.1 Finite element simulation

Finite Element Simulations of Laplace's equation have been performed using the open source tool FEniCS (Logg et al., 2012b) and GMSH (Geuzaine and Remacle, 2009). An overview of the simulation space is shown in Fig. 4.2 d and the full explanation can be found in Pesch et al. (2016) or in Appendix B. The dimensionless field of strength $E_0 = 1$ was applied

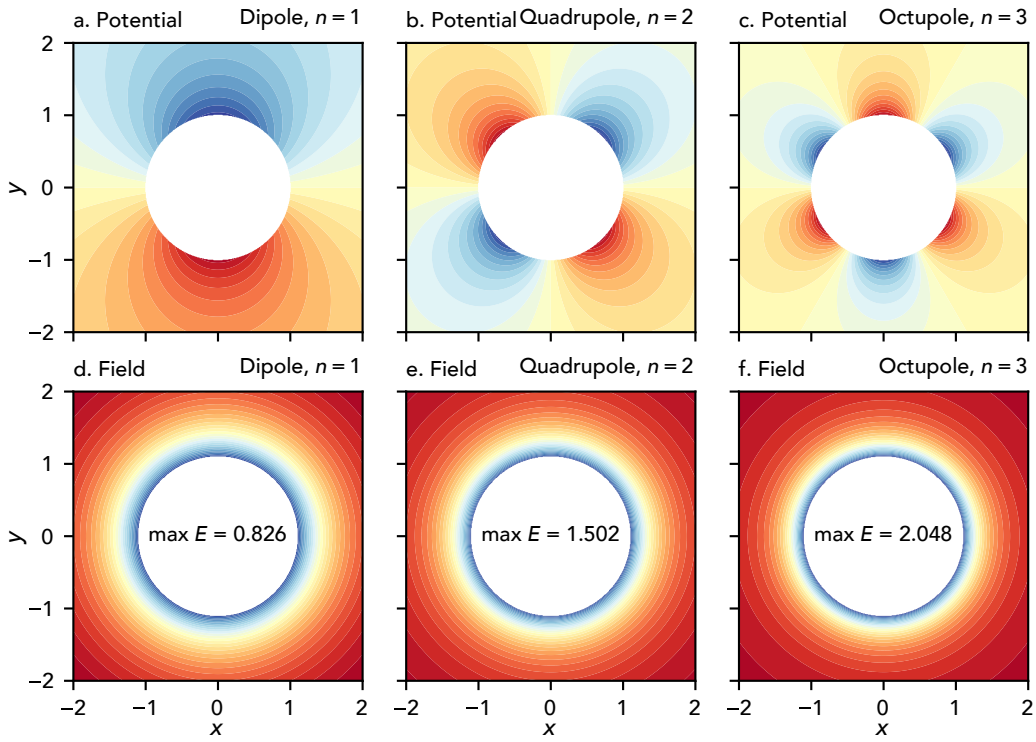

Fig. 4.3: Electrostatic potential (a, b, c) and electric field norm (d, e, f) of the first three multipoles assuming $p_n = 1$ ($n = 1, 2, 3$). The field is shown without the applied electric field (which considerably changes the picture). The color range has been scaled to the value range of each individual picture. Blue signals high values and red shows low values.

from bottom to top over a square simulation surface of size $L = 50$. The potential at top and bottom was fixed at $\Phi = \pm E_0 L/2$. Neumann boundary conditions where employed at the insulating boundaries on the left and right. The post (ε_1) was placed in the center of the simulation surface (ε_2). Mesh independence was achieved by gradually refining the mesh towards the four corners of the post until the sum over the first 1000 multipoles became independent of the mesh size. The extraction according to Eq. (4.3) was performed at $r' = 1.1$.

4.1.2 Important considerations: Complex permittivity and dimensionless parameters

In order to be generally applicable, the results are calculated using dimensionless parameters. In order to obtain the coefficients for real posts it is necessary to multiply the p_n by the actual applied field strength and the actual radius of the post.

Also, all results are presented as a function of the permittivity ratio. For simplification, this ratio was assumed to be real. For real dielectrics, the real part of the frequency dependent complex permittivities has to be used, $\varepsilon_2/\varepsilon_1$ is replaced by $\mathrm{Re}[\tilde{\varepsilon}_2(\omega)/\tilde{\varepsilon}_1(\omega)]$.

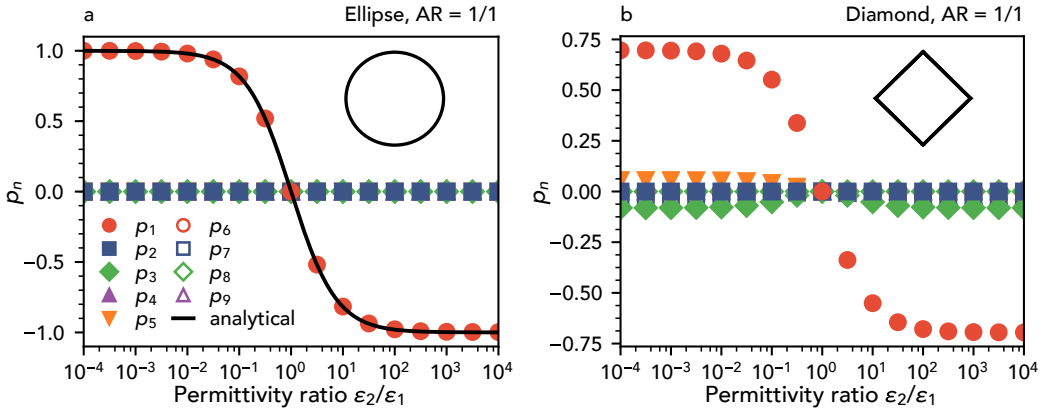

Fig. 4.4: First nine multipole moments p_n as a function of the permittivity ratio $\varepsilon_2/\varepsilon_1$ between the medium's and the post's permittivity for a circle with AR = 1 (a) and a diamond with AR = 1 (b). Also plotted in panel (a) is the analytical solution (Eq. (4.2).

4.2 Results

4.2.1 Potential and electric field due to the first three multipoles

Each multipole causes a specific electrostatic potential and consequently an electric field. The overall potential is the sum of the potentials due to each multipole. With increasing order of the multipole, the electric field due to that multipole moment will be stronger close to the multipole's center but will also decay faster.

The potential and the electric field norm due to the first three multipoles (dipole, $n = 1$, quadrupole, $n = 2$, and octupole, $n = 3$) is shown in Fig. 4.3. Due to the n in the sine function in Eq. (4.1) the potential oscillates quicker with θ with increasing n. As a consequence, the odd moments cause a charge separation between the upper and lower half, whereas the even moments show rotational symmetry. With increasing n the $1/r^n$ term falls quicker with r. Hence, with increasing n the field will be stronger for r approaching 1 (observe max. E from left to right in the second row of Fig. 4.3) but will also fall much quicker with r (color changes quicker from blue to red in panel f than in panel d).

This is the field only due to the multipole moment without the applied field. Both fields in combination will cause a substantially different configuration (Fig. 4.8).

4.2.2 Circle and diamond of equal width and height

The ellipse with AR = 1 only develops a dipole, all other p_n for $n > 1$ are 0 (Fig.4.4 a). Much like the Clausius-Mossotti factor the coefficient is one when the permittivity $\varepsilon_1 \gg \varepsilon_2$, that is $\varepsilon_2/\varepsilon_1$ approaches zero. The post then is much better polarizable than the surrounding medium and the dipole will be parallel to the electric field. The resulting potential looks like in Fig. 4.3 a. When $\varepsilon_2/\varepsilon_1 = 1$, there is no effective polarization. If the post is much less polarizable than the surrounding medium, $\varepsilon_1 \ll \varepsilon_2$ (i. e., $\varepsilon_2/\varepsilon_1 \to +\infty$), then $p_1 = -1$ and the resulting dipole will be anti-parallel to the applied field (the other way round than shown in Fig. 4.3). The analytical solution for the circle (Eq. (4.2)) matches very well the extracted Fourier coefficient p_1.

The maximum value value of p_1 for the diamond is ~ 0.7 and thus 30 % less in magnitude than the p_1 for the circle (Fig. 4.4 b). The odd higher order moments deviate from 0 (whereas the even higher order moments are still 0). If the post is better polarizable than the surrounding medium ($\varepsilon_2/\varepsilon_1 \to 0$), then every second coefficient switches sign, whereas all coefficients have the same sign when the post is less polarizable than the surrounding medium. When both permittivities match, all p_n are zero.

A polarized post will always have two points of maximum electric field and two points of minimum field (same as for particles). When a post is better polarizable than the surrounding medium (the left side of the graphs) the two points of maximum field are at the two edges parallel to the applied field, whereas the minimum points are at the two edges perpendicular to the field. The situation is exactly the opposite when the post is less polarizable than the surrounding medium (the right side of the graphs). This is also shown in Fig. 4.8. From now on: When the polarization field is discussed, it means the field at the two points where the electric field is maximum.

As a consequence of the non-zero p_n for $n > 1$, the diamond (as expected due to the 90° corner) has a much stronger field close the corner (potentially it's infinite at a very small point but this point is so small, that it can safely be neglected). The field will also decay slightly faster than for a circle with increasing r. This means, a particle close to the diamond post will experience a greater force than close to a circular post. A particle that is some distance away fro the diamond post will instead experience a lower force.

4.2.3 Influence of the aspect ratio

When the aspect ratio deviates from one, the first order coefficient becomes smaller and the higher order coefficients become more important (the polarization switches from a dipole to a multipole with higher order components). This is true for both, the ellipse (Fig. 4.5) and the diamond (Fig. 4.6). It is the same as in Fig. 4.4 b: when the post is better polarizable than the surrounding medium, every second odd coefficient switches sign, whereas when the post is less polarizable than the surrounding medium, all coefficients have the same sign. Also, the coefficients are generally higher for the two cases in which the post is less polarizable and the post is aligned with the longer axis perpendicular to the field (AR > 1 and $\varepsilon_2/\varepsilon_1 \to \infty$) and in which the post is aligned with the longer axis parallel to the field and is better polarizable (AR < 1 and $\varepsilon_2/\varepsilon_1 \to 0$). One more observation: The p_1 appears be always slightly higher in magnitude for the ellipse at the same AR than for the diamond; this makes sense since it does not possess the sharp corner.

The consequence of this is that when a post's cross-sectional aspect ratio deviates from 1, the percentage of the polarization that is caused by a dipole decreases and the the higher-order terms become more dominant. This effect is more pronounced for a diamond than for an ellipse, due to the sharper edge of the diamond. This can also be inferred from Fig. 4.7 a: The figure shows the p_1 and the sum of all p_n from $n = 3$ to $n = 999$ ($p_{1000} = 0$) for the two base geometries and for all aspect ratios from 1 to 10 (for a post much less polarizable than the surrounding medium, $\varepsilon_2/\varepsilon_1 \to \infty$). Obviously, p_1 decreases with increasing AR and the sum of the higher order p_n increases. The ellipse's p_1 is generally higher than the diamond's p_1. The

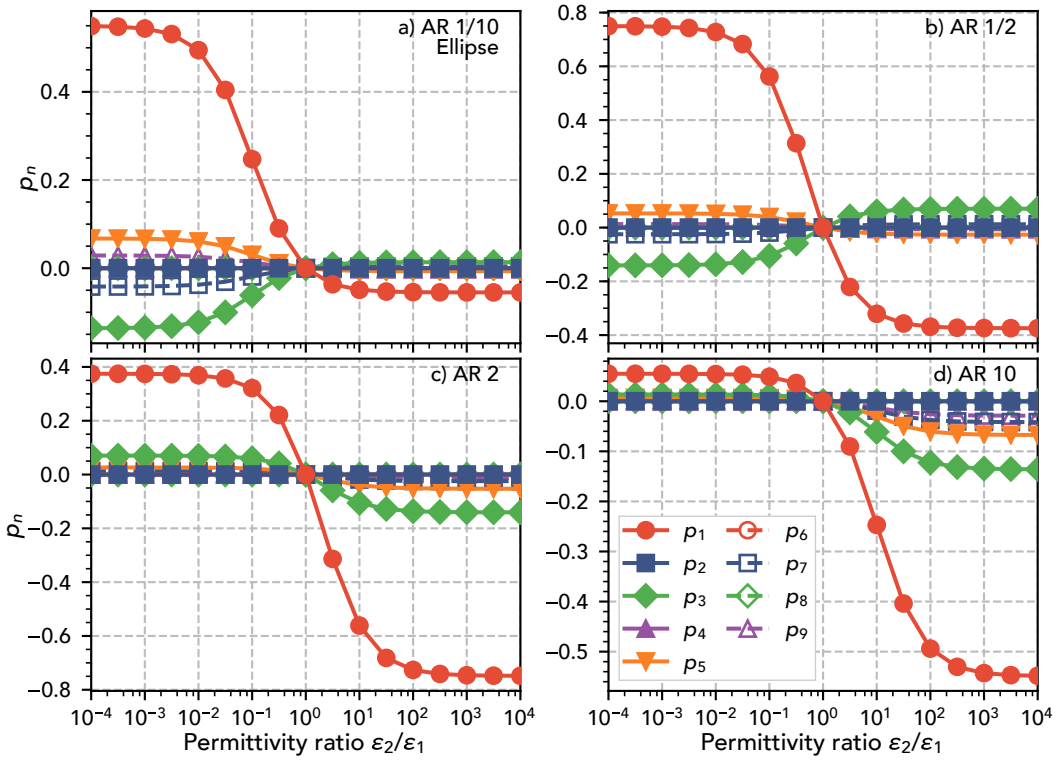

Fig. 4.5: First nine multipole coefficients p_n of a post with elliptical cross section and different aspect ratios (AR) as a function of its polarizability (as expressed by the permittivity ratio $\varepsilon_2/\varepsilon_1$; when $\varepsilon_2/\varepsilon_1 \to 0$, the post is much better polarizable than the surrounding medium, and conversely, when $\varepsilon_2/\varepsilon_1 \to \infty$, the post is much less polarizable than the surrounding medium).

higher-order sum is larger for the diamond than for the ellipse but the values approach each other as the aspect ratio increases.[2] As a side note: The picture is exactly the same for a much better polarizable post when 1/AR would be written on the x axis.

Consequently: The more the cross-sectional AR deviates from one, the higher the field becomes close to the post but the more rapidly it will decrease when the distance to the post is increased. This is more pronounced for the diamond than for the ellipse.

4.2.4 Influence of the post's orientation

As already described, the the polarization coefficients are much higher in general for the two cases AR > 1, $\varepsilon_2/\varepsilon_1 \to \infty$ and AR < 1, $\varepsilon_2/\varepsilon_1 \to 0$. For the other two cases the polarization coefficients are much smaller. This can also be inferred from Fig.4.7 b, which shows the sum over the first 999 coefficients (the 1000th is zero since it's even) for an ellipse and four different ARs. The polarization of a *much less polarizable* post is much larger when it's positioned with its longer axis perpendicular to the applied field than when it's oriented parallel to the field. Vice versa, a *much better polarizable* post shows much higher polarization when it's aligned in parallel with the field than when its longer axis is aligned perpendicular to the field. The effect becomes

[2] Actually, that indicates that 1000 multipoles are not enough for an accurate description because the p_n for $n > 1000$ appear to also have a substantial value: The sum of p_1 and all higher order terms should approach one and that is not the case for the diamond.

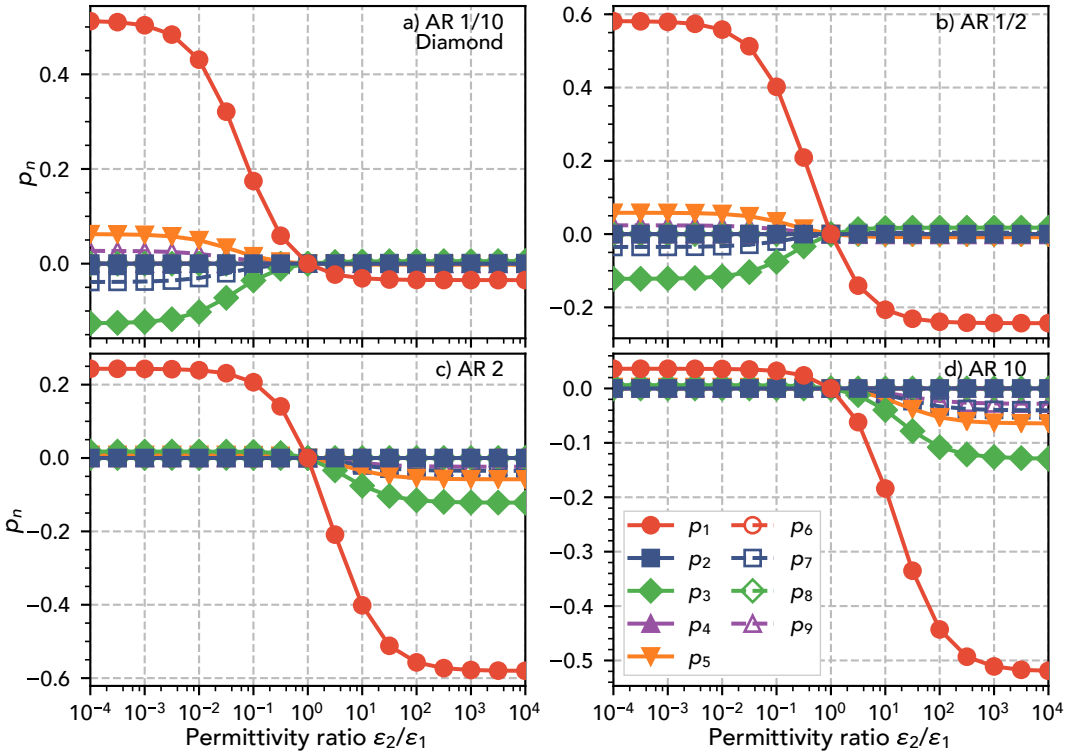

Fig. 4.6: First nine multipole coefficients p_n of a diamond post with different aspect ratios (AR) as a function of its polarizability (as expressed by the permittivity ratio $\varepsilon_2/\varepsilon_1$; when $\varepsilon_2/\varepsilon_1 \to 0$, the post is much better polarizable than the surrounding medium, and conversely, when $\varepsilon_2/\varepsilon_1 \to \infty$, the post is much less polarizable than the surrounding medium).

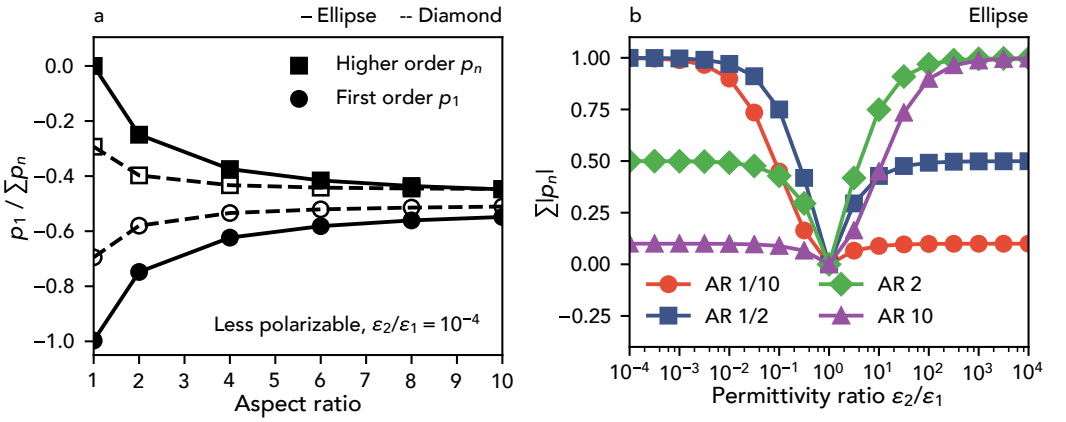

Fig. 4.7: a) Comparison of p_1 (circle) and the sum of all higher order coefficients $\sum_3^{999} p_n$ (square) for a diamond (dashed line, empty symbols) and an ellipse (solid line, filled symbols) as a function of the aspect ratio. The ellipse is much less polarizable than the surrounding medium and the longer axis is aligned perpendicular to the field. b) Sum of the magnitude of all multipole coefficients from $n = 1$ to $n = 999$, $\sum_1^{999} |p_n|$ for an ellipse with four different aspect ratios. When AR > 1, the post is aligned with the longer axis perpendicular to the field and conversely, when AR < 1, the post is aligned with the longer axis parallel to the field.

more pronounced with increasing deviation of AR from one. A post with a very compressed cross section shows almost no polarization when it is aligned "in the wrong way".

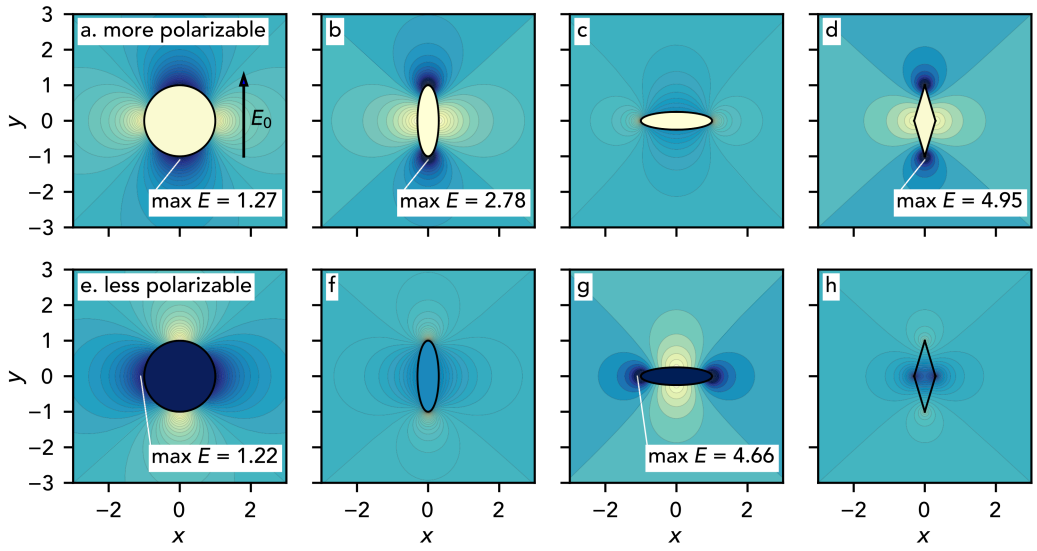

Fig. 4.8: Electric field magnitude for posts that are much better polarizable than the surrounding medium ($\varepsilon_2/\varepsilon_1 \to \infty$, a, b, c, d) and much less polarizable ($\varepsilon_2/\varepsilon_1 \to 0$, d, e, f, g) than the surrounding medium. For better comparison the color range was fixed from -1 (yellow) to 1 (blue) and the maximum value written on the plot. Shown is a circular post (a, e), an ellipse that is aligned parallel to the field (b, f), an ellipse that is aligned perpendicular to the field (c, g) and a diamond that is aligned parallel to the field (d, h).

Figure 4.8 shows a summary of these findings. It shows a contour plot of the polarization field for much better polarizable posts (a, b, c, d) and much less polarizable posts (e, f, g, h) that are aligned in parallel (AR < 1 for b, d, f, h) or perpendicular to the field (AR > 1 for c, g). To make the pictures comparable the color range was fixed from -1 to 1. The circle does not possess a preferred orientation with respect to its polarization.

From the figure it is possible to see several things: (i) The electric field maximum is at the two points that are on a imaginary line parallel to the applied field (bottom and top) when the post is better polarizable than the surrounding medium (a, b, c, d). Conversely, the electric field maximum is at two points on a line perpendicular to the applied field (left and right) when the post is less polarizable than the surrounding medium (e, f, g, h).

(ii) When a post that is much better polarizable is aligned with its longer axis parallel to the applied field (b, d) then the resulting field will be much stronger than when the post is aligned perpendicular to the field (c). Conversely, if a much less polarizable post is aligned perpendicular to the field (g), then its resulting field is much stronger than when it's aligned parallel to the field (f, h). (iii) The sharper the corner at which the maximum electric field occurs (top and bottom or left and right depending on the polarizability), the stronger the electric field at that point becomes (with decreasing maximum value from the diamond (d), over the ellipse (b) to the circle (a)). Additionally, the field will fall much faster with increasing distance (all plots have the same number of contour levels and the contour levels fall much quicker for the

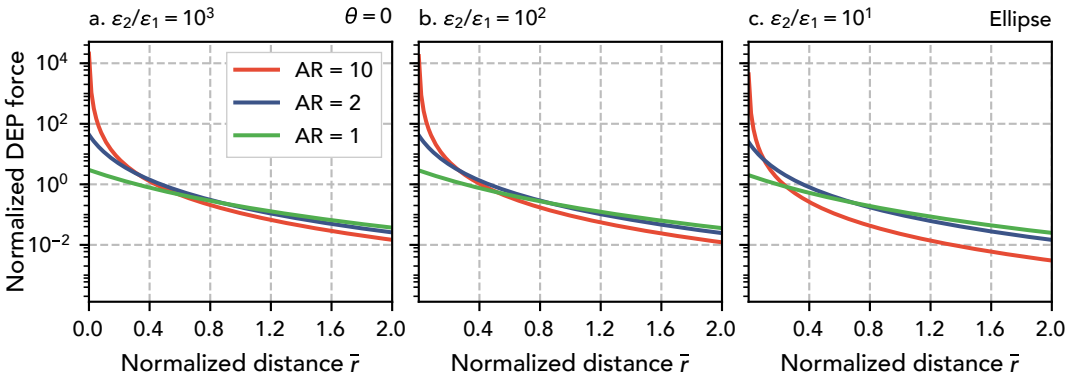

Fig. 4.9: Normalized DEP force $\overline{F}_{\mathrm{DEP}} = F_{\mathrm{DEP}}/\left(3/4V_{\mathrm{p}}\varepsilon_2 \mathrm{Re}\left[\tilde{f}_{\mathrm{CM}}\right]\right)$ as a function of the normalized distance $\overline{r} = (r-1)$ for an insulating post (less polarizable than the surrounding medium) for three different aspect ratios (1, 2, and 10). The post is always aligned perpendicular to the applied field. The relative polarizability of the post increases from left to right, $\varepsilon_2/\varepsilon_1 = 1000$ (a), 100 (b), and 10 (c). The angle $\theta = 0$ or $\theta = \pi$.

diamond (d) than for the ellipse (b) or the circle (a)). And finally (iv), the resulting electric field of situation (e) and (g) is just the rotation of the electric field by post (a) and (b), resp.[3]

4.2.5 Influence of higher-order multipole moments on DEP force

As already discussed, a polarization that has a substantial percentage of higher-order moments will generate a field that is more localized but stronger. The effect on the DEP force is shown in Fig. 4.9. The figure shows the normalized DEP force $\overline{F}_{\mathrm{DEP}} = F_{\mathrm{DEP}}/\left(3/4V_{\mathrm{p}}\varepsilon_2 \mathrm{Re}\left[\tilde{f}_{\mathrm{CM}}\right]\right)$ as a function of the normalized distance $\overline{r} = (r-1)$ for a post that is less polarizable than the surrounding medium at $\theta = 0$. That means, a straight line that extends outwards from the point of maximum electric field at the side of the post.

As expected, the force will become larger at the corner the more compressed the post is (almost four orders of magnitude for AR = 10 compared to AR = 1). At some point, approximately one quarter of the size of the post's longer axis away from it, the force from the non-compressed post (AR = 1) becomes stronger than for the compressed post. This is because the higher-order terms decay much faster with distance than the first-order term.

With decreasing difference in the polarization (from left to right, a to c) this intersection occurs nearer to the post. This is, because the higher-order terms fall quicker when $\varepsilon_2/\varepsilon_1$ approaches 1 than the first-order term. Hence, the overall polarization of a post that has a lot of higher-order terms is much smaller when the polarizabilities of medium and post almost match compared to the polarization of a post that develops only a dipole.

Consequently, a trade-off is required between maximum holding force and "equal" force distribution as a function of distance from the tip. When posts are spaced narrowly, it appears to make sense to use posts with an AR very different from 1 (and rather use diamonds than

[3] This is different from the polarization of spherical particles: The $\mathrm{Re}\left[\tilde{f}_{\mathrm{CM}}\right]$ is smaller in magnitude (-0.5) for a much less polarizable particle than for a much better polarizable particle (1).

ellipses). When posts are spaced widely apart, it appears to be beneficial to use non-compressed posts (that is, posts with AR = 1).

4.3 Conclusion

This chapter demonstrated how to simplify a complex porous medium and how to describe the field distribution as a function of it's properties. In a first step, the complex porous medium was replaced by a far simpler geometry, a rectangular array of quasi two-dimensional posts (cf. Fig. 4.1). Then, the electric field distribution around a single post was investigated in more detail, which allows to formulate some rules concerning the design of a porous medium for a field distribution that is optimized towards particle trapping.

To do so, a semi-analytical description of the potential around cylindrical geometries was established which is based on a multipole expansion. Investigation of the multipole coefficients as a function of the geometrical features and the effective polarizability of the post allows to obtain a very well-defined relationship between electric field and post geometry.

Using FEM simulations it is possible to obtain the effective moments of the multipole expansion by numerical integration. Each multipolar moment shows a different polarization potential (cf. Fig. 4.3). Posts with different geometry and different material show a distinct distribution of the overall polarization among the moments of varying order, from which several rules can be learned:

(i) The more the polarizability between the post and the surrounding medium differs (as expressed by $\varepsilon_2/\varepsilon_1$) the stronger the overall polarization is until a maximum is reached when the permittivities (note Sec. 4.1.2) differ by four orders of magnitude.

(ii) When the post is less polarizable than the surrounding medium ($\varepsilon_2/\varepsilon_1 \to \infty$) the maximum electric field will be located at two points that are located on a line perpendicular to the applied field. When it's better polarizable ($\varepsilon_2/\varepsilon_1 \to 0$), then the maximum electric field will be located at two points on a line parallel to the applied field.

(iii) The more the overall polarization of a post is distributed among higher order moments, the stronger the field (and thus the force) will be at the two points of maximum field strength. At the same time, the force will decay faster with distance (which means that there will either be a rather equally distributed force or a strong force with shorter reach). Posts that have sharp geometrical features show more higher order polarization (compare p_n for a circle, Fig. 4.4 a, and a diamond, Fig. 4.4 b). Also, the more a post's cross section is compressed (as expressed by the aspect ratio AR), the "sharper" its features are and thus the more higher-order polarization it shows (Fig. 4.7 a).

(iv) Posts that have an aspect ratio very different from 1 should be aligned with their longer axis parallel to the field if they are more polarizable than the surrounding medium and with their longer axis perpendicular to the field if they are less polarizable than the surrounding medium (cf. 4.7 b).

The contour plots of the electric field around posts with different polarizabilities and geometrical features as a summary is shown in Fig. 4.8. On a side note: The influence of the material is interesting from a theoretical point of view because it helps to better understand how

the underlying system behaves. In reality, most systems will either be virtually non-polarizable ($\varepsilon_2/\varepsilon_1 \to \infty$, as it would be the case for insulating posts) or perfectly polarizing ($\varepsilon_2/\varepsilon_1 \to 0$, as it would be the case for metal posts)[4]. In the case of metal posts (which are also termed floating electrodes) it is important to note that ICEO movement might occur and that, depending on the frequency of the applied field and the medium properties, the polarization behavior might be influenced by the double layer (cf. Sec. 2.10), that would effectively render the post insulating.

At this point the electric field distribution around a single post is well described. The next step is to understand how this interplay between post geometry and resulting field plays a part in the actual trapping of particles. The question is: What is the influence of the posts geometry on actual trapping of particles that move past the post in a fluid stream by DEP? This shall be answered in the next chapter, which offers a survey of the influence of several design and operational parameters on the effectiveness of trapping by posts.

[4] An exception from this are the early DEP filtration papers (Benguigui and Lin, 1982; Lin and Benguigui, 1982) in which all media where almost ideal dielectrics. There, the $\varepsilon_2/\varepsilon_1$ was below 10 and above 1.

5 Dielectrophoretic particle trapping at single posts

> *Truth is ever to be found in the simplicity, and not in the multiplicity and confusion of things.*
>
> **— Isaac Newton**

In the last chapter a method to describe the polarization behavior of a single post as a function of its polarizability (as expressed by $\varepsilon_2/\varepsilon_1$) and its geometry (as expressed by its base geometry and cross-sectional aspect ratio, AR) was established. This was considered the first step to describe the dielectrophoretic particle trapping behavior in porous media. The field distribution around cylindrical, quasi two-dimensional posts was chosen to approximate the complex porous medium by a far simpler geometry: an array of posts, whose cross-sectional geometry, spacing, and size is supposed to replicate certain features of the actual porous medium. The next logical step is to describe the particle trapping around single posts (employing the same concept as in Sec. 4 but taking it a step further). By this it is possible to link the rather conceptual "polarization field" or "electric field gradient due to polarization" with the easier conceivable particle trapping behavior.

The main idea of this study is to find a way to express a specific post's particle trapping potential (that means, a post with a specific size and geometrical features). The particle trapping potential is expressed in terms of a critical distance H_{crit} or a critical particle size $d_{\mathrm{P,crit}}$. By evaluating how the particle trapping behavior changes with key design and operational parameters (post size, post geometry, applied field strength, throughput, …) it is easy to deduce basic design rules for porous media that should be applied in DEP particle retention. What follows is based on G. R. Pesch, F. Du, M. Baune, and J. Thöming (2017). Influence of geometry and material of insulating posts on particle trapping using positive dielectrophoresis. *Journal of Chromatography A* 1483, 127–137.

5.1 Overview

The analysis goes as follows: Identically to the approach of chapter 4, the complex porous medium is approximated by a rectangular array of quasi two-dimensional posts (cf. Fig. 5.1 a). The analysis is limited to insulating posts (the permittivity of the post ε_1 is smaller than the surrounding medium's permittivity ε_2) and spherical particles experiencing positive DEP (that is Eq. (2.30) is valid and $\mathrm{Re}\left[\tilde{f}_{\mathrm{CM}}\right] = 1$). Particles flowing through the post array will be attracted by the maximum field points that are located at the two points on a line perpendicular to the applied field (cf. Fig. 4.8 (e - h)).

The analysis focuses on the investigation of the trapping behavior of a single post, for simplification it is arbitrarily assumed that particles flow past the post on the left side. A slightly different coordinate system compared to Fig. 4.2 is employed, (ξ, η), which has its origin at the

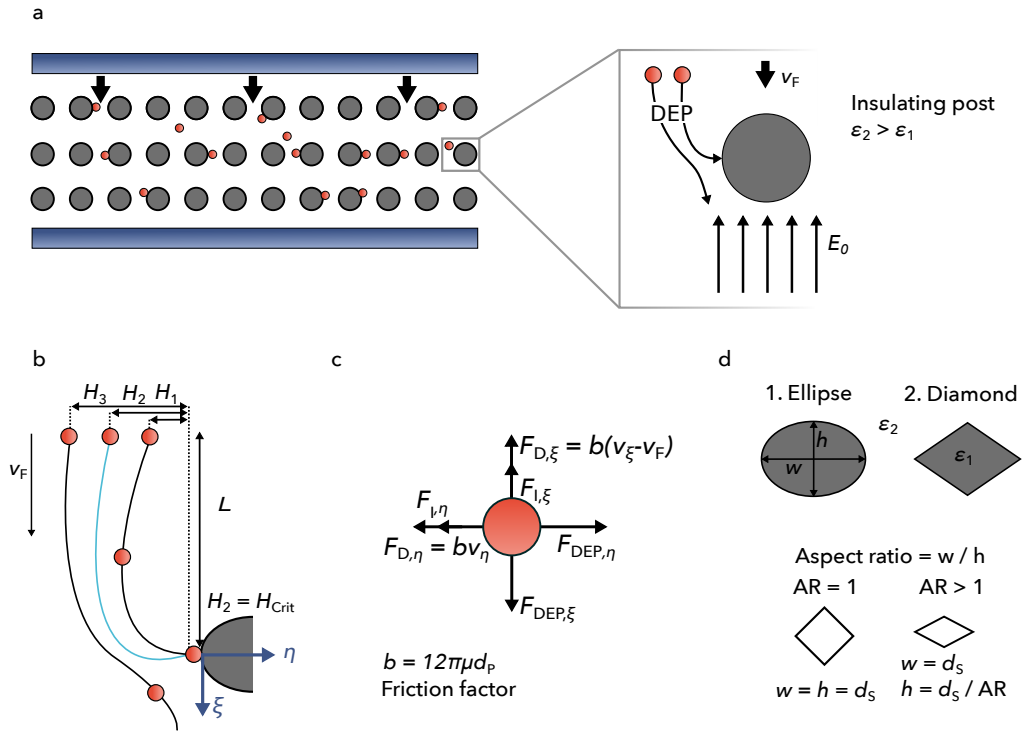

Fig. 5.1: Overview of the employed method for this analysis. Again, the complex porous medium is approximated by a rectangular array of quasi two-dimensional posts (a). Only insulating posts ($\varepsilon_1 < \varepsilon_2$) are investigated and particles that experience pDEP ($\mathrm{Re}\left[\tilde{f}_{\mathrm{CM}}\right] > 1$) will be attracted by the two points perpendicular to the applied field. When all other parameters are kept constant, it is possible to find a critical perpendicular starting distance a particle of size d_P can have from the post, H_{crit}, so that the DEP force is sufficiently strong to trap it from a fluid stream of velocity v_F. The coordinate system (ξ, η) has its origin at the left-most point of the post. The variable ξ points in flow direction and η perpendicularly towards the post's center (b). The forces acting on the particle are inertia $\boldsymbol{F}_\mathrm{I}$, drag $\boldsymbol{F}_\mathrm{D}$, and DEP $\boldsymbol{F}_{\mathrm{DEP}}$ (c). Investigated post geometries are posts with elliptical (ellipse) and rhomboidal (diamond) cross sections with varying cross-sectional width-to-height ratios (aspect ratio, AR). Only insulating posts with ideal arrangement are investigated, that is AR ≥ 1 (cf. Figs. 4.7 and 4.8).

outermost left point of the post. ξ points in direction of the fluid flow and η points perpendicularly towards the center of the post (Fig. 5.1 b). A particle sits in a constant fluid stream of velocity $\boldsymbol{v}_\mathrm{F}$ that is directed from top to bottom. It is assumed that the fluid flows parllel everywhere, so that $\boldsymbol{v}_\mathrm{F} = (v_\mathrm{F}, 0)^\intercal$ in (ξ, η)-coordinates. The superscript $^\intercal$ denotes the vector's transpose. The particle flowing past the post at a very small η-distance, H_1, will be readily attracted by the tip due to pDEP (thus DEP overcomes the fluid flow). When the distance in η direction is increased, it will be more difficult to trap the particle due to DEP, because it has to be moved a longer distance until it reaches the post's surface and because the force will be lower the further away the particle is from the post. There will be a critical distance, $H_2 = H_{\mathrm{crit}}$, at which the DEP force will be just sufficient to trap the particle. At larger distances, H_3, particles will be influenced by the post, but not strongly enough in order to become trapped; then, the fluid flow overcomes the DEP force. Depending on the initial starting distance H, particles could first be repulsed slightly by the field minima that are located on the line parallel to the

field (top and bottom of the post). They would thus move slightly in negative η direction while moving in ξ direction before moving in positive η direction.

Finding H_{crit} can be accomplished by solving the equation of motion for the particle's trajectory including all the forces that are acting on the particle (Fig. 5.1 c), that is inertia $\boldsymbol{F}_{\text{I}}$, fluid drag $\boldsymbol{F}_{\text{D}}$, and DEP $\boldsymbol{F}_{\text{DEP}}$. The H_{crit} is dependent on the geometry of the post (since differently shaped posts show different polarization, see Chapter 4). As before, the two base geometries, ellipse and diamond, have been investigated. Here, only insulating posts with optimal orientation were considered (Fig. 5.1 d). That means, the posts are always aligned with their longer axis perpendicular to the electric field, AR > 1, which is the optimal arrangement for $\varepsilon_2 > \varepsilon_1$ according to Figs. 4.7 and 4.8.

5.2 Method

In order to evaluate how well a specific post is suited for particle attraction it is necessary to obtain a value of the field gradient around the post, $\nabla|\boldsymbol{E}|^2$; that is one of the main requirements to calculate the DEP force, Eq. (2.30). In Sec. 4 an expression for the potential Φ around the polarized post was established (Eq. 4.1). Further, all multipole moments p_n up to $n = 1000$ where calculated. At this stage it is easy to obtain $\nabla|\boldsymbol{E}|^2$ by differentiating Eq. (4.1) twice:

$$\nabla|\boldsymbol{E}|^2 = \left(\partial_x|\boldsymbol{E}|^2, \partial_y|\boldsymbol{E}|^2\right)^{\mathsf{T}}, \tag{5.1a}$$

$$\begin{aligned}\partial_x|\boldsymbol{E}|^2 = &-\sum_{n=1}^{\infty}\sum_{k=1}^{\infty}\frac{k\,n(n+1)}{2r^{k+n+3}}p_n p_k\cos((k-n-1)\theta)\\ &-\sum_{n=1}^{\infty}\frac{n(n+1)}{2r^{n+2}}E_0 p_n\cos((n+2)\theta),\end{aligned} \tag{5.1b}$$

$$\begin{aligned}\partial_y|\boldsymbol{E}|^2 = &\sum_{n=1}^{\infty}\sum_{k=1}^{\infty}\frac{k\,n(n+1)}{2r^{k+n+3}}p_n p_k\sin((k-n-1)\theta)\\ &-\sum_{n=1}^{\infty}\frac{n(n+1)}{2r^{n+2}}E_0 p_n\sin((n+2)\theta).\end{aligned} \tag{5.1c}$$

Here, ∂_n is short for $\partial/\partial n$. Two polarization coefficients are present in Eq. (5.1), p_n and p_k, because $\boldsymbol{E}$ is squared and it is thus necessary to go through a double sum. This allows to calculate the force on a spherical particle in the vicinity of a polarized post under the assumption that the dipole approximation delivers reasonably accurate results. Equation (5.1) is still expressed in the (x, y) coordinates established in Fig. 4.2. Acquiring $\nabla|\boldsymbol{E}|^2$ in (ξ, η) coordinates is just a matter of a simple coordinate transformation.

For the analysis, posts with two distinct cross-sectional base geometries are investigated (Fig. 5.1 d), the ellipse and the diamond. The width of the post's cross section is always fixed to the d_{S} (structure diameter) and the aspect ratio AR changes from 1 to 10 (increasing compression of the cross section). A single particle of size d_{P} is initialized at $\xi = -L$ and $\eta = -H$ in the

fluid stream v_F (that only has a η component). According to Newton's third law and Fig. 5.1 c the equation of motion of the particle reads

$$\boldsymbol{F}_\mathrm{I} = \boldsymbol{F}_\mathrm{D} + \boldsymbol{F}_\mathrm{DEP}, \tag{5.2a}$$

$$\frac{\partial^2 \boldsymbol{x}}{\partial t^2} = -\frac{18\mu_\mathrm{F}}{\rho_\mathrm{P} d_\mathrm{P}^2}\left(\frac{\partial \boldsymbol{x}}{\partial t} - \boldsymbol{v}_\mathrm{F}\right) + \frac{3\varepsilon_0 \varepsilon_2}{2\rho_\mathrm{P}} \mathrm{Re}\left[\tilde{f}_\mathrm{CM}\right] \nabla \left|\boldsymbol{E}_\mathrm{RMS}\right|^2, \tag{5.2b}$$

with $\boldsymbol{x} = (\xi, \eta)^\intercal$ being the particle's position vector, $\boldsymbol{F}_\mathrm{I} = m_\mathrm{P}\left(\partial^2 \boldsymbol{x}/\partial t^2\right)$ being the inertia force with the particle's mass m_P, $\boldsymbol{F}_\mathrm{D} = -3\pi\mu_\mathrm{F} d_\mathrm{P} \boldsymbol{v}_\mathrm{rel}$ the Stokes drag force with the dynamic viscosity of the fluid μ_F, $\boldsymbol{v}_\mathrm{rel} = (\partial \boldsymbol{x}/\partial t - \boldsymbol{v}_\mathrm{F})$ the relative velocity between the particle $(\partial \boldsymbol{x}/\partial t)$ and the fluid $(\boldsymbol{v}_\mathrm{F})$ and $\boldsymbol{F}_\mathrm{DEP} = \langle \boldsymbol{F}_\mathrm{DEP} \rangle$ the time-averaged DEP force (Eq. (2.30)). Here, the $\boldsymbol{E}_\mathrm{RMS} = 0.5\boldsymbol{E}$ is used. This is an ordinary differential equation (ODE) of second order which in this specific case can be solved using the initial conditions:

$$\boldsymbol{x}_0 = (-L, -H)^\intercal, \tag{5.3a}$$

$$(\partial \boldsymbol{x}/\partial t)_0 = (v_\mathrm{F}, 0)^\intercal, \tag{5.3b}$$

$$\left(\partial^2 \boldsymbol{x}/\partial t^2\right)_0 = (0, 0)^\intercal. \tag{5.3c}$$

The p_n have been calculated in Chapter 4. Note the important considerations mentioned towards the dimensionless parameters and the complex permittivity ratio (Sec. 4.1.2). Equation Eq. (5.2b) has been solved employing the boundary conditions, Eq. (??), using the LSODAR wrapper from the odespy Python package.[1] Integration stopped as soon as ξ or η hit 0.

Two different methods are employed to assess a post's potential for particle trapping, the critical perpendicular distance from the post H_crit and the critical particle diameter $d_\mathrm{P,crit}$. Assuming a constant starting distance $\eta_0 = -H$, a very small particle will likely be affected by the post but maybe not enough in order to become trapped. When increasing the particle size, due to the volume dependence of the force, the DEP attraction will rise non-linearly. A specific particle size will then be just big enough in order for the particle to become trapped by the post. Particles that are even larger than that critical size $d_\mathrm{P,crit}$ will also become trapped. This is shown in Fig. 5.2 a, with red trajectories being particles with $d_\mathrm{P} < d_\mathrm{P,crit}$ and blue trajectories $d_\mathrm{P} > d_\mathrm{P,crit}$ (all employed parameters are given in the plot). The critical trajectory is black and dashed. Please note that ξ is plotted on the abscissa (thus from left to right instead of top to bottom as in Fig. 5.1) and η is plotted on the ordinate. The $d_\mathrm{P,crit}$ is thus the smallest trappable particle size for a given configuration.

Conversely, when all other parameters are kept constant it is also possible to evaluate a post's trapping potential in terms of the critical distance $\eta_0 = H$ a given particle of size d_P can have from the post and still be trapped. This is shown in 5.2 b, where all distances $H > H_\mathrm{crit}$ (and thus not-trapped trajectories) are plotted in blue and all $H < H_\mathrm{crit}$ are plotted in red. Red trajectories are thus safely trapped and blue trajectories are influenced by DEP but not strongly enough to be trapped.

[1] Available at http://hplgit.github.io/odespy/doc/api/odepack.html.

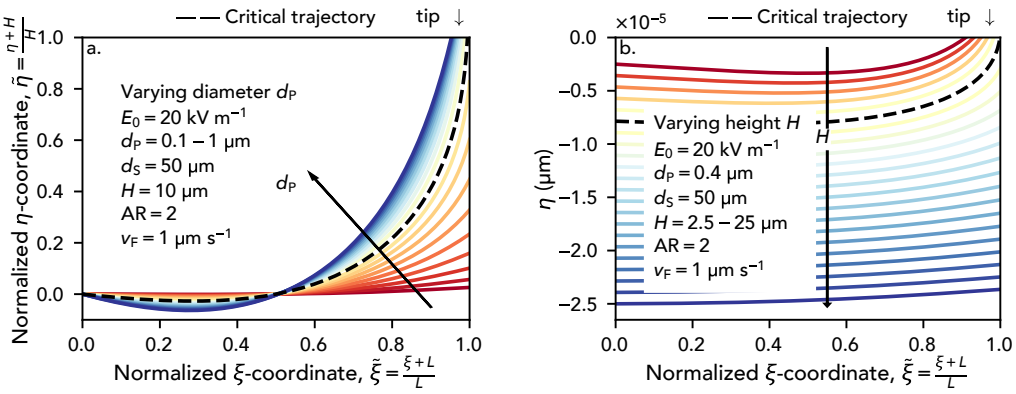

Fig. 5.2: Particle trajectories for varying d_P (a) and varying starting distances H (b) as obtained from solving Eq. (5.2b) and (5.3) for a rhomboidal post. The posts left-most tip is located at the top right of the figure (indicated by the arrow). The trajectories would have to be turned clock-wise by 90° to match the representation of Fig. 5.1. When the particle is too small, it will be attracted by the post but not enough in order to become trapped (red trajectories). A critical particle size $d_{P,crit}$ exists (black dashed), at which the particle is just trapped. Particles with $d_P > d_{P,crit}$ will be readily trapped (blue) (a). Another evaluation is to fix the particle size at d_P and to solve for the maximum η_0-distance a particle can have from the post to become trapped (H_{crit}, black dashed trajectory). Particle starting further away ($\eta_0 = H > H_{crit}$, blue) will not be trapped and particles starting closer ($\eta_0 = H < H_{crit}$, red) will be trapped (b).

5.3 Results

The trajectories presented in Fig. 5.2 were used to extract the results presented in this section. Each critical starting distance to the tip or critical particle diameter, H_{crit} or $d_{P,crit}$, resp., has been extracted from a series of particle trajectories which have been evaluated to find the critical trajectory. The attempt to give a validation of the approach against analytical methods can be found in Appendix C.

Appendix D also gives a qualitative comparison of the results obtained from this study with literature data from LaLonde et al. (2014) and Saucedo-Espinosa and Lapizco-Encinas (2015). All data presented in the following sections is for perfectly insulating posts, $\varepsilon_2/\varepsilon_1 = 1 \times 10^4$.

5.3.1 Influence of key design and operational parameters

To investigate the influence of the key design parameters (aspect ratio, cross-sectional geometry, and post size d_S) and operational parameters (excitatory field strength E_0, fluid velocity v_F, and particle diameter d_P) the critical distance H_{crit} has been extracted as a function of the cross-sectional aspect ratio (cf. Fig. 5.3). Here, filled symbols together with solid lines denote elliptical posts whereas dashed lines with empty symbols denote diamonds.

For simplification let us first only investigate the position of the lines towards each other and not the influence of the aspect ratio or the difference between the ellipse and the diamond. Obviously, with increasing field strength E_0, the critical distance (which could be considered the trapping reach) of a post increases (Fig. 5.3 a). This is because with increasing field strength there will be more polarization (all p_n increase) and thus a stronger field gradient. Conversely, an increase in v_F will cause a decrease of H_{crit} (Fig. 5.3 b), because with increasing v_F particles will move faster past the post. As a consequence, the time that a particle has to reach the post's

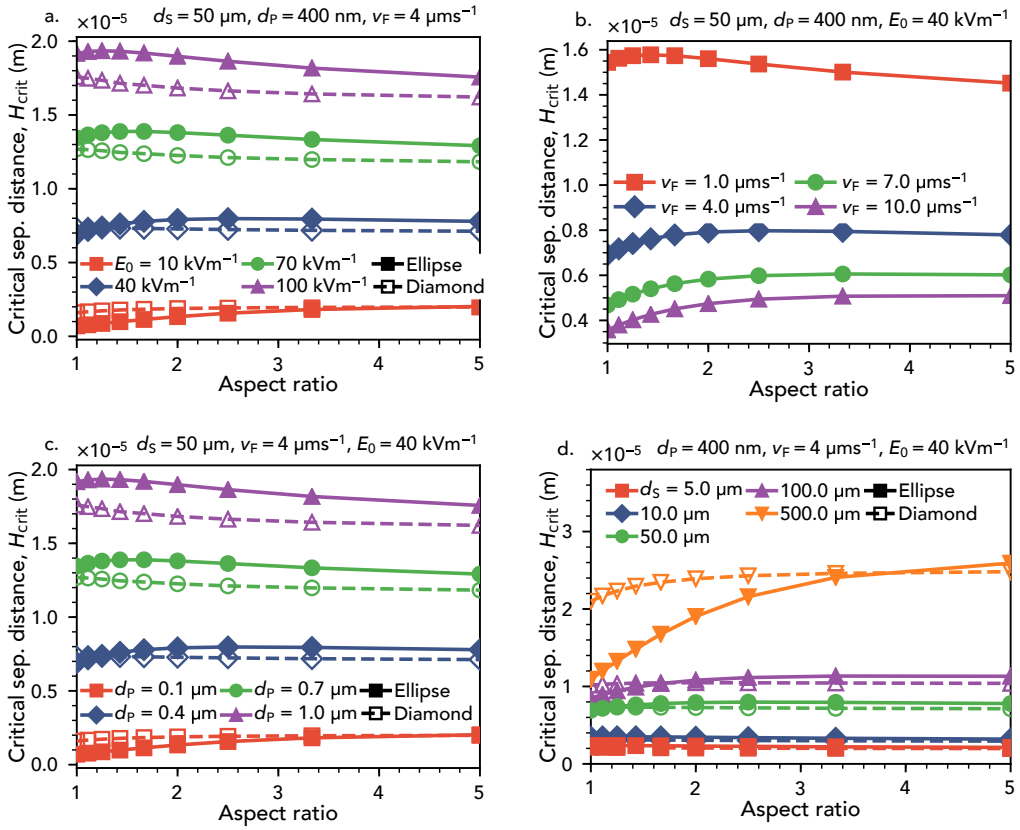

Fig. 5.3: Influence of various operational (a: field strength E_0, b: fluid velocity v_F, and c: particle diameter d_P) and design (d: post size d_S) parameters on the critical perpendicular distance a particle can have from a post to still become trapped, H_{crit}. Data is shown for various aspect ratios and for an ellipse (filled symbols, solid lines) and a diamond (empty symbols, dashed lines). Variations are always around the base values of $E_0 = 40\,\mathrm{kV\,m^{-1}}$, $v_F = 4\,\mu\mathrm{m\,s^{-1}}$, P = 400 nm, and $d_S = 50\,\mu\mathrm{m}$.

surface decreases which ultimately decreases the trapping range. Interestingly, if the acceleration in Eq. (5.2b) is assumed to be very fast, $\partial^2 \boldsymbol{x}/\partial t^2 = 0$, then the particles velocity will be proportional to $\partial \boldsymbol{x}/\partial t \propto d_P^2 \nabla |\boldsymbol{E}|^2$. Thus, the values of d_P and E_0 should be interchangeably as shown in Fig. 5.3 c: The curves for $E_0 = 40\,\mathrm{kV\,m^{-1}}$ and $d_P = 100$–1000 nm look exactly the same as the curves for $d_P = 400$ nm and $E_0 = 10$–$100\,\mathrm{kV\,m^{-1}}$ (Fig. 5.3 a). As a consequence, it is for example possible to trap particles half the size by doubling the applied voltage (when all other parameters are kept constant).

Increasing the post diameter d_S causes a large increase in the H_{crit} (Fig. 5.3 d). This increase is, however, not proportional to the change in d_S: Increasing the post size by factor 10 from $d_S = 50\,\mu\mathrm{m}$ to $d_S = 500\,\mu\mathrm{m}$ causes only a change in H_{crit} by a factor of three.

5.3.2 Ideal aspect ratio

Considering now the influence of the aspect ratio (AR) and base geometry (ellipse or diamond) in Fig. 5.3 (a – c) it is obvious that configurations that result in a H_{crit} that is large compared to d_S favor a cross-sectional aspect ratio close to 1. In that case the ellipse performs better than the diamond. When the H_{crit} comes close or below d_S the ideal aspect ratio is shifted

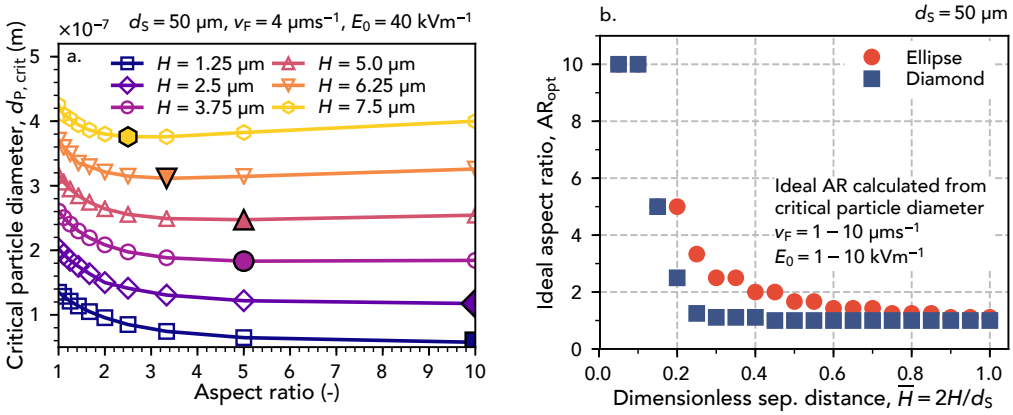

Fig. 5.4: Influence of the aspect ratio on the smallest trappable particle size $d_{P,crit}$ for different perpendicular starting distances H (a). With decreasing H the optimal aspect ratio (as denoted by the filled symbol) becomes larger. At a dimensionless distance $\overline{H} = 2H/d_S$ of one, that is the distance H divided by half of the post's width, the AR_{opt} is also one. It increases with decreasing $\overline{H}$ (b). This increase is happening at larger $\overline{H}$ for an ellipse (red circles) than for a diamond (blue squares).

towards higher values (that means, posts with a compressed cross section perform better). Also, at low AR the diamond performs better than the ellipse (albeit the maximum in H_{crit} is still shown by the ellipse with larger AR). This is expectable: Reiterating point (iii) from Sec. 4.3, the force due to a post with a lot of higher-order moments is stronger very close to the tip but it decays more rapidly with increasing distance from the tip whereas a post that shows mostly dipole polarization generates a force that is more equally distributed (see also Fig. 4.9). Hence, at large starting distances posts which have mostly dipole polarization (p_1, ellipse at AR close to 1) perform better. If now the H_{crit} becomes smaller a large force close to the post has a much larger impact because the particle itself is already close to it. Then, posts with higher-order polarization are better (AR > 1 and changing from an ellipse to a diamond). This appears to be not "black-and-white": Even when the ideal AR is shifted towards higher values, the ellipse still performs better in almost all configurations except for the two very small H_{crit} found in Figs. 5.3 a and c (red). This looks different in Fig. 5.3 d. Here, the value of d_S itself changes: The orange line (actually the largest H_{crit}) is the smallest H_{crit} in relation to the size of the post itself. That's why in that picture, the optimal AR moves towards larger values with *increasing* H_{crit}.

The dependence of the ideal AR on the separation distance becomes much clearer when solving for $d_{P,crit}$ while prescribing the initial $\eta_0 = H$ (cf. Fig. 5.4 a, note that in this case the smallest $d_{P,crit}$ is the best value). Two things can be seen here: it is obvious that with decreasing H the ideal aspect ratio moves towards larger values and, $d_{P,crit}$ decreases in concert with H because particles start closer to the post, thus giving the possibility to trap also smaller particles. This picture only shows the situation for an ellipse. The ideal AR_{opt} is denoted by a filled symbol. It is possible to extract AR_{opt} for a variety of H and the two base geometries. This is shown in Fig. 5.4 b. Here, the dimensionless distance $\overline{H} = 2H/d_S$ is the initial distance divided by half the post diameter. When $\overline{H}$ approaches 1, the ideal AR is also 1. When $\overline{H} < 1$, the AR_{opt}

increases and the increase occurs much faster for the ellipse than for the diamond: When $\overline{H} < 1$ more higher-order polarization is required. This means, the corner at the tip needs to be quite sharp and an ellipse requires a much higher AR to show the same higher-order moments than a diamond). This AR_{opt} only depends on $\overline{H} = H/d_S$, but is independent of particle size, volume flow, or field strength.

Interestingly, inspection of Fig. 4.9 a reveals that the force of the AR = 2 line becomes larger than the AR = 10 line at a distance of 0.3–0.4 times the radius of the post (that is, from the three AR shown in the Figure, two is the ideal AR).

At this point ($\overline{H} \approx 0.35$) also the optimal AR_{opt} is 2 in Fig. 5.4 b. Further, at a distance of approximately 1 post radius, the AR = 1 line becomes largest in Fig. 4.9 a which coincides with the AR_{opt} in Fig. 5.4 b that is 1 at $\overline{H} = 1$ for an ellipse.

5.3.3 Sensitivity

An effort to incorporate the influence of all key parameters in one Figure yields in Fig. 5.5 a. Here, the normalized critical separation distance $2H_{crit}/d_S$ (which could be understood as a post's trapping effectiveness) is plotted against a variation of the parameters volume flow v_F, electric field strength E_0, particle size d_P, and structure size d_S around a set of base values by two orders of magnitude. Variations are always around the base values of $E_0 = 40\,\mathrm{kV\,m^{-1}}$, $v_F = 4\,\mu\mathrm{m\,s^{-1}}$, $d_P = 400\,\mathrm{nm}$, and $d_S = 50\,\mu\mathrm{m}$. Only values for an ellipse with AR = 1 are shown.

Interestingly, d_P has the exact same influence than E_0. Also, v_F has exactly the same influence as d_S. This can also be inferred from the similar first-order sensitivity indices (Fig. 5.5 b) That means the overall trapping with respect to the size of the post is affected by v_F in the same way as by the system size d_S. Variations of E_0 and d_P by two orders of magnitude have

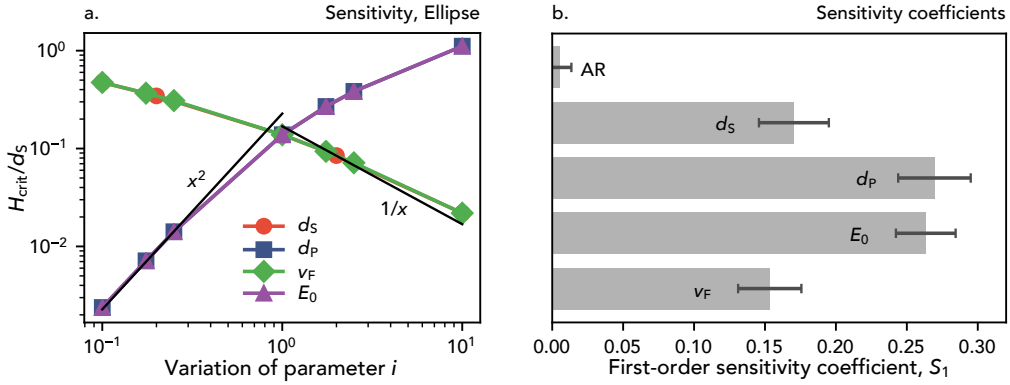

Fig. 5.5: a) Normalized critical separation distance H_{crit}/d_S for a variation of the key investigation parameters by two orders of magnitude around a base value of $v_F = 4\,\mu\mathrm{m\,s^{-1}}$, $d_P = 400\,\mathrm{nm}$, $d_S = 50\,\mu\mathrm{m}$, and $E_0 = 40\,\mathrm{kV\,m^{-1}}$ (aspect ratio is 1 and geometry is ellipse). b) First-order sensitivity index S_1 as obtained from a Sobol sensitivity analyses (performed using SALib for Python[2]) for the five parameters that have been varied in a range between AR = 0.1 to 1, $v_F = 0.4$ to $40\,\mu\mathrm{m\,s^{-1}}$, $d_P = 40\,\mathrm{nm}$ to $4\,\mu\mathrm{m}$, $d_S = 5$ to $500\,\mu\mathrm{m}$, and $E_0 = 4$ to $400\,\mathrm{kV\,m^{-1}}$. The error bars represent the confidence interval at a confidence level of 95 %. [2]Available at https://github.com/SALib/SALib.

a much larger influence on the target value H_{crit}/d_S than the variation of the system size d_S or the volume flow v_F. This can also be inferred from the larger S_1 values for E_0 and d_P. Interestingly, albeit causing a difference in force by several orders of magnitude (cf. Fig. 4.9) the AR (when varied between 1 and 10) has a negligible influence compared to all other parameters (very small S_1).

At $H_{crit} < 0.1 d_S$, the d_P and E_0 dependence is quadratic, as it might have been possible to expect from the DEP mobility equation (Eq. (2.37)), $\mu_{DEP} \propto d_P^2 \nabla |\boldsymbol{E}|^2$. At larger H_{crit} the dependence becomes sub-quadratic. Similarly, for small H_{crit} compared to d_S, the dependence on v_F and d_S is linearly reciprocal (roughly).

5.3.4 Summarizing discussion

A large H_{crit}/d_S is desirable because it results in a large trapping range while maintaining a high void fraction (low percentage of solid material). This would result in a higher throughput at constant pressure loss and also causes less overall field disturbance. At the same time it is desirable to have a small E_0 (less cost) and a large v_F (high troughput). Thus, a trade-off is required to balance all input parameters while simultaneously achieving a sufficient separation.

To summarize, the parameters with the largest influence on the overall separation are E_0 and d_P, followed by v_F and d_S. The aspect ratio, AR, can then be used to finally adjust the structure to a specific trapping distance. These parameters are not interchangeably variable. The particle size d_P is usually given by the problem (and thus not strictly a free variable), the AR and d_S are geometrical design parameters, and E_0 and v_F are operational parameters. Some relationships between these parameters are obvious; since H_{crit}/d_S has equal sensitivity towards E_0 and d_P it is possible to adjust towards a changing separation problem (say, particle size is half) by changing the applied field strength in a reciprocal manner (double). Equally, if the system size d_S changes, the volume flow should change reciprocally in order to compensate and maintain the separation quality. On the other hand, it is not possible to scale up a separation process by changing either v_F or the system size alone, since the target value has the same sensitivity towards both parameters: If the system size is scaled by the factor two at constant v_F, the throughput doubles but this comes at a cost of the separation efficiency. To compensate, the volume flow must by divided by two, which results in equal throughput and separation quality as before. A scale-up at constant particle size and separation efficiency is therefore always linked to a change in AR (small influence) or applied voltage.

It is also possible to adsorb a decrease in E_0 or d_P by a decrease in v_F or system size. Then, the latter parameters (v_F, d_S) need to change much more to compensate the former (E_0, d_P) due to the differences in sensitivity. As an example, a decrease in d_P by one order of magnitude requires a decrease in v_F by two to three orders of magnitude (estimated, not shown in Fig. 5.5 a).

5.4 Side note: Material influence

It was already mentioned in Sec. 4.3 that the discussion of the material influence on the polarization (or in the present section on the separation efficiency) is interesting only from a theoretical point of view (since most materials will either be perfectly insulating or perfectly conductive in the respective medium). Nevertheless, the influence of the relative polarizability

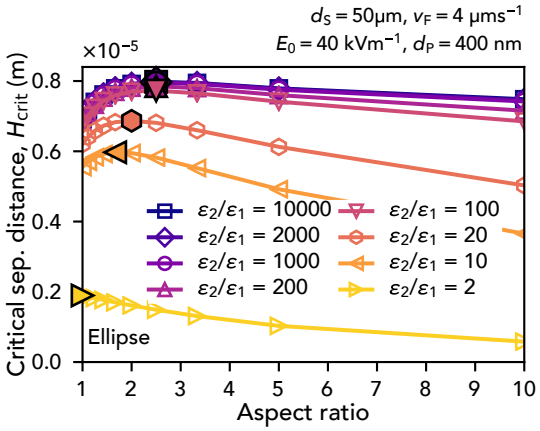

Fig. 5.6: Influence of the permittivity ratio on the separation as expressed by the critical trapping distance H_{crit} for aspect ratios from 1 to 10 and permittivity ratios $\varepsilon_2/\varepsilon_1$ from 1×10^4 to 1 for a post with elliptical cross section. The ideal aspect ratio for trapping (highest H_{crit}) is denoted by a filled symbol.

$\varepsilon_2/\varepsilon_1$ should be discussed briefly. As it can be inferred from Fig. 4.7 b, the higher the order of the multipole moment, the quicker its magnitude falls when $\varepsilon_2/\varepsilon_1$ approaches 1. As a result, the ideal aspect ratio as a function of $\varepsilon_2/\varepsilon_1$ moves from values above 1 at large permittivity differences, $\varepsilon_2/\varepsilon_1 \to \infty$, towards 1 when the permittivities are almost equal, $\varepsilon_2/\varepsilon_1 = 1$ (cf. Fig. 5.6). This is because when the permittivity of the medium and the post are almost equal, the higher-order multipoles are negligible compared to the dipole. This is contrary to Fig. 5.3 (a – c), where a configuration resulting in a lower H_{crit} shows an ideal AR above 1.

5.5 Conclusion

To conclude, in this section the particle trapping behavior of single polarized posts as a function of key operational and design parameters was discussed. This helps for the development of dielectrophoretic separation processes that are based on particle trapping in porous media. For a simpler description of the trapping mechanics, the porous medium is approximated by an array of quasi two-dimensional posts.

Particles are flowing through the post array at velocity v_F and the analysis focuses on a single particle around a single post. The separation efficiency of a single post was described by the critical initial distance that a particle can have from the post but still be trapped, H_{crit}, or the smallest trappable particle size at a constant distance, $d_{P,crit}$.

The separation efficiency as expressed by H_{crit} (Fig. 5.3) increases with increasing applied field strength E_0 and particle size d_P and decreases with fluid velocity v_F. Further H_{crit} increases with the post dimension d_S but not linearly so that H_{crit}/d_S decreases with increasing d_S. Surprisingly the influence of post's cross-sectional shape (ellipse vs. diamond and aspect ratio) is very small compared to the influence of all other parameters. Additionally, in most cases, ellipses with aspect ratios close to 1 are preferably except for cases where the separation distance as expressed by H_{crit} or H is much smaller than d_S (Fig. 5.4).

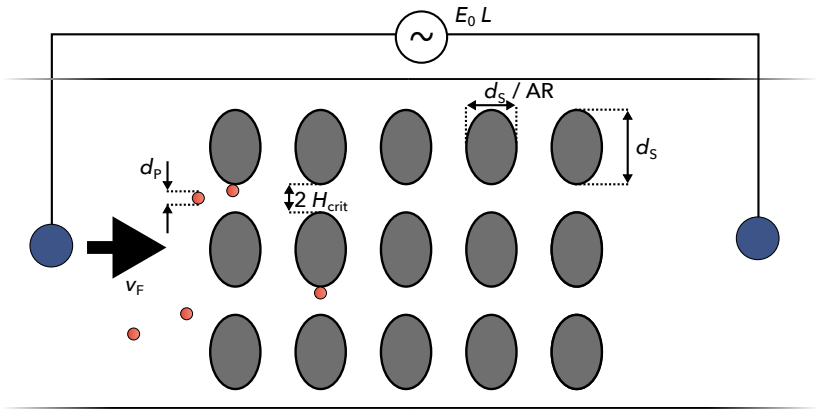

Fig. 5.7: Example of a flow channel containing an array of posts with all the key parameters labeled (oriented with a 90° counter-clockwise rotation compared to Fig. 5.1).

A sensitivity analysis (Fig. 5.5) shows the sensitivity of the solution towards the target value H_{crit}/d_S which could be understood as the normalized trapping reach (efficiency) of the post. The sensitivity is equal towards E_0 and d_P (strong influence) and equal towards v_F and d_S (weaker influence). When looking at the sensitivity coefficients, the aspect ratio has almost no influence. Fig. 5.7 shows a summary of these parameters in the post array.

A large H_{crit}/d_S is desirable because it yields high separation efficiency while maintaining a high void fraction (thus resulting in a low pressure loss in a real separation process). From these dependencies it is possible to learn, that there is no way to scale a separation process by changing only throughput v_F and system size d_S because due to the equal sensitivity towards both parameters, this will always affect the separation quality. When d_P is constant, a scale-up or down is always accompanied by a change in E_0 when the separation quality is supposed to be constant. A change in the separation problem (a change in the particle size d_P) can be compensated by a reciprocal change in E_0.

Concerning the post geometry, it appears that its influence is negligible, which was not expectable from the literature on that topic (cf. Sec. 2.14.3). In addition, sharp corners as field traps (as they would be usually found at pore windows in real porous media) appear to be more efficient in trapping particles *only* if the pore size (as expressed by H_{crit}; when shooting for an almost 100 % separation efficiency, H_{crit} represents the possible pore size) is much smaller than the solid fraction of the filter medium (as expressed by d_S). This would result in a "radial" porosity (perpendicular to the flow direction) ϵ_r below 50 %. This is reasonable for most iDEP applications in which the post spacing is much smaller than the post dimension. In real porous media one often encounters open porosities above 60 % which corresponds also to the requirement of a large H_{crit}/d_S. Hence, sharp corners in the porous layer should be avoided for optimized trapping. Additionally, the separation efficiency increases with decreasing d_S which indicates that, in a real separation processes, a very fine solid matrix with slender (small d_S) struts is beneficial.

The next step is an experimental validation of the dependencies derived in this section. Backing single post-single particle studies with experimental results is a very challenging tasks since the uncertainties in the measurement are higher than the differences that are supposed to be shown. In the next section, an finite element simulation of an entire flow-channel is presented. From this, it is possible to derive the parameter influence in a real-life scenario and compare the results to the idealized parameter influences presented here. Additionally, in the next chapter some of the results are backed by experimental data using actual microchannels made from PDMS.

6 Dielectrophoretic particle trapping in a model porous medium

> *The truth is, the science of nature has been already too long made only a work of the brain and the fancy: It is now high time that it should return to the plainness and soundness of observations on material and obvious things.*
>
> **— Robert Hooke**

Differently from the results presented in the previous two chapters, this chapter investigates the entire (still simplified) filtration system, not only single posts (as schematically outlined in Fig. 5.7). To do so, the fluid flow, electric field distribution and particle trajectories in a microchannel containing an array of insulating posts are simulated using the commercial FEM package COMSOL Multiphysics®. From the simulations it is possible to derive particle separation efficiencies (fraction of particles that is kept in the filter) as a function of geometrical and operational parameters (post size, post spacing, applied voltage, volume flow, …). The simulated separation efficiencies will be compared to the conceptional trapping efficiency H_{crit}/d_S that has been introduced in the last chapter to highlight the similarities and differences between the two approaches.

Further, the calculated separation efficiencies will be compared to actual separation efficiencies that have been obtained by experiments with microfluidic channels. This comparison allows to show how well it is possible to predict separation efficiencies by simple calculations and at which point and why these approaches fail. The experiments also serve as an illustration of the real-life processes occurring during DEP filtration.

Interestingly, it is the self-proclaimed aim of this thesis to scale-up a DEP separation process and thus to go *away* from microchannels. Nonetheless, this chapter investigates particle trapping in microchannels. This is because the typical dimensions of pores in porous media that could be applied in DEP filtration agree favorably with the post spacing and post sizes usually found in microfluidic channels. Microchannels allow a direct observation (due to their transparency) with a microscope and are very well-defined. This makes the analysis much easier compared to actual random structures.

6.1 Materials and method

A more detailed description of the simulation approach, the microchannel fabrication, the experimental setup, and the downstream video evaluation can be found in Appendix E.

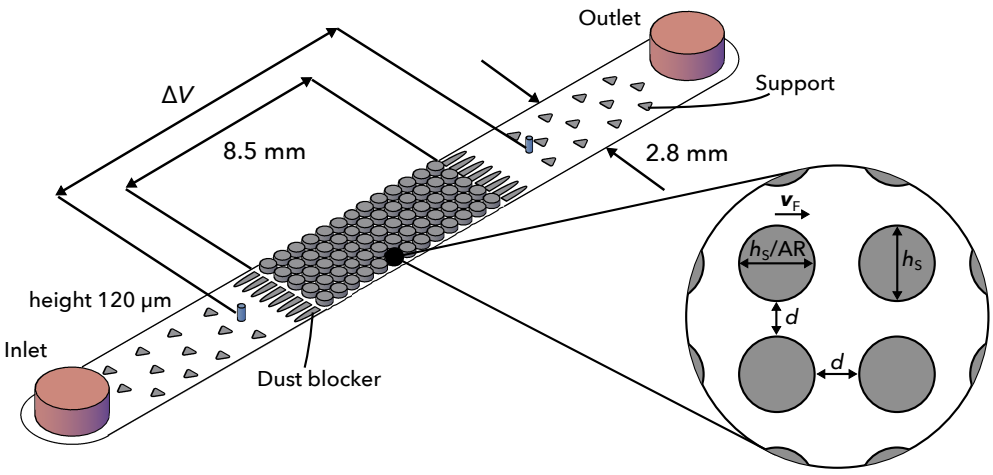

Fig. 6.1: Schematic drawing of the PDMS microfluidic channel employed in this study. The post array is positioned in the center of the channel and has a length of 8.5 mm. The dust blockers (that prevent clogging of the channel) and support structures (that prevent the channel from collapsing) have not been extruded in the graphic because they only serve supporting purposes. The voltage ΔV (and the resulting field) is applied across the array (incl. the dust blockers approx. 12 mm) by two platinum electrodes (blue). Fluid input and output is realized with PTFE capillaries (red). The channel is produced using the same mask as Kawale et al. (2017) with standard soft lithography techniques.

6.1.1 Microchannel and experimental setup

Fig. 6.1 shows a microfluidic channel as employed in the experimental study. The channels are made of polydimethylsiloxane (PDMS), produced with standard soft lithography techniques Duffy et al. (1998). The device is similar to the one employed by Kawale et al. (2017) in a study on flow of polymer solutions in model porous media. The post array of length 8.5 mm is positioned in the center of the channel. In front and in the back of the array half-elliptic posts are employed to avoid clogging of the channel due to any dust that has been entrapped in the device during production. Including the dust blockers, the array has a length of 12 mm. Triangular support structures are positioned in the remaining channel to keep it from collapsing. Holes of different sizes have been punched for the electrodes, the inlet, and the outlet using razor sharp biopsy punches. The channel has a width of 2.8 mm and a final height of approx. 120 µm.

The electric field is applied across the array using two 500 µm diameter platinum wires that are connected to an ac high-voltage source (Trek PZD2000A). Fluid input is realized using a syringe pump (kdScientific Legato® 270, loaded with 3 mL disposable syringes) and PTFE tubing (ID/OD 300 µm/1.6 mm, Kinesis). To calculate the separation efficiency, the particle flux into and out of the post array has been observed using an upright epifluorescence microscope (Carl Zeiss Axio Scope.A1 Vario equipped with a Lumenera Infinity 3S-1URM camera).

Standard monodisperse polystyrene particles have been employed; 1 µm, COOH-modified, fluorescent (Fluoresbrite® YG, ex/em 441/487; roughly FITC) micro particles in aqueous solution have been purchased from Polysciences Europe. The stock solution has been diluted to a final concentration of 2×10^5–8.5×10^5 particles mL^{-1}, depending on the flow rate employed.

The conductivity has been adjusted using KCl to a value of $3.7 \times 10^{-4}\,\mathrm{S\,m^{-1}}$. A homeopathic amount of Tween® 20 (0.05 vol%) has been added to the solution in order to avoid unspecific adsorption of the microspheres on the PDMS surface.

As shown in the inset of Fig. 6.1, the posts have been arranged in the array so that they always have the same spacing in x and y direction (when observed from the top of the channel). Mostly circular posts of diameter $h_S = 263\,\mu\mathrm{m}$ have been employed. For some experiments, elliptical posts have been employed with the major axis aligned perpendicular to the flow direction. The major axis then has a dimension of $h_S = 263\,\mu\mathrm{m}$ whereas the minor axis has a dimension of h_S/AR, where AR > 1 is the aspect ratio (as defined previously).

6.1.2 Experimental procedure

Each data set was obtained using four different channels (with the same geometry). Since PDMS channels experience hydrophobic recovery after bonding (due to aging) they are flushed with ethanol before use to achieve full wetting of the inner surface. Then, the particle suspension is filled in the channel; before first use, each channel was flushed for 10 min with particle suspension. Then, for each voltage and flow rate combination, three videos where recorded at the inlet, more precisely, the section of the dust blockers on the inlet side, for a duration of 70 s (to obtain the particle flux into the channel while the field is activated, which might be different from the undisturbed flux) and at the outlet for a duration of 100–160 s each (depending on the flow rate). After each video the flow has been increased to $10\,\mathrm{mL\,h^{-1}}$ for 10 s to flush trapped particles out of the channel. Particle fluxes have been calculated using an in-house MATLAB program that is able to detect particle centers on a dark background due to their gray value difference.[1] The Hungarian Linker algorithm[2] is used to create particle tracks. The separation efficiency is calculated as

$$\eta = \frac{\dot{n}_{\mathrm{in}} - \dot{n}_{\mathrm{out}}}{\dot{n}_{\mathrm{in}}} \tag{6.1}$$

where $\dot{n}_{\mathrm{in}}$ is the particle flux in the channel and $\dot{n}_{\mathrm{out}}$ is the particle flux out of the channel. Both fluxes have been obtained in the last 20 s of the recorded video because at this time the flux is stationary (thus time-independent). The particle influx decreases slightly after turning on the field (because particles could be trapped at the electrode before entering the channel). Because of this, the outlet side has to be recorded longer until a stable flux can be observed. For the smallest flow rate and the largest post-to-post distance it took approximately 120 s until the flux is stable, whereas for the highest flow rate and the smallest post-to-post distance it took only 50 s.

Separation efficiency is calculated by averaging over the total of 16 values (4 channels with 3 inlet-outlet video pairs each) that have been recorded for each geometry, voltage, and flow rate pair.

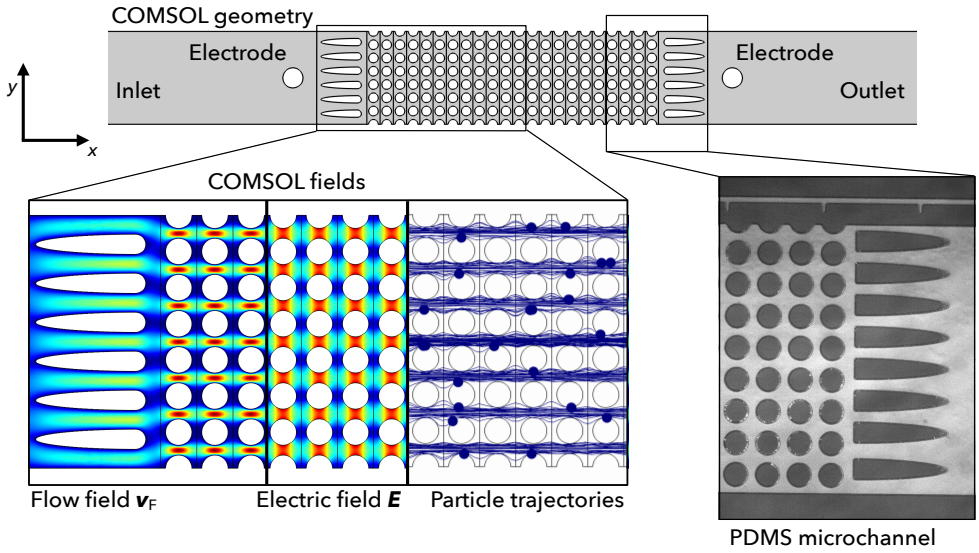

Fig. 6.2: Sketch of the geometry as simulated by COMSOL. The microchannel is two-dimensional and shows a similar cross-sectional geometry as the actual microchannels for experimentation. The inset shows a surface plot of the volume flow $\boldsymbol{v}_F$, the electric field $\boldsymbol{E}$, and a number of particle trajectories exported from COMSOL. The inset on the right shows, for comparison, a bright-field microscopy image of the actual PDMS channel.

6.1.3 Simulation

A similar looking geometry has been modeled in two dimensions in COMSOL Multiphysics® (cf. Fig. 6.2). The channel differed in width (2.8 mm for the experimental channel and approx. 2.5 mm, depending on the spacing and the post diameter, for the COMSOL channel); an adjustment of the flow rate in the simulation accounts for this difference so that both geometries experience the same superficial velocity. Also, the geometry of the dust blockers is slightly altered (so they do not show a 90° edge in the simulation); this might cause a slightly reduced (undesired) particle trapping at the edge of the dust blocker.

The velocity distribution, $\boldsymbol{v}_F$, and the electric field distribution, $\boldsymbol{E}$, were calculated for the entire channel geometry. The velocity field $\boldsymbol{v}_F$ is obtained by numerically solving the Stokes equation for $\boldsymbol{v}_F$ and the pressure p:

$$\mu_F \nabla^2 \boldsymbol{v}_F - \nabla p = 0, \tag{6.2a}$$

$$\nabla \cdot \boldsymbol{v}_F = 0. \tag{6.2b}$$

[1] based on the DIPimage library, http://www.diplib.org/

[2] Simple Tracker by Jean-Yves Tinevez, https://de.mathworks.com/matlabcentral/fileexchange/34040-simple-tracker

The velocity has been prescribed at the inlet so that it results in a given volume flow Q,

$$\begin{aligned} \boldsymbol{v}_{\mathrm{F,inlet}} &= (u_{\mathrm{in}}, 0)^{\mathsf{T}}, \\ u_{\mathrm{in}} &= Q/A, \end{aligned} \tag{6.3}$$

with the channel cross-sectional area $A = w \times h$, the width $w \approx 2.5\,\mathrm{mm}$ and $h = 120\,\mu\mathrm{m}$ the height. A constant pressure $p_{\mathrm{outlet}} = 0$ is prescribed on the outlet and a no-slip boundary condition, $\boldsymbol{v}_{\mathrm{F}} = 0$, is prescribed on all solid surfaces.

To obtain $\boldsymbol{E}$, Poisson's equation (Eq. (2.6)) is simplified to Laplace's equation (assuming charge-free space, $\rho = 0$):

$$\Delta \Phi = 0. \tag{6.4}$$

The potential is prescribed on the two electrodes, $\Phi_{\mathrm{electrode}} = \pm \Delta V/2$. Neumann boundary conditions are prescribed on all solid surfaces as well as on the inlet and outlet, $\partial \Phi / \partial \hat{\boldsymbol{n}} = 0$, with the normal unit vector $\hat{\boldsymbol{n}}$. Also, $\boldsymbol{E} = -\nabla \Phi$. Since the simulated particles are small ($d_{\mathrm{p}} = 1\,\mu\mathrm{m}$), it is possible to assume that they always move at their terminal velocity (no acceleration). The time-dependent particle position and velocity is then given by (assuming that the point-dipole approximation holds):

$$\frac{\partial \boldsymbol{x}_i(t)}{\partial t} = \boldsymbol{v}_{\mathrm{F}}(\boldsymbol{x}_i) + 2\mu_{\mathrm{DEP}} \nabla \left| \boldsymbol{E}_{\mathrm{RMS}}(\boldsymbol{x}_i) \right|^2. \tag{6.5}$$

where $\boldsymbol{x}_i = (x_i, y_i)^{\mathsf{T}}$ is the position vector of the i-th particle ($i \in [1, n]$, n is the total number of investigated particles). The DEP mobility is as before $\mu_{\mathrm{DEP}} = \left(d_{\mathrm{p}}^2 \varepsilon_{\mathrm{m}} \mathrm{Re}\left[\tilde{f}_{\mathrm{CM}} \right] \right) / 24 \mu_{\mathrm{F}}$ and the 2 is introduced to account for the RMS value of $\boldsymbol{E}$, because μ_{DEP} is defined for the $\boldsymbol{E}$-amplitude. For each simulated dataset, $n = 250$ particles were simulated that have been randomly distributed over the entire micro channel depth on a straight vertical line between the electrode and the dust blockers. That means particles were added to the fluid stream (initialized) well after the inlet; this significantly reduces simulation time because the unimportant part of the trajectory (from the inlet to the post array) is skipped. Each calculation was then performed three times with different random starting positions (on the initialization line) and subsequently averaged.

The simulation is two-dimensional and assumes particles of negligible volume, thus only traces particle centers. The acting forces due to DEP and drag were calculated assuming values at the particle center. As before, the flux is calculated according to Eq. (6.1). Mesh independence was investigated by changing the maximum element size between the posts by one order of magnitude in each direction. The separation efficiency (which is the target value) was not affected by that change, indicating mesh independence of the solution. The same holds for the number of simulated particles, the number of repetitions, and the relative tolerance of the time-dependent solver in COMSOL when these values were changed by significant amounts.

6.1.4 About measurement uncertainties

Both, experimental and simulated results, show uncertainties. The simulation has been averaged over three runs per parameter set (using a random distribution of the particles on a vertical line). The uncertainties are very small and not plotted to avoid confusing figures.

The experimental results show larger uncertainties. To cope with that, each parameter set has been investigated using four independent channels and three videos per channel have been recorded (resulting in a total of 16 values). The uncertainties have been calculated by first taking the mean for each channel and then averaging these means over the four channels. The uncertainties arise from the averaging over the four channels (as the uncertainties due to error propagation are much lower). In all plots the error bars indicate one standard error (in each direction). This means, that with a 67 % chance the actual mean is in that interval. One standard deviation, that is the interval in which the next recorded value falls with a 67 % chance, is double the standard error interval (for a sample size of 4).

6.2 Results

6.2.1 Experimental observations

Under absence of an electric field the particles move through the channel *relatively* unaffected. That means, in rare instances particles become trapped on the PDMS surface; this was at no time observed but instead some immobilized particles could be found on surfaces after using a channel for some time.

When the electric field is turned on, particles start to accumulate on the surface of the post at the points perpendicular to the flow and field direction. The particle accumulation is obvious from the appearance of bright spots (cf. Fig. 6.3) but it is not possible to tell of how many particles a single bright spot is composed. With increasing duration, more and more bright spots appear on the posts. Particles preferentially accumulate slightly above or below the narrowest points. When the field is turned off, the particles readily desorb from the surface and are re-entrained by the fluid. Depending on the throughput it could take up to a minute until all particles are re-suspended in the fluid flow. Especially at high flow rates, particles are not safely immobilized on the surface of the post but sometimes start to hop along from one post to the next. This effect is linked to a low separation efficiency.

From optical observations it appears that the particle accumulation is lower at lower frequencies and increases as the frequency increases (cf. Sec. 2.10.8). The output frequency of the employed high-voltage ac system is limited by the slope of the current (with respect to time) trough the system (eventually this will cause a decrease of the applied voltage when the frequency is too high). To avoid this, a frequency of 15 kHz was chosen as a trade-off.

6.2.2 Comparison of experiment and simulation: Clausius-Mossotti factor

The only unknown for the simulation is the $\mathrm{Re}\left[\tilde{f}_{\mathrm{CM}}\right]$. As outlined in Sec. 2.10.8, in aqueous suspension the polarizability of polystyrene particles is dependent on the surface conduc-

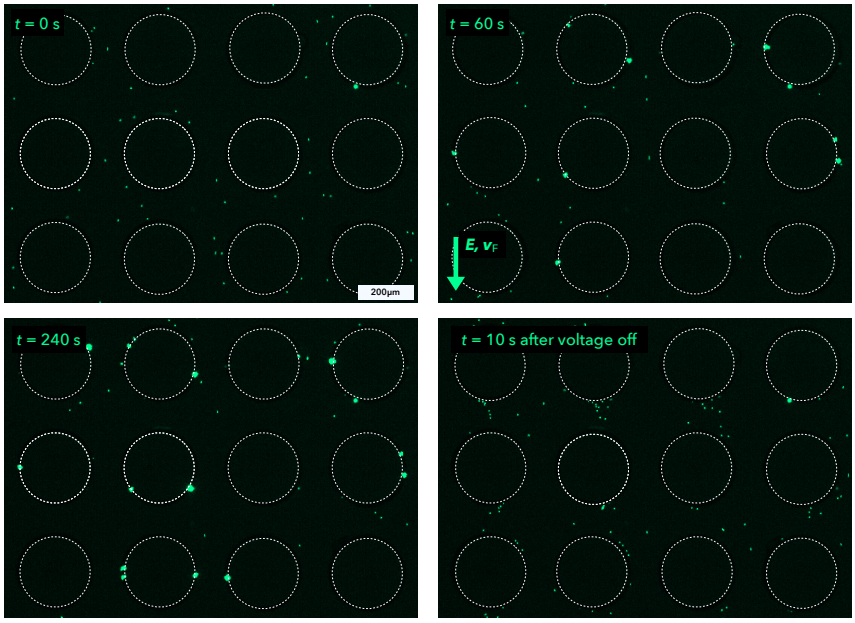

Fig. 6.3: Accumulation of 1 µm fluorescent microspheres in an array of insulating posts due to dielectrophoresis. The electric field is applied from top to bottom, which is also the main flow direction. With increasing time (from $t = 0$ to $t = 240\,\mathrm{s}$) more and more particles accumulate at the preferential trapping spots. This can be inferred from an increasing number of of bright spots that appear on the post's surface. Each bright spot appears to be composed of more than one particle but it is not possible to determine the exact number. After switching off the field, the particles readily desorb from the post (lower right panel shows the situation 10 s after the field is turned off). Array with $d = 100\,\mu\mathrm{m}$ spacing and $h_S = 262\,\mu\mathrm{m}$ post diameter, $\Delta V = 1050\,\mathrm{V_{RMS}}$, $Q = 0.1\,\mathrm{mL\,h^{-1}}$.

tance K_S, which is highly dependent on the material and its functionalization. A crude (manual) fit of the simulations through all available experimental data sets yields $\mathrm{Re}\left[\tilde{f}_{\mathrm{CM}}\right] = 0.5$ for a particle of $d_P = 1\,\mu\mathrm{m}$. When a surface conductance of 1 nS (Ermolina and Morgan, 2005) is assumed and the bulk conductivity of PS to be negligible, $\sigma_{PS} = 0$, the calculated $\mathrm{Re}\left[\tilde{f}_{\mathrm{CM}}\right]$ is 0.76. However, the surface conductance might as well be lower, as shown by Wei et al. (2009) who observed much lower cross-over frequencies compared to Ermolina and Morgan (2005) or as experimentally shown by Romero-Creel et al. (2017). Hence, $\mathrm{Re}\left[\tilde{f}_{\mathrm{CM}}\right] = 0.5$ appears to be a valid assumption.

6.2.3 Comparison of experiment and simulation: Influence of the applied voltage

For a given geometry (d and h_S) and particle size (d_P), the separation efficiency is a function of the applied voltage and the throughput through the channel (cf. Fig. 6.4). As expected from Chapter 5 and Fig. 5.5 a, with increasing applied voltage, the separation efficiency increases whereas with increasing throughput, the efficiency decreases. The comparison between the experimental results and the simulations is quite remarkable under the light that only a single fitting factor was employed (which takes a justifiable value): This is, to the best of the author's knowledge, the first time that the separation efficiency of insulator-based DEP devices has

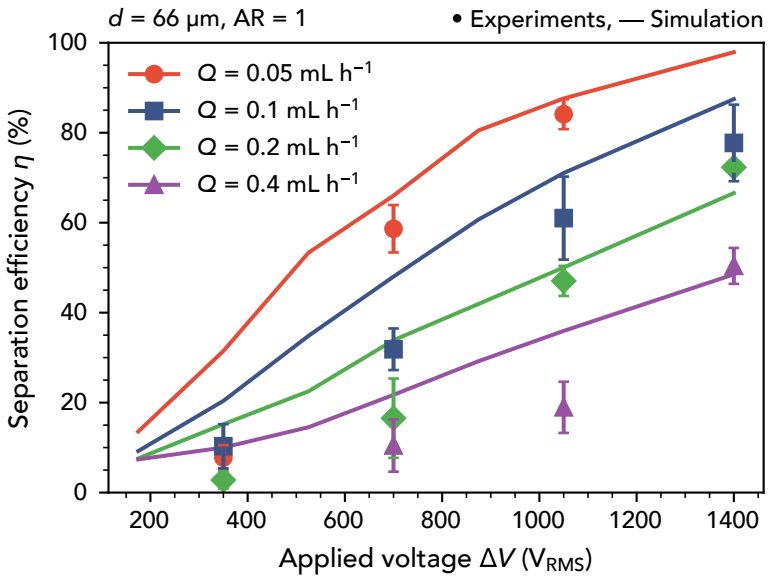

Fig. 6.4: Separation efficiency η as a function of the applied RMS voltage ΔV for four different throughputs $Q = 0.05$–$0.1\,\mathrm{mL\,h^{-1}}$ and a channel with $d = 66\,\mu\mathrm{m}$ distance and $h_S = 262\,\mu\mathrm{m}$ post size. Particle size is $d_p = 1\,\mu\mathrm{m}$. Lines show simulation results and points experimental data. The error bars show the standard error of the four mean values from the four independent channels (each channel's mean is due to three videos taken per channel and the error bar only shows the error of the mean of the four channels' means).

been described employing single particle trajectories. Commonly in iDEP (quite sophisticated) qualitative comparisons between optical observations and simulated results are based on the trapping coefficient; however, this coefficient relies on a correction factor that might be as high as 1000 in order to match the trapping bands commonly found in iDEP devices. In contrast, the presented method does not require a correction factor in order to deliver accurate results. It appears that especially at high voltages and low volume flows the fit is more accurate than at lower voltages and high throughputs.

6.2.4 Comparison of experiment and simulation: Influence of post spacing

When all parameters are constant, the separation efficiency increases with decreasing post spacing d (cf. Fig. 6.5). With smaller d particles pass the post closer (in average). When H_{crit} is the trapping range of a single post, then a decrease in d causes a higher amount of particles to pass the post at a distance smaller than H_{crit}, which increases the predicted trapping efficiency. In reality, this only holds for large d. For $d = 160\,\mu\mathrm{m}$ and (mostly) $d = 66\,\mu\mathrm{m}$, the experimental results match the simulations very well. For $d = 38\,\mu\mathrm{m}$ the simulations generally over-predict the observed separation efficiency. This discrepancy increases with flow rate (difference between experiment and simulation is larger for $Q = 0.4\,\mathrm{mL\,h^{-1}}$ than for $Q = 0.1\,\mathrm{mL\,h^{-1}}$ and the difference is non-existent for $Q = 0.05\,\mathrm{mL\,h^{-1}}$).

All simulated lines show a step in the separation efficiency from $d = 160\,\mu\mathrm{m}$ to $d = 130\,\mu\mathrm{m}$. This is due to the channel generation in the simulation: The channel in the simulation is automatically generated so that the first and last line of posts in y direction is cut in half (hence, the

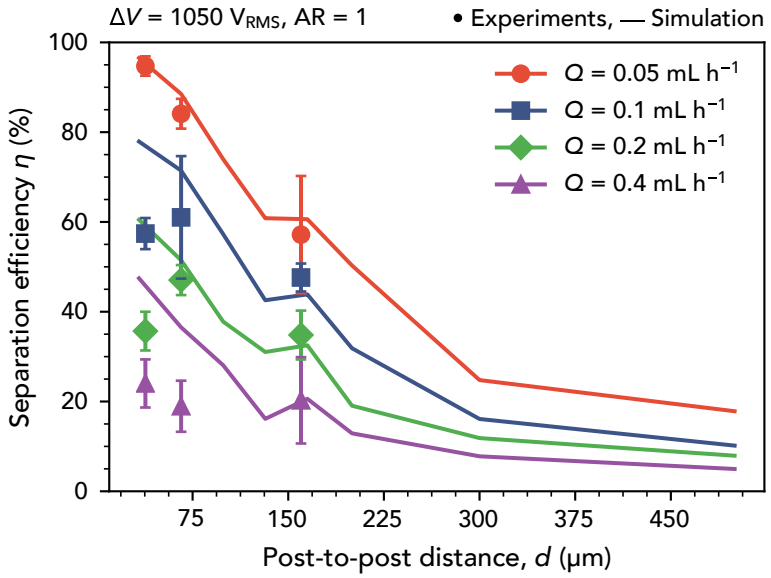

Fig. 6.5: Separation efficiency as a function of post-to-post distance d for four different throughputs $Q = 0.05$–$0.1\,\mathrm{mL\,h^{-1}}$ and an applied voltage of $\Delta V = 1050\,\mathrm{V_{RMS}}$. Post size $h_S = 262\,\mu\mathrm{m}$ and $d_P = 1\,\mu\mathrm{m}$. Lines show simulation results and points experimental data. The error bars show the standard error of the four mean values from the four independent channels.

channel width slightly adapts towards the employed post spacing). From 160 µm to 130 µm the automated routine, to keep constraints on the minimum channel width, increased the number of posts in y direction by one. Then, at $d = 130\,\mu\mathrm{m}$ the number of posts in y direction and the channel width are larger than in $d = 160\,\mu\mathrm{m}$ which causes a slight change in the flow pattern through the channel and causes the kink (the effect is assumed to reduce with increasing total number of posts in y direction, i. e., for wider channels).

6.2.5 Comparison of experiment and simulation: The finite size effect

From the comparison between the experimental results and the simulated predictions it appears that the predictions fail at high throughputs, low voltages or narrow post spacing (or combinations thereof). A possible explanation is that the simulation neglects the particle volume (its finite size). Hence, when particles are immobilized, their final (center!) location will be directly on the post surface. From the no-slip boundary condition for $\boldsymbol{v}_F$ it follows that particles will experience a zero drag force at that location, while at the same time the DEP force is maximum on the surface of the post and drops rapidly with increasing distance.

In reality, particles are located at a center position that is at least $d_P/2$ away from the post's surface and have a finite volume (cf. Fig. 6.6). Then, the drag force and DEP force actually have to be calculated by surface integration for $\boldsymbol{F}_{\mathrm{Drag}}$ and volume integration for $\boldsymbol{F}_{\mathrm{DEP}}$. This results in a different force distribution that might actually cause the particle's detachment from the surface, which has not been considered in the simulation. It only makes sense that this effect increases with decreasing ΔV, increasing v_F, and decreasing d because all three parameter changes cause a shift in the force balance from $\boldsymbol{F}_{\mathrm{DEP}}$ (holding force) to $\boldsymbol{F}_{\mathrm{Drag}}$ (elution force).

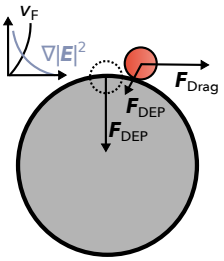

Fig. 6.6: Sketch of the finite size effect. The actual radial particle position is shown in red whereas the radial particle position of an immobilized particle in the simulation is denoted by the black-dotted circle. The qualitative curves of $\nabla |\boldsymbol{E}|^2$ and $\boldsymbol{v}_F$ as a function of the distance from the post are also plotted.

This effect can be quantified by a simple approximation, as shown in Fig. 6.7 a. The forces in x direction, $F_{DEP,x}$ and $F_{Drag,x}$, can be compared on the entire surface of the post (half a particle diameter away from it!). For easy evaluation we quickly define a new coordinate system at the center of the post (r, θ). The radial coordinate is fixed at $r = h_S/2 + d_P/2$ while $\theta \in [0 : \pi/2]$. At $\theta = 0$, $F_{DEP,x}$ is also 0, because the entire DEP force points only towards the center of the post (in $-y$ direction). Obviously then $F_{Drag,x}$ is larger. With increasing θ, $F_{DEP,x}$ also increases until it matches $F_{Drag,x}$ at the intersection angle $\theta = \theta_0$. Hence, particles trapped at $\theta < \theta_0$ should be washed off (because drag dominates over DEP) or move along the post's surface until reaching $\theta > \theta_0$ (where DEP dominates over drag). From observations of Fig. 6.3 it can also been seen that particles preferentially adsorb slightly above or below the narrowest region of the post.

The value of θ_0 is thus a measure of how well the simulation actually predicts the reality. A large value of θ_0 results in a lot of falsely simulated particle trapping, because the simulation predicts particle trapping at locations where trapping is not possible in reality (at least from

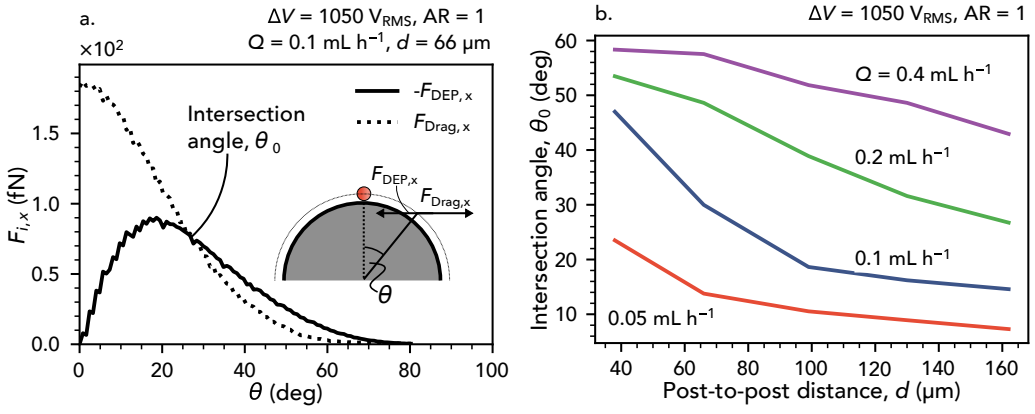

Fig. 6.7: a) Forces in x direction at locations $d_P/2$ away from the post's surface. Depending on the angular location of an immobilized particle (as expressed by θ) it either experiences higher holding forces ($F_{DEP,x}$, large θ) or higher elution forces ($F_{Drag,x}$, small θ). The intersection angle θ_0 is the angle at which DEP becomes dominant over drag and above which trapping should be possible. b) Intersection angle θ_0 for different post-to-post spacings and volume flows.

this simple force balance). As expected, θ_0 is low for low volume flows and large spacings but rapidly decreases with decreasing post-to-post spacing or increasing volume flow (Fig. 6.7 b).

6.2.6 Comparison of experiment and simulation: Influence of the aspect ratio

From Fig. 4.9 (Chapter 4) it is known that the force close to the post increases by several orders of magnitude when the aspect ratio is increased (for a less polarizable post, ideal orientation, …). At the same time, Fig. 5.5 b (Chapter 5) predicts a negligible influence of the AR on the overall separation (compared to other parameters). Technically, it would thus be possible to increase the holding forces (decrease θ_0) at almost constant η by changing the aspect ratio. This was first tested by calculating θ_0 (cf. Fig. 6.8 a) as a function of the aspect ratio at the smallest investigated $d = 38\,\mu\text{m}$ (note that for the evaluation $r = r(\theta)$ is not constant in this configuration but dependent on the angle in order to describe the elliptic surface, cf. ellipse equation in polar form). Indeed, a slight increase in the aspect ratio causes a significant drop in θ_0 so that it reaches the $d = 160\,\mu\text{m}$ value for $Q = 0.1\,\text{mL}\,\text{h}^{-1}$. This drop is more significant at $0.1\,\text{mL}\,\text{h}^{-1}$ than at $0.2\,\text{mL}\,\text{h}^{-1}$. This indicates more favorable trapping conditions.

Four simulations and experiments with two different aspect ratios (AR = 1.25 and AR = 1.67) and two flow rates ($Q = 0.1\,\text{mL}\,\text{min}^{-1}$ and $0.2\,\text{mL}\,\text{min}^{-1}$) were investigated (Fig. 6.8 b). In this case, the number of posts in x direction increases with increasing aspect ratio because the posts become thinner but their tip-to-tip spacing is kept constant. Obviously, for $d = 38\,\mu\text{m}$, the simulated aspect ratio influence is much larger than what was expected from the small sensitivity coefficient (Fig. 5.5 b). This shows that even without considering the finite size effect an increase in AR causes a significantly more efficient trapping. This increasing effi-

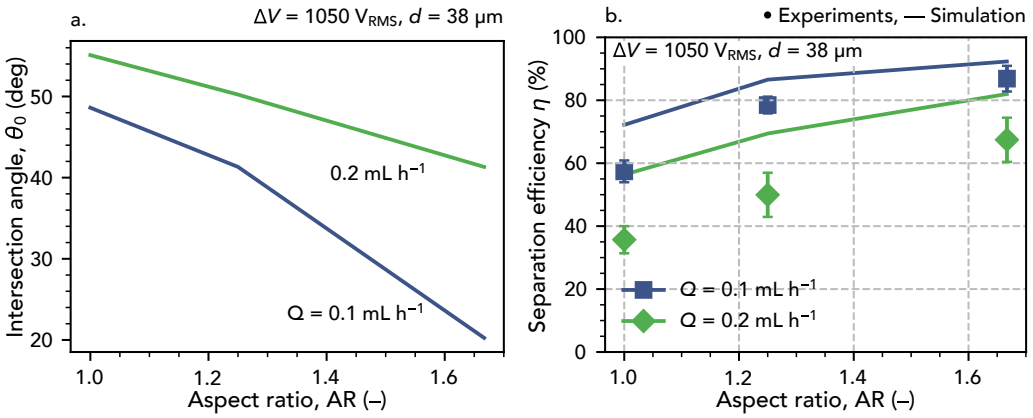

Fig. 6.8: a) Intersection angle θ_0 for two different flow rates ($Q = 0.1\,\text{mL}\,\text{h}^{-1}$ and $0.2\,\text{mL}\,\text{h}^{-1}$) as a function of the aspect ratio of a post array with $d = 38\,\mu\text{m}$ spacing at $\Delta V = 1050\,\text{V}_{\text{RMS}}$. b) Separation efficiency as a function of aspect ratio, AR, for the same throughputs and applied voltage. Lines show simulation results and points experimental data. The error bars show the standard error of the four mean values from the four independent channels. With increasing AR the simulated and the experimental η start to converge. This is more pronounced for the lower flow rate.

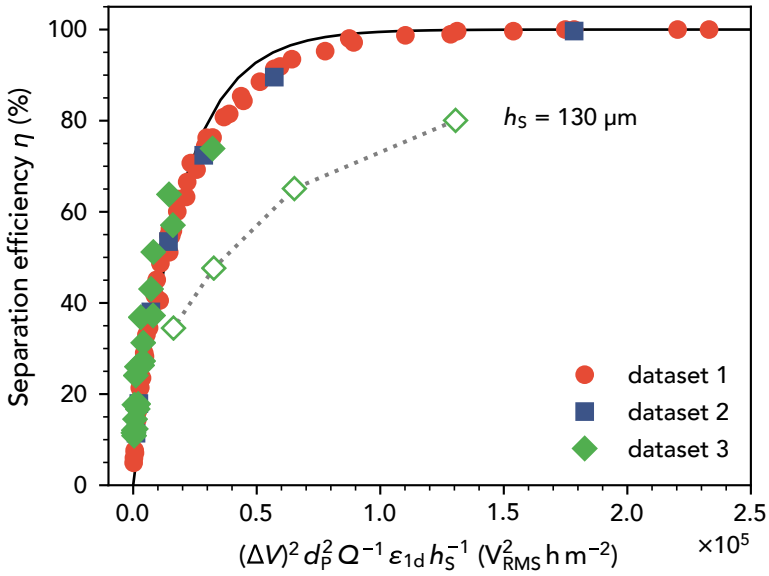

Fig. 6.9: Separation efficiency η as a function of (almost) all parameters employed in this study $(\Delta V)^2 d_P^2 Q^{-1} \epsilon_{1d} h_S^{-1}$ at *constant* post spacing $d = 100\,\mu m$. Since almost all points collapse, the separation is only dependent on one single variable. To obtain a constant η the parameters are interchangeably variable as long as d is kept constant and as long as h_S is sufficiently larger than d. Three different datasets in which different parameters have been changed independently have been used to compile the figure (cf. Tbl. 6.1). The empty symbols denote $h_S = 130\,\mu m$ (from dataset 3, green) which is too close to $d = 100\,\mu m$ so that η deviates from the other values. The black line shows a fit according to Eq. (6.6).

ciency was not predicted and is due to the small spacing. It vanishes for larger d[3]; this is what was expected from the force distribution presented in Chapter 4. Nevertheless, with increasing AR, the experimental results come closer towards the theoretical predictions. This holds especially for $Q = 0.1\,mL\,h^{-1}$ where the $\Delta\eta$ between simulation and experiment is almost 15 % at AR = 1 but only 5 % at AR = 1.67. This is directly linked to the rapid drop in θ_0 from AR 1 to 1.67. The drop in θ_0 is more moderate for $0.2\,mL\,h^{-1}$ and so is the decrease of $\Delta\eta$ which changes only from 20 % at AR = 1 to 15 % at AR = 1.67. It is expected that at higher AR, the θ_0 will also drop for the higher flow rate.

Albeit there might be other wonders at play, the results presented in Fig. 6.8 indicate that the deviation between simulation and experiment is caused by the unfavorable force balance at the surface of the post.

6.2.7 Influence of geometry and operational parameters on separation efficiency

As already shown in Fig. 5.5 a, it makes sense to incorporate the dependence of the separation effieciency on all parameters in one single figure (unfortunately, two figures are necessary). From Fig. 5.5 we know that the trapping effectiveness (H_{crit}/d_S) of a single post is proportional to E_0^2, d_P^2, $1/v_F$, and d_S (which is equivalent to h_S in this study) as long as $d_S > 10H_{crit}$. This is for a single post but the same dependencies hold for the entire post array. This was

[3]This is not shown, but for $d = 160\,\mu m$ a change of AR from 1 to 1.67 causes only an increase in η by less than 5 % compared to the 20 % increase at $d = 38\,\mu m$.

Tab. 6.1: List of the parameters employed in the three datasets that were used to compile Fig. 6.9.

dataset	ΔV	Q	d_P	h_S	d
1	350–4000 V_RMS	0.05–1 mL h^{-1}	1 µm	262 µm	100 µm
2	1400 V_RMS	0.05–0.1 mL h^{-1}	0.2–5 µm	262 µm	100 µm
3	1050 V_RMS	0.05–0.4 mL h^{-1}	1 µm	130–1200 µm	100 µm

tested using three different parameter sets in which several different parameters have been varied independently (cf. Table 6.1). The separation efficiency η is then plotted as a function of $(\Delta V)^2 d_\mathrm{P}^2 Q^{-1} \epsilon_\mathrm{1d} h_\mathrm{S}^{-1}$ (cf. Fig. 6.9). In Fig. 5.5 a, the variable defining the throughput is v_F. Here, instead, the volume flow is given. When h_S changes, then the void fraction changes and thus also the velocity will change (at constant d). The velocity directly between the posts is proportional to the volume flow scaled by the one-dimensional "projected" porosity $\epsilon_\mathrm{1d} = d/h_\mathrm{S}$, which has been introduced to the term defining the separation efficiency. As expected, all datasets collapse on one line.

This means that the separation efficiency (theoretically) only depends on a single parameter, $\eta = \eta\left((\Delta V)^2 d_\mathrm{P}^2 Q^{-1} \epsilon_\mathrm{1d} h_\mathrm{S}^{-1}\right)$ (and shows the same proportionality as $H_\mathrm{crit}/d_\mathrm{S}$). This is only valid if the post-to-post spacing d is kept constant (here, $d = 100\,\mu\mathrm{m}$ was chosen) and as long as the post is sufficiently larger than the post-to-post distance. When h_S and d come close, the separation efficiency deviates towards lower values, as it can be inferred from the labeled points for $h_\mathrm{S} = 130\,\mu\mathrm{m}$, which is quite close to $d = 100\,\mu\mathrm{m}$.

The black line shows a fit based on the equation

$$\eta(\overline{x}) = k_a \left(1 - \exp\frac{-\overline{x}}{k_b}\right) \tag{6.6}$$

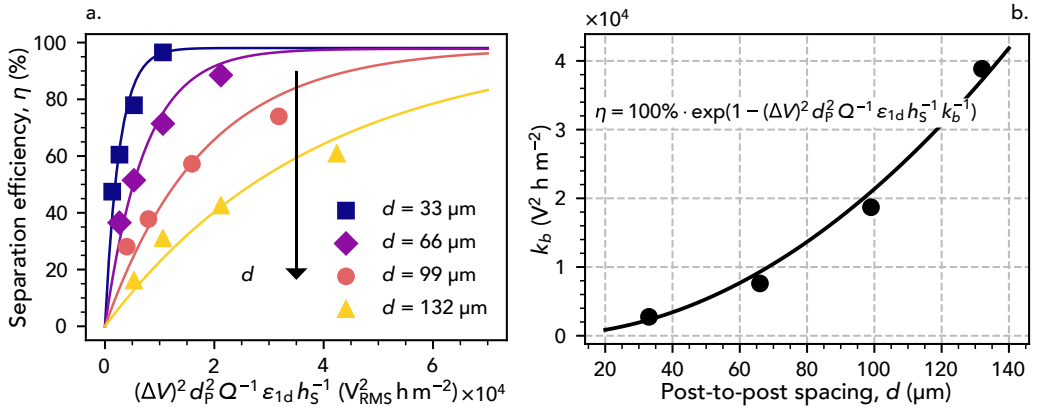

Fig. 6.10: Separation efficiency η as a function of all parameters employed in this study $(\Delta V)^2 d_\mathrm{P}^2 Q^{-1} \epsilon_\mathrm{1d} h_\mathrm{S}^{-1}$ at different post spacing $d = 33$–$130\,\mu\mathrm{m}$ (a). With increasing post spacing, the factor k_b of Eq. (6.6) increases (b). This decreases the responsiveness of η towards a change in the parameters and thus makes the separation less efficient. The fit in (b) is $k_b = a d^2$ with $a = 2.134 \times 10^{-12}\,V_\mathrm{RMS}\,\mathrm{h}^2\,\mathrm{m}^{-4}$.

with the term $\overline{x} = (\Delta V)^2 d_\mathrm{P}^2 Q^{-1} \epsilon_\mathrm{1d} h_\mathrm{S}^{-1}$ which incorporates all the parameters, $k_a = 100\,\%$ and $k_b = 18.93 \times 10^3\,\mathrm{V_{RMS}}^2\,\mathrm{h\,m^{-2}}$. The constant k_b defines how sensitive the system reacts to a change of one of the four key parameters. A variation of the post-to-post distance changes the parameter k_b as indicated by Fig. 6.10. In Fig. 6.10 a the results of Fig. 6.5 for $d = 33\,\mu\mathrm{m}$ up to $132\,\mu\mathrm{m}$ are plotted versus $\overline{x}$ instead of d. An increase in d decreases the η when the other parameters are kept constant. This is because k_b increases with d (Fig. 6.10 b) and thus η becomes less responsive to a change of the parameters $\overline{x}$. This means, when k_b is low, the system reacts fast to a change in the parameters. With increasing k_b the response becomes slower and the system becomes more difficult to adjust by changing the parameters.

The fit through $k_b\,(d)$ is $k_b = a d^2$ ($a = 2.134 \times 10^{-12}\,\mathrm{V_{RMS}}^2\,\mathrm{h\,m^{-4}}$). Thus, with increasing d, the possibility to tune the separation efficiency by a change in the parameters decreases quadratically. This holds until d comes close to h_S at which point these predictions fail. To put in other words: For all d, η is 0 when the parameter combination approaches 0 and η will always reach 100 % when the parameters ($\overline{x}$) are high enough. However, at intermediate values, η will decrease with increasing d.

When plugging ϵ_1d into $(\Delta V)^2 d_\mathrm{P}^2 Q^{-1} \epsilon_\mathrm{1d} h_\mathrm{S}^{-1}$, it yields $(\Delta V)^2 d_\mathrm{P}^2 Q^{-1} d\, h_\mathrm{S}^{-2}$. This means, a decrease in the post size could actually compensate a decrease in particle size or applied voltage one to one. This also means, that the separation can be tuned by decreasing h_S until h_S reaches d or by decreasing h_S and d in concert (decrease in $\overline{x}$ *and* decrease in k_b).

These findings match the results of Čemažar et al. (2016) for a contactless DEP device that have been discussed in Sec. 2.14.3. There, the post size was reduced from 100 µm to 20 µm at constant $d = 60\,\mu\mathrm{m}$ while simultaneously the throughput was increased by a factor of 6. Actually, from the model, a reduction of h_S at constant d should allow an increase in Q by a factor 25. Note, however, that $h_\mathrm{S} = 20\,\mu\mathrm{m}$ is reduced to a value three times smaller than $d = 60\,\mu\mathrm{m}$, thus the fit from Eq. (6.6) will over-predict the actual separation efficiency.

In Sec. 5.3.4 it was discussed that a change in v_F or system size alone is not enough to scale up a separation process, because a change in v_F will require a reciprocal change in post size to compensate and this would cause a reduction of the throughput. In that discussion it was assumed that the number of posts perpendicular to the flow direction is constant (that means, a reduction in post size would cause a reduction in channel size). In contrast, in this study it was assumed that the channel width is constant and that the number of posts adapts to the spacing and post diameter. Because of this it is possible in this study to increase the throughput by decreasing the system size (h_S^2/d). For a separation process employing actual macroscopic porous media, this means, at constant filtration area, the separation efficiency can be increased by an increase in porosity at constant pore size (that is, increase the pores per inch, ppi, but keep the d_pore constant).

6.2.8 Correction of the simulated separation efficiency

In general, Eq. (6.6) together with Fig. 6.10, is sufficient to (theoretically!) describe the separation dynamics in the microchannel. The actually employed proportionality factor a (Fig. 6.10 b) required for calculating k_b in Eq. (6.6), $k_b = a d^2$, depends on the details of the channel (for example channel height and width).

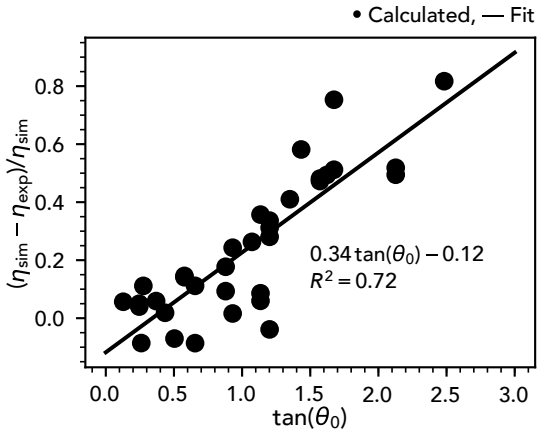

Fig. 6.11: Strictly empirical correlation between the results obtained via experiments and simulations η_{sim}, η_{exp} and the intersection angle θ_0 that gives a rough quantification of the finite size effect. The fit has been obtained with a trial-and-error approach.

To obtain the actual separation efficiency from the theoretical prediction a correction of η in cases where θ_0 is large is required. The concept of θ_0 (Sec. 6.2.5) to quantify the influence of the finite size effect is rather crude. Nevertheless, there might be a correlation between θ_0 and the difference between the simulated and experimental separation efficiency $\Delta\eta = \eta_{sim} - \eta_{exp}$, so that $f\left(\eta_{sim}, \eta_{exp}\right) = g\left(\theta_0\right)$. This would allow to entirely model the separation in the channel without the need to perform any experiments after the correlation has been obtained.

Several definitions for f and g have been tested (not shown) from which $\Delta\eta/\eta_{sim} \propto \tan\theta_0$ appears to show the best correlation (cf. 6.11). This proportionality is entirely empirical and has been obtained manually (that means, by testing several possible combinations until a satisfactory fit was obtained). The data points presented in Fig. 6.11 are compiled from all experimental data points presented so far (in total 35 points). The linear fit through the points yields

$$\frac{\eta_{sim} - \eta_{exp}}{\eta_{sim}} = 0.34 \tan\theta_0 - 0.12, \tag{6.7}$$

so that

$$\eta_{sim,cor} = \eta_{sim}\left(1.12 - 0.34 \tan\theta_0\right). \tag{6.8}$$

The R^2 is rather low, $R^2 = 0.72$.

Using the correlation, a simulated result can be corrected to account for the finite size effect. The 1.12 in the correction term indicates that for very low θ_0 the simulation under-predicts the experimental results, indicating that the first guess of the $\mathrm{Re}\left[\tilde{f}_{CM}\right]$ was too low. The correction according to Eq. (6.8) has been applied to the results of Figs. 6.4 and 6.5 which is shown in Fig. 6.12. As expected, $\eta_{sim,cor}$ matches η_{exp} much better as the uncorrected values. The trend of the four curves as a function of d in Fig. 6.12 b is different from what was expected. Only $Q = 0.1\,\mathrm{mL\,h^{-1}}$ (blue) shows the expected maximum of $\eta(d)$. This might be due to the to smaller number of data points plotted in both directions d and Q (spacing in d is 30 µm). It could also be that not all curves show a maximum due to the complex dependence of θ_0 on all parameters; more data points need to be evaluated to make better informed statements.

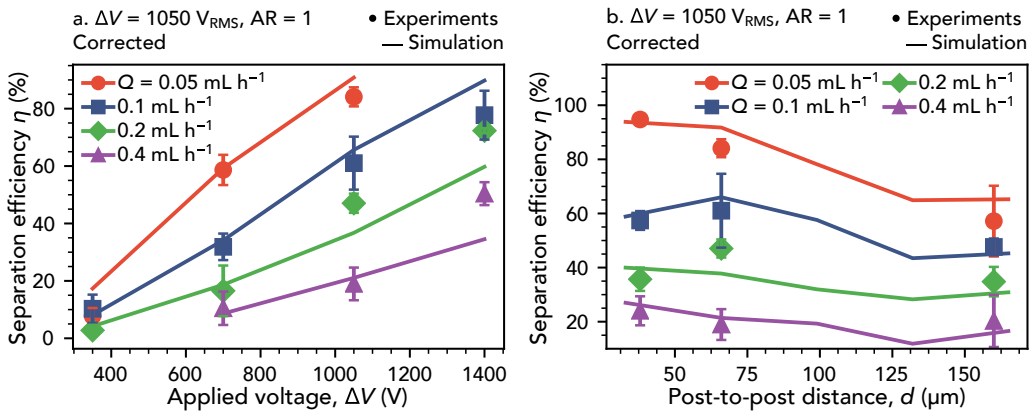

Fig. 6.12: Comparison of simulated and experimental separation efficiencies, $\eta_{\mathrm{sim,cor}}$ and η_{exp}, after correcting the simulated results by employing the correction function Eq. (6.8). The same parameters as in Fig. 6.4 (a) and Fig. 6.5 (b) are employed here.

Obviously, the procedure to find a fit that is based on existing values and then applying this fit in order to correct these values should give much better results than without the fit (as shown). This merely shows that the fitting and correction procedure was applied correctly. In order to test the fit itself it is necessary to apply it on other data points employing different parameters, that were not used before. However, all existing data points have been used to obtain a sufficiently large dataset for the fit. Nevertheless, the mere existence of a fit that relates $f\left(\eta_{\mathrm{sim}}, \eta_{\mathrm{exp}}\right)$ to $g\left(\theta_0\right)$ (irrespective of f and g itself if they are sufficiently simple) indicates that a correction of the simulated η_{sim} by a correction function is possible.

6.3 Discussion and conclusion

This chapter investigated the simulation and experimentation of dielectrophoretic particle retention in microchannels containing a rectangular array of insulating posts as a model porous medium. In most cases it is possible to predict experimentally obtained separation efficiencies with computer simulations based on particle trajectories with the requirement of only a single fitting parameter, $\mathrm{Re}\left[\tilde{f}_{\mathrm{CM}}\right]$, that takes a value that agrees well to values found in the literature. These predictions fail especially at high throughputs Q, low voltage drop ΔV, or narrow post-to-post spacing d, because the simulation neglects the finite size of the actual particle. Especially the finding that with increasing aspect ratio at narrow spacing the predicted and actual separation efficiencies fall closer together (cf. Fig. 6.8 b) due to the increased holding forces of elliptical posts compared to circular posts (as explained in Chapter 4) supports that point.

When the finite size effect is neglected it is possible to describe the separation efficiency in the channel by employing only one variable that is a combination of the important design and operational parameters $\eta = \eta(\overline{x})$ with $\overline{x} = (\Delta V)^2 d_{\mathrm{P}}^2 Q^{-1} \epsilon_{1\mathrm{d}} h_{\mathrm{S}}^{-1}$. In this, all parameters are interchangeable as long as h_{S} is "much" larger than d and as long as d is constant (Fig. 6.9). The separation could then be described by $\eta = 100\,\%\,(1 - \exp(-\overline{x}/k_b))$ where k_b is a parameter that depends on the post spacing d and that defines how responsive η is to a change of the parameters. For this specific microchannel (height of 120 µm and length of 8.5 mm) the relationship between k_b and d is $k_b = 2.134 \times 10^{-12}\,\mathrm{V^2\,h\,m^{-4}}\,d^2$, as long as d is "much" smaller

(it was not tested how much "much" actually is) than h_S. These relationships are similar to the relationships found in the sensitivity analysis (Sec. 5.3.3 and Fig. 5.5). A scale up of the separation process could thus be achieved by an increase in the volume flow. To maintain a high separation efficiency, one of the other parameters has to compensate, for example the applied field strength. It is even possible to increase the separation efficiency by a decrease in the post size h_S until h_S reaches d or by simultaneously reducing h_S and d (this causes a decrease in $\overline{x}$ *and* k_b). It is also possible to compensate a decrease in d_P by a change in Q, ΔV, or h_S, and so on….

In order to find the actual separation efficiency from the simulated results a relationship between some quantification of the finite size effect and the differences in the the separation efficiencies between experiment and simulation must be found. In a very simple manner, the finite size effect can be quantified by the intersection angle θ_0 that defines the point at which the DEP force against the flow direction $-F_{\mathrm{DEP},x}$ becomes larger than the drag force due to the flow $F_{\mathrm{Drag},x}$. In simple words it says at which points particles should stick on the post since DEP dominates and where they should be washed off since drag dominates. It is a measure of how well the calculations describe the actual separation. Using entirely empirical correlations between the calculated θ_0 for all investigated parameters it was possible to correct the simulations to incorporate the finite size effect. Then, the simulated and experimental results agree much better (cf. 6.12). Neither the physical model for the quantification of θ_0 (or even the definition of θ_0 itself) nor the the mathematical correlations are very sophisticated. Nevertheless the mere possibility to find a physical model that could be correlated mathematically indicates that a correction of η_{sim} is possible. Using a more educated quantification of the finite size effect (force balance in both directions x and y and including lift forces) together with an algorithm that finds a correlation between that quantification and the $\Delta\eta$ (instead of the trial-and-error approach employed here) should give much better results. Another approach would be a simulation method that incorporates the particle volume, as for example described by Hossan et al. (2014) or others, which should be independent of any corrections.

The performance of the channels employed here ($\eta = 70\,\%$ at $Q = 200\,\mu\mathrm{L\,h^{-1}}$ and $E_0 = 1400\,\mathrm{V_{RMS}}/8.5\,\mathrm{mm} = 1 \times 10^5\,\mathrm{V_{RMS}\,m^{-1}}$) is rather moderate compared to existing technologies. Even classical iDEP devices that are based on the balance of electrokinetic forces and DEP present higher throughput and much better discriminatory ability at equal field strengths (cf. Tbl. 2.1). The classic electrode-based designs, for example the microchannel for the selective trapping of yeast cells as described by Markx et al. (1994), shows a much higher throughput of $Q = 30\,\mathrm{mL\,h^{-1}}$ at much lower applied voltage. As already discussed extensively, such classical electrode-based designs will always be limited to smaller overall sample sizes (are limited in their scale-up possibilities) because the channel must not be too large so that particles will always pass the electrode array at small distance. Also, since the electrodes and the target particles are in the same order of magnitude, the array will be crowded with trapped particles sooner or later, which will reduce the overall separation efficiency due to electrode fouling. The microchannels employed here are merely a model for a more complex, random filter that has macroscopic dimensions and that is too opaque to look into. Typical characteristic dimensions of the pores of such filters are in the same range as the typical post-to-post spacing and post size

in microfluidic channels, which makes microfluidics an excellent tool for the detailed investigation and observation of particle trapping dynamics. It is believed that the relations learned from this study, especially Fig. 6.10 in combination with Eq. (6.6), are equally applicable in real filtration processes.

Conclusion and outlook

7

> *You can't possibly be a scientist if you mind people thinking that you're a fool.*
>
> **— Douglas Adams**
> (So Long, and Thanks for All the Fish)

The proclaimed overall goal set by this thesis is the establishment of an industrial scale separation process based on dielectrophoresis with application in technical or industrial separation problems. This is contrary to the typical applications of dielectrophoresis that are (nowadays) mostly based on microfluidic chips and focus on analytical or bio-analytical separation or detection problems. Instead, it is the aim of our working group to establish a separation process that could be applied everywhere where conventional separation methods are either to expensive, too tedious, or impossible to apply (cf. Chapter 3). Dielectrophoresis is a very suitable technique because it does not require labeling and, if applied correctly, is highly selective (cf. Sec. 2.13).

One way of applying DEP in high-throughput processes is the dielectrophoresis-driven particle retention in porous media. This retention relies on the electric field distortion at the material boundaries in the porous medium. The concept was pre-existing to this thesis (cf. Sec. 2.14.4) but was tested here for the first time using monolithic foams as separation matrix (which are easier to handle and show a lower pressure drop). Preliminary results on the separation of Layer-by-Layer produced nanocapsules were very promising (cf. Secs. 1.4 and 1.5) but did show room for improvement, especially in the selection of a suitable filter as matrix. Since—if not especially designed for that purpose—filters are usually opaque the dynamics inside of them can only be observed using imaging techniques such as X-ray tomography (CT) or magnetic resonance imaging (MRI), as explained by Günther and Odenbach (2016) and Huang and Ou-Yang (2017). The time resolution of these methods is limited and it poses several restrictions on the employed materials and setup sizes. Here, the dielectrophoretic particle retention in porous media is investigated by employing model porous structures which have approximately the same geometrical features as the real (random) porous media. In this work, an array of quasi two-dimensional posts with different cross-sectional geometries was chosen as a model (see for example Fig. 4.1 of Chapter 4). The cross-sectional geometry of each post (its base geometry and aspect ratio, cf. Fig. 4.2 a) is supposed to represent actual features of the porous medium. With this approach it is much easier to describe the separation process because of the clearer definition of such a post array compared to random porous media.

The overall approach of this thesis shall be summarized here again(cf. Sec. 1.6 and Fig.1.4). The model porous medium is decomposed into single posts. In Chapter 4 the polarization of a single post was theoretically investigated as a function of its cross-sectional geometry and relative polarizability, to obtain a better understanding on the influence of its boundary shape and material on the field distribution around it. It was, for example, possible to learn how to adequately align a post with non-equal cross-sectional width and height in an electric field

depending on the posts polarizability in the suspending medium; or that the force distriubtion as a function of the distance from the post becomes much steeper (larger force close to it, lower force far away from it, cf. Fig. 4.9) with increasing deviation of AR from one. The semi-analytical expression of the field distribution from Chapter 4 (Eq. (4.1)) was further used to derive calculated trajectories of particles in the vicinity of the post that are subject to DEP and drag forces (cf. Chapter 5). From these trajectories one can quantify the effectiveness of a given post for particle trapping. Either by a critical initial distance a particle could have from the post in order to become trapped from a fluid stream or by a minimum particle size that could be trapped by the post at a given distance. The variation of these two target values was used to identify key parameters that influence the separation process (cf. Fig. 5.5). This delivered guidelines on how to effectively design the porous medium for particle retention and how it is possible to tune the overall separation process. These design guidelines were subsequently tested in an experimental separation process employing microfluidic channels (cf. Chapter 6). Microfluidic channels have been employed because the size range of the model porous medium fits excellently into the range of characteristic dimensions usually employed in microfluidics.

It was further tested how adequately the microfluidic experiments could be predicted by integral simulations of particle trajectories in the channel using the well-known software package COMSOL. In general, the simulations predict the experiments well but tend to over-predict at high throughput, low voltage, or narrow post spacing. This could be attributed to the finite size effect that was neglected in the simulation (which only calculated mass- and volume-less particles). It was possible to physically quantify the finite size effect. From this, a purely empirical correction function was established with which separation efficiencies can correctly be predicted without any further knowledge (cf. Fig. 6.12). In a specific microchannel the separation efficiency is only a function of a single variable $\overline{x}$ that incorporates all the geometrical and operational parameters which are then interchangeably variable (cf. Fig. 6.9). Interestingly, the four key parameters, throughput, applied field strength, particle size, and post size are in the same relation in $\overline{x}$ as in their influence on the trapping effectiveness of a single post (Fig. 5.5 a). The application of a fit function for η as a function of $\overline{x}$ (Eq. (6.6)) together with the parameter k_b taken from Fig. 6.10 b is sufficient to predict a separation efficiency in the model porous medium (at least theoretically). This separation efficiency could then be corrected by the previously derived correction function (to account for the finite size of the particle).

Obvious from Chapter 6, the parameter selection as well as the discussion and interpretation of the resultswas often helped by going back to the chapters that described the polarization of single posts and the particle trajectories around them. This was especially true for the influence of the aspect ratio on the DEP force (Fig. 4.9) and its influence on the overall separation (Fig. 5.5 b) which helped to support the concept of the finite size effect (Fig. 6.8). Also, the influence of the four key parameters on $H_{\mathrm{crit}}/d_{\mathrm{S}}$ in Fig. 5.5 was used to compose the term $\overline{x}$, which enabled to use only a single variable to describe the entire separation process. This ultimately justifies the approach taken in this thesis: that is, starting off with the simplest possible unit of a very complex system and gradually increase its complexity until reaching the final system. Of course it would have been possible to directly start simulating and experimenting with the entire system (be it microfluidic or even real filters). Then, basic descriptions of polarization

and particle dynamics in those systems would not have been especially addressed. This would have ultimately decreased the amount of knowledge gained from an analysis of the results It is the most profound aim of science to create knowledge and to gain deeper understandings of processes, and not to find mere correlations. Albeit this thesis will be (or has been) submitted to acquire a doctor of engineering, it is probably the author's wish to approach a problem from a very scientific point of view by trying to understand all the basic phenomena before increasing the complexity.

At this point in time, a setup that allows the observation of particle motion and their retention exists (Fig. 6.1). Further, using the equations from Chapter 6 or more FEM simulations it is possible to predict the separation efficiency in these channels with good accuracy. It is believed that the correlation, $\overline{x} = (\Delta V)^2 d_{\mathrm{P}}^2 Q^{-1} \epsilon_{1\mathrm{d}} h_{\mathrm{S}}^{-1}$, is equally applicable (at least to a certain extend) to predict the separation efficiency in real porous media. As discussed before, the overall aim is to establish an improved DEP filtration setup that is based on the early proof-of-principle results (Chapter 1) and that could be used for the separation of sub-micron particles from solution. By the time this thesis is written a (bench-scale) separation setup exists; a thorough parametric study using sub-micron polystyrene particles indicate that our group is on the right track towards an industrial scale separation process. This holds for the retention of a single type of particles from suspension. In fact, as discussed in Chapter 3, one of the key strengths of DEP is the possibility to selectively trap one kind of particle while all non-target particles are not trapped. It is therefore our goal, after studying the influence of all parameters, to use the DEP filter for the selective retention of, as an example, gold from polystyrene particles. The microfluidic separator developed in this thesis not only helps to understand the influence of the parameters on the separation efficiency but it can also be used to test the selectivity of the process towards either gold or polystyrene in their suspension. This can, for example, be achieved by using two different fluorescent stains on both particle types. Then, by switching the light filter set of the microscope, it is possible to independently monitor the accumulation of either gold or polystyrene in the setup. This delivers necessary guidelines for the separation in the macroscopic DEP filter (for example, which field frequency to use, restrictions on the possible particle sizes, and so on). These guidelines are in principle known from literature but DEP separation systems are quite fragile towards the employed parameters. Thus, real-life observations are the ultimate key to fully understand the system's behavior. It is the author's believe that, in order to be able to effectively use a macroscopic setup for the selective retention of a target particle from a particle mixture, knowledge and visualization of the microscopic processes are unavoidable.

Apart from being a stepping-stone towards the construction of a high-throughput DEP separator, it is the author's belief that the results presented in this thesis are a very valuable addition to the dielectrophoresis literature. This holds for the post polarization studies which might as well be used for the design of insulator-based DEP devices. But this is especially true for the results presented in the last chapter, which not only exploit the possibility to use simulations to predict the reality but also offer very simple correlations to calculate the particle separation in porous media.

Finally, it is the author's wish to express his hope that the results presented as well as the papers published in the framework of this thesis, will—one way or another—actually have a purpose, albeit the fundamental approach taken in this thesis. This might be a bold request, but it is possible to argue with an anecdote about the physicist Robert Wilson who, in a 1969 Congressional testimony on the need for a particle accelerator (which, funnily, later became Fermilab, the world's fourth largest particle accelerator until its decommissioning in 2011), was required to a answer the question of a congressmen whether the accelerator would have anything to do with "the security of the country". His answer explains the value of fundamental science, just for its own sake[1]:

"It has only to do with the respect with which we regard one another, the dignity of man, our love of culture. It has to do with: Are we good painters, good sculptors, great poets? I mean all the things we really venerate in our country and are patriotic about. It has nothing to do directly with defending our country except to make it worth defending."

[1] Anecdote based on a blog entry which could be found on https://oikosjournal.wordpress.com/2012/04/05/on-science-for-sciences-sake/

A Multipole potential in cylindrical coordinates (Chapter 4)

Assuming a homogeneous material and charge-free space, Poisson's equation (Eq. (2.6)) simplifies to Laplace's equation:

$$\Delta \Phi = 0. \tag{A.1}$$

The polarization of cylindrical posts in the presence of an external electric field E_0, which is applied perpendicular to the z-axis is studied. The cylinder's height is assumed to be much larger than its radial extension. The geometry is then given in two-dimensional polar coordinates (r, θ) (Fig. 4.2 b).

It is convenient to define two separate domains Ω_1 and Ω_2, which describe the inner part of the post and the surrounding medium, respectively. The domains are separated by $\partial\Omega$ (Fig. 4.2 b). Both domains separately have to fulfill Eq. (A.1).

This yields two separate potentials, the inside and outside potential, ϕ_1 and ϕ_2, respectively, which are only valid in their respective domains. The potentials are coupled at $\partial\Omega$ by (Zangwill, 2013)

$$\begin{cases} \varepsilon_1 \dfrac{\partial \Phi_1}{\partial \hat{\boldsymbol{n}}}\Big|_{\forall(r,\theta)\in\partial\Omega} = \varepsilon_2 \dfrac{\partial \Phi_2}{\partial \hat{\boldsymbol{n}}}\Big|_{\forall(r,\theta)\in\partial\Omega} \\ \dfrac{\partial \Phi_1}{\partial \hat{\boldsymbol{t}}}\Big|_{\forall(r,\theta)\in\partial\Omega} = \dfrac{\partial \Phi_2}{\partial \hat{\boldsymbol{t}}}\Big|_{\forall(r,\theta)\in\partial\Omega} \\ \Phi_1|_{\forall(r,\theta)\in\partial\Omega} = \Phi_2|_{\forall(r,\theta)\in\partial\Omega} \end{cases} \tag{A.2}$$

with $\hat{\boldsymbol{n}}$ being the outward pointing normal unit vector and $\hat{\boldsymbol{t}}$ being the perpendicular tangential unit vector. A separated variable solution for Eq. (A.1) in polar coordinates reads (Zangwill, 2013)

$$\begin{aligned} \Phi(r,\theta) &= (A_0 + B_0 \ln r)(x_0 + y_0\theta) + \\ + &\sum_{n=1}^{\infty} (A_n r^n + B_n r^{-n})(x_n \sin(n\theta) + y_n \cos(n\theta)) \end{aligned} \tag{A.3}$$

with A_0, A_n, B_0, B_n, x_0, x_n, y_0, and y_n being constants, which differ between the inside potential Φ_1 and the outside potential Φ_2. The post is placed in the center of origin and the excitatory electric field of magnitude E_0 is applied parallel to the y-axis, $\boldsymbol{E} = E_0 \hat{\boldsymbol{y}}$. The outside potential has to match the electric potential which is causing the excitatory field as $r \to \infty$, thus

$\lim_{r\to\infty} \Phi_2(r,\theta) = E_0 r \sin\theta$. Additionally, the inside potential cannot be singular as $r \to 0$. By enforcing these boundary conditions as well as the matching conditions (A.2) we find

$$\Phi_2(r,\theta) = E_0 r \sin\theta + \sum_{n=1}^{\infty} \frac{p_n \sin(n\theta) + q_n \cos(n\theta)}{r^n}, \tag{A.4a}$$

$$\Phi_1(r,\theta) = A + B\theta + \sum_{n=1}^{\infty} r^n (v_n \sin(n\theta) + w_n \cos(n\theta)) \tag{A.4b}$$

with A, B, p_n, q_n, v_n, and w_n again being constants. Since the posts have a rotational symmetry with respect to the origin, the resulting electrostatic potentials are odd functions with respect to θ, i. e., $\Phi(r^*, -\varphi) = -\Phi(r^*, \varphi)$. Additionally, we can set $\Phi(r, \pi) = 0$, as Φ is only defined up to an additive constant. In that case A, B, q_n, and w_n vanish:

$$\Phi_2(r,\theta) = E_0 r \sin\theta + \sum_{n=1}^{\infty} \frac{p_n \sin(n\theta)}{r^n}, \tag{A.5a}$$

$$\Phi_1(r,\theta) = \sum_{n=1}^{\infty} r^n w_n \sin(n\theta). \tag{A.5b}$$

Simulation details of multipole extraction method (Chapter 4)

B

The polarization potential of the post has been obtained by performing 2d dimensionless FE simulations in Cartesian coordinates. The post is placed in the center of the rectangular simulation surface of size $L \times L$ (Fig. 4.2 d). The longest dimension of the obstacle is set to 1. A simulation surface size of $L = 50$ turned out to be sufficiently large for the simulation result being independent of the boundary. To simulate the polarization of the obstacle the material-dependent Laplace equation (Eq. (A.1)) has to be solved. Dirichlet boundary conditions are applied at the electrodes (top and bottom),

$$\Phi(x, y)|_{\forall y=\mp L/2} = \pm\frac{E_0 L}{2}, \tag{B.1}$$

whereas Neumann boundary conditions are applied at the insulating boundaries (left and right) of the simulation surface:

$$\left.\frac{\partial\Phi(x, y)}{\partial\hat{\boldsymbol{x}}}\right|_{\forall x=\pm L/2} = 0. \tag{B.2}$$

The applied field is E_0 and $\hat{\boldsymbol{x}}$ represents the unit vector in x direction (i. e., towards the insulating boundary).

An electric field of strength $E_0 = 1$ has been applied in order to excite the obstacle polarization.

Simulations have been performed using the open-source FEniCS project (Alnæs et al., 2014; Alnæs et al., 2009; Kirby, 2004; Kirby and Logg, 2006; Logg et al., 2012b; Logg and Wells, 2010) operated with an IPython (Perez and Granger, 2007) front-end including NumPy and SciPy. The generation of geometry and mesh was obtained by using the open-source tool GMSH (Geuzaine and Remacle, 2009). Four points of minimum mesh size are defined at the four corners of the structure. The mesh was gradually expanded towards the boundaries of the simulation surface. To verify mesh-independent results, the first 1000 multipoles for every structure have been extracted while reducing the maximum mesh size step-by-step at the four points until a stable sum is reached. The final mesh consisted of approx. 2×10^6–4×10^6 elements depending on the geometry and aspect ratio.

The polarization coefficients have been extracted by firstly subtracting the applied potential from the FE result to find the potential caused only by the polarization. In a second step a trapezoidal method for integration (NumPy's `trapz` function) was used to find p_n for different integration radii R.

Example files for GMSH and Python can be obtained from the CD that is accompanying this thesis or by directly contacting the author.

C

Comparison of analytical and simulated trajectories (Chapter 5)

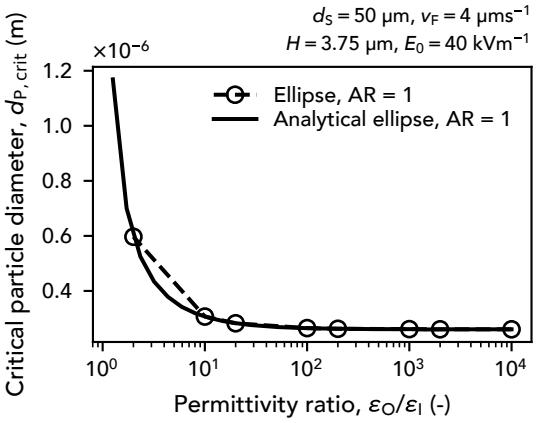

Fig. C.1: Comparison between calculation using multipole coefficients and analytical solution

Figure C.1 shows the critical particle diameter for separation, $d_{\mathrm{P,crit}}$, as a function of the permittivity ratio $\varepsilon_2/\varepsilon_1$ for an ellipse with aspect ratio, AR = 1. The symbols together with the dotted line represent calculations based on the extracted multipole moments (similar to almost all other results presented in Chapter 5) whereas the solid line represents an analytical solution.

The solid black line shows the results of the analysis when the analytical solution for the first-order polarization coefficient of the AR 1 ellipse is put into the $\nabla|\boldsymbol{E}|^2$ term (Eq. (5.1a)) of the equation of motion (Eq. (5.2b)) (Pesch et al., 2016):

$$p_1 = \frac{1-\varepsilon_2/\varepsilon_1}{1+\varepsilon_2/\varepsilon_1} \tag{C.1}$$

The post diameter (or characteristic dimension) d_S is 50 µm, the volume flow $v_F = 4\,\mu\mathrm{m\,s^{-1}}$, the initial y-distance to the tip $H = 3.75\,\mu\mathrm{m}$ and the excitatory field strength $E_0 = 40\,\mathrm{kV\,m^{-1}}$. The analytical solution and the solution due to the coefficients obtained by numerical integration agree very well.

Comparison with literature results (Chapter 5)

D

This section is adapted from Pesch et al. (2017) with permission.

The group of Lapizco-Encinas published two very comprehensive studies on the influence of post characteristics on their efficiency in immobilizing particles (LaLonde et al., 2014; Saucedo-Espinosa and Lapizco-Encinas, 2015) in channels containing arrays of insulating posts using *negative* DEP. The results are compared with the results of Chapter 5.

LaLonde et al. (2014) found that for quite narrowly spaced posts (post-to-post distance is one quarter of post's characteristic dimension) the posts with diamond-shaped cross section perform better than posts with ellipsoidal cross section at an aspect ratio of 1. This is consistent with the results from Fig. 5.3, at small values of H_{crit} usually the rhomboidal posts perform better (larger H_{crit}).

Also, when comparing the minimum required voltage for trapping and the mean field gradient between posts, LaLonde et al. (2014) found that the influence of the cross-sectional aspect ratio is more important for ellipsoidal posts than for posts with diamond-shaped cross section which is also consistent with our findings (again, cf. Fig. 5.3, the H_{crit} changes much more rapidly with AR for an ellipse than for a diamond).

Saucedo-Espinosa and Lapizco-Encinas (2015) indicate that both, the electric field and the resulting field gradient, on the centerline between two posts are stronger for an elliptical post than for an rhomboidal post with a characteristic dimension of 200 µm and a post-to-post distance of 50 µm. However, when comparing the minimum required voltage for trapping (Fig. 7), it is evident that diamond-shaped posts perform better in this base geometry case than ellipsoidal posts, which is also consistent with their previous results (LaLonde et al., 2014). Therefore, the centerline value of the field and the field gradient does not appear to be an adequate measure for assessment of the posts performance. The variation of the gradient with y is very different for different cross-sectional post geometries.

Further, Saucedo-Espinosa and Lapizco-Encinas (2015) found that their (geometrically averaged) trapping coefficient (which is a measure for the post's particle trapping effectivity) increases with increasing aspect ratio until a maximum is reached after which the trapping coefficient decreases again with aspect ratio. This increase and maximum is more significant for ellipsoidal posts than for rhomboidal. We found the same maximum for ellipsoidal posts but cannot see it for rhomboidal except for very small distances ($d_S = 500$ µm line in Fig. 5.3 d). It is assumed that the critical value shifts towards larger aspect ratios with decreasing post-to-post distance. According to the single post studies a decreasing spacing in y-direction between posts is beneficial because it forces particles to pass the posts closer to their surface (and thus they experience a higher gradient).

Additional experimental and simulative details (Chapter 6)

E

E.1 Microchannel design, experiments and simulation

The microchannels employed in the experiments and for the simulations employed slightly different geometries.

The microchannels used for experimentation have been drawn using Autodesk AutoCAD 2015 (student version for macOS). Two different masks and wafers were used for production; hence some channels show slightly different entrance lengths and heights.

Figure E.1 shows a generic drawing of a channel from AutoCAD used for experiments including the main parameters. Table E.1 gives values for that parameters for all channels used in the experimental section.

The flow rate Q is accurate for channels with $h = 120\,\mu\text{m}$ height, for channels with different height the flow rate was adjusted to compensate. The post array is centered in the channel in x direction, the placement in y direction does not follow a pattern and is random (that is, the first and last spacing could be different and one or two post's cross-sections could be cut in half in y direction). Eight dust blockers are employed on both sides of the array that were 1 mm long, 250 µm wide, and 150 µm spaced in y direction.

Figure E.2 shows a generic drawing of a channel from COMSOL used for simulations including the main parameters. The length of the array was fixed to $L_1 = 8\,\text{mm}$. Depending on h_S, $w_\text{S} = h_\text{S}/\text{AR}$, and d, the number of pillars in x direction is $n_x = \lfloor L_1/(d + w_\text{S})\rfloor$. Here, $\lfloor x\rfloor$ denote the floor function of x. The number of posts in y direction is $n_y = \lceil 2500\,\mu\text{m}/(h_\text{S} + d)\rceil$ with the ceil function of x, $\lceil x\rceil$. The channel width was always $W = (n_y + 1)(h_\text{S} + d)$. The posts were arranged in the center of the channel in both, x and y direction, so that half of the post's cross-section is cut off in y direction. Six dust blockers are positioned on both ends

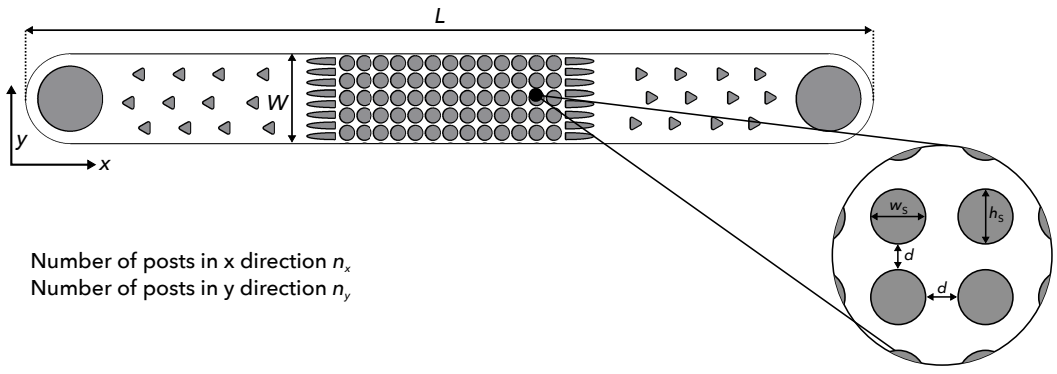

Fig. E.1: Channel design as used for the experiments including the important parameters

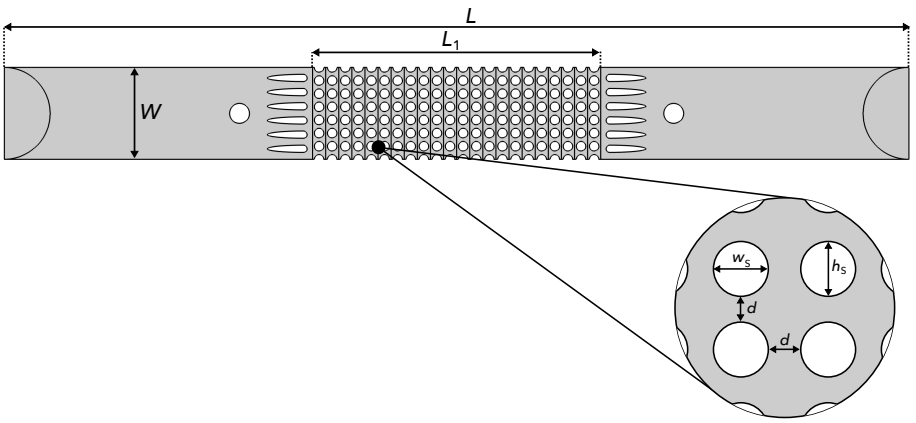

Fig. E.2: Channel design as used for the simulations including the important parameters

of the array that are approximately 1.1 mm long, 200 µm wide, and equally spaced in y direction. Since W depends on the channel geometry, the set flow rate was scaled according to $Q = Q_{\text{exp}} W / (2800\,\mu\text{m})$ where Q_{exp} is the nominal flow rate and Q is the set flow rate.

E.2 Experimental details

The microchannels have been produced using standard soft lithography techniques (Duffy et al., 1998) from polydimethylsiloxane (PDMS, Sylgard®184). The negative of the designs of Fig. E.1 and Tbl. E.1 where produced on 10 cm silica wafer using photo lithography with SU8. The masks for the photo lithography step are provided by CAD/Art Services Inc. and has a resolution of 20 000 DPI, that is, a single dot printed has a diameter of 1.27 µm (Kawale et al., 2017). According to CAD/Art Services, the smallest feature size is limited to 10 µm. Before the soft lithography step the SU8 negative was preconditioned with Trichloro(1*H*,1*H*,2*H*,2*H*-perfluorooctyl)silane in an evacuated desiccator for a minimum duration of 60 min. That allows an easier peel-off after curing. Sylgard®184 was mixed in a ratio of 10:1 (polymer to curing agent), degassed, and poured on the preconditioned SU8/Silica negative. Channels were cured at 140 °C for 15 min. After peeling off the PDMS designs from the wafer, three chips were diced according to the size of a microscope slide. Holes for the connection of the PTFE tubing (ID/OD 300 µm/1.6 mm, Kinesis) were punched with 1.5 mm diameter biopsy punches (World Precision Instruments Germany GmbH). Two holes for the electrodes (500 µm platinum wire) were punched with 0.5 mm diameter biopsy punches (also World Precision Instruments). PDMS-covered glass slides were prepared by spin coating isopropanol cleaned microscope slides with uncured PDMS at 3000 RPM for a duration of 1:30 minutes. The glass slides were subsequently cured at 70 °C for 60 min. The PDMS-covered glass slides and the diced PDMS chips were cleaned 5–6 times using scotch tape and ethanol. Both sides of the channel were activated by exposing them to a low-pressure air plasma for 1:30 minutes. They were subsequently bonded by gently pressing them together.

Electrodes and tubing were simply stuck into the channel and were holding without aid. Fluid movement through the channel was realized using a kDScientific Legato®270 syringe

Tab. E.1: List of the parameters (as labeled in Fig. E.1) used in the experimental part of Chapter 6.

h_S in µm	w_S in µm	d in µm	W in mm	L in mm	height h in µm	n_x –	n_y –
262	262	38	2.78	43.75	120	27	9
262	262	66.4	2.78	43.75	120	25	8.5
262	262	162	2.78	43.75	120	20	6.5
262	209.6	38	2.79	30	130	33	9
262	157.2	38	2.79	30	130	42	9

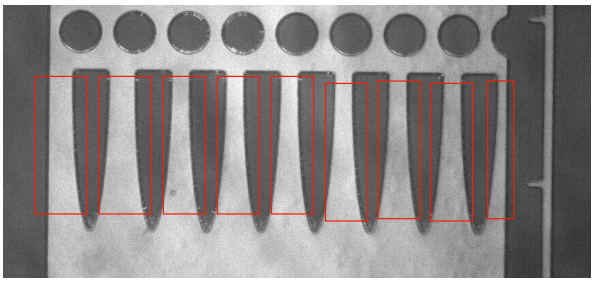

Fig. E.3: Example segmentation of a bright-field image into 9 independent parts

pump together with 3-mL BD LuerLock syringes. The connection between the syringe and the tubing was realized with Upchurch adapters. The electric field is applied across the electrodes with an ac high-voltage source (Trek PZD2000A) that was connected to a Rigol DG4062 arbitrary function generator. To calculate the separation efficiency, the particle flux into and out of the post array has been observed using an upright epifluorescence microscope (Carl Zeiss Axio Scope.A1 Vario equipped with a Lumenera Infinity 3S-1URM camera).

Standard monodisperse polystyrene particles have been employed, 1 µm, COOH-modified, fluorescent (Fluoresbrite®YG, ex/em 441/487; roughly FITC) from Polysciences Europe. The stock solution has been diluted to a final concentration of 2×10^5–8.5×10^5 particles per mL, depending on the flow rate employed. The conductivity has been adjusted using KCl to a value of 3.7×10^{-4} S m^{-1}. A homeopathic amount of Tween®20 (0.05 vol%) has been added to the solution in order to avoid unspecific adsorption of the microspheres on the PDMS surface. For clear fluorescent observation, the microscope was equipped with a HBO 100 mercury short-arc lamp together with the Carl Zeiss 65 HE filter set.

Three videos each were taken per channel and data point at the inlet (duration 70 s) and outlet (duration 100–160 s depending on the flow rate). Then, each video was segmented into 9 parts as outlined by Fig. E.3. This yields 9 independent videos. Each of them was binarized individually by setting a threshold and minimum particle size that were chosen per video according to the respective gray value distribution (not all videos are illuminated equally). The videos were binarized frame-by-frame using DIPimage toolbox for MATLAB[1]. Subsequently, in every frame all isolated bright spots were counted as a single particle. For each particle, the center location was extracted. The most probable tracks across all centers in the video for all

[1] http://www.diplib.org

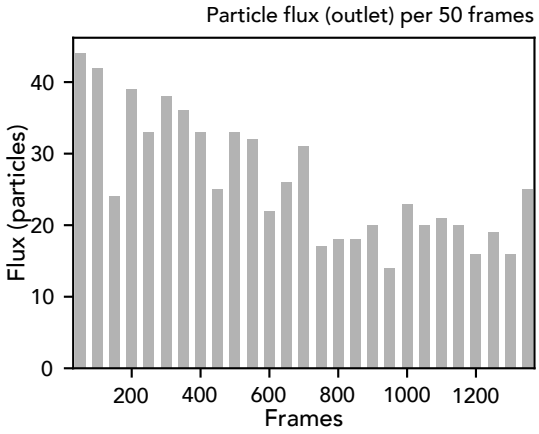

Fig. E.4: Particle flux at the outlet (arbitrary parameters) per 50 frames. DEP was switched on after 10 s which are approximately 135 frames.

time steps were obtained by applying the Simple Tracker Algorithm of Jean-Yves Tinevez[2]. The particle flux is the amount of particles that crosses exactly the centerline of the video segment in flow direction in a specific time frame. It was recorded in bins of 50 frames. All videos were recorded with a variable frame rate that was always between 12.5 and 14.5 FPS. That means that the particle flux in 50 frames is roughly the flux in 3.33 s. The flux per video is then the sum over all 9 segments. Fig. E.4 shows an example of such a flux plot. The average flux of an inlet video is averaged over frames 300–950 and the outlet flux over frames 650–1300 (for flowrates $Q \geq 0.1\,\mathrm{mL\,h^{-1}}$) or 1500–1750 ($Q = 0.05\,\mathrm{mL\,h^{-1}}$).

E.3 Simulation details

The simulation was performed according to Fig. E.5 using the electrostatics and creeping flow modules. A fixed velocity $\boldsymbol{u} = (0, v_0)^\mathsf{T}$ was prescribed on the fluid inlet (Inlet boundary condition) with $v_0 = Q/W/h$ with $h = 120\,\mu\mathrm{m}$ and W according to Sec. E.1. A constant pressure of $p = 0\,\mathrm{bar}$ was prescribed for the fluid outlet (Outlet boundary condition). No-slip boundary conditions ($\boldsymbol{u} = 0$) were prescribed on all walls (Wall boundary condition). Constant potentials were prescribed on the two electrodes ($\Phi = U_0/2$ on the left electrode and $\Phi = -U_0/2$ on the right electrode). Zero charge boundary conditions (gradient in normal direction is zero, $\partial\Phi/\partial\hat{\boldsymbol{n}} = 0$) are applied on all other walls. 250 particles are initialized on random positions on a straight line between the electrode and the dust blockers at $t = 0$. The separation efficiency is obtained by comparing the amount of particles entering the channel with the amount of particles exiting the channel after. For the mesh generation, the maximum element size in the post array was set to the 1.2 µm. The relative tolerance of the time-dependent GMRES solver was set to 1.1×10^{-5}. The simulation duration was chosen according to the time that the particles need to pass the post array. 200 time steps have been calculated (albeit the GMRES solver adapts the time step according to the tolerance, the output times define the first time step taken by the solver before adapting).

[2]V1.5, https://de.mathworks.com/matlabcentral/fileexchange/34040-simple-tracker

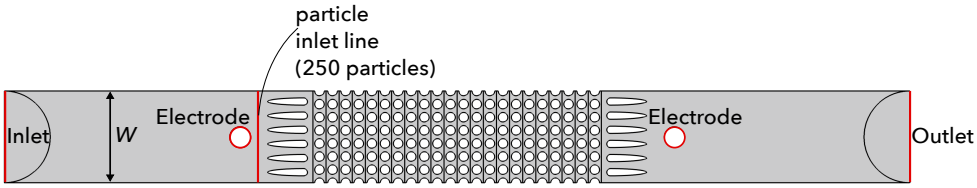

Fig. E.5: Outline of the simulated geometry including the boundary conditions

Bibliography

Abd Rahman, N., F. Ibrahim, and B. Yafouz (2017). Dielectrophoresis for Biomedical Sciences Applications: A Review. *Sensors* 17, 449.

Abdallah, B. G., S. Roy-Chowdhury, J. Coe, P. Fromme, and A. Ros (2015). High Throughput Protein Nanocrystal Fractionation in a Microfluidic Sorter. *Analytical Chemistry* 87, 4159–4167.

Ai, Y. and S. Qian (2010). DC dielectrophoretic particle–particle interactions and their relative motions. *Journal of Colloid and Interface Science* 346, 448–454.

Ai, Y., Z. Zeng, and S. Qian (2014). Direct numerical simulation of AC dielectrophoretic particle-particle interactive motions. *Journal of colloid and interface science* 417, 72–9.

Alnæs, M. S., A. Logg, K. B. Ølgaard, M. E. Rognes, and G. N. Wells (2014). Unified form language. *ACM Transactions on Mathematical Software* 40, 1–37.

Alnæs, M., A. Logg, K. A. Mardal, O. Skavhaug, and H. Langtangen (2009). Unified framework for finite element assembly. *International Journal of Computational Science and Engineering* 4, 231.

Aoki, R., N. Shirao, S. Uchida, and F. Tochikubo (2016). Numerical Investigation of the Correlation between Electrode Structure and Number of Captured Particles in a Dielectrophoretic Device. *Electronics and Communications in Japan* 99, 21–28.

Arcenegui, J. J., A. Ramos, P. García-Sánchez, and H. Morgan (2013). Electrorotation of titanium microspheres. *Electrophoresis* 34, 979–86.

Arnold, W. M., H. P. Schwan, and U. Zimmermann (1987). Surface conductance and other properties of latex particles measured by electrorotation. *The Journal of Physical Chemistry* 91, 5093–5098.

Aubry, N. and P. Singh (2006). Control of electrostatic particle-particle interactions in dielectrophoresis. *Europhysics Letters (EPL)* 74, 623–629.

Balasubramanian, P., R. J. Kinders, S. Kummar, et al. (2017). Antibody-independent capture of circulating tumor cells of non-epithelial origin with the ApoStream® system. *PLOS ONE* 12. Ed. by J. Najbauer, e0175414.

Ballantyne, G. and P. Holtham (2010). Application of dielectrophoresis for the separation of minerals. *Minerals Engineering* 23, 350–358.

Ballantyne, G. and P. Holtham (2014). Evaluation of the potential for using dielectrophoresis to separate minerals. *Minerals Engineering* 55, 75–79.

Baylon-Cardiel, J. L., B. H. Lapizco-Encinas, C. Reyes-Betanzo, A. V. Chávez-Santoscoy, and S. O. Martínez-Chapa (2009). Prediction of trapping zones in an insulator-based dielectrophoretic device. *Lab on a chip* 9, 2896–2901.

Bazant, M. Z. (2011). „Induced-Charge Electrokinetic Phenomena". In: *Electrokinetics and Electrohydrodynamics in Microsystems*. Ed. by A. Ramos. 1st ed. Wien, New York: Springer, pp. 221–297.

Becker, F. F., X. B. Wang, Y. Huang, R. Pethig, J. Vykoukal, and P. R. Gascoyne (1995). Separation of human breast cancer cells from blood by differential dielectric affinity. *Proceedings of the National Academy of Sciences* 92, 860–864.

Benguigui, L. and I. J. Lin (1982). Dielectrophoretic Filtration of Nonconductive Liquids. *Separation Science and Technology* 17, 1003–1017.

Bharti, B., G. H. Findenegg, and O. D. Velev (2014). Analysis of the Field-Assisted Permanent Assembly of Oppositely Charged Particles. *Langmuir* 30, 6577–6587.

Bharti, B. and O. D. Velev (2015). Assembly of Reconfigurable Colloidal Structures by Multidirectional Field-Induced Interactions. *Langmuir* 31, 7897–7908.

Bowen, W. R. and H. A. Sabuni (1994). Electroosmotic Membrane Backwashing. *Ind. Eng. Chem. Res.* 33, 1245–1249.

Braasch, K., M. Nikolic-Jaric, T. Cabel, E. Salimi, G. E. Bridges, D. J. Thomson, and M. Butler (2013). The changing dielectric properties of CHO cells can be used to determine early apoptotic events in a bioprocess. *Biotechnology and Bioengineering* 110, 2902–2914.

Braff, W., A. Pignier, and C. R. Buie (2012). High sensitivity three-dimensional insulator-based dielectrophoresis. *Lab on a chip* 12, 1327–31.

Castellanos, A., A. Ramos, A. González, N. G. Green, and H. Morgan (2003). Electrohydrodynamics and dielectrophoresis in microsystems: scaling laws. *Journal of Physics D: Applied Physics* 36, 2584–2597.

Čemažar, J., T. A. Douglas, E. M. Schmelz, and R. V. Davalos (2016). Enhanced contactless dielectrophoresis enrichment and isolation platform via cell-scale microstructures. *Biomicrofluidics* 10, 014109.

Çetin, B., S. D. Öner, and B. Baranoğlu (2017). Modeling of dielectrophoretic particle motion: Point particle versus finite-sized particle. *Electrophoresis* 38, 1407–1418.

Chaurey, V., A. Rohani, Y. H. Su, K. T. Liao, C. F. Chou, and N. S. Swami (2013). Scaling down constriction-based (electrodeless) dielectrophoresis devices for trapping nanoscale bioparticles in physiological media of high-conductivity. *Electrophoresis* 34, 1097–1104.

Chen, H., Y. Liu, H. Zhang, L. Yu, Y. Zhu, and D. Li (2010). Separation and Manipulation of Rare-earth Oxide Particles by Dielectrophoresis. *Chinese Journal of Chemical Engineering* 18, 1034–1037.

Cheng, I.-F., H.-C. Chang, D. Hou, and H.-C. Chang (2007). An integrated dielectrophoretic chip for continuous bioparticle filtering, focusing, sorting, trapping, and detecting. *Biomicrofluidics* 1, 021503.

Cheng, I.-F., V. E. Froude, Y. Zhu, H.-C. Chang, and H.-C. Chang (2009). A continuous high-throughput bioparticle sorter based on 3D traveling-wave dielectrophoresis. *Lab on a Chip* 9, 3193.

Choongho Yu, J. Vykoukal, D. Vykoukal, J. Schwartz, Li Shi, and P. Gascoyne (2005). A three-dimensional dielectrophoretic particle focusing channel for microcytometry applications. *Journal of Microelectromechanical Systems* 14, 480–487.

Chou, C. F. and F. Zenhausern (2003). Electrodeless Dielectrophoresis for Micro Total Analysis Systems. *IEEE Engineering in Medicine and Biology Magazine* 22, 62–67.

Chou, C.-F., J. O. Tegenfeldt, O. Bakajin, S. S. Chan, E. C. Cox, N. Darnton, T. Duke, and R. H. Austin (2002). Electrodeless dielectrophoresis of single- and double-stranded DNA. *Biophysical journal* 83, 2170–9.

Chuang, C.-J., C.-Y. Wu, and C.-C. Wu (2008). Combination of crossflow and electric field for microfiltration of protein/microbial cell suspensions. *Desalination* 233, 295–302.

Crane, J. S. and H. A. Pohl (1968). A Study of Living and Dead Yeast Cells Using Dielectrophoresis. *Journal of The Electrochemical Society* 115, 584.

Crowther, C. V. and M. A. Hayes (2017). Refinement of insulator-based dielectrophoresis. *The Analyst* 142, 1608–1618.

Cummings, E. B. and A. K. Singh (2003). Dielectrophoresis in microchips containing arrays of insulating posts: theoretical and experimental results. *Analytical chemistry* 75, 4724–4731.

Decher, G. (1997). Fuzzy Nanoassemblies: Toward Layered Polymeric Multicomposites. *Science* 277, 1232–1237.

Delcea, M., H. Möhwald, and A. G. Skirtach (2011). Stimuli-responsive LbL capsules and nanoshells for drug delivery. *Advanced Drug Delivery Reviews* 63, 730–747.

Ding, J., R. M. Lawrence, P. V. Jones, B. G. Hogue, and M. A. Hayes (2016). Concentration of Sindbis virus with optimized gradient insulator-based dielectrophoresis. en. *The Analyst* 141, 1997–2008.

Du, F., M. Baune, A. Kück, and J. Thöming (2008). Dielectrophoretic Gold Particle Separation. *Separation Science and Technology* 43, 3842–3855.

Du, F., P. Ciaciuch, S. Bohlen, Y. Wang, M. Baune, and J. Thöming (2013). Intensification of crossflow membrane filtration using dielectrophoresis with a novel electrode configuration. *Journal of Membrane Science* 448, 256–261.

Du, F., A. Hawari, M. Baune, and J. Thöming (2009). Dielectrophoretically intensified cross-flow membrane filtration. *Journal of Membrane Science* 336, 71–78.

Duffy, D. C., J. C. McDonald, O. J. A. Schueller, and G. M. Whitesides (1998). Rapid Prototyping of Microfluidic Systems in Poly(dimethylsiloxane). *Analytical Chemistry* 70, 4974–4984.

Ermolina, I. and H. Morgan (2005). The electrokinetic properties of latex particles: comparison of electrophoresis and dielectrophoresis. *Journal of colloid and interface science* 285, 419–28.

Evoy, S., N. DiLello, V. Deshpande, et al. (2004). Dielectrophoretic assembly and integration of nanowire devices with functional CMOS operating circuitry. *Microelectronic Engineering* 75, 31–42.

Freer, E. M., O. Grachev, and D. P. Stumbo (2010). High-yield self-limiting single-nanowire assembly with dielectrophoresis. *Nature Nanotechnology* 5, 525–530.

Fritsche, G. R., R. S. V. Bujas, and G. C. Caprioglio (1994). „Electrostatic separator using a bead bed".

Gadish, N. and J. Voldman (2006). High-Throughput Positive-Dielectrophoretic Bioparticle Microconcentrator. *Analytical Chemistry* 78, 7870–7876.

Gallo-Villanueva, R. C., M. B. Sano, B. H. Lapizco-Encinas, and R. V. Davalos (2013). Joule heating effects on particle immobilization in insulator-based dielectrophoretic devices. *Electrophoresis*.

Gan, L., T. C. Chao, F. Camacho-Alanis, and A. Ros (2013). Six-helix bundle and triangle DNA origami insulator-based dielectrophoresis. *Analytical Chemistry* 85, 11427–11434.

Gangwal, S., O. J. Cayre, M. Z. Bazant, and O. D. Velev (2008). Induced-charge electrophoresis of metallodielectric particles. *Physical review letters* 100, 058302.

García-Sánchez, P., Y. Ren, J. J. Arcenegui, H. Morgan, and A. Ramos (2012). Alternating Current Electrokinetic Properties of Gold-Coated Microspheres. *Langmuir* 28, 13861–13870.

Gascoyne, P. R. C., J. Noshari, T. J. Anderson, and F. F. Becker (2009). Isolation of rare cells from cell mixtures by dielectrophoresis. *Electrophoresis* 30, 1388–1398.

Gascoyne, P., C. Mahidol, M. Ruchirawat, J. Satayavivad, P. Watcharasit, and F. F. Becker (2002). Microsample preparation by dielectrophoresis: isolation of malaria. *Lab on a Chip* 2, 70.

Gascoyne, P. and S. Shim (2014). Isolation of Circulating Tumor Cells by Dielectrophoresis. *Cancers* 6, 545–579.

Geuzaine, C. and J.-F. Remacle (2009). Gmsh: A 3-D finite element mesh generator with built-in pre- and post-processing facilities. *International Journal for Numerical Methods in Engineering* 79, 1309–1331.

Gierhart, B. C., D. G. Howitt, S. J. Chen, R. L. Smith, and S. D. Collins (2007). Frequency Dependence of Gold Nanoparticle Superassembly by Dielectrophoresis. *Langmuir* 23, 12450–12456.

Gimsa, J. (2001). A comprehensive approach to electro-orientation, electrodeformation, dielectrophoresis, and electrorotation of ellipsoidal particles and biological cells. *Bioelectrochemistry* 54, 23–31.

Green, N. G. and H. Morgan (1997). Dielectrophoretic investigations of sub-micrometre latex spheres. *Journal of Physics D: Applied Physics* 30, 2626–2633.

Green, N. G., A. Ramos, A. González, H. Morgan, and A. Castellanos (2000a). Fluid flow induced by nonuniform ac electric fields in electrolytes on microelectrodes. I. Experimental measurements. *Physical Review E* 61, 4011–4018.

Green, N. G., A. Ramos, A. González, H. Morgan, and A. Castellanos (2002a). Fluid flow induced by nonuniform ac electric fields in electrolytes on microelectrodes. III. Observation of streamlines and numerical simulation. *Physical Review E* 66, 026305.

Green, N. G., A. Ramos, and H. Morgan (2000b). Ac electrokinetics: a survey of sub-micrometre particle dynamics. en. *Journal of Physics D: Applied Physics* 33, 632–641.

Green, N., A. Ramos, and H. Morgan (2002b). Numerical solution of the dielectrophoretic and travelling wave forces for interdigitated electrode arrays using the finite element method. *Journal of Electrostatics* 56, 235–254.

Green, N. G. (2011a). „Dielectrophoresis and AC Electrokinetics". In: *Electrokinetics and Electrohydrodynamics in Microsystems*. Ed. by Ramos. 1st ed. Wien, New York: Springer, pp. 61–84.

Green, N. G. (2011b). „Electrostatics and Quasielectrostatics". In: *Electrokinetics and Electrohydrodynamics in Microsystems*. Ed. by A. Ramos. 1st ed. Wien, New York: Springer, pp. 29–59.

Green, N. G. and T. B. Jones (2007). Numerical determination of the effective moments of non-spherical particles. en. *Journal of Physics D: Applied Physics* 40, 78–85.

Green, N. G. and H. Morgan (1999). Dielectrophoresis of Submicrometer Latex Spheres. 1. Experimental Results. *The Journal of Physical Chemistry B* 103, 41–50.

Gu, Q., M. Guezo, H. Folliot, T. Batte, S. Loualiche, and J. Stervinou (2017). Heating-Enhanced Dielectrophoresis for Aligned Single-Walled Carbon Nanotube Film of Ultrahigh Density. *Nanoscale Research Letters* 12, 429.

Günther, S. and S. Odenbach (2016). A Method for Image Decomposition and Particle Quantification in Multiphase Systems. *Transport in Porous Media* 112, 105–116.

Hanson, C. and E. Vargis (2017). Alternative cDEP Design to Facilitate Cell Isolation for Identification by Raman Spectroscopy. *Sensors* 17, 327.

Hawari, A. H., F. Du, M. Baune, and J. Thöming (2015). A fouling suppression system in submerged membrane bioreactors using dielectrophoretic forces. *Journal of Environmental Sciences* 29, 139–145.

Hermanson, K. D., S. O. Lumsdon, J. P. Williams, E. W. Kaler, and O. D. Velev (2001). Dielectrophoretic Assembly of Electrically Functional Microwires from Nanoparticle Suspensions. *Science* 294.

Hoettges, K. F., J. W. Dale, and M. P. Hughes (2007). Rapid determination of antibiotic resistance in E. coli using dielectrophoresis. *Physics in Medicine and Biology* 52, 6001–6009.

Hölzel, R., N. Calander, Z. Chiragwandi, M. Willander, and F. F. Bier (2005). Trapping single molecules by dielectrophoresis. *Physical Review Letters* 95, 18–21.

Honegger, T., K. Berton, E. Picard, and D. Peyrade (2011). Determination of Clausius–Mossotti factors and surface capacitances for colloidal particles. *Applied Physics Letters* 98, 181906.

Hossan, M. R., R. Dillon, and P. Dutta (2014). Hybrid immersed interface-immersed boundary methods for AC dielectrophoresis. *Journal of Computational Physics* 270, 640–659.

Hossan, M. R., R. Dillon, A. K. Roy, and P. Dutta (2013). Modeling and simulation of dielectrophoretic particle–particle interactions and assembly. *Journal of Colloid and Interface Science* 394, 619–629.

Huang, H. and H. D. Ou-Yang (2017). A novel dielectrophoresis potential spectroscopy for colloidal nanoparticles. *Electrophoresis* 38, 1609–1616.

Huang, Y., R. Holzel, R. Pethig, and X.-B. Wang (1992). Differences in the AC electrodynamics of viable and non-viable yeast cells determined through combined dielectrophoresis and electrorotation studies. *Physics in Medicine and Biology* 37, 1499–1517.

Huang, Y., X. Wang, F. Becker, and P. Gascoyne (1997). Introducing dielectrophoresis as a new force field for field-flow fractionation. *Biophysical Journal* 73, 1118–1129.

Hughes, M. P. and H. Morgan (1999). Dielectrophoretic Characterization and Separation of Antibody-Coated Submicrometer Latex Spheres. *Analytical Chemistry* 71, 3441–3445.

Hughes, M. P. (2002a). Dielectrophoretic behavior of latex nanospheres: low-frequency dispersion. *Journal of colloid and interface science* 250, 291–4.

Hughes, M. P. (2002b). *Nanoelectromechanics in Engineering and Biology*. 1st ed. Boca Raton: CRC Press.

Hughes, M., H. Morgan, and M. Flynn (1999). The Dielectrophoretic Behavior of Submicron Latex Spheres: Influence of Surface Conductance. *Journal of colloid and interface science* 220, 454–457.

Huotari, H., G. Trägårdh, and I. Huisman (1999). Crossflow Membrane Filtration Enhanced by an External DC Electric Field: A Review. *Chemical Engineering Research and Design* 77, 461–468.

Iliescu, C., G. Tresset, and G. Xu (2007a). Continuous field-flow separation of particle populations in a dielectrophoretic chip with three dimensional electrodes. *Applied Physics Letters* 90, 234104.

Iliescu, C., G. L. Xu, P. L. Ong, and K. J. Leck (2007b). Dielectrophoretic separation of biological samples in a 3D filtering chip. *Journal of Micromechanics and Microengineering* 17, S128–S136.

Iliescu, C., G. Xu, F. C. Loe, P. L. Ong, and F. E. H. Tay (2007c). A 3-D dielectrophoretic filter chip. *Electrophoresis* 28, 1107–1114.

Iliescu, C., L. Yu, G. Xu, and F. E. H. Tay (2006). A Dielectrophoretic Chip With a 3-D Electric Field Gradient. *Journal of Microelectromechanical Systems* 15, 1506–1513.

Jackson, J. D. (2013). *Klassische Elektrodynamik*. 5th ed. Berlin, Boston: Walter de Gruyter.

Jia, Y., Y. Ren, and H. Jiang (2015). Continuous dielectrophoretic particle separation using a microfluidic device with 3D electrodes and vaulted obstacles. *Electrophoresis* 36, 1744–1753.

Jones, P. V. and M. A. Hayes (2015). Development of the resolution theory for gradient insulator-based dielectrophoresis. *Electrophoresis* 36, 1098–106.

Jones, P. V., S. Huey, P. Davis, R. McLemore, A. McLaren, and M. A. Hayes (2015). Biophysical separation of Staphylococcus epidermidis strains based on antibiotic resistance. *The Analyst* 140, 5152–5161.

Jones, P. V., S. J. R. Staton, and M. A. Hayes (2011). Blood cell capture in a sawtooth dielectrophoretic microchannel. *Analytical and Bioanalytical Chemistry* 401, 2103–2111.

Jones, P. V., G. L. Salmon, and A. Ros (2017). Continuous Separation of DNA Molecules by Size Using Insulator-Based Dielectrophoresis. *Analytical Chemistry* 89, 1531–1539.

Jones, T. and M. Washizu (1996). Multipolar dielectrophoretic and electrorotation theory. *Journal of Electrostatics* 37, 121–134.

Jones, T. B. (1995). *Electromechanics of Particles*. 1st ed. Cambridge: Cambridge University Press.

Kadaksham, J., P. Singh, and N. Aubry (2005). Dielectrophoresis induced clustering regimes of viable yeast cells. *Electrophoresis* 26, 3738–44.

Kang, H., B. Wang, S. Hong, J. J. Bae, D. Kim, C.-s. Han, Y. H. Lee, and S. Baik (2013). Dielectrophoretic separation of metallic arc-discharge single-walled carbon nanotubes in a microfluidic channel. *Synthetic Metals* 184, 23–28.

Kang, J., S. Hong, Y. Kim, and S. Baik (2009). Controlling the Carbon Nanotube-to-Medium Conductivity Ratio for Dielectrophoretic Separation. *Langmuir* 25, 12471–12474.

Kang, K. H., Y. Kang, X. Xuan, and D. Li (2006a). Continuous separation of microparticles by size with Direct current-dielectrophoresis. *Electrophoresis* 27, 694–702.

Kang, K. H., X. Xuan, Y. Kang, and D. Li (2006b). Effects of dc-dielectrophoretic force on particle trajectories in microchannels. *Journal of Applied Physics* 99, 064702.

Kang, S. (2014). Dielectrophoretic motion of two particles with diverse sets of the electric conductivity under a uniform electric field. *Computers & Fluids*.

Kang, Y., D. Li, S. A. Kalams, and J. E. Eid (2008). DC-Dielectrophoretic separation of biological cells by size. *Biomedical Microdevices* 10, 243–249.

Kawabata, T. and M. Washizu (2001). Dielectrophoretic detection of molecular bindings. *IEEE Transactions on Industry Applications* 37, 1625–1633.

Kawale, D., E. Marques, P. L. J. Zitha, M. T. Kreutzer, W. R. Rossen, and P. E. Boukany (2017). Elastic instabilities during the flow of hydrolyzed polyacrylamide solution in porous media: effect of pore-shape and salt. *Soft Matter* 13, 765–775.

Kim, B. C., S. W. Park, and D. G. Lee (2008a). Fracture toughness of the nano-particle reinforced epoxy composite. *Composite Structures* 86, 69–77.

Kim, S., Y. Xuan, P. Ye, S. Mohammadi, and S. Lee (2008b). Single-walled carbon nanotube transistors fabricated by advanced alignment techniques utilizing CVD growth and dielectrophoresis. *Solid-State Electronics* 52, 1260–1263.

Kim, U., J. Qian, S. A. Kenrick, P. S. Daugherty, and H. T. Soh (2008c). Multitarget Dielectrophoresis Activated Cell Sorter. *Analytical Chemistry* 80, 8656–8661.

Kirby, R. C. (2004). Algorithm 839. *ACM Transactions on Mathematical Software* 30, 502–516.

Kirby, R. C. and A. Logg (2006). A compiler for variational forms. *ACM Transactions on Mathematical Software* 32, 417–444.

Koh, J. B. Y. and Marcos (2014). Effect of dielectrophoresis on spermatozoa. *Microfluidics and Nanofluidics* 17, 613–622.

Kralj, J. G., M. T. W. Lis, M. A. Schmidt, and K. F. Jensen (2006). Continuous Dielectrophoretic Size-Based Particle Sorting. *Analytical Chemistry* 78, 5019–5025.

Krupke, R., F. Hennrich, H. v. Löhneysen, and M. M. Kappes (2003). Separation of Metallic from Semiconducting Single-Walled Carbon Nanotubes. *Science* 301.

Kumar, S., S. Rajaraman, R. A. Gerhardt, Z. L. Wang, and P. J. Hesketh (2005). Tin oxide nanosensor fabrication using AC dielectrophoretic manipulation of nanobelts. *Electrochimica Acta* 51, 943–951.

LaLonde, A., A. Gencoglu, M. F. Romero-Creel, K. S. Koppula, and B. H. Lapizco-Encinas (2014). Effect of insulating posts geometry on particle manipulation in insulator based dielectrophoretic devices. *Journal of Chromatography A* 1344, 99–108.

LaLonde, A., M. F. Romero-Creel, and B. H. Lapizco-Encinas (2015a). Assessment of cell viability after manipulation with insulator-based dielectrophoresis. *Electrophoresis* 36, 1479–1484.

LaLonde, A., M. F. Romero-Creel, M. A. Saucedo-Espinosa, and B. H. Lapizco-Encinas (2015b). Isolation and enrichment of low abundant particles with insulator-based dielectrophoresis. *Biomicrofluidics* 9, 064113.

Lapizco-Encinas, B. H., B. A. Simmons, E. B. Cummings, and Y. Fintschenko (2004a). Dielectrophoretic Concentration and Separation of Live and Dead Bacteria in an Array of Insulators. *Analytical Chemistry* 76, 1571–1579.

Lapizco-Encinas, B. H., B. A. Simmons, E. B. Cummings, and Y. Fintschenko (2004b). Insulator-based dielectrophoresis for the selective concentration and separation of live bacteria in water. *Electrophoresis* 25, 1695–1704.

Lee, J.-W., K.-J. Moon, M.-H. Ham, and J.-M. Myoung (2008). Dielectrophoretic assembly of GaN nanowires for UV sensor applications. *Solid State Communications* 148, 194–198.

Lewpiriyawong, N. and C. Yang (2014). Continuous separation of multiple particles by negative and positive dielectrophoresis in a modified H-filter. *Electrophoresis* 35, 714–20.

Lewpiriyawong, N., C. Yang, and Y. C. Lam (2008). Dielectrophoretic manipulation of particles in a modified microfluidic H filter with multi-insulating blocks. *Biomicrofluidics* 2, 034105.

Lewpiriyawong, N., C. Yang, and Y. C. Lam (2012). Electrokinetically driven concentration of particles and cells by dielectrophoresis with DC-offset AC electric field. *Microfluidics and Nanofluidics* 12, 723–733.

Li, J., Q. Zhang, D. Yang, and J. Tian (2004). Fabrication of carbon nanotube field effect transistors by AC dielectrophoresis method. *Carbon* 42, 2263–2267.

Liao, K.-T., M. Tsegaye, V. Chaurey, C.-F. Chou, and N. S. Swami (2012). Nano-constriction device for rapid protein preconcentration in physiological media through a balance of electrokinetic forces. *Electrophoresis* 33, 1958–66.

Lin, I. J. and L. Benguigui (1982). Dielectrophoretic Filtration of Liquids. II. Conducting Liquids. *Separation Science and Technology* 17, 645–654.

Lin, I. J. and L. Benguigui (1985). Dielectrophoretic Filtration in Time-Dependent Fields. *Separation Science and Technology* 20, 359–376.

Liu, L., C. Xie, B. Chen, and J. Wu (2015). Iterative dipole moment method for calculating dielectrophoretic forces of particle-particle electric field interactions. *Applied Mathematics and Mechanics* 36, 1499–1512.

Liu, W., C. Wang, H. Ding, J. Shao, and Y. Ding (2016). AC Electric field Induced Dielectrophoretic Assembly Behaviour of Gold Nanoparticles in a Wide Frequency Range. *Applied Surface Science* 370, 184–192.

Liu, X., J. L. Spencer, A. B. Kaiser, and W. M. Arnold (2006). Selective purification of multiwalled carbon nanotubes by dielectrophoresis within a large array. *Current Applied Physics* 6, 427–431.

Liu, X., J. L. Spencer, A. B. Kaiser, and W. Arnold (2004). Electric-field oriented carbon nanotubes in different dielectric solvents. *Current Applied Physics* 4, 125–128.

Logg, A., K.-A. Mardal, and G. N. Wells, eds. (2012a). *Automated Solution of Differential Equations by the Finite Element Method*. 1st ed. Heidelberg, Dordrecht, London, New York: Springer.

Logg, A., K.-A. Mardal, and G. Wells, eds. (2012b). *Automated Solution of Differential Equations by the Finite Element Method*. Vol. 84. Lecture Notes in Computational Science and Engineering. Berlin, Heidelberg: Springer Berlin Heidelberg.

Logg, A. and G. N. Wells (2010). DOLFIN: Automated finite element computing. *ACM Transactions on Mathematical Software* 37, 1–28.

Loginov, M., M. Citeau, N. Lebovka, and E. Vorobiev (2013). Electro-dewatering of drilling sludge with liming and electrode heating. *Separation and Purification Technology* 104, 89–99.

Lucci, M., P. Regoliosi, A. Reale, et al. (2005). Gas sensing using single wall carbon nanotubes ordered with dielectrophoresis. *Sensors and Actuators B: Chemical* 111-112, 181–186.

Lungu, M. (2006). Separation of small metallic nonferrous particles in low concentration from mineral wastes using dielectrophoresis. *International Journal of Mineral Processing* 78, 215–219.

Markx, G. H., P. A. Dyda, and R. Pethig (1996). Dielectrophoretic separation of bacteria using a conductivity gradient. *Journal of Biotechnology* 51, 175–180.

Markx, G. H. and R. Pethig (1995). Dielectrophoretic separation of cells: Continuous separation. *Biotechnology and Bioengineering* 45, 337–343.

Markx, G. H., R. Pethig, and J. Rousselet (1997a). The dielectrophoretic levitation of latex beads, with reference to field-flow fractionation. *Journal of Physics D: Applied Physics* 30, 2470–2477.

Markx, G. H., J. Rousselet, and R. Pethig (1997b). DEP-FFF: Field-Flow Fractionation Using Non-Uniform Electric Fields. *Journal of Liquid Chromatography & Related Technologies* 20, 2857–2872.

Markx, G. H., M. S. Talary, and R. Pethig (1994). Separation of viable and non-viable yeast using dielectrophoresis. *Journal of Biotechnology* 32, 29–37.

Mata-Gómez, M. A., R. C. Gallo-Villanueva, J. González-Valdez, S. O. Martínez-Chapa, and M. Rito-Palomares (2016a). Dielectrophoretic behavior of PEGylated RNase A inside a microchannel with diamond-shaped insulating posts. *Electrophoresis* 37, 519–528.

Mata-Gómez, M. A., V. H. Perez-Gonzalez, R. C. Gallo-Villanueva, J. Gonzalez-Valdez, M. Rito-Palomares, and S. O. Martinez-Chapa (2016b). Modelling of electrokinetic phenomena for capture of PEGylated ribonuclease A in a microdevice with insulating structures. *Biomicrofluidics* 10, 033106.

Mernier, G., N. Piacentini, R. Tornay, N. Buffi, and P. Renaud (2011). Cell viability assessment by flow cytometry using yeast as cell model. *Sensors and Actuators B: Chemical* 154, 160–163.

Miloh, T. (2011). Dipolophoresis of interacting conducting nano-particles of finite electric double layer thickness. *Physics of Fluids* 23, 122002.

Mohammadi, M., M. J. Zare, H. Madadi, J. Sellarès, and J. Casals-Terré (2016). A new approach to design an efficient micropost array for enhanced direct-current insulator-based dielectrophoretic trapping. *Analytical and bioanalytical chemistry*.

Molla, S. H., J. H. Masliyah, and S. Bhattacharjee (2005). Simulations of a dielectrophoretic membrane filtration process for removal of water droplets from water-in-oil emulsions. *Journal of Colloid and Interface Science* 287, 338–350.

Molla, S. and S. Bhattacharjee (2007). Dielectrophoretic levitation in the presence of shear flow: implications for colloidal fouling of filtration membranes. *Langmuir : the ACS journal of surfaces and colloids* 23, 10618–27.

Moncada-Hernandez, H., J. L. Baylon-Cardiel, V. H. Pérez-González, and B. H. Lapizco-Encinas (2011). Insulator-based dielectrophoresis of microorganisms: Theoretical and experimental results. *Electrophoresis* 32, 2502–2511.

Morgan, H. and N. G. Green (2002). *AC Electrokinetics: colloids and nanoparticles*. 1st ed. Baldock: Research Studies Press.

Morgan, H., A. G. Izquierdo, D. Bakewell, N. G. Green, and A. Ramos (2001). The dielectrophoretic and travelling wave forces generated by interdigitated electrode arrays: analytical solution using Fourier series. *Journal of Physics D: Applied Physics* 34, 1553–1561.

Nerowski, A., M. Poetschke, M. Bobeth, J. Opitz, and G. Cuniberti (2012). Dielectrophoretic Growth of Platinum Nanowires: Concentration and Temperature Dependence of the Growth Velocity. *Langmuir* 28, 7498–7504.

Nikolic-Jaric, M., T. Cabel, E. Salimi, A. Bhide, K. Braasch, M. Butler, G. E. Bridges, and D. J. Thomson (2013). Differential electronic detector to monitor apoptosis using dielectrophoresis-induced translation of flowing cells (dielectrophoresis cytometry). *Biomicrofluidics* 7, 024101.

Nili, H. and N. G. Green (2014). Higher-order dielectrophoresis of nonspherical particles. *Physical Review E* 89, 063302.

Oh, K., J.-H. Chung, J. J. Riley, Y. Liu, and W. K. Liu (2007). Fluid flow-assisted dielectrophoretic assembly of nanowires. *Langmuir : the ACS journal of surfaces and colloids* 23, 11932–40.

O'Konski, C. T. (1960). Electric properties of macromolecules. V. Theory of ionic polarization in polyelectrolytes. *The Journal of Physical Chemistry* 64, 605–619.

Olariu, M., A. Arcire, and M. E. Plonska-Brzezinska (2017). Controlled Trapping of Onion-Like Carbon (OLC) via Dielectrophoresis. *Journal of Electronic Materials* 46, 443–450.

Park, S., Y. Zhang, T.-H. Wang, and S. Yang (2011). Continuous dielectrophoretic bacterial separation and concentration from physiological media of high conductivity. *Lab on a Chip* 11, 2893.

Patel, S., D. Showers, P. Vedantam, T.-R. Tzeng, S. Qian, and X. Xuan (2012). Microfluidic separation of live and dead yeast cells using reservoir-based dielectrophoresis. *Biomicrofluidics* 6, 034102.

Perez, F. and B. E. Granger (2007). IPython: A System for Interactive Scientific Computing. *Computing in Science & Engineering* 9, 21–29.

Pesch, G. R., F. Du, M. Baune, and J. Thöming (2017). Influence of geometry and material of insulating posts on particle trapping using positive dielectrophoresis. *Journal of Chromatography A* 1483, 127–137.

Pesch, G. R., F. Du, U. Schwientek, C. Gehrmeyer, A. Maurer, J. Thöming, and M. Baune (2014). Recovery of submicron particles using high-throughput dielectrophoretically switchable filtration. *Separation and Purification Technology* 132, 728–735.

Pesch, G. R., L. Kiewidt, F. Du, M. Baune, and J. Thöming (2016). Electrodeless dielectrophoresis: Impact of geometry and material on obstacle polarization. *Electrophoresis* 37, 291–301.

Pethig, R. (2017). *Dielectrophoresis*. 1st ed. Hoboken: John Wiley & Sons, Ltd.

Pethig, R. and M. Talary (2007). Dielectrophoretic detection of membrane morphology changes in Jurkat T-cells undergoing etoposide-induced apoptosis. *IET Nanobiotechnology* 1, 2.

Pethig, R. (2010). Review article-dielectrophoresis: status of the theory, technology, and applications. *Biomicrofluidics* 4, 1–35.

Pethig, R. (2013). Dielectrophoresis: an assessment of its potential to aid the research and practice of drug discovery and delivery. *Advanced drug delivery reviews* 65, 1589–99.

Pohl, H. A. and J. P. Schwar (1959). Factors Affecting Separations of Suspensions in Nonuniform Electric Fields. *Journal of Applied Physics* 30, 69–73.

Pohl, H. A. (1951). The Motion and Precipitation of Suspensoids in Divergent Electric Fields. *Journal of Applied Physics* 22, 869–871.

Pohl, H. A. (1978). *Dielectrophoresis*. London, New York, Melbourne: Cambridge University Press.

Pohl, H. A. and I. Hawk (1966). Separation of Living and Dead Cells by Dielectrophoresis. *Science* 152, 647–649.

Pohl, H. A. (1958). Some Effects of Nonuniform Fields on Dielectrics. *Journal of Applied Physics* 29, 1182–1188.

Polomska, A., J.-C. Leroux, and D. Brambilla (2016). Layer-by-Layer Coating of Solid Drug Cores: A Versatile Method to Improve Stability, Control Release and Tune Surface Properties. *Macromolecular Bioscience*.

Pysher, M. D. and M. A. Hayes (2007). Electrophoretic and dielectrophoretic field gradient technique for separating bioparticles. *Analytical chemistry* 79, 4552–7.

Ramos, A., H. Morgan, N. G. Green, and a. Castellanos (1998). Ac electrokinetics: a review of forces in microelectrode structures. en. *Journal of Physics D: Applied Physics* 31, 2338–2353.

Ramos, A., P. G. A-Sánchez, and H. Morgan (2016). AC Electrokinetics of conducting microparticles: A review. *Current Opinion in Colloid & Interface Science* 24, 79–90.

Ranjan, N., H. Vinzelberg, and M. Mertig (2006). Growing One-Dimensional Metallic Nanowires by Dielectrophoresis. *Small* 2, 1490–1496.

Raychaudhuri, S., S. A. Dayeh, D. Wang, and E. T. Yu (2009). Precise semiconductor nanowire placement through dielectrophoresis. *Nano letters* 9, 2260–6.

Regtmeier, J., T. T. Duong, R. Eichhorn, D. Anselmetti, and A. Ros (2007). Dielectrophoretic Manipulation of DNA: Separation and Polarizability. *Analytical Chemistry* 79, 3925–3932.

Regtmeier, J., R. Eichhorn, L. Bogunovic, A. Ros, and D. Anselmetti (2010). Dielectrophoretic Trapping and Polarizability of DNA: The Role of Spatial Conformation. *Analytical Chemistry* 82, 7141–7149.

Regtmeier, J., R. Eichhorn, M. Viefhues, L. Bogunovic, and D. Anselmetti (2011). Electrodeless dielectrophoresis for bioanalysis: theory, devices and applications. *Electrophoresis* 32, 2253–73.

Ren, Y. K., D. Morganti, H. Y. Jiang, A. Ramos, and H. Morgan (2011). Electrorotation of Metallic Microspheres. *Langmuir* 27, 2128–2131.

Rohani, A., B. J. Sanghavi, A. Salahi, K.-T. Liao, C.-F. Chou, N. S. Swami, C.-F. Chou, and N. S. Swami (2017). Frequency-selective electrokinetic enrichment of biomolecules in physiological media based on electrical double-layer polarization. *Nanoscale* 311, 507–513.

Romero-Creel, M., E. Goodrich, D. Polniak, and B. Lapizco-Encinas (2017). Assessment of Sub-Micron Particles by Exploiting Charge Differences with Dielectrophoresis. *Micromachines* 8, 239.

Rosales, C. and K. M. Lim (2005). Numerical comparison between Maxwell stress method and equivalent multipole approach for calculation of the dielectrophoretic force in single-cell traps. *Electrophoresis* 26, 2057–2065.

Rouabah, H. A., B. Y. Park, R. B. Zaouk, H. Morgan, M. J. Madou, and N. G. Green (2011). Design and fabrication of an ac-electro-osmosis micropump with 3D high-aspect-ratio electrodes using only SU-8. *Journal of Micromechanics and Microengineering* 21, 035018.

Salmanzadeh, A., L. Romero, H. Shafiee, R. C. Gallo-Villanueva, M. A. Stremler, S. D. Cramer, and R. V. Davalos (2012). Isolation of prostate tumor initiating cells (TICs) through their dielectrophoretic signature. *Lab Chip* 12, 182–189.

Salmanzadeh, A., H. Shafiee, M. B. Sano, M. A. Stremler, and R. V. Davalos (2011). „Enrichment of Cancer Cells Using a High Throughput Contactless Dielectrophoretic (CDEP) Microfluidic Device". In: *ASME 2011 Summer Bioengineering Conference, Parts A and B*. ASME, p. 47.

Sano, N., K. Iwase, and H. Tamon (2013). In-Situ Estimation of Selective Capture of Tungsten Carbide Particles from Mixture with Diatomite Particles by Mesh-Stacked Dielectrophoresis Separator. *Journal of Chemical Engineering of Japan* 46, 535–540.

Sano, N., B. Matsukura, Y. Ikeyama, and H. Tamon (2012). Dielectrophoretic particle separator using mesh stacked electrodes and simplified model for multistage separation. *Chemical Engineering Science* 84, 345–350.

Sano, N., S. Matsuoka, and H. Tamon (2014). Purification of titanate nanotubes using a mesh-stacked dielectrophoretic separator equipped with carbon nanotube electrodes. *Chemical Engineering Science* 108, 188–193.

Sano, N., Y. Tanemori, and H. Tamon (2016). A selective dielectrophoretic particle separator using flat electrodes covered with vertically aligned carbon nanotubes. *Chemical Engineering Science* 144, 321–325.

Saucedo-Espinosa, M. and B. Lapizco-Encinas (2015). Design of insulator-based dielectrophoretic devices: Effect of insulator posts characteristics. *Journal of Chromatography A* 1422, 325–333.

Saucedo-Espinosa, M. A., M. M. Rauch, A. LaLonde, and B. H. Lapizco-Encinas (2016). Polarization behavior of polystyrene particles under direct current and low-frequency (<1 kHz) electric fields in dielectrophoretic systems. *Electrophoresis* 37, 635–644.

Saucedo-Espinosa, M. A. and B. H. Lapizco-Encinas (2017). Exploiting Particle Mutual Interactions To Enable Challenging Dielectrophoretic Processes. *Analytical Chemistry* 89, 8459–8467.

Seo, H.-W., C.-S. Han, D.-G. Choi, K.-S. Kim, and Y.-H. Lee (2005). Controlled assembly of single SWNTs bundle using dielectrophoresis. *Microelectronic Engineering* 81, 83–89.

Shafiee, H., J. L. Caldwell, M. B. Sano, and R. V. Davalos (2009). Contactless dielectrophoresis: a new technique for cell manipulation. *Biomedical Microdevices* 11, 997–1006.

Shafiee, H., M. B. Sano, E. A. Henslee, J. L. Caldwell, and R. V. Davalos (2010). Selective isolation of live/dead cells using contactless dielectrophoresis (cDEP). *Lab on a Chip* 10, 438.

Shim, H. C., Y. K. Kwak, C.-S. Han, and S. Kim (2009). Effect of a square wave on an assembly of multi-walled carbon nanotubes using AC dielectrophoresis. *Physica E: Low-dimensional Systems and Nanostructures* 41, 1137–1142.

Shim, S., K. Stemke-Hale, A. M. Tsimberidou, J. Noshari, T. E. Anderson, and P. R. C. Gascoyne (2013). Antibody-independent isolation of circulating tumor cells by continuous-flow dielectrophoresis. *Biomicrofluidics* 7, 011807.

Shin, D. H., J.-E. Kim, H. C. Shim, et al. (2008). Continuous Extraction of Highly Pure Metallic Single-Walled Carbon Nanotubes in a Microfluidic Channel. *Nano Letters* 8, 4380–4385.

Squires, T. M. and M. Z. Bazant (2006). Breaking symmetries in induced-charge electro-osmosis and electrophoresis. English. *Journal of Fluid Mechanics* 560, 65.

Srivastava, S. K., A. Artemiou, and A. R. Minerick (2011a). Direct current insulator-based dielectrophoretic characterization of erythrocytes: ABO-Rh human blood typing. *Electrophoresis* 32, 2530–2540.

Srivastava, S. K., A. Gencoglu, and A. R. Minerick (2011b). DC insulator dielectrophoretic applications in microdevice technology: a review. *Analytical and bioanalytical chemistry* 399, 301–321.

Srivastava, S. K., J. L. Baylon-Cardiel, B. H. Lapizco-Encinas, and A. R. Minerick (2011c). A continuous DC-insulator dielectrophoretic sorter of microparticles. *Journal of Chromatography A* 1218, 1780–1789.

Suehiro, J., S.-I. Hidaka, S. Yamane, and K. Imasaka (2007). Fabrication of interfaces between carbon nanotubes and catalytic palladium using dielectrophoresis and its application to hydrogen gas sensor. *Sensors and Actuators B: Chemical* 127, 505–511.

Suehiro, J. and R. Pethig (1998). The dielectrophoretic movement and positioning of a biological cell using a three-dimensional grid electrode system. *Journal of Physics D: Applied Physics* 31, 3298–3305.

Suehiro, J., G. Zhou, M. Imamura, and M. Hara (2003). Dielectrophoretic filter for separation and recovery of biological cells in water. *IEEE Transactions on Industry Applications* 39, 1514–1521.

Tang, J., G. Yang, Q. Zhang, A. Parhat, B. Maynor, J. Liu, L.-C. Qin, and O. Zhou (2005). Rapid and Reproducible Fabrication of Carbon Nanotube AFM Probes by Dielectrophoresis. *Nano Letters* 5, 11–14.

Turcu, I. and C. M. Lucaciu (1989). Dielectrophoresis: a spherical shell model. *Journal of Physics A: Mathematical and General* 22, 985–993.

Vahey, M. D., L. Quiros Pesudo, J. P. Svensson, L. D. Samson, and J. Voldman (2013). Microfluidic genome-wide profiling of intrinsic electrical properties in Saccharomyces cerevisiae. *Lab on a Chip* 13, 2754.

Vijayaraghavan, A., S. Blatt, D. Weissenberger, M. Oron-Carl, F. Hennrich, D. Gerthsen, H. Hahn, and R. Krupke (2007). Ultra-Large-Scale Directed Assembly of Single-Walled Carbon Nanotube Devices. *Nano Letters* 7, 1556–1560.

Voigt, A., H. Lichtenfeld, G. B. Sukhorukov, H. Zastrow, E. Donath, H. Bäumler, and H. Möhwald (1999). Membrane Filtration for Microencapsulation and Microcapsules Fabrication by Layer-by-Layer Polyelectrolyte Adsorption. *Industrial & Engineering Chemistry Research* 38, 4037–4043.

Vykoukal, J., D. M. Vykoukal, S. Freyberg, E. U. Alt, and P. R. C. Gascoyne (2008). Enrichment of putative stem cells from adipose tissue using dielectrophoretic field-flow fractionation. *Lab on a Chip* 8, 1386.

Wakeman, R. and G. Butt (2003). An Investigation of High Gradient Dielectrophoretic Filtration. *Chemical Engineering Research and Design* 81, 924–935.

Wang, M. C. and B. D. Gates (2009). Directed assembly of nanowires. *Materials Today* 12, 34–43.

Wang, Q., N. N. Dingari, and C. R. Buie (2017). Nonlinear electrokinetic effects in insulator-based dielectrophoretic systems. *Electrophoresis*.

Wang, X.-B., R. Pethig, and T. B. Jones (1992). Relationship of dielectrophoretic and electrorotational behaviour exhibited by polarized particles. *Journal of Physics D: Applied Physics* 25, 905–912.

Wang, X.-B., J. Vykoukal, F. F. Becker, and P. R. Gascoyne (1998). Separation of Polystyrene Microbeads Using Dielectrophoretic/Gravitational Field-Flow-Fractionation. *Biophysical Journal* 74, 2689–2701.

Wang, X., F. F. Becker, and P. R. Gascoyne (2002). Membrane dielectric changes indicate induced apoptosis in HL-60 cells more sensitively than surface phosphatidylserine expression or DNA fragmentation. *Biochimica et Biophysica Acta (BBA) - Biomembranes* 1564, 412–420.

Wang, X., X.-B. Wang, and P. R. Gascoyne (1997). General expressions for dielectrophoretic force and electrorotational torque derived using the Maxwell stress tensor method. *Journal of Electrostatics* 39, 277–295.

Wang, Y., F. Du, M. Baune, and J. Thöming (2015). Predicting and eliminating Joule heating constraints in large dielectrophoretic IDE separators. *Chemical Engineering Science* 137, 235–242.

Wang, Y. (2016). „Continuous separation of microparticles in aqueous medium by means of dielectrophoresis“. Dissertation. University of Bremen.

Wei, M.-T., J. Junio, and H. D. Ou-Yang (2009). Direct measurements of the frequency-dependent dielectrophoresis force. *Biomicrofluidics* 3, 012003.

Wei, Y., W. Wei, L. Liu, and S. Fan (2008). Mounting multi-walled carbon nanotubes on probes by dielectrophoresis. *Diamond and Related Materials* 17, 1877–1880.

Wigley, N. M. (1988). An efficient method for subtracting off singularities at corners for laplace's equation. *Journal of Computational Physics* 78, 369–377.

Winter, W. T. and M. E. Welland (2009). Dielectrophoresis of non-spherical particles. *Journal of Physics D: Applied Physics* 42, 045501.

Xie, C., B. Chen, C.-O. Ng, X. Zhou, and J. Wu (2015). Numerical study of interactive motion of dielectrophoretic particles. *European Journal of Mechanics - B/Fluids* 49, 208–216.

Yang, J., Y. Huang, X.-B. Wang, F. F. Becker, and P. R. C. Gascoyne (1999). Cell Separation on Microfabricated Electrodes Using Dielectrophoretic/Gravitational Field-Flow Fractionation. *Analytical Chemistry* 71, 911–918.

Zangwill, A. (2013). *Modern Electrodynamics*. 1st ed. Cambridge, New York, Melbourne, Madrid, Cape Town, Singapore, São Paulo, Delhi, Mexico City: Cambridge University Press.

Zhang, H., J. Tang, P. Zhu, J. Ma, and L.-C. Qin (2009). High tensile modulus of carbon nanotube nano-fibers produced by dielectrophoresis. *Chemical Physics Letters* 478, 230–233.

Zhang, J., B. A. Grzybowski, and S. Granick (2017). Janus Particle Synthesis, Assembly, and Application. *Langmuir* 33, 6964–6977.

Zhang, W., J. Luo, L. Ding, and M. Y. Jaffrin (2015). A Review on Flux Decline Control Strategies in Pressure-Driven Membrane Processes. *Industrial & Engineering Chemistry Research* 54, 2843–2861.

Zhao, H. (2010). On the effect of hydrodynamic slip on the polarization of a nonconducting spherical particle in an alternating electric field. *Physics of Fluids* 22, 072004.

Zhao, H. (2011). Double-layer polarization of a non-conducting particle in an alternating current field with applications to dielectrophoresis. *Electrophoresis* 32, 2232–44.

Zhao, H. and H. H. Bau (2009). The polarization of a nanoparticle surrounded by a thick electric double layer. *Journal of Colloid and Interface Science* 333, 663–671.

Zhao, K. and D. Li (2017a). Continuous separation of nanoparticles by type via localized DC-dielectrophoresis using asymmetric nano-orifice in pressure-driven flow. *Sensors and Actuators B: Chemical* 250, 274–284.

Zhao, K. and D. Li (2017b). Numerical studies of manipulation and separation of Janus particles in nano-orifice based DC-dielectrophoretic microfluidic chips. *Journal of Micromechanics and Microengineering* 27, 095007.

Zhao, Y., J. Brcka, J. Faguet, and G. Zhang (2017). Elucidating the DEP phenomena using a volumetric polarization approach with consideration of the electric double layer. *Biomicrofluidics* 11, 024106.

Zhou, J. and F. Schmid (2013). Computer simulations of charged colloids in alternating electric fields. *The European Physical Journal Special Topics* 222, 2911–2922.

Zhou, J. and F. Schmid (2015). Computer simulations of single particles in external electric fields. *Soft Matter* 11, 6728–6739.

List of symbols

Symbol	Description	Unit
Roman		
AR	A post's cross-sectional width-to-height ratio	–
C	Correction factor (Eq. (2.45))	–
c	Volumetric number concentration (of particles)	m^{-3}
$\boldsymbol{D}$	Electric displacement field	$\mathrm{C\,m}^{-2}$
d	A distance, charge separation distance	m
d	Post-to-post spacing (Chapter 6)	m
d_P	Particle diameter	m
d_S	Major axis of the post's cross section	m
$d_\mathrm{P,crit}$	Critical particle diameter (Chapter 5)	m
$\boldsymbol{E}$	Electric field vector	$\mathrm{V\,m}^{-1}$
$\boldsymbol{E}_\mathrm{RMS}$	Electric field vector	$\mathrm{V_{RMS}\,m}^{-1}$
E_0	Excitatory electric field strength	$\mathrm{V\,m}^{-1}$
$\boldsymbol{F}$	A force	N
$\boldsymbol{F}_\mathrm{D}$	Drag force	N
$\boldsymbol{F}_\mathrm{DEP}$	Dielectrophoretic force	N
$\boldsymbol{F}_\mathrm{I}$	Inertia force	N
$\boldsymbol{F}_\mathrm{ip}$	Force between particle	N
f	Frequency (of the applied field)	Hz
f	Friction factor (Stokes' drag)	$\mathrm{kg\,s}^{-1}$
$\tilde{f}_\mathrm{CM}$	Clausius-Mossotti function	–
H, L	Starting distances in η and $-\xi$ direction	m
H_crit	Critical initial distance (Chapter 5)	m
h	Dimensionless cross-sectional height of the post	–
h	Channel height (Chapter 6)	m
h_S	Post size, Major axis of the post (Chapter 6)	m
$\boldsymbol{J}$	Electric current density	$\mathrm{A\,m}^{-2}$
j	Imaginary unit, $j^2 = -1$	–
K_s	Surface conductance	S
K_s^d	Diffuse layer conductance	S
K_s^s	Stern layer conductance	S
k_a, k_b	Constants (Eq. (6.6))	Depends

…(continued from previous page)

Symbol	Description	Unit
n	Iterator	–
$\hat{\boldsymbol{n}}$	Normal unit vector (to a surface)	–
$\boldsymbol{P}$	Polarization, volumetric dipole moment density	$\mathrm{C\,m^{-2}}$
$\boldsymbol{p}$, $\tilde{\boldsymbol{p}}$	(Complex) dipole moment	C m
p_n, p_k	Multipole moments (Chapters 4 and 5)	Depends
Q	Volumetric flow rate	$\mathrm{m^3\,s^{-1}}$
Q_1	Source charge	C
Q_2	Test charge	C
q	Volumetric flux	$\mathrm{m^3\,m^{-2}\,h^{-1}}$
R	Particle radius	m
r	A distance	m
r	Radial coordinate in (r, θ)	m
r'	Integration radius (Chapter 4)	–
$\boldsymbol{r}_{ij}$	Vector pointing from position 1 to 2	m
$\hat{\boldsymbol{r}}_{12}$	Unit vector between Q_1 and Q_2	–
t	Time	s
$\hat{\boldsymbol{t}}$	Tangential unit vector (to a surface)	–
V_P	Particle volume	$\mathrm{m^3}$
$\boldsymbol{u}$	A velocity	$\mathrm{m\,s^{-1}}$
$\boldsymbol{v}$	A velocity	$\mathrm{m\,s^{-1}}$
$\boldsymbol{v}_\mathrm{DEP}$	Terminal dielectrophoretic velocity	$\mathrm{m\,s^{-1}}$
$\boldsymbol{v}_\mathrm{F}$	Fluid velocity	$\mathrm{m\,s^{-1}}$
$\boldsymbol{v}_\mathrm{rel}$	Relative velocity between particle and fluid	$\mathrm{m\,s^{-1}}$
v_F	Velocity in ξ-direction (Chapter 5)	$\mathrm{m\,s^{-1}}$
w	Dimensionless cross-sectional width of the post	–
w	Channel width (Chapter 6)	m
$\boldsymbol{x}$	Position vector	m
$\overline{x}$	$\overline{x} = (\Delta V)^2 d_\mathrm{P}^2 Q^{-1} \epsilon_\mathrm{1d} h_\mathrm{S}^{-1}$ (Chapter 6)	$\mathrm{V_{RMS}{}^2\,h\,m^{-2}}$
Greek		
Γ_ROT	Electrorotational torque	N m
ΔV	Applied voltage drop (Chapter 6)	$\mathrm{V_{RMS}}$
δ	Loss angle	rad
ϵ_1d	One-dimensional projected porosity	–
ε_r	Relative permittivity	–
ε_1	Post's relative permittivity (Chapters 4 and 5)	–
ε_2	Surrounding medium's permittivity (Chapters 4 and 5)	–
$\tilde{\varepsilon}$	Complex permittivity	$\mathrm{F\,m^{-1}}$
$\tilde{\varepsilon}_\mathrm{i}$	Complex inside (particle) permittivity	$\mathrm{F\,m^{-1}}$
$\tilde{\varepsilon}_\mathrm{o}$	Complex outside (medium) permittivity	$\mathrm{F\,m^{-1}}$

…(continued from previous page)

Symbol	Description	Unit
$\tilde{\varepsilon}_p$	Complex particle permittivity	$F\,m^{-1}$
$\tilde{\varepsilon}_m$	Complex medium permittivity	$F\,m^{-1}$
η	Separation efficiency	%
η_{exp}	Experimentally obtained separation efficiency	%
η_{sim}	Simulated separation efficiency	%
μ_{DEP}	Dielectrophoretic mobility	$m^4\,V^{-2}\,s^{-1}$
μ_F	Dynamic viscosity of the medium	Pa s
θ	Angular coordinate in (r, θ)	°, rad
θ_0	Intersection angle (Chapter 6)	°, rad
ξ, η	Coordinate system (Chapter 5)	m
ρ	Volumetric electric charge density	$C\,m^{-3}$
ρ_b	Bound charge density	$C\,m^{-3}$
ρ_f	Free charge density	$C\,m^{-3}$
σ	Electric conductivity	$S\,m^{-1}$
σ_m	Medium conductivity	$S\,m^{-1}$
σ_P	Particle conductivity	$S\,m^{-1}$
τ	Relaxation time	s
Φ	Electrostatic potential	V, V_{RMS}, V_{pp}
Φ_0	Applied potential, applied voltage	V, V_{RMS}, V_{pp}
Φ_2	Polarization potential (due to a post, Chapter 4)	–
χ_{ae}	Electric susceptibility	–
Ω_1	Inside (post) domain (Chapter 4)	–
Ω_2	Outside (surrounding medium) domain (Chapter 4)	–
ω	Angular frequency	$rad\,s^{-1}$
Constants		
ε_0	Vacuum permittivity, $\varepsilon_0 = 8.854 \times 10^{-12}\,F\,m^{-1}$	
Abbreviations		
ac	Alternating current	
CNT	Carbon nanotube	
COOH	Carboxylic acid	
CTC	Circulating tumor cell	
dc	Direct current	
DEP	Dielectrophoresis	
eDEP	electrodeless/electrode-based dielectrophoresis	
EP	Electrophoresis	
EO	Electro-osmosis	
EOr	Electro-orientation	
FFF	Field flow fractionation	

…(continued from previous page)

Symbol	Description	Unit
ID	Inner diameter	
iDEP	insulator-based dielectrophoresis	
LbL	Layer-by-layer	
OD	Outer diameter	
PDMS	Polydimethylsiloxane	
PMMA	Poly(methyl methacrylate)	
PS	Polystyrene	
PTFE	Polytetrafluoroethylene	
PVC	Polyvinyl chloride	
ROT	Electrorotation	
RMS	Root mean square	

Students' work

In this disseration, the results from the supervision of the following students' works are included:

Lukas Büther, „Dielektrophoretische Filtration von Mikro- und Nanopartikeln in porösen Schichten“, *M. Sc. Thesis*, March 2016

Harm Ridder, „Simulation der dielektrophoretischen Partikelabscheidung in Kugelschüttungen“, *B. Sc. Thesis*, May 2016

Additionally, the following two students' works were supervised by Fei Du. Their results have been used to prepare the manuscript presented in Chapter 1:

Udo Schwientek und Caspar Gehrmeyer, „Elektromembranverfahren zur Aufreinigung von Nanokapseln“, *B. Sc. Thesis*, August 2010

Alexander Maurer, „Elektromembranverfahren zur Nanopartikelseparation - Anwendungsbezogene Verfahrensentwicklung“, *M. Sc. Thesis*, April 2011

Colophon

This thesis was typeset with LaTeX 2_ε in Adobe Garamond Pro and Avenir Next. Plots were created with Matplotlib for Python 3 or Inkscape. The cover picture is based on a photograph of fluorescent microspheres in a microchannel and was designed by Konrad Pesch. The thesis uses the *Clean Thesis* style developed by Ricardo Langner. The design of the *Clean Thesis* style is inspired by user guide documents from Apple Inc.

Download the *Clean Thesis* style at `http://cleanthesis.der-ric.de/`.